

DISS. ETH NO. 23772

**Beyond debuttressing: Thermo-hydro-mechanical  
rock slope damage during glacial cycles**

A thesis submitted to attain the degree of  
DOCTOR OF SCIENCES of ETH Zurich  
(Dr. sc. ETH Zurich)

presented by  
LORENZ MAURUS GRÄMIGER

MSc ETH Engineering Geology, ETH Zurich

born on 29.10.1986  
citizen of Kirchberg, St. Gallen

Accepted on the recommendation of  
Prof. Dr. Simon Loew, examiner  
Prof. Dr. Jeffrey Moore, co-examiner  
Dr. Valentin Gischig, co-examiner  
Prof. Dr. Oliver Korup, co-examiner

2017



## Abstract

Cycles of glaciation drive *in-situ* stress changes in underlying bedrock as glaciers advance, erode, and retreat, generating damage in adjacent rock slopes and influencing paraglacial slope stability. Glacial debuitressing is frequently implicated as a trigger for paraglacial rock slope failures, despite commonly observed large lag-times between deglaciation and the timing of failure and often without clear mechanical reasoning. Rock slope damage generated during glacial cycles is hypothesized to have a strong role in preparing rock slope failures, however, the mechanics of paraglacial rock slope damage remain poorly characterized.

Glacial cycles mechanically load and unload proximal rock slopes by the changing weight of ice, and in addition produce strongly varying thermal and hydraulic rock-surface boundary conditions tied to the fluctuating glacier. Bedrock beneath temperate glacier ice maintains near isothermal surface temperatures at  $\sim 0$  °C. Glacier retreat exposes rock walls to new thermal boundary conditions with strongly varying daily and seasonal cycles, a transition we term *paraglacial thermal shock*. Temperature changes generate thermal strain, inducing thermo-mechanical stresses capable of generating rock mass damage. In addition, high subglacial water pressures near the ice overburden level prevail at the base of temperate glaciers, and affect groundwater conditions in proximal valley flanks. Groundwater recharge by precipitation and snowmelt raises the water table seasonally, which is superposed on changes in hillslope groundwater tied to varying glacial ice elevations. Changing cleft water pressures control effective stresses and the strength of rock mass discontinuities. Together, these thermo-hydro-mechanical stresses act in concert with glacial loading cycles to generate rock slope damage, preparing slopes for future failure.

We study thermo-hydro-mechanical induced stresses and resulting rock slope damage during repeat glacial cycles in the valley of the Great Aletsch Glacier in Switzerland. Following Lateglacial deglaciation, the surrounding valley rock slopes in the Aletsch region experienced several minor glacier cycles during the Holocene. The foliated gneissic rock mass of the Aletsch valley contains several large rock slope instabilities with a concentration around the retreating, present-day glacier tongue. Surface exposure dating of the Driest instability head scarp reveals a Mid-Holocene initialization age ( $7.4 \pm 0.7$  ky), matching post-Egesen / pre-Little Ice Age relative ages for the majority of other rock instabilities in the Aletsch Valley. To investigate progressive rock slope damage induced during glacier cycles, we used detailed, conceptual numerical models closely based on our Aletsch Valley study area. Modeled glacier scenarios represent mapped ice fluctuations at Aletsch, while rock mass strength parameters applied in our models are based on local rock mass characterization. Ground surface temperature measurements, monitoring of subglacial water pressures in ice boreholes, regional spring-line mapping, and monitoring of rock slope deformation at Aletsch each contribute to parameterizing and validating our thermal and hydraulic model boundary conditions.

Our simulations reveal that purely mechanical loading and unloading of rock slopes by ice during glacial cycles generates relatively limited new damage. This result supports our view that glaciers make a poor buttress for adjacent slopes due to the ductile behavior of ice over long time scales. However, ice fluctuations in our models do increase the criticality of fractures in adjacent slopes (bringing them closer to the failure envelope), which may in turn increase the efficacy of additional fatigue processes. On the other hand, bedrock erosion during glaciation (i.e., rock debuitressing) promotes significant new rock slope damage during first deglaciation. The amount of initial damage, inherited from pre-glacial, ice-free topographic and *in-situ* stress conditions, strongly controls the susceptibility of the slope to new damage from ice loading. The slope response during glacial cycles is path-dependent and varies in damage

kinematics: glacier advance in our models enhances toppling failure while glacial retreat promotes sliding.

Changing thermal boundary conditions during glacier retreat and advance in our models affects the temperature regime in the adjacent rock slopes. Thermal strain from long-term temperature changes induces stresses at depths exceeding 100 m, generating significantly more rock slope damage than predicted for purely mechanical loading cycles. Thermal expansion of the rock mass due to warming after glacier retreat causes increased stresses propagating fractures, while cooling during glacier advance results in contraction, reducing joint normal stresses and promoting toppling. First time exposure to seasonal temperature cycles during deglaciation induces a strong but shallow damage front that follows the retreating ice margin. Glacial loading cycles in parallel with thermal stresses (i.e., *thermo-mechanical fatigue*) are capable of generating significant rock slope damage.

We extend our models by accounting for changing groundwater conditions in proximal valley rock slopes tied to high subglacial water pressures. Glacier loading cycles in parallel with long-term mountain water table variations generate substantial fracture propagation. Major damage occurs during initial ice occupation and first glacier retreat, while subsequent readvances result in minor damage. Superposition of annual groundwater cycles (i.e., *hydro-mechanical fatigue*) strongly increases rock slope damage during glacial loading cycles, destabilizing the toppling-mode valley flank in our models. The kinematics and dimensions of the predicted instability closely resemble observed characteristics of major landslides in the field at Aletsch. Our results extend simplified assumptions of glacial debuitressing, demonstrating in detail how thermo-hydro-mechanical stresses acting in concert with glacier cycles drive progressive rock mass failure preparing future paraglacial slope instabilities.

## Zusammenfassung

Zyklen der Vergletscherung verursachen *in-situ* Spannungsänderungen im darunterliegenden Felsuntergrund während Gletscher vorstossen, erodieren und sich wieder zurückziehen, führen dabei zur Schädigung des Gebirges im benachbarten Felshang und beeinflussen die Stabilität von paraglazialen Hängen. Die fehlende Stützwirkung eines zurückweichenden Gletschers wird oft mit einem Auslösemechanismus von paraglazialen Felsrutschungen impliziert, trotz allgemein beobachteten grossen Verzögerungszeiten zwischen Entgletscherung und dem Zeitpunkt des Versagens und oft ohne klare mechanische Argumentation. Es wird vermutet, dass während Gletscherzyklen generierte Gebirgsschädigung eine wichtige Rolle bei der Versagensvorbereitung von paraglazialen Hangrutschungen spielt, obwohl die Mechanik von paraglazialer Felsschädigung schlecht charakterisiert bleibt.

Gletscherzyklen laden und entladen nahegelegene Felshänge durch das sich ändernde Gewicht des Eises und produzieren zusätzlich sich stark ändernde thermische und hydraulische Randbedingungen an der Felsoberfläche, welche an den fluktuierenden Gletscher gebunden sind. Oberflächentemperaturen von anstehendem Fels unterhalb von temperiertem Gletschereis wird nahe von isothermalen Temperaturen von  $\sim 0$  °C gehalten. Gletscherschwund exponiert Felswände zu neuen thermischen Randbedingungen mit stark schwankenden täglichen und saisonalen Zyklen, ein Übergang, den wir *paraglazialen thermischen Schock* nennen. Temperaturänderungen verursachen thermische Dehnung, welche thermo-mechanische Spannungen induziert, imstande den Fels zu schädigen. Ausserdem herrschen hohe subglaziale Wasserdrücke nahe der Eisüberlast an der Basis von temperierten Gletschern, welche die Grundwasserverhältnisse in der proximalen Talflanke beeinflussen. Grundwasserneubildung durch Niederschläge und Schmelzwasser erhöht den Bergwasserspiegel saisonal, was überlagert ist von Änderungen des Grundwassers im Berghang geknüpft an sich ändernde Gletscherhöhen. Ändernde Kluftwasserdrücke kontrollieren die effektiven Spannungen und Festigkeit von Gebirgsklüften. Zusammen, diese thermo-hydro-mechanischen Spannungen wirken gemeinsam mit glazialen Belastungszyklen und schädigen den Fels, was zu zukünftigem Hangversagen führen kann.

Wir untersuchen thermo-hydro-mechanisch induzierte Spannungen und resultierende Felsschädigung während wiederholten glazialen Zyklen im Tal des Grossen Aletschgletschers in der Schweiz. Die umliegenden Felshänge in der Aletsch Region erleben nach der spätglazialen Entgletscherung mehrere kleinere Gletscherzyklen im Holozän. Der blätterige Gneis der Talflanken im Aletsch umfasst mehrere grosse Felsinstabilitäten mit einer Konzentration um die sich zurückziehende, heutige Gletscherzunge. Oberflächenexpositionsdatierung an der Anrisskante der Driest Instabilität zeigt Initialisierungsalter Mitte Holozän ( $7.4 \pm 0.7$  ky), passend zur Mehrheit der anderen Felsinstabilitäten im Aletschtal mit relativen Alterslimiten nach Egesen und vor der Kleinen Eiszeit. Um fortschreitende Felsschädigung induziert während Gletscherzyklen zu untersuchen, verwendeten wir detaillierte, konzeptionelle numerische Modelle in enger Anlehnung an unser Untersuchungsgebiet im Aletschtal. Modellerte Gletscherszenarien repräsentieren kartierte Gletscherfluktuationen im Aletsch, während in unserem Modell verwendete Gebirgsfestigkeitswerte auf lokaler Gebirgscharakterisierung basieren. Messungen von oberflächennahen Felstemperaturen, die Überwachung von subglazialen Wasserdrücken in Eisbohrlöchern, die Kartierung von Quellwasseraustritten und die Überwachung von Hangdeformationen am Aletsch tragen alle zur Parametrisierung und Validierung unserer thermischen und hydraulischen Modellrandbedingungen bei.

Unsere Simulationen zeigen, dass die rein mechanische Belastung und Entlastung einer Talflanke durch Eis während Gletscherzyklen relativ begrenzten neuen Schaden im Fels erzeugt. Dieses Resultat

unterstützt unsere Ansicht, dass Gletscher, aufgrund des duktilen Verhaltens von Eis über lange Zeitskalen, eine schlechte Stütze für benachbarte Hänge bilden. Allerdings können in unseren Modellen Eisschwankungen die Kritikalität von Felsklüften in angrenzenden Hängen erhöhen (sie näher an die Hüllkurve des Versagenskriteriums bringen), was wiederum die Wirksamkeit von zusätzlichen Ermüdungsprozessen erhöht. Andererseits fördert glaziale Erosion von anstehendem Fels (i.e., fehlende Stützwirkung durch Fels) bedeutende neue Gebirgsschädigung während der ersten Entgletscherung. Der Betrag der initialen Gebirgsschädigung, vererbt durch eine präglaziale, eisfreie Topographie und ein in-situ Spannungszustand, steuert stark die Anfälligkeit des Felshanges für neuen Schaden während glazialer Belastung. Die Gebirgsreaktion während Gletscherzyklen ist pfadabhängig und variiert in der Schadenskinematik: Gletschervorstoss in unseren Modellen fördert Hackenwurf und Gletscherrückzug begünstigt Rutschen.

Sich ändernde thermische Randbedingungen während Gletscherschwund und Gletschervorstoss in unseren Modellen wirkt sich auf das Temperaturregime im benachbarten Felshang aus. Thermische Dehnung von langzeitlichen Temperaturänderungen induziert Spannungen bis in Tiefen von mehr als 100 m und generiert deutlich mehr Gebirgsschädigung als bei rein mechanischen Belastungszyklen vorhergesagt. Die thermische Ausdehnung des Gesteinsmassivs auf Grund der Erwärmung während des Gletscherrückzugs verursacht Spannungen und propagiert Bruchbildung, während Abkühlung beim Gletschervorstoss in Kontraktion resultiert, wodurch Normalspannungen von Klüften reduziert werden und Hackenwurf begünstigt wird. Die erstmalige Exposition zu saisonalen Temperaturzyklen während der Entgletscherung induziert eine starke, aber flachgründige Schadensfront, die dem sich zurückziehenden Eisrand folgt. Glaziale Belastungszyklen parallel mit thermischen Spannungen (d.h., *thermo-mechanische Ermüdung*) ist fähig signifikante Gebirgsschädigung zu generieren.

Wir erweitern unsere Modelle mit der Berücksichtigung von ändernden Grundwasserverhältnissen in benachbarten Talflanken, die an hohen subglazialen Wasserdrücke gebunden sind. Gletscherbelastungszyklen parallel mit langfristigen Bergwasserspiegel Variationen erzeugen erhebliche Bruchausbreitung. Der grösste Schaden tritt während der anfänglichen Eisbelastung und dem ersten Gletscherschwund auf, während nachfolgende Vorstösse kleinere Schäden zur Folge haben. Die Überlagerung mit jährlichen Grundwasserzyklen (d.h., *hydro-mechanische Ermüdung*) erhöht die Gebirgsschädigung stark während glazialen Belastungszyklen und destabilisiert die dem Hackenwurf unterworfenen Talflanke in unseren Modellen. Die Kinematik und Dimensionen der vorhergesagten Instabilität entsprechen stark der Charakterisierung der Hauptrutschungen, welche am Aletsch beobachtet wurden. Unsere Ergebnisse erweitern die vereinfachten Annahmen einer fehlenden Stützwirkung eines zurückweichenden Gletschers und demonstrieren im Detail wie thermo-hydro-mechanische Spannungen zusammen mit Gletscherzyklen wirken und fortschreitende Gebirgsschädigung vorantreiben und zukünftige paraglaziale Felsinstabilitäten in Gebirgshängen vorbereiten.

# Content

1	INTRODUCTION .....	1
1.1	Background.....	1
1.2	Thesis structure.....	2
2	BEYOND DEBUTTRESSING: MECHANICS OF PARAGLACIAL ROCK SLOPE DAMAGE DURING REPEAT GLACIAL CYCLES .....	5
2.1	Introduction .....	6
2.2	Paraglacial setting of the Aletsch region .....	8
2.2.1	Study site .....	8
2.2.2	Late Pleistocene and Holocene glaciation .....	9
2.2.3	Spatial and temporal distribution of paraglacial rock slope instabilities.....	10
2.3	Rock mass characterization and structural analysis.....	15
2.4	Numerical study of paraglacial rock slope damage and displacement .....	17
2.4.1	Model approach and inputs.....	17
2.4.2	Initialization: Critically stressed alpine valley before and during the LGM.....	20
2.4.3	Transient rock slope damage.....	23
2.4.4	Spatial damage patterns .....	24
2.4.5	Stress redistribution .....	25
2.4.6	Slope displacement .....	26
2.4.7	Influence of LGM valley erosion.....	28
2.4.8	Weakened rock slope response.....	29
2.5	Implications for paraglacial rock slope instabilities .....	33
2.6	Summary and Conclusions .....	35
2.7	Acknowledgements .....	36
2.8	Appendix 1: Cosmogenic nuclide exposure dating of the Driest instability.....	37
2.9	Appendix 2: Modelling approach for glacial ice .....	38
2.10	References.....	40
3	BEYOND DEBUTTRESSING: THERMO-MECHANICAL ROCK SLOPE DAMAGE DURING REPEAT GLACIAL CYCLES .....	49
3.1	Introduction .....	50
3.2	Paraglacial setting of the Aletsch region .....	52
3.2.1	Study site and rock slope instabilities .....	52
3.2.2	Lateglacial and Holocene glaciation .....	52
3.2.3	Present and Lateglacial temperature regime .....	54
3.3	Numerical study of TM rock slope damage and displacement .....	55
3.3.1	Model approach and inputs.....	55
3.3.2	Long-term thermo-mechanical effects .....	58

3.3.3	Seasonal thermo-mechanical effects.....	62
3.3.4	Influence of initial rock mass strength.....	66
3.4	Discussion.....	70
3.5	Summary and conclusions .....	73
3.6	Acknowledgments.....	74
3.7	Appendix: Ground temperature measurements at Aletsch.....	74
3.8	References.....	79
4	BEYOND DEBUTTRESSING: HYDRO-MECHANICAL ROCK SLOPE DAMAGE DURING REPEAT GLACIAL CYCLES .....	85
4.1	Introduction .....	86
4.2	Paraglacial setting of the Aletsch region .....	88
4.3	Hydro-mechanical data .....	90
4.3.1	Subglacial water pressure and temperature .....	90
4.3.2	Slope hydrology.....	93
4.3.3	Bedrock deformations.....	94
4.4	Numerical study of HM rock slope damage and displacement.....	96
4.4.1	Model approach and inputs.....	96
4.4.2	Slope deformation caused by seasonal groundwater recharge .....	100
4.4.3	Pre-LGM and LGM rock slope damage .....	101
4.4.4	Transient HM rock slope damage .....	102
4.4.5	Long-term hydro-mechanical effects.....	103
4.4.6	Seasonal hydro-mechanical effects .....	105
4.5	Discussion.....	106
4.6	Comparison of preparatory factors for paraglacial rock slope instabilities.....	107
4.7	Summary and conclusions .....	110
4.8	Acknowledgments.....	110
4.9	References.....	111
5	CONCLUSIONS .....	119
5.1	Summary.....	119
5.2	Outlook.....	120
6	BIBLIOGRAPHY .....	121



# 1 INTRODUCTION

## 1.1 Background

Cycles of glacier advance and retreat impose mechanical stresses on underlying bedrock. Induced stress changes interact with *in-situ* stress conditions, rock mass structure, rock strength and topography [Augustinus, 1995; Ballantyne, 2002; McColl, 2012]. Critical stresses initiate failure of intact rock, propagate fractures and promote slip along existing joints, all of which constitute rock mass damage. Numerous case studies of active rock slope failures in the vicinity of retreating glaciers suggest a connection between glacier retreat and slope stability [e.g., Evans and Clague, 1994; Holm et al., 2004; Oppikofer et al., 2008; Strozzi et al., 2010; Clayton et al., 2013; McColl and Davies, 2013]. Glacier retreat is frequently associated with preparing rock slopes for failure (i.e., generating damage that leads to a persistent, connected failure surface) [e.g., Bovis, 1990; Cossart et al., 2008; Jaboyedoff et al., 2012], however, the detailed mechanics of paraglacial rock slope damage remain poorly characterized. Furthermore, many large prehistoric slope failures demonstrate lag-times of several thousand years between local deglaciation and failure [e.g. Prager et al., 2008; Ivy-Ochs et al., 2009; McColl, 2012; Ballantyne et al., 2014a, b], obfuscating the role of glacial debuitressing. Mechanical examination of glacial debuitressing reveals that glaciers provide limited slope support due to the ductile behavior of ice [McColl et al., 2010; McColl and Davis, 2013]; glaciers load adjacent slopes by their weight alone not providing rigid buttressing support. Several recent studies exclude debuitressing as a direct trigger and rather ascribe glacial rebound and uplift as predominant cause of landslides [Ballantyne et al., 2014a, b], or emphasize stress redistribution induced by valley erosion as a principle driver of damage [Augustinus, 1995; Leith et al., 2014]. In most cases, however, the mechanical linkage between glacier cycles and rock slope damage remains vague.

Simply removing an ice buttress inadequately describes the mechanical effects of glacial retreat on adjacent rock slopes. Ice fluctuations are accompanied by complex changes in thermal and hydrological field and boundary conditions on various temporal and spatial scales (Figure 1.1). Bedrock in contact with temperate glacial ice is near isothermal at  $\sim 0^\circ\text{C}$ , and glacier retreat exposes these surfaces to new thermal boundary conditions with daily and seasonal temperature cycles [Wegmann et al., 1998; Baroni et al., 2014]. Thermal strain induces thermo-mechanical stresses [Harrison and Herbst, 1977], and temperature changes also control secondary thermal effects such as permafrost and ice segregation [Wegmann et al., 1998; Boulton and Hartikainen, 2004; Murton et al., 2006; Gruber and Haeblerli, 2007]. Exposure of rock surfaces to the atmosphere further facilitates chemical weathering [Nicholson, 2008]. On the other hand, bedrock beneath a glacier experiences more than simple ice loading. Subglacial water pressures near the ice overburden level are frequently observed at the bed of temperate glaciers, which are subject to strong seasonal variability in space and time [Weertman, 1957; Fountain and Walder, 1998; Harper et al., 2005; Fudge et al., 2005]. Furthermore, glaciers erode their substrate, shaping topography and altering *in-situ* stresses [Leith et al., 2014; Herman et al., 2015].

Thermal stress cycles (i.e., *thermo-mechanical fatigue*) can contribute to progressive rock slope damage and failure [e.g., Gunzburger et al., 2005; Gischig et al., 2011a, b; Collins and Stock, 2016; Eppes et al., 2016]. In addition, annual water pressure fluctuations (i.e., *hydro-mechanical fatigue*) are recognized as driving factors for rock slope strength degradation [e.g., Guglielmi et al., 2005; Eberhardt et al., 2016; Preisig et al., 2016], while subglacial pressure variations are known to play an important role in bedrock fracturing [Iverson, 1991; Hallet, 1996; Cohen et al., 2006; Iverson, 2012]. Preisig et al. [2016] and Eberhardt et al. [2016] demonstrated that such fatigue mechanisms following or acting in combination with another large-scale, low-frequency loading process (e.g., *seismic fatigue*; Gischig et al., [2015])

become more effective in propagating damage. Thermo-hydro-mechanical fatigue in combination with glacier loading cycles had previously not been investigated in detail and may play an important role in contributing to progressive rock slope failure during glacier advance and retreat. Thermo-hydro-mechanical impacts of glaciation on deep geological repositories were discussed for ice sheets [Boulton *et al.*, 2004; Chan *et al.*, 2005; Vidstrand *et al.*, 2008; Selvadurai *et al.*, 2015], but these concepts were not transferred to glaciated alpine valleys and their potential as a preparatory factor for paraglacial rock slope instabilities was previously unexplored.

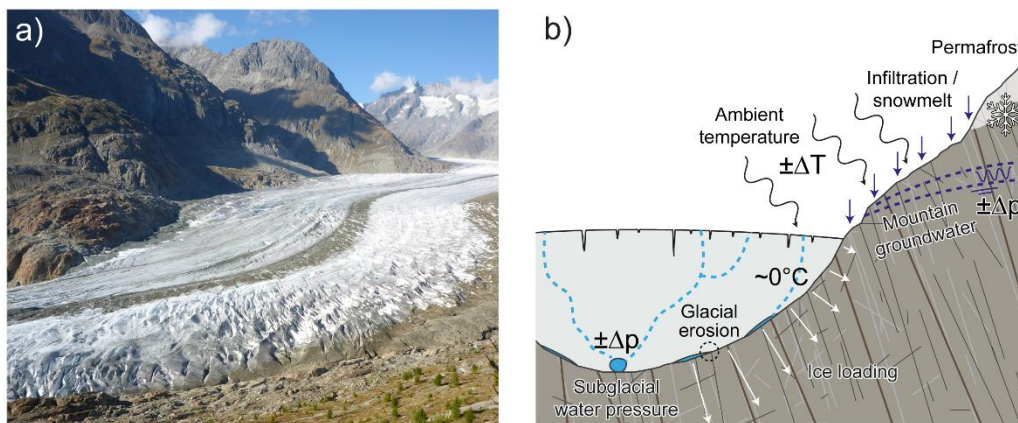


**Figure 1.1.** a) The paraglacial environment in the high-alpine region of the Great Aletsch Glacier in Switzerland. b) Conceptual profile of changing paraglacial (i.e., thermal, hydraulic, and mechanical) boundary conditions affecting adjacent rock slopes.

In this comprehensive study, we aim to critically evaluate the response of alpine rock walls subjected to glacial cycles and discern relevant failure processes. We investigate glacier loading cycles acting on adjacent valley rock slopes, focusing on induced *in-situ* stress changes and resulting rock slope damage. Furthermore, we extend simplified assumptions of glacial debuttressing and analyze thermo-hydro-mechanical stresses acting in combination with fluctuating ice loads. These processes are investigated using detailed, conceptual numerical models closely based on the Aletsch Glacier region of Switzerland. Our modeling framework relies on field-based monitoring data, rock mass characterization, and mapping of local glacier extents. Spatial and temporal landslide distributions mapped in the Aletsch region help validate our modeled rock mass damage predictions. Our results demonstrate in detail how glacier loading cycles in parallel with thermo-hydro-mechanical stresses drive damage propagation and act as a preparatory factor for paraglacial rock slope failures.

## 1.2 Thesis structure

This thesis consists of three principle chapters (Chapters 2, 3, 4) analyzing thermo-hydro-mechanical paraglacial rock slope damage during repeat glacial cycles. The study uses conceptual numerical models based on the Aletsch Glacier region of Switzerland. In Chapter 2, the study area is outlined and the effects of purely mechanical loading and unloading during glacier cycles explored. In Chapter 3, fluctuating ice loads are combined with thermal effects. In Chapter 4, we combine changes in the mountain groundwater table together with glacier loading cycles. These three companion studies are assembled in succession, using the same modeling framework to allow direct comparison of results. The three chapters are outlined as individual journal publications and are currently either in review or in

preparation for submission. The sections are briefly summarized below. In the final chapter (Chapter 5), summarized conclusions of this thesis are presented along with suggestions for future research on mechanisms driving paraglacial rock slope damage.

**Chapter 2:** First, the Aletsch valley study site is characterized in detail to establish the framework and parameters of the numerical models. Rock mass characterization and a synopsis of Lateglacial and Holocene glacier extents are presented. Spatial and temporal landslide distributions assessed at the Aletsch are described in detail. In a second step, model assumptions for the simulation of glacier fluctuations in the Aletsch valley are discussed. Results of predicted rock slope damage during repeat glacier loading cycles are presented in detail and compared with field observations.

**Chapter 3:** This chapter describes subsurface temperature changes during glacier advance and retreat, supported by ground temperature measurements at Aletsch. Thermo-mechanical stresses on both seasonal and long time-scales in concert with glacier loading cycles are investigated using numerical models. Modeled spatial and temporal damage patterns resulting from thermo-mechanical stresses acting in parallel with changing ice loads are described in detail.

**Chapter 4:** This chapter focuses on subglacial water pressures affecting the mountain water table in a proximal valley rock slope. Hydro-mechanical effects resulting from long-term and seasonal groundwater variations in parallel with glacier cycles are modeled and resulting rock slope damage is predicted. Local monitoring data of subglacial water pressure in ice boreholes, as well as continuous bedrock deformation monitoring by permanent GNSS stations at Aletsch are presented and help to justify the model assumptions. Damage predictions of purely mechanical, thermo- and hydro-mechanical models are compared.



## 2 BEYOND DEBUTTRESSING: MECHANICS OF PARAGLACIAL ROCK SLOPE DAMAGE DURING REPEAT GLACIAL CYCLES

Lorenz M. Grämiger<sup>1</sup>, Jeffrey R. Moore<sup>1,2</sup>, Valentin S. Gischig<sup>1</sup>, Susan Ivy-Ochs<sup>3</sup>, Simon Loew<sup>1</sup>

<sup>1</sup> Department of Earth Sciences, ETH Zurich, Zurich, Switzerland.

<sup>2</sup> Department of Geology and Geophysics, University of Utah, Salt Lake City, Utah, USA.

<sup>3</sup> Laboratory of Ion Beam Physics, ETH Zurich, Zurich, Switzerland.

**Abstract:** Cycles of glaciation impose mechanical stresses on underlying bedrock as glaciers advance, erode, and retreat. Fracture initiation and propagation constitute rock mass damage, and act as preparatory factors for slope failures, however, the mechanics of paraglacial rock slope damage remain poorly characterized. Using conceptual numerical models closely based on the Aletsch Glacier region of Switzerland, we explore how *in-situ* stress changes associated with fluctuating ice thickness can drive progressive rock mass failure preparing future slope instabilities. Our simulations reveal that glacial cycles as purely mechanical loading and unloading phenomena produce relatively limited new damage. However, ice fluctuations can increase the criticality of fractures in adjacent slopes, which may in turn increase the efficacy of fatigue processes. Bedrock erosion during glaciation promotes significant new damage during first deglaciation. An already weakened rock slope is more susceptible to damage from glacier loading and unloading, and may fail completely. We find damage kinematics are controlled by discontinuity geometry and the relative position of the glacier; ice advance and retreat both generate damage. We correlate model results with mapped landslides around the Great Aletsch Glacier. Our result that most damage occurs during first deglaciation agrees with the relative age of the majority of identified landslides. The kinematics and dimensions of a slope failure produced in our models is also in good agreement with characteristics of instabilities observed in the field. Our results extend simplified assumptions of glacial debuttreassing, demonstrating in detail how cycles of ice loading, erosion, and unloading drive paraglacial rock slope damage.

## 2.1 Introduction

Glacier advance and retreat imposes mechanical stress cycles on underlying bedrock and alters stress trajectories in adjacent valley slopes. The rock slope response to these stress changes will vary with *in-situ* stress conditions, rock mass properties, valley geometry and local environment [Augustinus, 1995; Ballantyne, 2002; McColl, 2012], however, induced mechanical stress changes can generate both elastic (e.g. glacio-isostatic rebound) and inelastic (i.e. irreversible) deformations. Creation of new fractures, propagation of slip along existing joints, and failure of intact rock bridges connecting non-persistent discontinuities constitutes rock slope damage and rock mass strength degradation, conditioning slope instability and preparing paraglacial valley walls for failure [Terzaghi, 1962; Eberhardt *et al.*, 2004; McColl, 2012].

In most previous studies, the mechanical reasoning explaining the temporal and spatial distribution of paraglacial (*sensu* Slaymaker [2009]) slope failures remains vague. Some studies relate slope failure activity with confinement loss due to glacier retreat [Cossart *et al.*, 2008; Deline, 2009], while others emphasize the role of stress redistribution induced by valley erosion [Augustinus, 1995; Leith *et al.*, 2014a] or glacial rebound and uplift [Cossart *et al.*, 2014; Ballantyne *et al.*, 2014a, b]. Slope debuttressing associated with deglaciation (i.e. removal of an ice buttress) is often assumed to be the predominant cause of post-glacial alpine slope failures [e.g. Bovis, 1990; Cossart *et al.*, 2008; Jaboyedoff *et al.*, 2012], and while spatial correlation of landslides with glacial debuttressing patterns could be identified in some studies [Holm *et al.*, 2004; Cossart *et al.*, 2008], it was not evident in others [Cossart *et al.*, 2014]. McColl *et al.* [2010] questioned the mechanical reasoning behind glacial debuttressing, pointing out that at long time scales (>10's of years) and small strain rates (<10<sup>-3</sup> s<sup>-1</sup>; Schulson [1990]), ice behaves in a ductile manner thereby loading underlying bedrock by its weight alone and not providing significant rigid lateral support to adjacent rock slopes. Field evidence of squeezed glaciers adjacent to active slope failures supports this hypothesis [McColl and Davies, 2013]. Meanwhile, frequently observed large lag-times between deglaciation and large-scale slope instability [e.g. Prager *et al.*, 2008; Ivy-Ochs *et al.*, 2009a; Ballantyne *et al.*, 2014a, b; Zerathe *et al.*, 2014] cast doubt on the importance of glacial debuttressing as a direct failure trigger and point to the need to further understand time-dependent effects. These results underscore the importance of additional research into the mechanics of the paraglacial rock slope response, and specifically how stress cycles imposed by the changing weight of glaciers generates rock mass damage as a first-order control on slope failure processes.

Unique measurements seek to unravel the forces acting at the rock-ice interface beneath a glacier over time. Ongoing elastic rebound of bedrock on the margins of an actively retreating ice sheet is currently monitored in Greenland using GPS [Khan *et al.*, 2010; Bevis *et al.*, 2012], showing nominal uplift rates in the range of a few mm y<sup>-1</sup>. *In-situ* stress measurements at an ice/bedrock contact are rare and only a few measurements of ice pressure on bedrock exist from subglacial laboratories showing a wide range of measured normal stresses, which is attributed to disturbances of the local ice flow, with values commonly close to the hydrostatic pressure of the ice overburden [Hagen *et al.*, 1993; Cohen *et al.*, 2000; Cohen *et al.*, 2005; Cohen *et al.*, 2006]. Measured basal shear stress reached up to 350 kPa with 210 m ice overburden [Cohen *et al.*, 2000]. Till deformation beneath glaciers has been studied in detail [Alley *et al.*, 1986; Iverson *et al.*, 1999; Iverson *et al.*, 2007], but rarely reported are deformation measurements in subglacial bedrock. In one study, strain meters in tunnels reaching within 10 m of the ice / rock interface below an alpine glacier, detected small elastic strain excursions perpendicular to glacier flow, which were believed to originate from changes in surface traction between the glacier and its bed due to frozen patches at the bedrock interface [Goodman *et al.*, 1979].

Increasingly detailed attempts to quantify the bedrock response to glacial cycles have been accomplished through numerical modeling studies. *Ustaszewski et al.* [2008] studied fault slip induced by post-glacial rebound in a Swiss alpine valley, and connected the formation of uphill-facing scarps with postglacial unloading. In the context of hazard assessment for a deep repository, the role of coupled thermo-hydro-mechanical bedrock response to a glacial cycle (ice sheet) have been previously studied [*Boulton et al.*, 2004; *Chan et al.*, 2005; *Vidstrand et al.*, 2008; *Selvadurai et al.*, 2015]. However, such studies lack holistic treatment coupling an alpine valley glacier with adjacent rock slopes. Several site-specific modeling studies have been conducted investigating the evolution of rock slopes undergoing glacier retreat [e.g. *Eberhardt et al.*, 2004; *Fischer et al.*, 2010; *Jaboyedoff et al.*, 2012; *Agliardi and Crosta*, 2014], using both continuum and discontinuum approaches. In all of these studies, however, glacier ice was implemented as a rigid, elastic material, which is most likely inappropriate when considering long time scales ( $>10^3$  years) and small strain rates ( $<10^{-3} \text{ s}^{-1}$ ) [*McColl et al.*, 2010; *McColl and Davies*, 2013]. Furthermore these studies simply model multiple stages of glacier retreat, ignoring past glacial cycles and inherited rock mass damage. *Leith et al.* [2014a], on the other hand, examined the path-dependency of subglacial fracturing in a detailed manner using a continuum modeling approach, simulating alpine valley evolution over Pleistocene time scales.

In this study, we seek to clarify the mechanics of how cyclic stress changes associated with glacial cycles create rock mass damage in adjacent valley slopes, helping prepare these slopes for future failure. Our investigation spanning glacial time scales necessitates a modeling study parameterized and tested against conclusions from present-day observations. We present a new numerical modeling framework, founded in extensive field mapping and characterization at our Aletsch Valley study site, Switzerland, and implemented in a distinct element code. Coupled thermo- and hydro-mechanical effects are detailed in following companion studies. Here we show how simple stress changes associated with repeat glacier advance and retreat cycles may propagate fractures, enhance slip along discontinuities, and lead to failure of intact rock bridges; all mechanisms that result in time-dependent rock mass strength degradation and preparation of rock slope failures. We describe spatial and temporal damage patterns, stress redistribution, and displacement associated with Late Pleistocene and Holocene glacial cycles, and compare numerical predictions with spatial and temporal landslide patterns in the Aletsch area (Figure 2.1). Our results help quantify the mechanical role of glacier advance, retreat, and erosion cycles as a preparatory factor for rock slope instabilities, and further improve the mechanical understanding underlying development of paraglacial slope failures.

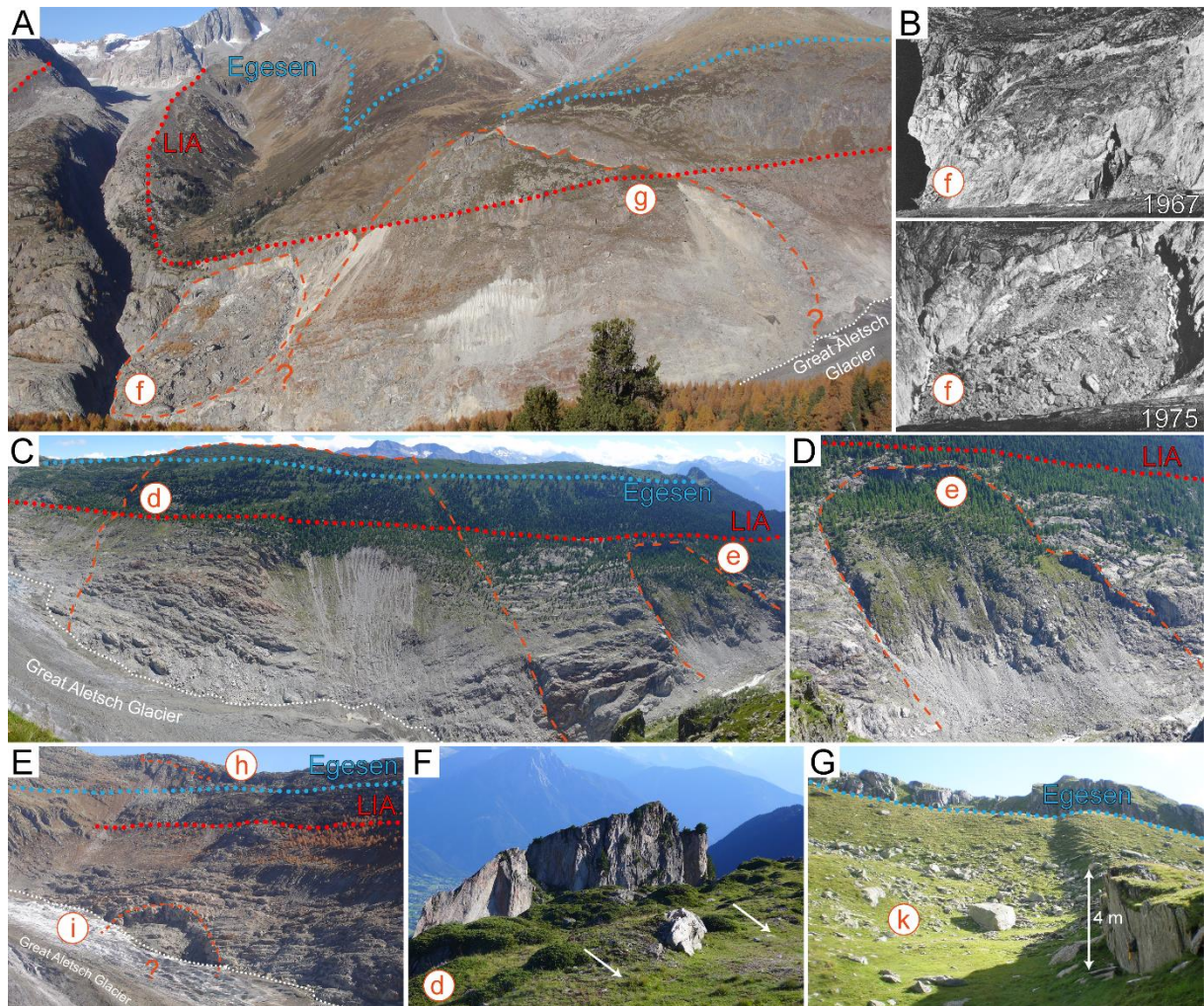


**Figure 2.1.** Concentration of rock slope instabilities around the glacier terminus and near LIA extents. Lower-case labels correspond to mapped extents in Figure 2.2. A: Tälli instability (f) with Driest instability (g) at the western valley flank at the junction of Upper Aletsch Glacier and Great Aletsch Glacier. B: Historic photos of Tälli from 1967 and 1975 reproduced from Kasser et al. [1982]. C: Moosfluh instability (d) and Silbersand instability (e) on the eastern valley flank. D: Zoom of the Silbersand instability. E: Small rock slope instability at the crest (h) with debris cones truncated at LIA extents, and a possible relict landslide (i) being revealed by present-day ice retreat. F: Head scarp of the Moosfluh instability. G: Uphill facing scarps with offset Egesen moraine at Galkina (k).

## 2.2 Paraglacial setting of the Aletsch region

### 2.2.1 Study site

Our study area encompasses the Aletsch Glacier region of Switzerland, including the Upper-, Middle- and Great Aletsch Glaciers (Figure 2.2), and focusing primarily on the Great Aletsch Glacier and surrounding valley rock slopes. The Great Aletsch Glacier is the largest and longest glacier in Europe, extending nearly 22 km through the heart of the Central Alps. It is thickest at Concordia, where the depth to bedrock has been measured at over 900 m [Hock et al., 1999]. This study area was selected based upon a number of factors, including: large ice volume changes over time affecting well-mapped and relatively homogenous bedrock, well-established spatial and temporal extents of the glacial record, and steep valley rock slopes prone to instability (Figure 2.1), some of which have been previously monitored in detail [e.g. Strozzi et al., 2010; Kos et al., 2016; Loew et al., 2017]. The study area is situated in the Aar Massif, the largest external crystalline massif in the Central Alps. Lithologies around the Great



Aletsch Glacier consist primarily of gneisses of the metamorphic Altkristallin near the glacier terminus, and the Central Aare granites in the upper parts of the study area [Steck, 2011].

### 2.2.2 Late Pleistocene and Holocene glaciation

Detailed information describing Lateglacial and Holocene glacier extents exists for the Aletsch region. Lateglacial moraines and Little Ice Age (LIA) maxima are well preserved and documented, providing information on spatial extents, while absolute ages of different glacial features in the study area constrain the timing of several stadia. We compiled and combined glacial extents from available literature [Landestopographie and VAW, 1962; Holzhauser, 1995; Kelly *et al.*, 2004a] with our own mapping of moraines and trimlines using available aerial photography and LiDAR DEM data, and confirmed findings through field inspection. Figure 2.2 displays a synopsis of the Lateglacial and Holocene glacier extents in the Aletsch region, while Figure 2.3 illustrates the change in glacier length over time.

Previous studies have suggested that the deep trough form of major Alpine valleys was initially carved around the Mid-Pleistocene Revolution (~0.9 Ma), during the onset of the first major Pleistocene glaciation in the Alps [Muttoni *et al.*, 2003; Haeuselmann *et al.*, 2007; Leith *et al.*, 2014a]. Several glacial / interglacial cycles since that time helped revitalize and maintain these characteristic glacial trough valleys. The Aletsch region was most likely ice-free during the penultimate Eemian interglacial period (~130 to ~115 ky; Dahl-Jensen *et al.* [2013]) (Figure 2.3). Eemian climate was likely warmer than the Holocene [Dahl-Jensen *et al.*, 2013], and therefore we assume ice abandoned the Aletsch area completely. The last glacial period (Würmian) peaked at the Last Glacial Maximum (LGM) [Ivy-Ochs *et al.*, 2008]. The LGM in the Alps is dated at ~28 to 18 ky [Ivy-Ochs *et al.*, 2008; Ivy-Ochs, 2015] (Figure 2.3), and ice extents have been mapped by Kelly *et al.* [2004b]. The LGM glacier system had extensively retreated by ~19 to 18 ky [Ivy-Ochs, 2015]. Between ~17 and ~11 ky, a series of successive Lateglacial readvances occurred, termed (from oldest to youngest) Gschnitz, Clavadel, Daun, and Egesen stadia (Figure 2.3) [Maisch *et al.*, 1999; Ivy-Ochs *et al.*, 2008; Darnault *et al.*, 2012]. In the Aletsch region, the elevation of LGM ice is visible through trimlines (Figure 2.2). During the Oldest Dryas (Gschnitz, Clavadel and Daun stadia) ice elevations dropped steadily with several readvances, but the Aletsch glacier still flowed over the ridge above Bettmeralp towards the Rhone Valley, covering rock slopes in our study area (Figure 2.2). Ice retreated significantly during the Bølling/Allerød interstadial [Ivy-Ochs *et al.*, 2008] (Figure 2.3).

The onset of the Younger Dryas (YD) caused dramatic ice readvance in high Alpine valleys, sending the Aletsch glacier several km downstream to the Rhone Valley at Brig [Kelly *et al.*, 2004a and references therein] (Figure 2.3). Nested moraines of the Egesen stadial are well preserved today (Figure 2.2) and age constraints provided by surface exposure dating (<sup>10</sup>Be) [Kelly *et al.*, 2004a; Schindelwig *et al.*, 2012]. We recalculated published exposure ages using the northeastern North America (NENA) production rate for cosmogenic <sup>10</sup>Be of  $3.88 \pm 0.19$  atoms g<sup>-1</sup> y<sup>-1</sup> [Balco *et al.*, 2009] and a time-dependent spallation production model [Lal, 1991; Stone, 2000]. Recalculated ages of boulders from the left-lateral moraine (AG-1, 2, 4-WM, 5 in Kelly *et al.* [2004a]) resulted in a mean age of  $12.3 \pm 0.9$  ky (Figure 2.3), while the recalculated mean age of glacially striated bedrock at the right-lateral moraine (VBA-8, 9, 10 in Schindelwig *et al.* [2012]) was  $13.7 \pm 1.0$  ky (Figure 2.3). These ages match global timing for the YD of 12.8-11.5 ky BP [Alley *et al.*, 1993]. Boulder ages of the moraine system at the Unnerbäch cirque at Belalp (Figure 2.2) dated by Schindelwig *et al.* [2012] were also recalculated: the outer moraine (VBA-1 to 6, 11 to 16, 22 to 26) has a mean age of  $12.1 \pm 0.9$  ky while the age of the inner moraine (VBA-17 to 20) is  $10.6 \pm 0.8$  ky (Figure 2.3). Recalculated exposure ages show good fit with the YD for the outer moraine, and may relate the inner moraine to the Pre-Boreal Oscillation [Moran *et al.*, 2016]. A single boulder (VBA-21) beyond these moraines at Belalp has a recalculated age of  $14.2 \pm 1.0$  ky (Figure 2.3), which may be related to the latest Lateglacial readvance (Daun: >14.7 ky, Ivy-

Ochs *et al.* [2008]). Local dated peat bog profiles by *Welten* [1982] provide complementary evidence of the timing of Egesen deglaciation (Figure 2.3).

Retreat of Egesen glaciers following the YD marked the onset of the Holocene, which saw a number of minor glacier fluctuations culminating in the Little Ice Age (LIA) around 1850 [*Joerin et al.*, 2006; *Ivy-Ochs et al.*, 2009b]. Early Holocene readvances in the Aletsch region are not well constrained, but Late Holocene (past ~3500 years) glacier fluctuations are revealed through radiocarbon dated fossil tree trunks, which were overrun by advancing ice and exposed during later retreat [*Holzhauser et al.*, 2005] (Figure 2.2 and Figure 2.3). The LIA marks the Holocene glacial maximum, however this extent may have been reached several times, creating compound moraines [*Röthlisberger and Schneebeli*, 1979; *Schimmelpfennig et al.*, 2012] (Figure 2.2 and Figure 2.3). Complementary studies at nearby sites [*Hormes et al.*, 2001; *Goehring et al.*, 2011; *Luetscher et al.*, 2011], together with tree-line variability in the Kauner Valley, Austria [*Nicolussi and Patzelt*, 2000] suggest that Alpine glacier extents during the Mid-Holocene were mostly smaller than today, but interrupted by a few readvances not exceeding the LIA (e.g. 8.2 ky event, *Nicolussi and Schlüchter* [2012]). *Holzhauser et al.* [2005] postulated that during the Bronze Age Optimum (3350-3250 y ago) the Great Aletsch Glacier was approximately 1 km shorter than today. Combining this assumption with three-dimensional retreat models of the Great Aletsch Glacier [*Jouvet et al.*, 2011], allows us to estimate a plausible Holocene minimum extent (Figure 2.2 and Figure 2.3). However, we cannot exclude that glacier retreat during the Holocene Climatic Optimum (Figure 2.3) exceeded this minimum. These results suggest that bedrock above and outside of the LIA extents most likely experienced only a single glacier readvance (Egesen stadial) following LGM ice retreat, whereas rock slopes within and below the LIA extent were affected by five (or more) glacier cycles.

### 2.2.3 Spatial and temporal distribution of paraglacial rock slope instabilities

We mapped the distribution of landslides in the Aletsch region using available aerial photography and LiDAR DEM data, as well as relevant literature, and complemented these findings with field inspection. To better understand links between deglaciation and initiation of landsliding, we also attempted to estimate or constrain initial failure ages of the mapped slope instabilities. Observations of glacially striated bedrock and/or offset moraines allowed relative age constraints for several mapped slope failures (e.g. post-LIA, pre-LIA / post-Egesen, pre-Egesen / post-LGM), while absolute cosmogenic surface exposure dating using was applied at the Driest instability (Figure 2.2). The summarized spatial and temporal distribution of paraglacial rock slope instabilities, superimposed with the Lateglacial and Holocene ice extents, is displayed in Figure 2.2.

The largest landslide in our study area is the deep-seated gravitational slope deformation (DSGSD) along the western flank of the Rhone Valley, extending from Riederalp to Fiescheralp. This so-called Riederalp-Bettmeralp-Fiescheralp DSGSD (Figure 2.2a) is evident from morphological surface features [*Crosta et al.*, 2013], but does not show signs of recent activity. Unusually high sedimentation rates in a peat bog within the landslide investigated by *Welten* [1982] (P5 in Figure 2.2) may indicate activity during the Mid-Holocene. This landslide does not directly affect the Aletsch glacier system. Meanwhile, the Nessel rock slope instability (Figure 2.2b) is located at the lower end of the Aletsch Valley on the western valley flank. Unmodified landslide deposits within the Egesen extents indicates a post-Egesen failure age. The Belalp DSGSD (Figure 2.2c) is located on the same bench. Large graben structures indicate displacement, and the prominent, well-preserved Egesen moraine described by *Schindelwig et al.* [2012] is offset indicating post-Egesen activity. Geodetic measurements at Belalp and Nessel show recent displacement rates of a few mm y<sup>-1</sup> at both sites [*Glaus*, 1992].

Higher in the Aletsch Valley, we mapped a concentration of large landslides around the present-day glacier terminus. The Moosfluh instability on the southeastern valley flank (Figure 2.1C,F and Figure 2.2d) is an active toppling-mode landslide, described and monitored by *Strozzi et al.* [2010], *Kos et al.* [2016] and *Loew et al.* [2017]. Remote sensing reveals accelerated displacements over the past 20 years from  $\sim 4 \text{ cm y}^{-1}$  to more than  $30 \text{ cm y}^{-1}$  [*Strozzi et al.*, 2010; *Kos et al.*, 2016]. Historic maps and orthoimages confirm the existence of the head scarp (Figure 2.1F) prior to this recent acceleration. We postulate a post-Egesen initialization age due to the discontinuity and deformation of the Egesen moraine in the landslide area (Figure 2.2d). The nearby Silbersand instability (Figure 2.1C,D and Figure 2.2e) has a relict appearance: large displacement at the head scarp with a missing landslide deposit and glacial erosion features along the scarp indicate post-Egesen / pre-LIA age, although offset moraines from 1926/27 on the landslide body reveal recent movement [*Crisinel*, 1978]. The Tälli instability is located at the intersection of the Upper Aletsch Glacier and the Great Aletsch Glacier (Figure 2.1A and Figure 2.2f). Historic photographs (Figure 2.1B) and orthoimages (Swisstopo) limit the initial failure timing to 1965 or 1966, when the Great Aletsch Glacier was just retreating from the toe of the developing unstable slope [*Kasser et al.*, 1982]. During the following  $\sim 5 \text{ y}$ , the ice-free slope developed into a disaggregated body. The adjacent Driest instability (Figure 2.1A and Figure 2.2g) is a compound rock slide that shows recent movement, visible by the freshly exposed band at the bottom of the head scarp and evaluated through remote monitoring [*Kääb*, 2002; *Vogler*, 2015; *Kos et al.*, 2016]. The steep head scarp lies around 50 m below the Egesen moraine. A LIA moraine is clearly visible within the disaggregated landslide body, around 100 m below the head scarp. A secondary failure occurred after LIA retreat. To constrain the initial failure age of the Driest landslide, we extracted five bedrock samples along a vertical transect down the scarp for  $^{10}\text{Be}$  cosmogenic nuclide surface exposure dating (see Appendix 1). Exposure dates reveal an initiation age of  $7.4 \pm 0.7 \text{ ky}$  (Figure 2.4), not directly following LGM or Egesen ice retreat (lag-time of several thousand years). Figure 2.3a,b illustrates the presumed interaction of major landslide activity in our study area with Lateglacial / Holocene glacier fluctuations.

Smaller rock slope instabilities are located at Hohbalm (Figure 2.1E and Figure 2.2h), just above the Egesen moraine, resulting in debris cones cross-cutting the Egesen but not the LIA extents. Therefore these instabilities must be post-Egesen / pre-LIA, although recent rock fall suggests ongoing activity. Areas above LGM trimlines are strongly weathered with a broken rock mass structure in the near-surface (especially the region between Bettmerhorn and Eggishorn, Figure 2.2), being exposed to weathering processes over the entire last glacial period. Rock fall from some of these regions is the source for several rock glaciers in the study area. We also observed the head scarp of a possible relict landslide being revealed by recent glacier retreat (Figure 2.1E and Figure 2.2i), suggesting that relict landslides from previous retreat episodes may be hidden beneath the present glacier. Prominent uphill-facing scarps at Galkina (Figure 2.1G and Figure 2.2k) are described by *Eckardt et al.* [1983]. Our on-site investigations show relative scarp displacements up to 4 m, and tilted Egesen moraines constrain this activity to post-Egesen / pre-LIA. Despite observations and structural measurements in the field, it remains unclear whether the uphill-facing scarps are part of a localized instability with toppling style kinematics or whether they represent regional large-scale differential uplift [*Ustaszewski et al.*, 2008].

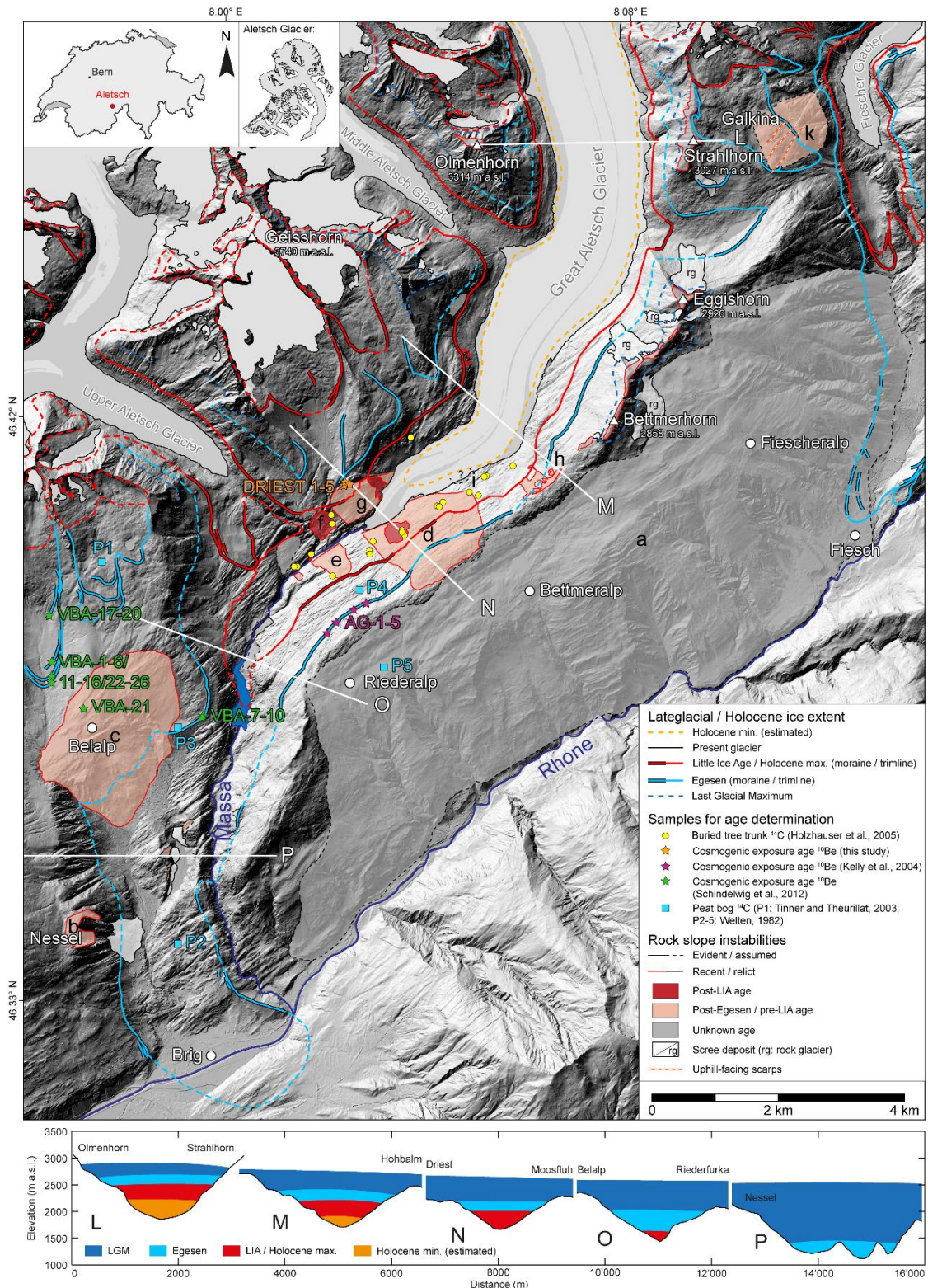


**Figure 2.2.** Synopsis of Lateglacial and Holocene glacier extents combined with spatial and temporal landslide distributions mapped at the Great Aletsch Glacier: Hillshade derived from DTM (swissALTI3D by Swisstopo). Mapped ice extents with present-day glacier and estimated Holocene minimum based on assumptions by Holzhauser et al. [2005] and Juvet et al. [2011] (for details see text). Sample locations of exposure ages [Kelly et al., 2004a; Schindelwig et al., 2012], peat bog profiles [Welten, 1982; Tinner and Theurillat, 2003], buried tree trunks [Holzhauser et al., 2005] used for age determination of glacier retreat / advance and landslide initiation age (this study). Mapped extent of rock slope instabilities (a-k) (extent of d modified from Strozzi et al. [2010]) and estimated failure timing (for details see text). Topographic cross-sections L-P with glacier surface and present-day subglacial bedrock profiles based on ground penetrating radar measurements by Farinotti et al. [2009].

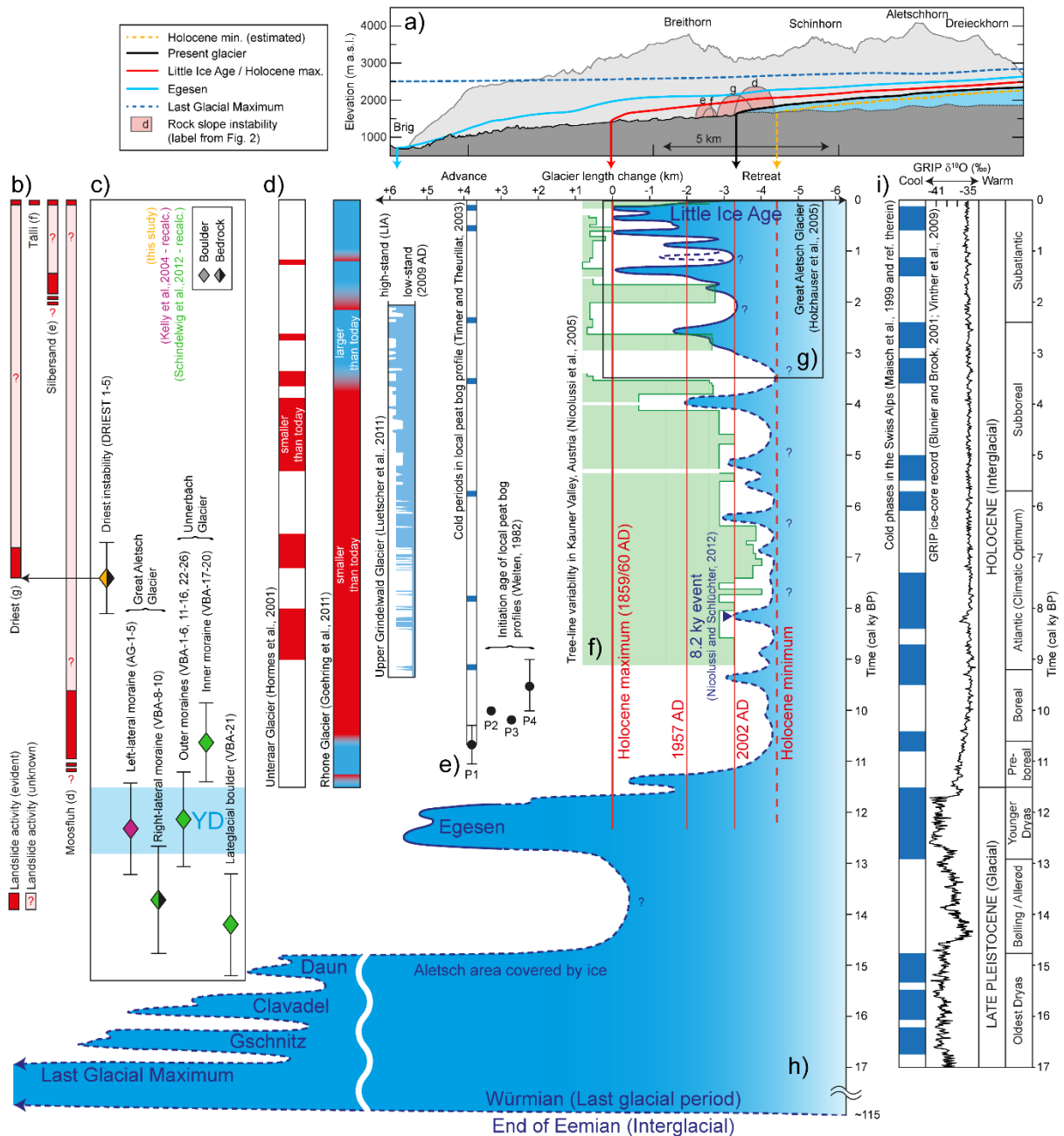


**Figure 2.3.** Synopsis of glacier fluctuations of the Great Aletsch Glacier during the Lateglacial and Holocene: a) Cross-section along the Aletsch Valley visualizing length of the Great Aletsch Glacier based on interpolations of mapped spatial extents. b) Landslide activity of major instabilities in the study area. c) Local  $^{10}\text{Be}$  cosmogenic exposure ages (mean values) illustrating Lateglacial advances [Kelly et al., 2004a; Schindelwig et al., 2012] and landslide initiation (this study – see Figure 2.4). d) Reconstruction of nearby glacier fluctuations; Unteraar Glacier ( $^{14}\text{C}$ ) [Hormes et al., 2001], Rhone Glacier ( $^{14}\text{C}/^{10}\text{Be}$ ) [Goehring et al., 2011], Upper Grindelwald Glacier (speleothems) [Luetscher et al., 2011]. e) Initiation age ( $^{14}\text{C}$ ) of local peat profiles within Egesen extent marking minimum age of Egesen retreat and indicating cold phases (P1; Tinner and Theurillat [2003]. P2-4; Welten [1982]). Profile location is shown in Figure 2.2. f) Tree-line variability in the Kauner Valley, Austria [Nicolussi et al., 2005] scaled to reference length of the Great Aletsch Glacier to illustrate glacier fluctuation. g) Detailed length reconstruction of the Great Aletsch Glacier from fossil tree trunks ( $^{14}\text{C}$ ) [Holzhauser et al., 2005]. h) Estimated length of the Great Aletsch Glacier in respect to the LIA extent compiling available information since the onset of last glacial period until today [cf. Ivy-Ochs et al., 2009b]. i) Summary of cold phases in the Swiss Alps after Maisch et al. [1999] and references therein, with oxygen isotope record [Blunier and Brook, 2001; Vinther et al., 2009] illustrating climatic fluctuations.

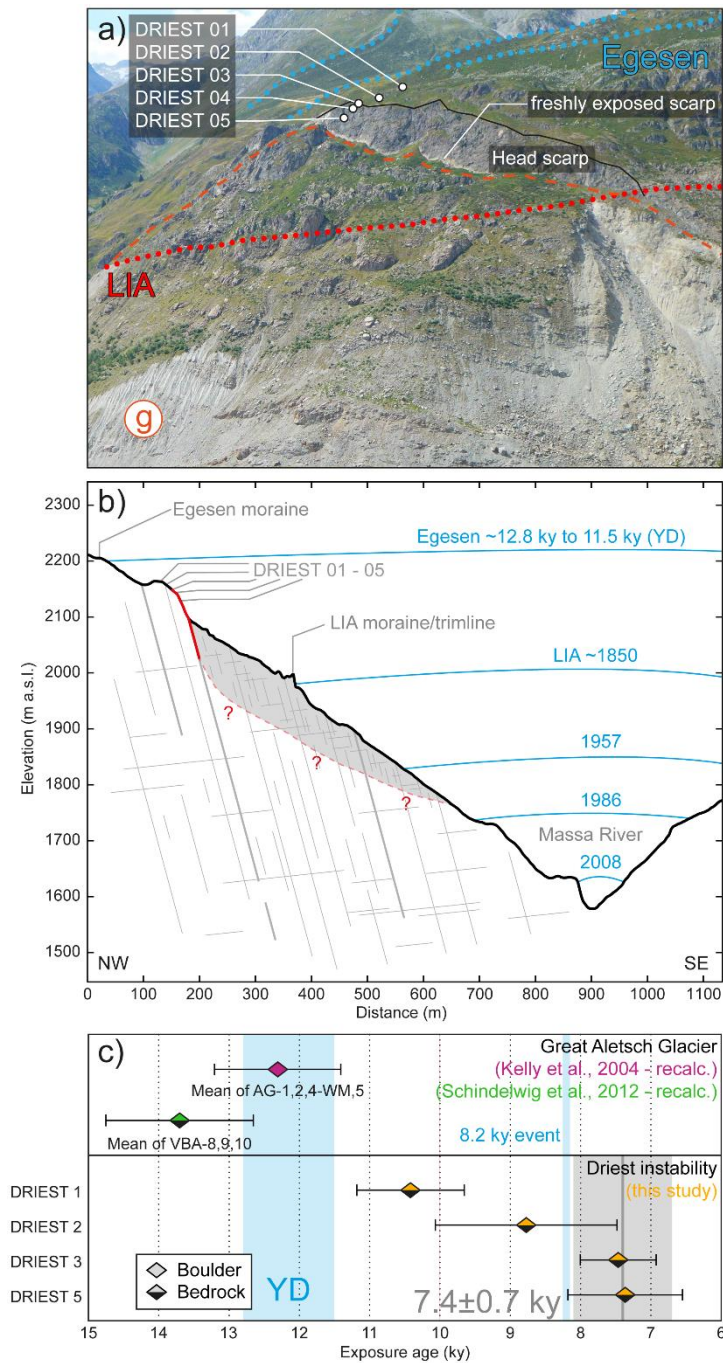


**Figure 2.4.** Exposure ages of the Driest instability: a) Overview of the sampling location along the failure scarp with moraines shown. b) Cross-section through the instability with sampling elevation, assumed extent of the instability and glacier surface elevations (1957: Landestopographie and VAW [1962], 1986: Holzhauser [1995], 2008: DTM (swissALTI3D by Swisstopo)). c) Exposure ages from the Driest site with selected mean of  $7.4 \pm 0.7$  ky for failure initiation indicated by the grey bar. For comparison to glacier extents indicated in blue, the Egesen stadial during Younger Dryas (YD) (12.8-11.5 ky BP) [Alley et al., 1993] measured locally with exposure ages at the Great Aletsch Glacier [Kelly et al., 2004a; Schindelwig et al., 2012] and 8.2 ky event [Nicolussi and Schlüchter, 2012].

## 2.3 Rock mass characterization and structural analysis

In order to create an adequate geological model representing the Aletsch Valley, we performed field-based rock mass characterization. The following rock mass parameters were collected on a regional scale: Geological Strength Index (GSI), Schmidt hammer hardness, and joint properties including dip / dip direction, spacing, persistence and Joint Roughness Coefficient (JRC). Orthoimages and a LiDAR DTM were used to map large-scale lineaments (i.e. faults) across the study area (Figure 2.5), and orientations determined by fitting a plane through the trace data using linear regression. Results of our structural analysis are summarized in Figure 2.5. Three main joint sets were observed with the following average properties across all measurements:

- F1 follows foliation, dipping steep to sub-vertical towards SE (dip direction / dip:  $122^\circ / 76^\circ$ ). Joints are persistent (trace length of 3-10 m), with spacing in the range of cm. This is the most abundant joint set, correlating with the alpine foliation in the Aar Massif [Steck, 2011]. On occasion, foliation is divided into two subsets: F1a ( $138^\circ / 77^\circ$ ) and F1b ( $101^\circ / 78^\circ$ ), whereas F1a is more abundant.
- F2 dips very steep to sub-vertical towards S to SW ( $198^\circ / 83^\circ$ ). Joints have minor persistence (1-3 m) and medium spacing (0.5-2 m).
- F3 dips gently SW ( $240^\circ / 20^\circ$ ), although the orientation can vary. Joints are moderately persistent (3-5 m) and exhibit larger spacing (1-5 m).
- F4 includes large-scale lineaments (i.e. faults), which in general follow foliation (F1). Minor lineaments may be oriented W-E or N-S, following the subsets F1a or F1b. Field observation correlates these lineaments with fault zones, which typically exhibit strong internal foliation and fracturing due to tectonic shearing and rarely contain gouge.

GSI [Hoek and Brown, 1997] was measured across the study area and found to be relatively uniform between lithologies. The rock mass is generally blocky, undisturbed with good surface conditions (GSI 65-80). We evaluated detailed joint properties at several outcrops within the Augengneiss at Bettmerhorn and Chatzulecher (k and i, respectively in Figure 2.5). Mean measurement values are given together with one standard deviation and the number of measurements (#):

- Spacing was measured at Bettmerhorn and Chatzulecher: F1 =  $0.4 \pm 0.3$  m (#68), F2 =  $0.5 \pm 0.3$  m (#52), F3 =  $0.6 \pm 0.4$  m (#32). Since the upper boundary of the spacing was often not captured due to the scale of the outcrop, these measurements likely represent lower limits. Additional field observations were therefore used for global description.
- Schmidt hammer rebound hardness was evaluated using an L-type instrument and processed according to Aydin [2015] at Bettmerhorn for joint sets: F1 =  $48 \pm 10$  (#53), F2 =  $52 \pm 11$  (#41), F3 =  $51 \pm 5$  (#31). The estimated joint wall compressive strength from those rebound values is: F1 = 90-200 MPa, F2 = 90-270 MPa, F3 = 130-200 MPa.
- JRC was evaluated at Bettmerhorn and resulted in relatively smooth values: F1 =  $6.1 \pm 3.1$  (#10), F2 =  $6.1 \pm 2.8$  (#7), F3 =  $6.9 \pm 3.5$  (#11).

Table 2.1 summarizes discontinuity characterization along the cross-section between Bettmerhorn and Geishhorn. In the more massive Aar granite, joint set F3 is accompanied by exfoliation joints, e.g. at outcrop g in Figure 2.5.

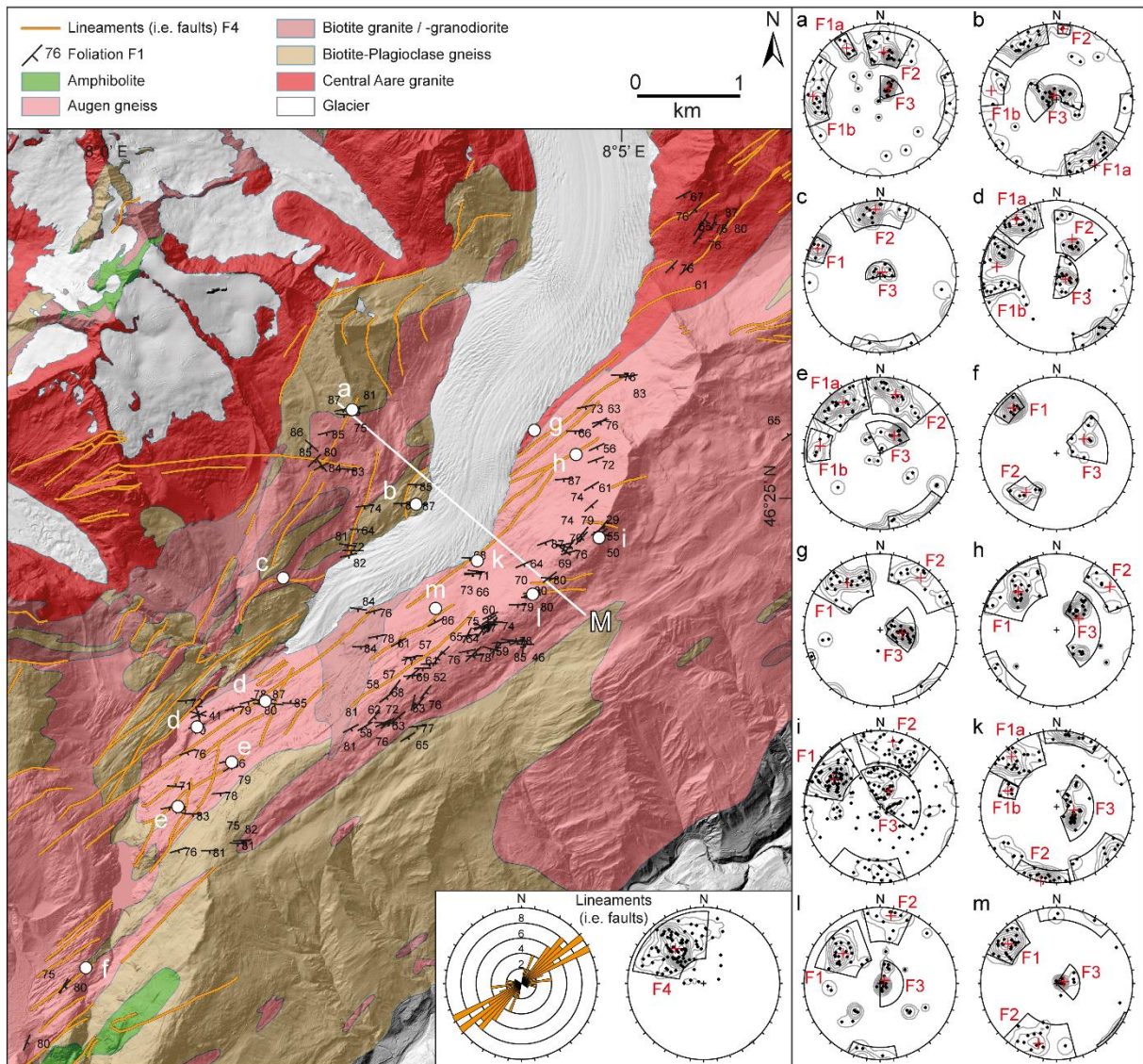


**Figure 2.5.** Geological and structural setting of the Aletsch region: Geological units adapted from Steck [2011] and mapped foliation in the field with hillshade derived from DTM (swissALTI3D by Swisstopo) in the background. Mapped large-scale lineaments (e.g. faults) and their derived orientation from DTM and synopsis of joint measurements in the field from several locations presented as stereoplots. Representative cross-section M used in the models.



**Table 2.1.** Summary of discontinuity characterization along the cross-section between Bettmerhorn and Geisshorn.

Set	Type	Dip direction / Dip	Spacing	Persistence	JRC	Schmidt hammer rebound hardness	Description
F1	Foliation	124° / 75°	0.1-0.5 m	very persistent (3-10 m)	6 ± 3	48 ± 10	no infilling, no aperture, unweathered to slightly weathered
F2	Fractures	198° / 84°	0.5-2 (>5) m	minor persistent (1-3 m)	6 ± 3	52 ± 11	no infilling, 1-5 mm aperture, unweathered to slightly weathered
F3	Fractures	244° / 18°	1-5 (>5) m	moderately persistent (3-5 m)	7 ± 4	51 ± 5	no infilling, 1-5 mm aperture, unweathered to slightly weathered
F4	Fault zones	141° / 61°	25-50 m	very persistent (>20 m)	-	-	strongly foliated, 1-5mm aperture, moderately to highly weathered

## 2.4 Numerical study of paraglacial rock slope damage and displacement

### 2.4.1 Model approach and inputs

Paraglacial rock slope damage and displacements were computed using the 2D distinct-element code UDEC [Cundall and Hart, 1992; Itasca, 2014], which is well-suited for analyzing the behavior of a discontinuous rock mass; i.e. a large number of discontinuities separating intact blocks. Deformable blocks are connected through contacts representing discontinuities. The contacts mimic joint stiffness and are assigned a strength criterion (e.g. Mohr-Coulomb). Shear slip or joint opening can promote irreversible displacement once the failure criterion is reached.

Our model geometry and initialization steps are shown in Figure 2.6. To accurately represent the stress field in the Aletsch Valley and to minimize boundary effects, our area of interest was embedded into a 10 km wide large-scale model including the neighboring Rhone Valley. Model cross-sections are based on a DTM (swissALTI3D by Swisstopo) complemented with ice penetrating radar data [Farinotti *et al.*, 2009] below the present-day glacier. The area of interest (Figure 2.6) contains three rock mass elements: 1. intact rock, 2. discontinuities (joints), and 3. brittle-ductile fault zones. Intact rock is represented by randomly oriented discontinuities, so called *Voronoi* polygons [Lorig and Cundall, 1989], which allow failure along new potential pathways simulating failure of rock bridges. The orientation, spacing, persistence and strength parameters for each rock mass constituent were evaluated through field assessment and data collection at outcrops along the representative cross-section M (Figure 2.5). Blocks between discontinuities were assigned elastic properties, while Voronoi contacts, discontinuities, and faults were assigned a Mohr-Coulomb constitutive law including slip-weakening of friction, cohesion, and tensile strength properties (i.e. a drop from peak to residual strength at failure).

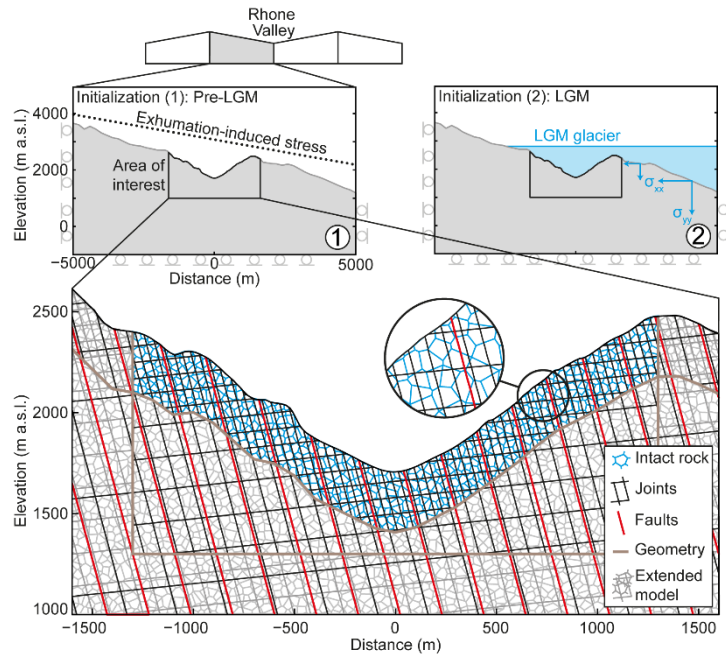


**Figure 2.6.** Initialization procedure, boundary conditions and model geometry (here showing cross-section M) in UDEC: Large-scale model with roller boundary conditions representing western slope of the Rhone Valley undergoing two-stage initialization (Pre-LGM / LGM). Embedded area of interest containing three rock mass elements: intact rock (Voronoi contacts), joints, and fault zones (including additional discontinuities in the extended model).

Based on reported literature values for intact rock (Table 2.2) and an assumed Geological Strength Index (GSI) of 75 obtained from field observation, we calculated rock mass strength properties using the GSI approach [Hoek et al., 2002]. This resulted in estimated values of cohesion,  $c = 7.8$  MPa, friction angle,  $\varphi = 50.6^\circ$ , tensile strength,  $t = -0.6$  MPa, and elastic modulus,  $E = 31.8$  GPa. Rounded values were implemented in UDEC for blocks and Voronoi contacts representing the rock mass (Table 2.2 and Table 2.3). These bulk rock mass properties match well with previous studies in similar lithologies [e.g. Gischig et al., 2011a; Kinakin and Stead, 2005]. Bulk modulus ( $K$ ) and shear modulus ( $G$ ) were calculated assuming homogeneous isotropic materials [Hudson and Harrison, 1997].

For discontinuities (peak strength, without intact rock bridges), we assumed a peak friction angle of  $30^\circ$  and peak cohesion of 0.1 MPa, with no tensile strength [Gischig et al., 2011a]. Residual friction was set to  $27^\circ$  and residual cohesion to 0.03 MPa (Table 2.3) [Gischig et al., 2011a]. Jennings' approach [Jennings, 1970] was used to determine peak composite Mohr-Coulomb strength properties for discontinuities including effects of intact rock bridges; we assumed F1 contains 10% rock bridges and F3 20% rock bridges (see persistence in Table 2.1). The resulting discontinuity friction angles (Table 2.3) are within the range of past measurements in the same lithology [e.g. Steiner et al., 1996]. Peak strength values of faults (F4) were set to residual values.

The orientation and spacing of discontinuities and faults in our model are taken from field observations along cross-section M (Table 2.1). For this profile, the apparent dip of foliation (F1) and faults (F4) does not change. However, the apparent dip of set F2 reduces to  $77^\circ$  and falls together with F1. The flat dip angle of F3 is reduced to  $6^\circ$  apparent dip along the cross-section. Input spacing for discontinuities in UDEC is based on field observations (Table 2.1), however a single joint in UDEC represents several joints in reality. The spacing of F1 discontinuities was thus set to 40 m, F3 to 80 m, and faults F4 to 200 m. Joint spacing in the model increases with depth ( $>300$  m) by a factor of two accounting for a near-

surface fractured zone in alpine rock slopes [Masset and Loew, 2010; Zangerl et al., 2008a, b]. The Voronoi contacts have maximum length of 40 m. Blocks generated by intersecting joints are meshed with a mesh size of 15 m in the upper 300 m, while the mesh size increased stepwise with depth and beyond the area of interest. We assumed linear joint normal stiffness of 10 GPa m<sup>-1</sup> and a joint shear stiffness of 5 GPa m<sup>-1</sup> (Table 2.3), as used in past similar studies [Gischig et al., 2011a]. The stiffness of Voronoi contacts was twice as high. For faults, we assigned a normal stiffness of 1 GPa m<sup>-1</sup> and shear stiffness of 0.5 GPa m<sup>-1</sup> (Table 2.3) [Zangerl et al., 2008b, c].

Selecting a physically meaningful modelling approach to represent glacier ice and its influence on surrounding rock slopes is crucial for analyzing paraglacial rock slope mechanics. Previous studies [e.g. Eberhardt et al., 2004; Jaboyedoff et al., 2012] have modeled glacier ice as either an elastic or plastic material. Recent investigations [McColl et al., 2010; McColl and Davies, 2013] emphasize that ice will undergo ductile flow under small strain rates and is not capable of providing shear resistance to adjacent rock slopes, instead loading underlying bedrock by its weight alone. Furthermore, ice will relax through plastic deformation (creep) at stresses above a yield shear stress of ~100 kPa [Schulson, 1999; Cuffey and Paterson, 2010]. We therefore model glacier ice as a hydrostatic stress boundary condition, rather than an elastic material, as similarly applied by Leith et al. [2014a, b]. A comparison between modelling ice as a time-varying stress boundary condition versus an elastic material is presented in Appendix 2. Out-of-plane stresses at the glacier bed (i.e. basal shear stress due to ice flow) are limited by the yield shear stress of ice and the presence of water at the interface. Basal shear stresses are typically in a range from 50 to 150 kPa [Cuffey and Paterson, 2010]), an order of magnitude smaller than overburden stress during Lateglacial and Holocene glacier cycles.

We also perform large-scale transient models in UDEC to model ice loading cycles, once the initial conditions have been established. These models are computationally intensive and require a reduced geometry (Figure 2.6). The area of interest is restricted to a smaller window around the valley and surrounded by a buffer zone with fewer model elements. Voronoi contacts, allowing creation of new joints through intact rock, are restricted to the uppermost 300 m. Joint spacing is increased by a factor of three within the buffer zone, and to account for the change in compliance, joints within this zone are assigned a normal stiffness which is three times lower [cf. Zangerl et al., 2003]. The mesh size in the uppermost 300 m is 35 m, increasing stepwise toward the boundary of the area of interest.

**Table 2.2.** Intact rock and rock mass properties implemented in UDEC.

<b>Intact rock</b>			
Density $\rho$	(kg m <sup>-3</sup> )	2700	Wegmann [1998]
Poisson's ratio	()	0.2	
Stress ratio $k$	()	1.0	Kastrup et al. [2004]
UCS	(MPa)	110	Steiner et al. [1996]
Young's modulus	(GPa)	39	Wegmann [1998]
<b>Rock Mass (UDEC)</b>			
Young's modulus	(GPa)	30	GSI = 75
Friction angle $\phi$	(°)	50	GSI = 75
Cohesion $c$	(MPa)	8	GSI = 75
Tensile strength $t$	(MPa)	1	GSI = 75

**Table 2.3.** Discontinuity properties for the Mohr-Coulomb constitutive law including slip-weakening implemented in UDEC.

Discontinuity parameters	Unit	Intact rock (Voronoi)	F1 foliation	F3	F4 faults
Peak friction angle $\phi$	( $^{\circ}$ )	50	33.7	37.2	27
Peak cohesion $c$	(MPa)	8	1.8	3.5	0.03
Peak tensile strength $t$	(MPa)	1	0.4	0.8	0
Residual friction angle $\phi_R$	( $^{\circ}$ )	27	27	27	27
Residual cohesion $c_R$	(MPa)	0.03	0.03	0.03	0.03
Residual tensile strength $t_R$	(MPa)	0	0	0	0
Dilation angle	( $^{\circ}$ )	5	5	5	5
Dip angle	( $^{\circ}$ )	-	75	6	75
Normal stiffness	(GPa m $^{-1}$ )	20	10	10	1
Shear stiffness	(GPa m $^{-1}$ )	10	5	5	0.5

#### 2.4.2 Initialization: Critically stressed alpine valley before and during the LGM

We argue for ice-free initial conditions that represent the Aletsch Valley prior to the LGM. Otherwise initial damage (i.e. failure occurring during initialization, representing inherited damage resulting from all prior processes) is strongly underestimated due to relaxation under LGM ice occupation. Initialization of our model is thus undertaken in two primary steps (Figure 2.7): 1a) First, initial stresses are calculated under elastic, ice-free conditions (Figure 2.7a-d). The initial far-field stresses applied represent exhumation-induced and tectonic stresses in a simplified (linear hillslope) paleo-alpine valley (i.e.  $\sigma_{yy} = -\rho g \Delta z$ ,  $g$  is gravitational acceleration and  $\Delta z$  is vertical distance to paleo-alpine valley). A strike-slip stress regime prevails in our study area [Kastrup *et al.*, 2004], we therefore use a stress ratio ( $\sigma_h/\sigma_v$ ) of  $k = 1$  (i.e.  $\sigma_{xx} = k\sigma_{yy}$ ), as values of  $k \neq 1$  would represent normal or thrust faulting in a 2D model. Out-of-plane stresses ( $\sigma_{zz}$ ) are calculated assuming plane-strain conditions. 1b) Unrealistically high stresses are avoided during initialization using an elastoplastic equilibration phase with a simple Mohr-Coulomb failure criterion for blocks ( $\phi = 50^{\circ}$ ,  $c = 8$  MPa,  $t = 1$  MPa). 1c) The elastoplastic failure criterion for discontinuities is assigned (strength properties listed in Table 2.3) allowing joints to fail. Thereby, initial damage was simulated during the ice-free pre-LGM interglacial (Eemian) period (Figure 2.7e,f). 2) In the second step, we add ice loading to the mapped LGM elevation (2800 m a.s.l.). Stress redistribution is calculated under elastic conditions before again allowing joint failure (Figure 2.7g,h). This represents the starting point for subsequent transient models investigating Lateglacial and Holocene glacier cycles.

In Figure 2.7, we display the stress state along cross-section M (see Figure 2.2) during our initialization procedure. Under initial ice-free conditions, in-plane major principle stresses ( $\sigma_1$ ) reach maximum values at the valley bottom (up to  $\sim 50$  MPa) and decrease towards the flanks (Figure 2.7a). Stresses are around 10-20 MPa at the valley shoulders, and stress orientations generally parallel to topography. In-plane minor principle stresses ( $\sigma_3$ ) are defined by overburden and oriented orthogonal to topography (Figure 2.7b). Out-of-plane stresses ( $\sigma_{zz}$ ) are in a similar range as  $\sigma_1$  (Figure 2.7c). Differential stresses in the valley bottom exceed 25 MPa within  $\sim 500$  m of the axis (Figure 2.7d). Allowing blocks then joints to fail, these differential stresses lead to a  $\sim 300$  m deep damage zone focused mostly around the lower valley flanks (Figure 2.7e,f). All failed joint segments are critically stressed (here defined as within 1 MPa of the Mohr-Coulomb failure criterion), while steeply-dipping joints on the western flank are critically

stressed in tension at the surface and faults are critically stressed in shear on both sides (Figure 2.7f). The ice-free Aletsch Valley is at critical conditions. Adding LGM ice in the second initialization step changes the differential stress state (assuming zero glacial erosion during LGM). Differential stresses decrease in the valley bottom by up to 18 MPa, but increase slightly at the surface on the western flank and even more at the toe of the slope on both sides (Figure 2.7g). LGM ice occupation thus alleviates critical stresses within the valley; only a few failed joints are still critical under tension (Figure 2.7h). Furthermore, stress redistribution under LGM ice leads to a change in failure mode from a mixed shear / tensile regime towards a shearing dominated regime. The glacier ice load prevents most tensile failure. This illustrates the importance of selecting a model starting point prior to LGM ice occupation, otherwise the unstressed rock slope experiences unrealistically high stresses and damage accumulation during deglaciation.

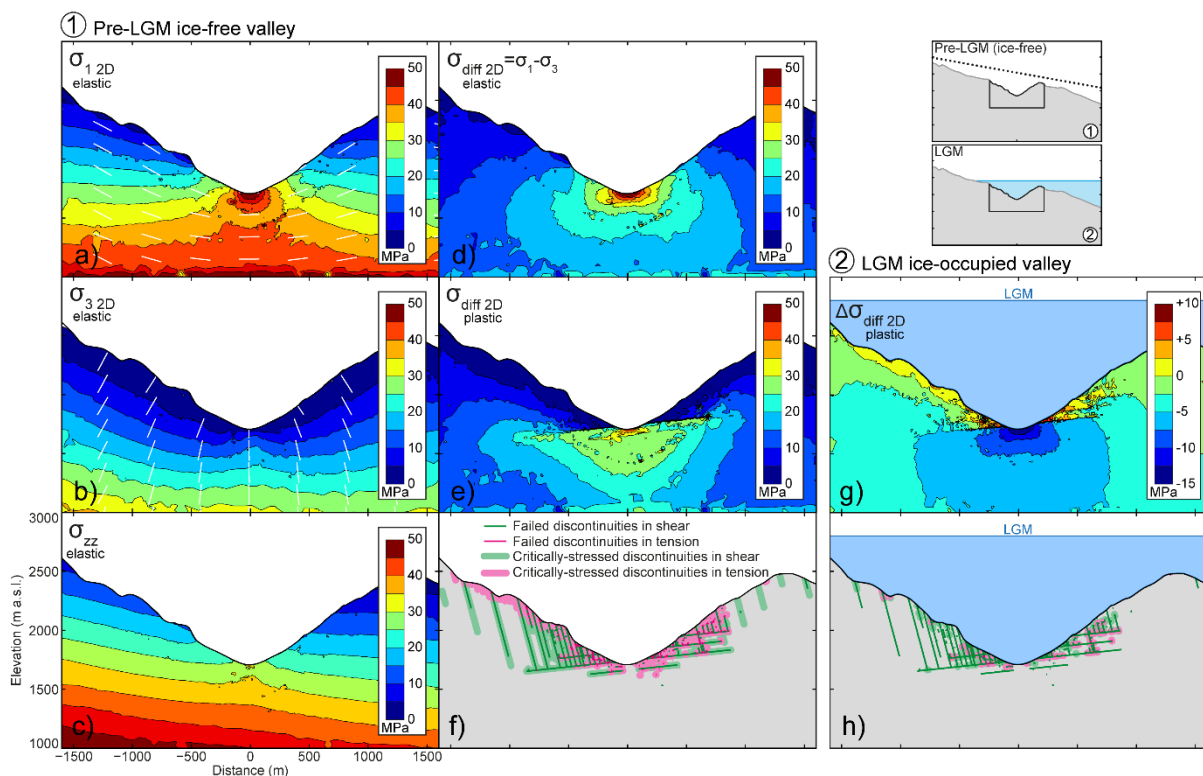


**Figure 2.7.** Critically stressed alpine valley before (1) and during LGM (2): a-d) Stress states of the initial elastic model; in-plane major ( $\sigma_1$ ) and minor ( $\sigma_3$ ) principle stresses, out-of-plane stresses ( $\sigma_{zz}$ ), and in-plane differential stresses ( $\sigma_{diff-2D} = \sigma_1 - \sigma_3$ ). e) Subsequent stress change in  $\sigma_{diff-2D}$  by allowing plastic failure in an ice-free valley. f) Failure mode of yielded joint segments and critically stressed joint segments (here defined as within 1 MPa of the Mohr-Coulomb failure criterion) in shear and tension for an ice-free valley. g) Differential stress change in  $\sigma_{diff-2D}$  resulting from adding LGM ice to an ice-free valley, h) as well as failure mode and critically stressed joints during LGM.

We simulated initial damage for different cross-sections along the Aletsch Valley. The same modelling procedure as described above was applied to the extended model geometry (see Figure 2.6) for different profiles (L-P, Figure 2.2). The thickness of LGM ice was adapted for each cross-section based on field data, and the same model geometry and rock structure were used for all profiles. Figure 2.8 shows the resulting initial damage distribution and damage propagation during LGM ice occupation. The total failed joint length ranges between 8 to 21 x 10<sup>3</sup> m (summed length of discontinuities at residual strength).

Additional damage propagation during LGM ice occupation varies between 0.5% and 2.5%. Profile M, N, and O show small variability in the damage field, but differ from damage in profile L with its distinct U-shaped form. Additional damage occurs in all profiles close to the valley bottom during LGM conditions, even though general rock slope conditions are less stressed. We conclude that topographic effects on the initial damage field and subsequent damage during LGM ice occupation exist, but variations are small and the general patterns of damage are comparable throughout the Aletsch Valley.

A fluctuating glacier affects different areas of an alpine valley over time. Since we seek to investigate the isolated influence of glacier cycles on an adjacent rock slope, and not focus on variable topographic effects, we model different glacier histories along the same cross-section, conceptually representing different sections of the valley. The Aletsch Valley is situated in a relatively homogeneous crystalline massif and aligned parallel to the main foliation. In the preceding Figure 2.8, we showed that the spatial damage distribution for different topographic profiles along the valley does not vary markedly, justifying the following analysis along a single cross-section for different glacier histories.

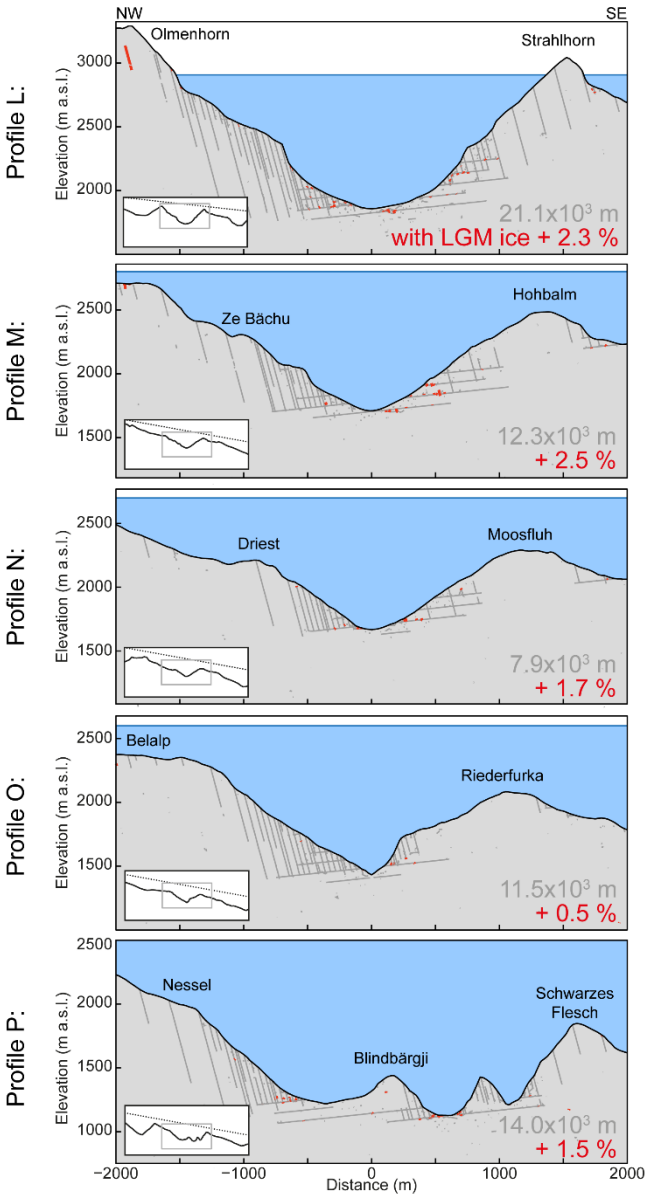


**Figure 2.8.** Initial damage distribution for an ice-free valley (grey) and damage propagation during LGM ice occupation (red) for different profiles along the Aletsch Valley. Full scale model with initial far-field stress level applied is illustrated in small inset in lower-left corner. Total amount of failed joint length in grey (m) and new damage during LGM ice occupation in red (% of initial damage).

### 2.4.3 Transient rock slope damage

Fracture development in an alpine valley subject to Late Pleistocene glaciation is strongly path-dependent [Leith *et al.*, 2014a, b]. Transient numerical models are therefore crucial to investigate the influence of repeat glacier cycles on progressive damage. Here we use a quasi-steady-state approach to simulate cycles of glacier retreat and advance. Changes in stress boundary conditions over glacial time scales are relatively slow, so the system has sufficient time to maintain mechanical equilibrium. Discretization into small steps, with subsequent equilibration to steady-state after each step, is therefore a valid approach for our simulations. We conducted a sensitivity analysis for the model step size to justify that the value we use to discretize glacier change is small enough so that model behavior is stage-dependent and not rate-dependent, i.e., the model is always in steady-state. We emphasize that due to the quasi-steady-state approach, there is no *real* time in these models. Slope response is an instantaneous reaction to the glacier load at each model step.

Transient models are performed using the reduced model geometry (Figure 2.6). Cross-section M was selected to represent the Aletsch Valley, and subjected to different glacier histories related to other cross-sections (M, N, O, and P in Figure 2.2). We performed a sensitivity study to evaluate the impact of reduced model complexity on initial and subsequent damage. We compared damage accumulation during our initialization procedure for different model configurations: a) Voronoi contacts throughout the area of interest, b) Voronoi contact restricted to the uppermost 300 m, and c) finer model geometry with joint spacing reduced by a factor of two. A reduction in joint density results in smaller absolute damage, but the amount of failed joints relative to total available joints remains similar. Initial damage patterns, as well as the location and amount of subsequent damage with added LGM ice remained similar. While the reduced model geometry may slightly underestimate progressive damage, results do not vary significantly. Therefore we use the more computationally efficient reduced geometry in the following transient models.

Based on mapped Lateglacial and Holocene ice extents along profiles M, N, O, and P (Figure 2.2), we generated different conceptual glacier scenarios for cross-section M (Figure 2.9a). All scenarios begin with LGM ice and the initialization procedure described previously. In the first 300 model steps, LGM ice is lowered in the Aletsch and Rhone Valleys simultaneously, until the glacier elevation reaches the crest that divides the valleys. LGM deglaciation continues in the Rhone Valley until 1000 steps. All four glacier scenarios undergo Egesen readvance after LGM deglaciation. Subsequent Holocene fluctuations are represented by three repeat cycles. Depending on the position of the profile, the Egesen readvance and Holocene fluctuations vary in amplitude.

The temporal evolution of damage under different glacier scenarios is presented in Figure 2.9b. Damage within the rock slope is quantified as the summed length of failed discontinuities (i.e. joints, faults, and Voronoi contacts) at each model step. The final additional damage accumulated in all models is relatively small (3-4% of initial damage). We find that most damage occurs when ice elevations lower from 2200 to 2000 m a.s.l. during first glacier retreat. Holocene fluctuations only result in subsequent damage for scenario N (0.5% of initial). Damage propagation is greater during Holocene glacier advance than during subsequent retreat. Model scenario M, which never reaches ice-free conditions, shows the least total damage. We conclude that the amplitude of glacial cycles must be large (>300 m in this example), and the Holocene minimum must reach close to the valley bottom causing the slope to become most critically stressed, to be effective in damage propagation, and even then only the first cycle appears to produce additional damage.

Figure 2.9c presents the amount of failed and critically-stressed discontinuities over time for scenario N containing pronounced Holocene glacier fluctuations. While Holocene cycles produce only minor

additional damage, the amount of critically stressed joints varies strongly. Deglaciation is accompanied by an increase in critically stressed joints as normal stresses are alleviated. During glacier advance, the number of critically stressed joints decreases, and discontinuities preferring tensile failure shift to shearing mode, while the reverse is encountered with glacier retreat.

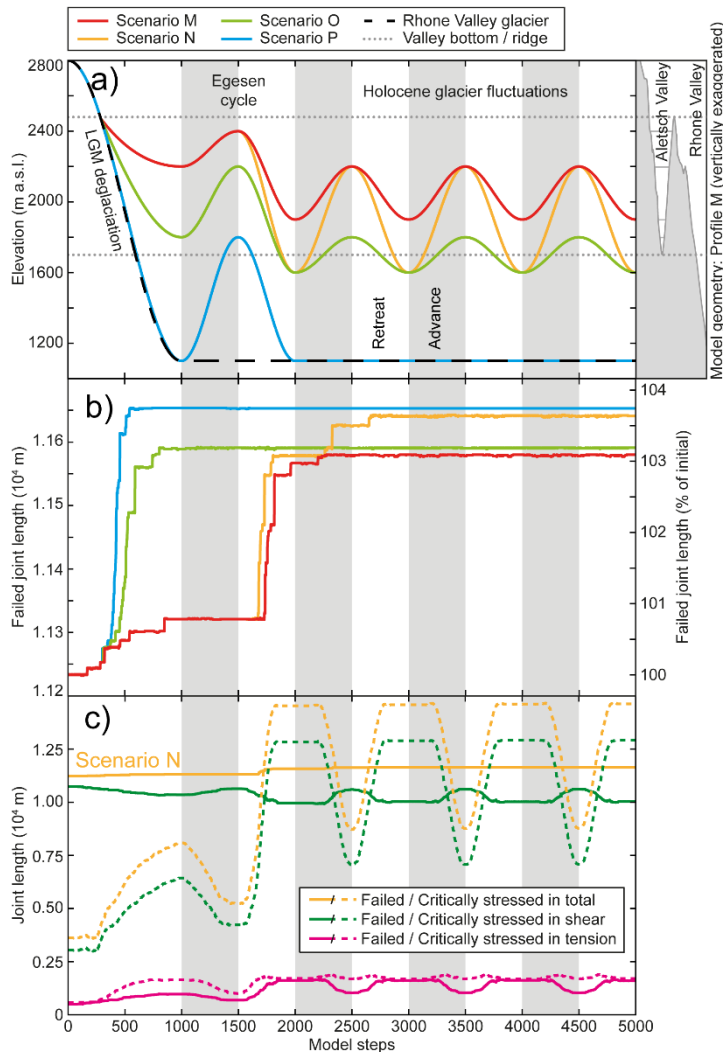


**Figure 2.9.** Transient rock slope damage during repeat glacial cycles: a) Applied glacier scenarios based on mapped glacier extents along profiles M, N, O, and P (see Figure 2.2) with compressed profile M as reference. b) Temporal evolution of damage for different glacier scenarios illustrated as the sum of failed joint length and percentage of initial damage. c) Critically stressed joints (here defined as within 1 MPa of the Mohr-Coulomb failure criterion) and failed joints over time for scenario N.

#### 2.4.4 Spatial damage patterns

Depending on the site-specific glacial history, adjacent rock slopes are affected differently by the ice load, leading to a spatially variable damage patterns. Figure 2.10 compares spatial damage predictions for the different glacier model scenarios introduced previously. Spatial damage over time for model scenario N is displayed in Figure 2.10a,b. New damage occurs mainly on the eastern flank in the form of fracture propagation of initially failed discontinuities, or a fault zone at its yield limit in the mid-portion of the slope. Comparison of damage for alternative model scenarios (Figure 2.10b) shows that similar spatial patterns occur with or without Holocene glacier fluctuations. Most new rock slope damage accumulates in the mid-portion of the valley at the time when the glacier surface first lowers past this area. By comparison, in Figure 2.7 we showed that this mid-slope region was critically stressed, but not yet failed, at initialization. Through stress redistribution, i.e. due to additional damage during LGM occupation and deglaciation, joints in the mid-slope area may now reach their failure limit. The location of critically stressed areas prone to failure is thus more important in controlling the pattern of spatial damage than the elevation of Holocene ice extents.



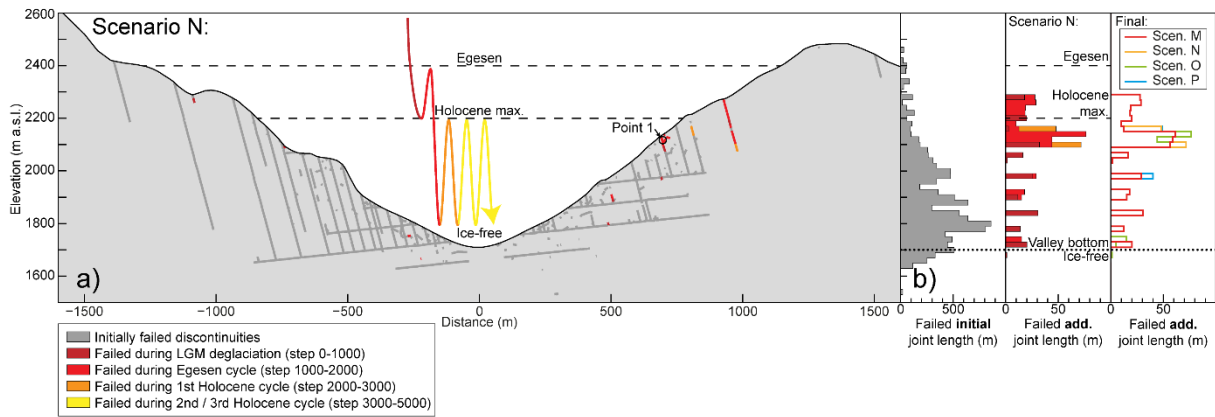


**Figure 2.10.** a) Spatio-temporal damage distribution during repeat glacial cycles for scenario N in the cross-section. b) Damage elevations at initial conditions, additional damage with time for scenario N, and final additional damage for scenario M, N, O, and P displayed as a histogram.

### 2.4.5 Stress redistribution

Stress redistribution as a result of incremental failure drives further damage within the slopes during our simulations. Figure 2.11 displays stress redistribution in the valley slopes for various glacier cycles. Limited by failure within the rock slope, differential stresses increase during LGM deglaciation and attain a maximum value of  $\sim 10$  MPa at the valley bottom (Figure 2.11a). In contrast, the valley flanks experience a reduction in differential stress of similar magnitude. LIA deglaciation shows a similar pattern but with approximately half the magnitude (Figure 2.11b). The missing weight of the valley glacier allows higher stresses to concentrate on the valley bottom, while the slope flanks experience concomitant stress reduction. Deglaciation, independent of the model scenario, results in stress redistribution, which reallocates high stresses from the mid-slope area to the valley bottom. Internal failure limits the magnitude of stress increase and promotes further stress redistribution. The full extent of stress redistribution during a complete glacial cycle is shown in Figure 2.11c; at the tips of failed joint segments, stress changes are in the range of  $\pm 2.5$  MPa and affect depths up to 200 m on the slope.

An example stress path is shown in Figure 2.12a for a failing mid-slope joint, highlighting localized stress changes during glacier fluctuations. At initial stress conditions, this discontinuity is close to failure. The additional load of LGM ice makes the joint less critically stressed (i.e. stresses move away from the failure envelope). Nearby joint failures and accompanying stress redistribution then leads to an irreversible change in the stress path during first deglaciation (LGM / Egesen ice retreat). The joint segment is more critically stressed during deglaciation than during initial ice-free conditions (shift from 1 to 3 in Figure 2.12a). Stresses exceed the failure criterion, the joint fails, and stress redistribution results as the joint assumes residual strength. This particular discontinuity then remains critically stressed (at residual strength) throughout the Holocene, although glacier advance leads to slight stress relaxation. The stress path during repeat Holocene cycles describes a closed loop following the residual strength envelope. Shear displacements attributed to the stress path are illustrated in Figure 2.12b. Irreversible joint slip occurs during first deglaciation as the joint fails. Further minor irreversible slip occurs during the first Holocene advance and later during repeat glacier retreat.

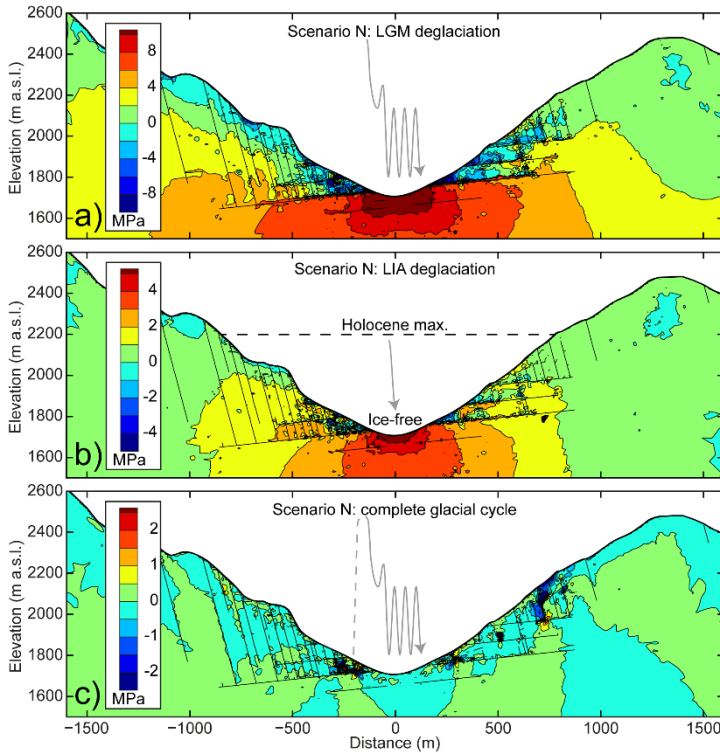


**Figure 2.11.** Stress redistribution during repeat glacial cycles: Changes in differential stress ( $\sigma_{diff-2D}$ ) for a) LGM deglaciation (step 0 to 5000), b) LIA deglaciation (step 4500 to 5000), and c) complete glacial cycle (ice-free initialization to step 5000), each for model initialization scenario N. Positive values indicate stress increase while negative values represent stress decrease.

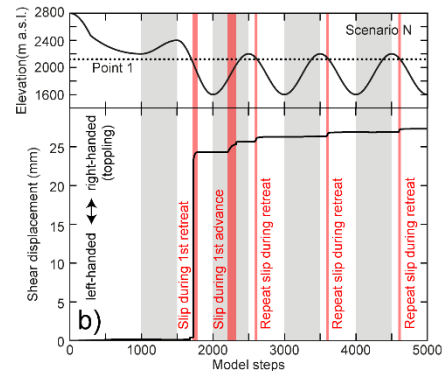
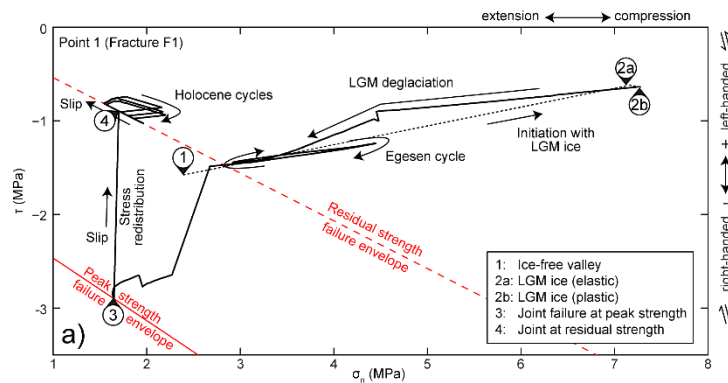


**Figure 2.12.** a) Stress path at discontinuity at Point 1 (location see Figure 2.10) in a normal versus shear stress diagram with peak and residual Mohr-Coulomb strength failure envelopes. b) Shear displacement and highlighted irreversible joint slip at Point 1 together with applied model scenario N.

## 2.4.6 Slope displacement

The modeled Aletsch Valley rock slopes experience not only distinct, localized failure along discontinuities, but also bulk rock mass displacement as a result of elastic rock mass deformation and accumulated joint displacement (Figure 2.13). Estimated uplift magnitudes for LGM deglaciation range from 300-600 mm, whereas LIA deglaciation results in 60-160 mm of simulated uplift (Figure 2.13a,b). The displacement pattern for LGM deglaciation is asymmetric due to greater ice loss in the Rhone Valley (see Figure 2.6). We observe left-handed block displacement along steeply-dipping joints on the western slope and right-handed shearing on the eastern slope, resulting in uphill-facing counterscarps (inset in Figure 2.13a). These calculated uplift values are within the same order of magnitude as determined in previous studies, e.g. *Memin et al.* [2009] estimated 5-9 mm uplift for 30-50 m ice loss in the Mont Blanc region. Our predicted post-LIA uplift at Aletsch corresponds to a mean uplift rate of 0.4-1.1 mm  $y^{-1}$ , which

is in good agreement with a rebound modeling study at Aletsch estimating an uplift rate of up to  $1.5 \text{ mm y}^{-1}$  due to recent glacier retreat [Melini et al., 2015].

Figure 2.13c shows that the eastern mid-slope region and the toe area in the west are most strongly affected by a complete modeled glacial cycle. The differences between valley slopes arise mainly from the prevailing joint patterns. Although modeled glacial cycles during the Holocene do not produce a large amount of additional rock slope damage (Figure 2.9), varying ice extents do influence slope displacements. The displacement patterns in scenarios M and N are similar, but the magnitudes increase by a factor of four with larger amplitude glacial fluctuations (Figure 2.13d,e). Holocene displacements for scenario O, with only minor Holocene ice fluctuation, are  $<0.1 \text{ mm}$ .

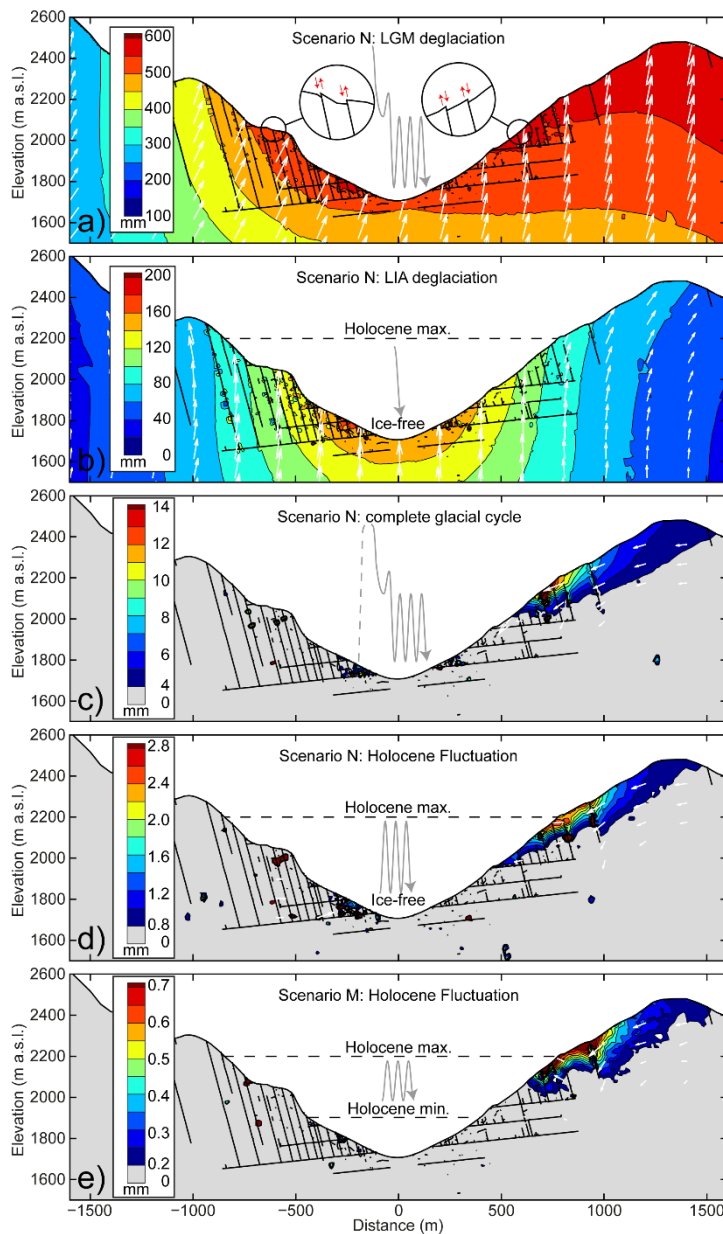


**Figure 2.13.** Slope displacement during repeat glacial cycles: Maximum displacement and displacement vectors (white arrows) for a) LGM deglaciation (step 0 to 5000), b) LIA deglaciation (step 4500 to 5000), and c) complete glacial cycle (ice-free initialization to step 5000), each for model scenario N. Comparison of displacement during Holocene fluctuation (step 2000 to 5000) between d) scenario N and e) scenario M.

## 2.4.7 Influence of LGM valley erosion

Current rates of glacial erosion measured in the Aletsch Valley are around  $1 \text{ mm y}^{-1}$  [Hallet *et al.*, 1996 and references therein], but these values may decrease by one or two orders of magnitude when integrated over glacial cycles [Koppes and Montgomery, 2009]. The influence of topographic change due to glacial erosion during the last glacial period ( $\sim 100 \text{ ky}$ ) may be small compared to landscape modifications during the Mid-Pleistocene Revolution [Haeuselmann *et al.*, 2007], but plays an important role in our mechanical model. We investigated rock slope damage under different erosion scenarios, assuming maximum glacial erosion rates of 0.1, 0.2, and 0.4  $\text{mm y}^{-1}$  for the modeled cross-section (maximum values occur in the Rhone Valley). For simplicity, we let the amount of total erosion decrease linearly with decreasing ice overburden. This resulted in maximum erosion within the Aletsch Valley of 8, 15, and 30 m, respectively, thinning towards adjacent valley flanks (Figure 2.14a). Less than 30 m of total erosion through abrasion during the last glacial cycle is likely a reasonable assumption [see Leith *et al.*, 2014a and references therein]. In all modeled erosion scenarios, the ice-free valley was initialized with plastic deformation including the additional, uneroded rock overburden, which was then instantaneously removed during LGM ice occupation.

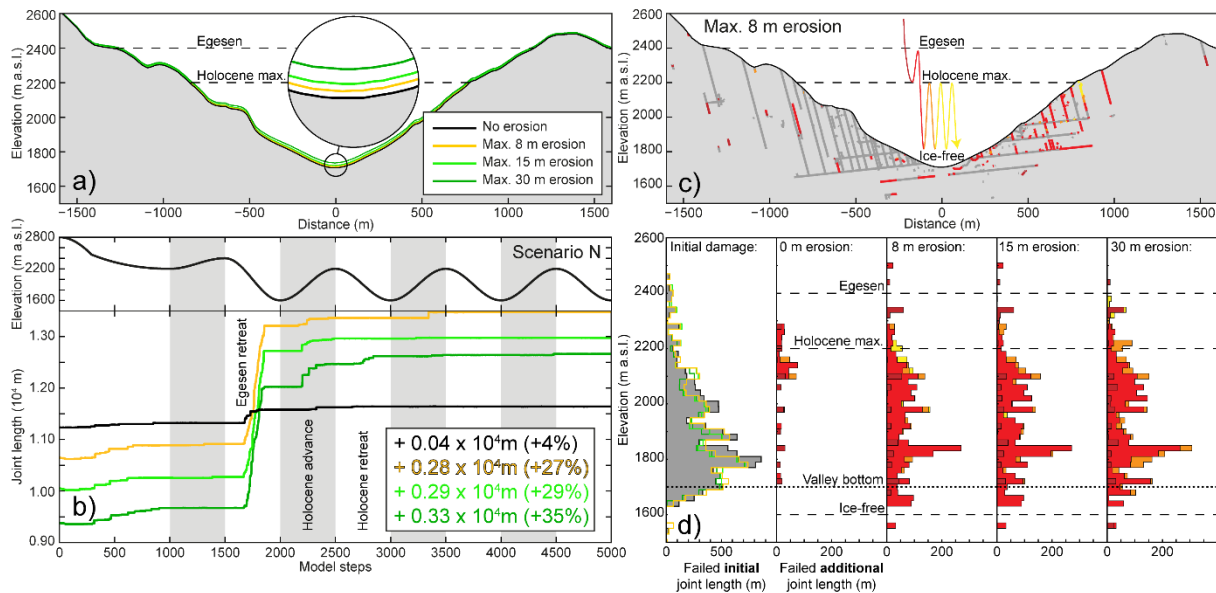


**Figure 2.14.** Influence of LGM valley erosion: a) Topographic profiles of models with various erosion scenarios. b) Temporal evolution of damage for various erosion scenarios together with applied model scenario N. c) Spatio-temporal damage distribution for scenario with maximum last-glacial erosion of 8 m (legend see in Figure 2.10). d) Damage propagation for various erosion scenarios displayed as histograms.

The temporal evolution of damage for model scenario N including erosion is shown in Figure 2.14b, revealing a strong increase in damage. A major damage event occurs when the ice elevation first reaches the mid-slope region, and continues until ice-free conditions are reached. Greater uneroded rock overburden included during initialization leads to a reduction in initial damage by loading the toe of the slope. New damage during deglaciation varies between 27% and 35% of initial damage, increasing with greater glacial erosion. The increased successive damage does not compensate the lower initial damage that comes with these erosion scenarios. Therefore the smallest erosion scenario creates the greatest amount of final damage. However, the period of adjustment to LGM erosion is longer for greater erosion rates, since stress conditions are shifted farther from the initial conditions. Therefore Holocene

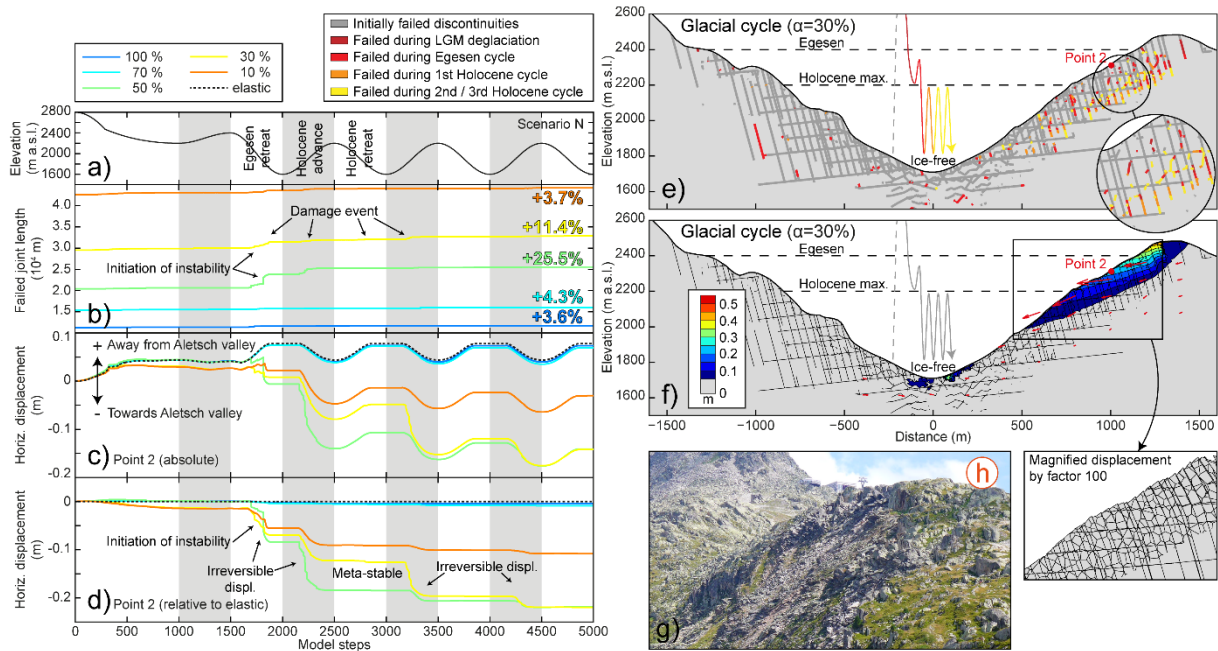
cycles can create more new damage. Figure 2.14c,d displays the spatial damage distribution for various erosion scenarios. New damage appears mostly in the mid-slope and lower regions of the eastern flank. We conclude that glacial erosion (i.e. rock debuttrressing) during the last glacial period has a strong influence on damage accumulation during first deglaciation and during subsequent glacial cycles. Buttressing by uneroded rock during the preceding ice-free interglacial (Eemian) prevents the development of initial damage.

#### 2.4.8 Weakened rock slope response

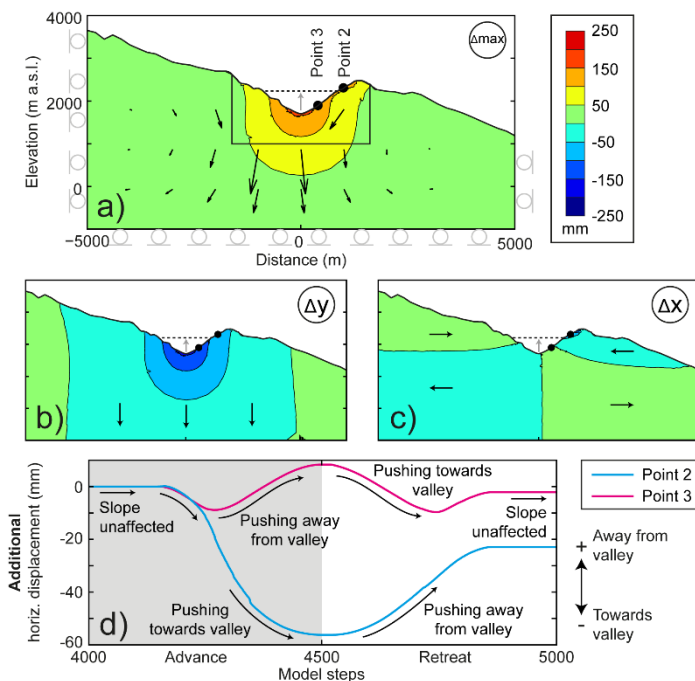
Here we investigate the efficacy of glacial loading cycles in creating damage within an already weakened rock slope, performing a series of simulations assuming reduced initial rock mass strength. The initial stress state remained the same for all scenarios, but we reduced the peak friction angle, peak cohesion, and peak tensile strength for all rock mass elements (except fault zones, which were already at residual strength). Reduced strengths were varied between the previously applied peak and residual values (see Table 2.3), scaled linearly by a factor ( $\alpha$ ); e.g.  $c_{red} = c_R + \alpha(c - c_R)$  (i.e.  $\alpha = 100\%$  represents peak strength properties as in previous models,  $\alpha = 0\%$  represents residual strength).

Figure 2.15 displays results for strength reduction factors  $\alpha = 70\%$ ,  $50\%$ ,  $30\%$ , and  $10\%$  for model scenario N. Reduced rock mass strength results in increased initial damage (Figure 2.15b). However, new damage accumulation during Holocene cycles is greatest for  $\alpha = 50\%$  and  $30\%$ . In a weaker rock slope close to residual strength (e.g.  $\alpha = 10\%$ ), all critically stressed discontinuities have already failed during initialization, and the magnitude of stress redistribution by slip-weakening is small. Major damage propagation for  $\alpha = 50\%$  and  $30\%$  occurs during Egesen ice retreat, while minor damage events follow subsequent Holocene advance and retreat cycles. Compared with models assuming higher rock mass strength (Figure 2.10a), weaker slopes have increased initial damage with more intact rock failure near the valley bottom (Figure 2.15e). New damage during glacial cycles occurs mostly on the eastern valley flank, in the form of fracture propagation along pre-existing, steeply-dipping discontinuities. Failure of intact rock bridges (i.e. Voronoi contacts) parallel to topography connects steeply-dipping joints and generates a shear failure surface. Maximum displacements in Figure 2.15f reach 0.5 m, revealing the extent of a slope instability with toppling kinematics and a graben structure as back scarp (see magnified displacement in Figure 2.15f). The kinematics and dimensions of the unstable rock slope produced in this simulation (Figure 2.15e,f) generally resemble field observations at the Moosfluh instability (Figure 2.1C,F) as well as the instability at Hohbalm (Figure 2.15i). No substantial sliding was produced on the western valley slope as is observed in the field (e.g. at the Driest instability, Figure 2.1A).

The evolution of slope instability is illustrated in the temporal damage and point displacement plot in Figure 2.15c,d. Damage during Egesen ice retreat leads to major irreversible displacement (Figure 2.15d), initiating slope failure. Interestingly, further displacement accumulates during the first and second Holocene ice *advances*, while later glacier *retreat* does not promote significant movement. The reason for enhanced displacement during Holocene advances is revealed by the elastic rock slope response shown in Figure 2.16: Glacier advance pushes the lower slope away from the valley axis, rotating the upper slope inward towards the valley, and vice versa during glacier retreat (Figure 2.16c,d). Inward rotation of the upper slope during glacier advance helps drive irreversible slip and damage propagation in the rock slope with joint orientations favoring flexural toppling.



**Figure 2.15.** Weakened rock slope affected by repeat glacial cycles: a) Applied glacier scenario N. b) Temporal evolution of damage for different reduction in rock mass strength ( $\alpha = 100\%$  to  $10\%$ ) illustrated as the sum of failed joint length. c) Absolute displacement and d) displacement relative to the elastic model at Point 2 in the upper slope. e) Spatio-temporal damage distribution for  $\alpha = 30\%$  for a complete glacial cycle (ice-free initialization until end of 3<sup>rd</sup> Holocene cycle). f) Maximum slope displacement and displacement vectors for scenario for  $\alpha = 30\%$  and magnified displacement and block geometry illustrating toppling-mode kinematics. g) Rock slope instability with toppling kinematics at Hohbalm (h in Figure 2.2) matching location of displacement in model results.



**Figure 2.16.** Slope displacement during a glacier cycle: a) Maximum displacement with displacement vectors, b) vertical displacement, c) and horizontal displacement with sketched movement direction during glacier advance (ice-free to Holocene maximum) for reduced rock mass strength ( $\alpha = 30\%$ ). d) Additional horizontal displacement at Points 2 and 3 (upper and lower slope) for the last Holocene cycle.

Figure 2.17 provides further insight into the mechanics of a weakened rock slope ( $\alpha = 30\%$ ) and illustrates how glacier cycles promote additional damage and shear displacement; different glacial stages applied in our models are queried in detail for shear displacement and additional failed discontinuities. LGM and Egesen deglaciation leads to large shearing near the valley bottom and along steeply-dipping discontinuities (F1) on the eastern flank near the slope crest (Figure 2.17a; 1). Most fault zones are affected by minor shear displacement of a few millimeters. New damage is distributed over the entire rock slope, but concentrates in the upper part of the eastern slope in the form of fracture propagation extending pre-existing joints. During the first Holocene advance (Figure 2.17a; 2), right-handed shearing dominates the steeply-dipping joints on the eastern flank (i.e. toppling), induced by inward rotation of the upper slope (see Figure 2.16). Prevailing joint patterns promote toppling kinematics. Although the glacier surface remains near the toe of the slope, the entire flank is affected. Later Holocene ice advance (Figure 2.17a; 3) reduces the affected region of the rock slope, but enhances shearing along faults close to the valley axis. Glacier fluctuations around the toe of an unstable rock slope are more effective at driving damage than glacier fluctuations affecting the upper part of the instability. Holocene ice retreat generates only minor shearing and damage in the lower slope region, mostly as the glacier reaches the toe of the slope (Figure 2.17a; 4 and 5). The same mechanical interaction between the glacier and rock slope appears during the second and third cycles, although the magnitude of shearing and the amount of new damage decreases with each cycle (Figure 2.17a; 6 to 9).

Shear displacement of four example points are shown in Figure 2.17c with location and corresponding joint orientation in Figure 2.17b. Instances of irreversible slip along these joints are highlighted. Planar sliding along gently-dipping joints (Points 4 and 5 in Figure 2.17c) occurs only during glacier retreat. On the other hand, shearing along steeply-dipping toppling joints (Points 6 and 7 in Figure 2.17c) happens during Egesen retreat and again during Holocene ice advances. This demonstrates that different joint patterns are affected differently by glacial loading and unloading cycles.

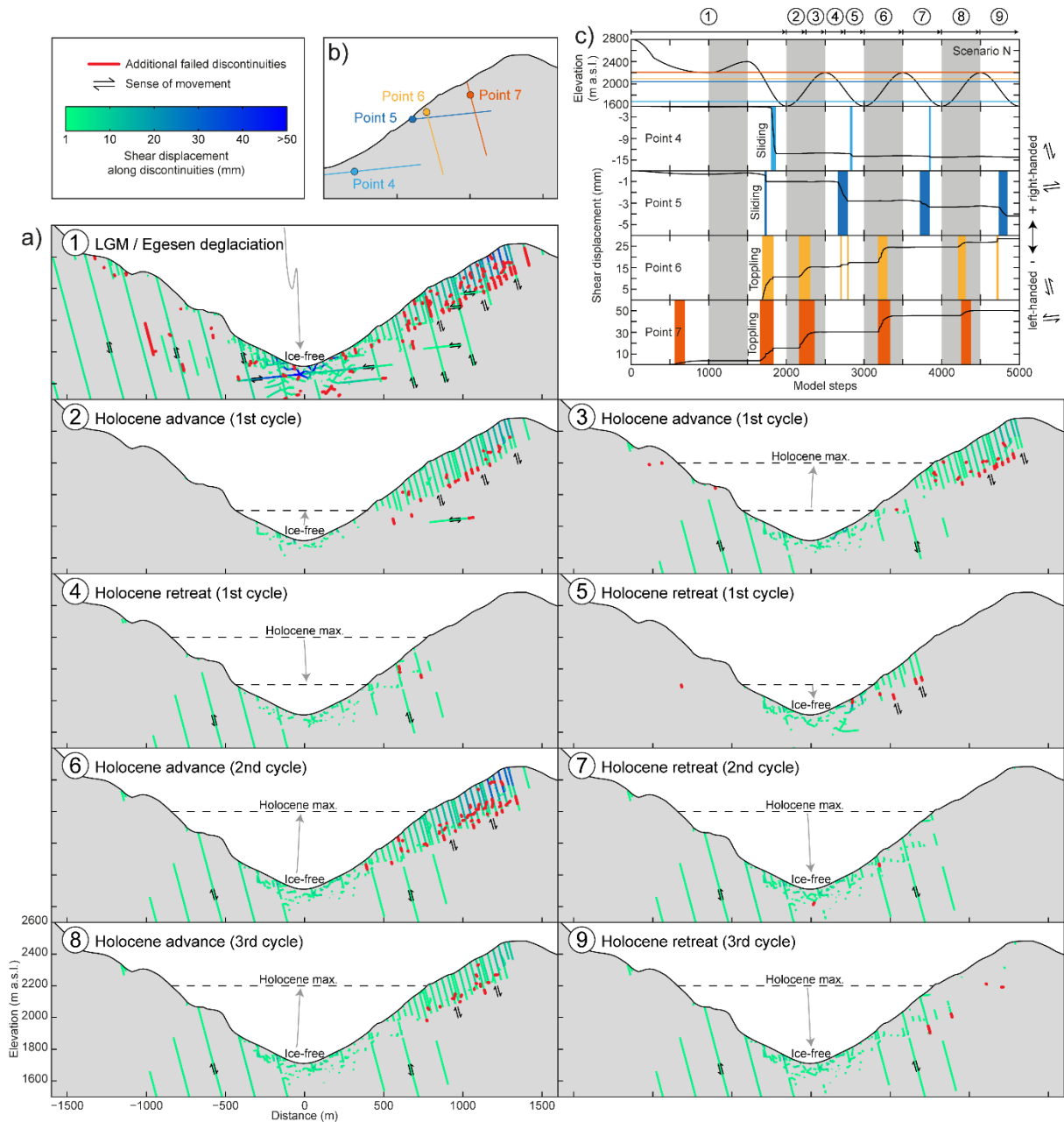


**Figure 2.17.** Mechanics of a weakened paraglacial rock slope: a) Evolution of failure and shear displacement along discontinuities for different stages of model scenario N with reduced rock mass strength ( $\alpha = 30\%$ ). b) Location of observation points showing orientation of discontinuities. c) Glacier scenario N with numbering of previously illustrated stages and elevation of observed points in the same colors. Shear displacement displayed for different points with phases of irreversible slip highlighted in the same colors.



## 2.5 Implications for paraglacial rock slope instabilities

Our simulations provide new insights into the mechanical development of damage produced by glacial cycles as a preparatory factor for paraglacial rock slope instabilities. At the Aletsch Glacier, we observe a concentration of large landslides around the present-day terminus (Figure 2.2). The landslide density decreases in the lower part of the valley affected only by the LGM and subsequent Egesen stadia, and we observe fewer slope failures in the upper Aletsch Valley, which was affected by fewer Holocene glacier fluctuations (Figure 2.2). There exist numerous other examples of rock slope failures located around present-day glacier termini [Bovis, 1990; Oppikofer *et al.*, 2008; Clayton *et al.*, 2013; McColl and Davies, 2013], the area where ice fluctuated most during the Holocene. In our study area, the majority of identified instabilities have post-Egesen / pre-LIA relative initialization age, while post-LIA landslides are less frequent (Figure 2.2). Post-LIA initiation of the Tälli instability coincided with ice retreat from the toe of the unstable slope. Exposure age dating constraining initiation of the Driest instability ( $7.4 \pm 0.7$  ky) shows a large lag-time between LGM or Egesen ice retreat and initial displacement, although initiation may be related to a minor Holocene readvance around 8.2 ky reaching an extent similar to today [Nicolussi and Schlüchter, 2012] affecting the toe of the landslide. Other past studies have suggested that paraglacial rock slope instabilities were more frequent during the early Holocene after deglaciation but often with large lag-times [e.g. Prager *et al.*, 2008; Ivy-Ochs *et al.*, 2009a; Ballantyne *et al.*, 2014a, b]. Rock slope failures associated with LIA retreat are generally less common [e.g. Evans and Clague, 1994; Jaboyedoff *et al.*, 2012].

In our simulated rock slope cross-section assuming realistic, moderate rock mass strength properties, the effects of glacier cycles as purely mechanical loading and unloading phenomena resulted in only minor damage (Figure 2.10). Glacier ice loading does not significantly buttress the adjacent slope, but does alter the *in-situ* stress field (Figure 2.11) potentially driving damage propagation. Most observed damage in our model was inherited, and occurred during initialization under Eemian ice-free conditions (Figure 2.10). However, we demonstrated that fluctuating glacier elevations strongly influence the criticality of adjacent rock slopes, which may in turn control the efficacy of other fatigue processes not explicitly considered in our models. Glacial erosion during the last glacial period is an effective way to change the *in-situ* stress conditions, stimulating new damage during LGM deglaciation and potentially acting as a significant contributor in preparing future rock slope instabilities. Meanwhile, reduced initial rock mass strength similarly enhances damage accumulation during subsequent glacial cycles. Therefore, acting in concert with a change in boundary conditions or material properties, fluctuating glacier ice can represent a significant preparatory factor for paraglacial rock slope failures.

Spatial patterns of landslides at Aletsch correlate with results of our numerical modeling. The kinematics and dimensions of the instability produced in our weakened slope closely resemble characteristics of the Moosfluh instability [Strozzi *et al.*, 2010; Kos *et al.*, 2016], however our numerical analysis was unable to reproduce substantial displacement on the western valley slope as observed at Driest [Kääb, 2002; Kos *et al.*, 2016]. Using moderate, presumed realistic, rock mass strength conditions, we were unable to generate large-displacement slope instability through glacial cycling. However, we did observe greater slope displacements in the presence of larger Holocene ice fluctuations, representing a slope profile around the present-day glacier terminus, as compared to smaller glacial cycles representing a higher valley profile (Figure 2.13). Furthermore, only large amplitude Holocene cycles, whose minima reached near the valley bottom, produced additional damage. These results indicate the potential influence of Holocene glacier fluctuations on the preparation of rock slope instabilities, and agree with the mapped landslide concentration around the present glacier tongue, as well as with field observations of fewer landslides in the upper Aletsch Valley, where ice has likely remained throughout the Holocene. However, we note that the rock slope reaction to glacier activity also depends strongly on site-specific

rock mass conditions [cf. *McColl*, 2012], which are in turn controlled by geological predisposition (i.e. rock strength and structure) as well as the damage history [*Terzaghi*, 1962; *Augustinus*, 1995; *Stead and Wolter*, 2015].

Correlating the temporal distribution of landslides assessed from field evidence with damage propagation in our numerical simulations reveals several similarities. In our models, most damage occurs during first deglaciation, when the glacier elevation drops for the first time below the critically stressed mid-slope region. For a weakened valley flank, this damage event may even initiate slope failure. The timing of large damage events during first deglaciation correlates well with the majority of post-Egesen / pre-LIA landslide ages assessed at Aletsch. Subsequent fracture propagation and slope displacement in our models accumulate during each Holocene cycle, especially at times when the glacier reaches the toe of the slope. Possible correlation between initiation of the Driest instability and timing of the minor 8.2 ky Holocene advance, as well as the coincidence of the Tälli landslide with recent glacier retreat, support the role of Holocene fluctuations in creating new slope damage. High sensitivity to glaciers in the slope toe region matches field observations indicating highly active and accelerating displacements at the Moosfluh instability as the present-day Aletsch glacier retreats from its toe [*Strozzi et al.*, 2010; *Kos et al.*, 2016; *Loew et al.*, 2017]. Rock slopes higher in the Aletsch valley, which have likely remained ice-covered since the LGM, might similarly be more prone to damage as they undergo first-time glacier retreat, potentially resulting in increased instances of slope failure.

Detailed temporal correlations between field observations and our numerical results remain challenging to assess, since damage propagation in our models is the immediate response to glacier change. Aside from glacier cycles, no other time-dependent processes act in our model and equilibrium is reached after each step, therefore it is not possible to simulate lag-times between deglaciation and slope failure. Furthermore, it is important to point out that initial gross displacement of a landslide body does not necessarily correlate with the timing of the genesis of that landslide. Slope displacement can appear long after the amount of internal rock mass damage has reached a critical level when an ultimate trigger finally initiates movement. We investigated the mechanics and evolution of rock mass damage as a preparatory factor for paraglacial slope instabilities, indicating times when new damage accumulation may be most prominent. The temporal evolution of a fully-developed slope instability, and its interplay with retreating or advancing ice, is beyond the focus of this research [see *McColl and Davies*, 2013]. We demonstrated that even when neglecting ice buttressing effects, most damage occurs during first deglaciation, bringing the slope closer to potential failure. In nature, other environmental processes following deglaciation may additionally reduce slope stability over time until failure occurs [*Eberhardt et al.*, 2004; *Prager et al.*, 2008; *McColl*, 2012].

In our models, we include explicit mechanical reasoning explaining the development and accumulation of rock slope damage associated with cyclic ice loading. Driving mechanisms for damage include stress changes during glacier cycles, stress redistribution by slip-weakening following incremental failure, or changes in rock slope boundary conditions. However, additional driving mechanisms may be important for preparing paraglacial rock slope instabilities. We demonstrated that glacial cycles strongly affect the amount of critically stressed joints within an alpine valley (Figure 2.7f,h), and each phase of glacier retreat places adjacent rock slopes into a more critically stressed condition (Figure 2.9c). Other environmental processes can act on the critically stressed slopes contributing to additional damage and promoting time-dependent failure, e.g. chemical weathering within joints [*Jaboyedoff et al.*, 2004], stress corrosion at fracture tips [*Faillettaz et al.*, 2010], ice segregation [*Wegmann et al.*, 1998; *Hales and Roering*, 2007; *Sanders et al.*, 2012; *Krautblatter et al.*, 2013], changes in joint water pressure [*Hansmann et al.*, 2012; *Preisig et al.*, 2016], thermal stresses [*Wegmann and Gudmundsson*, 1999; *Gischig et al.*, 2011b, c; *Baroni et al.*, 2014], or seismic fatigue [*Gischig et al.*, 2015]. Each of these

processes can contribute to further rock slope damage, especially at times when ice loading conditions increase the criticality of the slope. Over time, reduced rock mass strength may then favor increasing slope sensitivity to glacial mechanical loading and unloading cycles as shown in Figure 2.15. Thermo- and hydro-mechanical effects acting in concert with glacier cycles likely also play an important additional role in preparing slopes for failure, which we investigate in detail in following companion studies.

## 2.6 Summary and Conclusions

We investigated the mechanical development of rock slope damage induced by loading and unloading of Late Pleistocene and Holocene glaciers. Using detailed, conceptual numerical models, based on realistic site conditions at the Aletsch Glacier in Switzerland, we explored how stress changes associated with repeat glacial cycles generate progressive rock mass failure and prepare paraglacial slope instabilities. We first evaluated the transition from an ice-free valley during the Eemian interglacial towards LGM conditions for several cross-sections along the Aletsch Valley. Conceptualized glacier scenarios based on site-specific field mapping were then applied to investigate transient rock slope damage, *in-situ* stress changes, and displacement. We further highlighted the role of LGM valley erosion on damage propagation during deglaciation, and showed how a weaker rock mass is more sensitive to damage accumulation. Stress changes and resulting damage distributions were compared with mapped spatial and temporal landslide distributions at our Aletsch Valley study sites. Key outcomes of our study are:

1. Following initialization under ice-free conditions and reoccupation by LGM glaciers, damage accumulation during subsequent deglaciation and Lateglacial / Holocene cycles was minor and originated in our models from stress changes during glacier cycles and stress redistribution as a result of subglacial fracturing. The purely mechanical response to simple glacial loading and unloading thus represents a comparatively minor preparatory factor for paraglacial rock slope instabilities under moderate strength conditions; glacial debuitressing alone has limited effect. However including even minor amounts of bedrock erosion, i.e. rock debuitressing, during the LGM promoted significant new damage accumulation during first deglaciation. Major damage occurs during first ice retreat in our models not due to the removal of an ice buttress, but rather because stress conditions within the slope reach a critical state for the first time.
2. The mechanical interaction between a rock slope and glacier varies over time: the location of damage changes in conjunction with changing ice thickness. The first deglaciation (LGM and Egesen retreat) and subsequent Holocene ice *advances* are more effective in creating damage than glacier retreat in general. Ice advance generates shear dislocation and damage along toppling discontinuities in our models, while ice retreat promotes planar sliding. Weaker rock slopes showed increased sensitivity to glacial loading cycles, accumulating greater damage and displacements, which in some cases led to full development of an instability.
3. Temporal and spatial landslide patterns assessed in the field support conclusions from our numerical study. The kinematics and dimensions of a modeled instability on the eastern slope matches characteristics of landslides at Aletsch (Moosfluh and Hohbalm instabilities). Major damage during first deglaciation in our models correlates with the postulated post-Egesen initiation ages for these failures. Our modeled rock slope is most sensitive to ice loss in the toe region, which is confirmed by recent landslide monitoring at Aletsch. The eastern flank (toppling) in our numerical study showed enhanced slope displacement and subsequent damage propagation with repeat high amplitude ice elevation changes during Holocene advances. Local

predisposition, in combination with large amplitude ice fluctuations, may explain the observed concentration of landslides around the current tongue of the Great Aletsch Glacier.

4. Fluctuating ice in an alpine valley has a strong influence on the criticality of rock slopes. Retreating ice places adjacent slopes into a more critical state (reducing normal stress and increasing shear stress on joints). Critically stressed joints may be more susceptible to fatigue weathering processes resulting in time-dependent damage. Coupled processes acting in parallel with glacial cycles, e.g. changing ground temperatures or hillslope hydrology, should be considered in order to more broadly evaluate the efficacy of glacial cycles as a preparatory factor for paraglacial rock slope instabilities. Such processes likely play a significant role in creating new rock mass damage during deglaciation.
5. We demonstrate the importance of exploring paraglacial rock mechanics beyond simple glacial debuitressing through physically and geologically meaningful numerical models. We highlight proper modeling assumptions essential for implementing glacial ice into mechanical models over long time-scales, arguing for the use of stress boundary conditions rather than simulating ice as an elastic material. Furthermore, we showed that initial conditions are crucial for obtaining valid model results. We argue for using an ice-free valley during the Eemian interglacial as initial conditions, rather than peak LGM ice occupation, in order to avoid overestimating new damage during deglaciation. An entire transient glacial cycle should be considered to evaluate rock slope damage, since both glacier retreat and advance affect the valley's *in-situ* stress conditions.

## 2.7 Acknowledgements

This project was funded by the Swiss National Science Foundation (projects 135184 and 146593). Data used for this paper is properly cited and referred to in the reference list. Data output of this study is included in the tables and figures. Raw data are available on request from L.G. (E-mail: graemiger.lorenz@gmail.com). We thank Marcus Christl and the Ion Beam Physics group at ETH Zurich for  $^{10}\text{Be}$  accelerator mass spectrometry measurements. Special thanks to Johnny Sanders for field assistance and initial data collection, and Christian Wirsig for help in the lab. Thanks to Kerry Leith and Florian Amann for fruitful discussions, and to Martin Funk and Martin Lüthi for input on the behavior of ice. Andreas Bauder provided ice thickness distribution data of the Great Aletsch Glacier. Constructive comments from Sam McColl and Stuart Dunning, as well as the associate editor, are greatly appreciated and helped improve this manuscript.

## 2.8 Appendix 1: Cosmogenic nuclide exposure dating of the Driest instability

Exposure dating, exploiting the concentration of *in-situ* cosmogenic nuclides produced by cosmic rays [Ivy-Ochs and Kober, 2008], can be used to determine the initiation ages and paleo-slip rates of landslides [e.g. Hermanns *et al.*, 2013; Zerathe *et al.*, 2014]. The Driest instability is a promising site for exposure dating in the Aletsch area since it has a clear head scarp that was not covered by the LIA glacier. We collected five samples along a transect down the scarp to constrain the initial age of the Driest instability using cosmogenic  $^{10}\text{Be}$  (Figure 2.2 and Figure 2.4). DRIEST 01 was taken from glacially polished bedrock above the LIA trimline but 50 m below the Egesen moraine. DRIEST 02 was located on a 3 m high wall behind the main back-scarp. DRIEST 03 – 05 were located on the 50-70 m high main back-scarp. Sampling locations showing evidence of recent slabbing were avoided.

Sample preparation, quartz separation and Be extraction was undertaken according to procedures described by Ivy-Ochs [1996]. Total Be and  $^{10}\text{Be}$  measurements were carried out on the 600 kV TANDY system [Christl *et al.*, 2013] at the accelerator mass spectrometry facility of the Laboratory of Ion Beam Physics, ETH Zurich (Table 2.A1). The ETH internal standard S2007 N, calibrated against the primary 07KNSTD standard, was used to normalize the  $^{10}\text{Be}/^9\text{Be}$  ratios of the samples [Christl *et al.*, 2013]. Measurements were corrected by subtracting full process chemistry blanks with a  $^{10}\text{Be}/^9\text{Be}$  ratio of  $(3.6 \pm 2.6) \times 10^{-15}$ . Exposure ages were calculated with the CRONUS-Earth online calculator [Balco *et al.*, 2008] using local production rates derived from the NENA calibration data set [Balco *et al.*, 2009] and a time-dependent spallation production model [Lal, 1991; Stone, 2000]. Corrections for topographic shielding were calculated with the CRONUS-Earth online calculator [Balco *et al.*, 2008]. A surface erosion rate of  $1 \text{ mm ky}^{-1}$  was assumed for all samples, while corrections for snow cover were not included. DRIEST 04 was lost during sample processing. Calculated exposure ages are shown in Figure 2.4 and Table 2.A1.

DRIEST 01 was sampled from glacially polished bedrock exposed by the retreating Egesen glacier. Therefore the expected exposure age is close to Egesen. Recalculation (using the NENA production rate [Balco *et al.*, 2009]) of nearby bedrock exposure ages within the Egesen extent from Schindelwig *et al.* [2012] resulted in a mean age of  $13.7 \pm 1.0 \text{ ky}$  (Figure 2.2 and Figure 2.4). These ages, slightly older than Egesen (during YD dated at 12.8-11.5 ky BP [Alley *et al.*, 1993]), may indicate inherited nuclides from pre-exposure [Ivy-Ochs and Kober, 2008] during the preceding ice-free Bølling/Allerød. The calculated exposure age of DRIEST 01 ( $10.4 \pm 0.8 \text{ ky}$ ), however, is slightly younger than Egesen. DRIEST 03 and 05, with a mean exposure age of  $7.4 \pm 0.7 \text{ ky}$ , best represent the initiation age of sliding along the head scarp. Initial exposure of the head scarp thus seems to have occurred during the Holocene Climatic Optimum and not directly following LGM or Egesen ice retreat. DRIEST 02, not being located on the main head scarp but also not showing distinct marks of glacial erosion, has an intermediate exposure age ( $8.8 \pm 1.3 \text{ ky}$ ). The data are too sparse to calculate estimates of paleo slip rates, but nonetheless more than 20 m (elevation difference between DRIEST 03 and 05) of the sliding surface was exposed in a relatively short period (within the uncertainty of the dating method).

**Table 2.A1.** Sample names, measured  $^{10}\text{Be}$  concentrations, and calculated exposure ages of the Driest instability.

Sample name	Latitude	Longitude	Elevation	Thickness	Density	Shielding corr. factor	$^{10}\text{Be}$	$^{10}\text{Be}$ error	Exposure age	External uncertainty
	(DD.DDDD)	(DD.DDDD)	(m a.s.l.)	(cm)	(g cm <sup>-3</sup> )	0	(10 <sup>4</sup> at g <sup>-1</sup> )	(10 <sup>4</sup> at g <sup>-1</sup> )	ky	ky
DRIEST 1	46.4057	8.0245	2163	3.5	2.65	0.989	22.66	1.22	10.42	0.76
DRIEST 2	46.4056	8.0245	2157	3.0	2.65	0.752	14.62	2.01	8.77	1.29
DRIEST 3	46.4054	8.0244	2148	2.0	2.65	0.789	13.12	0.70	7.46	0.54
DRIEST 4	46.4054	8.0243	2143	4.0	2.65	0.701	-	-	-	-
DRIEST 5	46.4053	8.0242	2129	2.0	2.65	0.752	12.18	1.20	7.37	0.82

## 2.9 Appendix 2: Modelling approach for glacial ice

Changing glacial ice loading is the main factor driving rock slope damage in this study. The mechanical behavior of ice on different time scales and its effect on adjacent slopes is complex. An adequate modelling approach is therefore crucial to simulate glacial ice loading in a realistic manner. Here we present a comparison between modelling glacial ice as a hydrostatic stress boundary condition versus as an elastic material. The comparison emphasizes differences in the *in-situ* stress field of underlying bedrock using these two approaches, and the resulting rock slope damage.

Our extended model geometry presented in Figure 2.6 was initialized elastically with a glacier level at 2200 m a.s.l. We then subsequently allowed plastic deformation under the ice load. The glacier ice was removed completely under elastic conditions and a new mechanical equilibrium was established, before plasticity was again allowed. The same procedure was calculated with hydrostatic stress boundary conditions (Figure 2.A1a) and with an elastic ice body filling the valley (Figure 2.A1b). A density of 917 kg m<sup>-3</sup>, Young's modulus (E) of 10 GPa, and a Poisson's ratio ( $\nu$ ) of 0.3 were assumed for the elastic properties of ice [Schulson, 1999], similar to other studies [e.g. Eberhardt *et al.*, 2004].

Results of our comparison are shown in Figure 2.A1 and reveal that modelling the glacier as a stress boundary produces more initial damage in the rock slope than treating ice as an elastic material. In the former case, the glacier provides less lateral support and the situation is closer to an ice-free valley. In the latter case, almost no damage appears initially underneath the ice due to the strong buttressing effect of the elastic ice body. Removing the ice leads to an extreme increase in rock slope damage for the elastic material case (+351% of initial damage) compared to simulating ice as a stress boundary (+85% of initial damage) (Figure A1a,b). Both models are similar in how the vertical glacier load affects underlying bedrock (Figure 2.A1d). However, we observe higher horizontal stress in the valley bottom for the stress-boundary condition as compared to the elastic assumption (Figure 2.A1c). Vice-versa, higher horizontal stresses exist at the glacier surface elevation for the elastic assumption. Subsequent slope debuttressing causes a strong damage increase for the elastic material approach.

This brief comparison shows that modelling a valley glacier as an elastic material provides significantly more lateral confinement to adjacent rock slopes and reduces stresses in the valley bottom. Modelling

ice as an elastic material will thus lead to significantly overestimated damage accompanying glacier retreat. Our comparison further shows that stress redistribution in the adjacent rock slope is also not comparable between reducing the thickness of a valley glacier by 100 m ( $\rho = 917 \text{ kg m}^{-3}$ ) or eroding 30 m of rock at the valley bottom ( $\rho = 2700 \text{ kg m}^{-3}$ ), since the latter provides strong lateral support, unlike plastic ice. A modelling approach for glacial ice assuming elastic material properties might be reasonable for short-term rapid loading [e.g. *McColl et al.*, 2012], but not for long-term mechanical studies on glacial time scales.

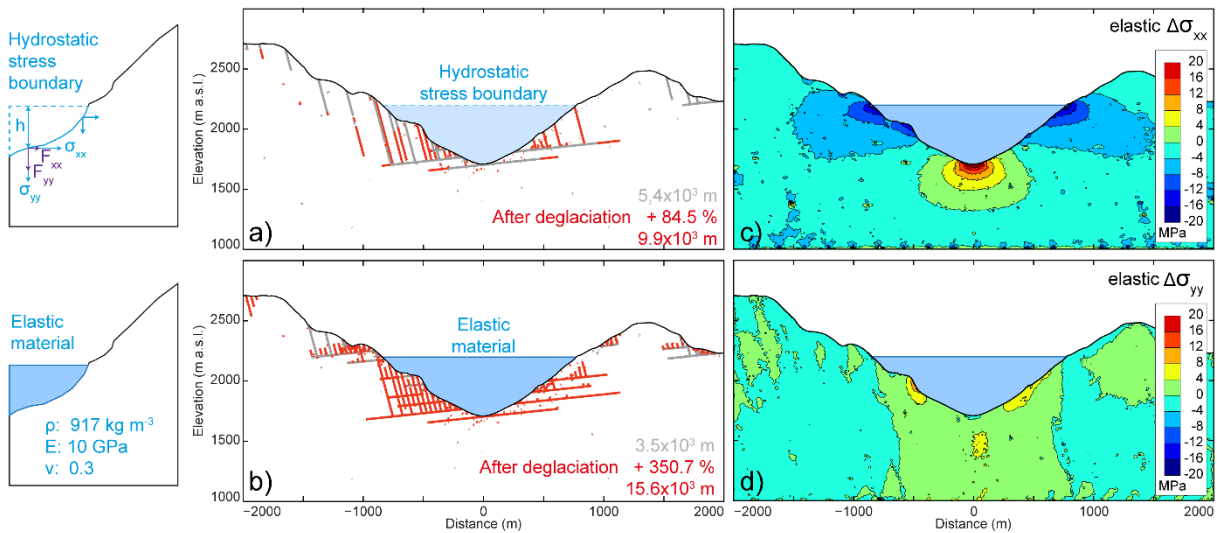


**Figure 2.A1.** Comparison between modelling glacial ice as a hydrostatic stress boundary condition versus as an elastic material: a) and b) Spatial damage distribution with initial glacier level at 2200 m a.s.l. and subsequent instantaneous ice removal for different modelling approaches. c) Horizontal and vertical stress differences between hydrostatic stress boundary condition model minus elastic material model with elastic rock properties during glacier ice occupation.

## 2.10 References

- Agliardi, F., and G. Crosta (2014), Long-and Short-term Controls on the Spriana Rockslide (Central Alps, Italy), in *Landslide Science for a Safer Geoenvironment*, edited by K. Sassa, P. Canuti and Y. Yin, pp. 243-249, Springer International Publishing, doi:10.1007/978-3-319-05050-8\_39.
- Alley, R. B., D. D. Blankenship, C. R. Bentley, and S. T. Rooney (1986), Deformation of till beneath ice stream B, West Antarctica, *Nature*, 322(6074), 57-59.
- Alley, R. B., et al. (1993), Abrupt increase in Greenland snow accumulation at the end of the Younger Dryas event, *Nature*, 362(6420), 527-529.
- Augustinus, P. C. (1995), Glacial valley cross-profile development: the influence of in situ rock stress and rock mass strength, with examples from the Southern Alps, New Zealand, *Geomorphology*, 14(2), 87-97, doi:10.1016/0169-555x(95)00050-x.
- Aydin, A. (2015), ISRM Suggested Method for Determination of the Schmidt Hammer Rebound Hardness: Revised Version, in *The ISRM Suggested Methods for Rock Characterization, Testing and Monitoring: 2007-2014*, edited by R. Ulusay, pp. 25-33.
- Balco, G., J. O. Stone, N. A. Lifton, and T. J. Dunai (2008), A complete and easily accessible means of calculating surface exposure ages or erosion rates from <sup>10</sup>Be and <sup>26</sup>Al measurements, *Quaternary Geochronology*, 3(3), 174-195, doi:http://dx.doi.org/10.1016/j.quageo.2007.12.001.
- Balco, G., J. Briner, R. C. Finkel, J. A. Rayburn, J. C. Ridge, and J. M. Schaefer (2009), Regional beryllium-10 production rate calibration for late-glacial northeastern North America, *Quaternary Geochronology*, 4(2), 93-107, doi:http://dx.doi.org/10.1016/j.quageo.2008.09.001.
- Ballantyne, C. K. (2002), Paraglacial geomorphology, *Quaternary Science Reviews*, 21(18–19), 1935-2017, doi:10.1016/s0277-3791(02)00005-7.
- Ballantyne, C. K., G. F. Sandeman, J. O. Stone, and P. Wilson (2014a), Rock-slope failure following Late Pleistocene deglaciation on tectonically stable mountainous terrain, *Quaternary Science Reviews*, 86, 144-157, doi:http://dx.doi.org/10.1016/j.quascirev.2013.12.021.
- Ballantyne, C. K., P. Wilson, D. Gheorghiu, and À. Rodés (2014b), Enhanced rock-slope failure following ice-sheet deglaciation: timing and causes, *Earth Surface Processes and Landforms*, 39(7), 900-913, doi:10.1002/esp.3495.
- Baroni, C., S. Martino, M. C. Salvatore, G. Scarascia Mugnozza, and L. Schilirò (2014), Thermomechanical stress–strain numerical modelling of deglaciation since the Last Glacial Maximum in the Adamello Group (Rhaetian Alps, Italy), *Geomorphology*, 226, 278-299, doi:http://dx.doi.org/10.1016/j.geomorph.2014.08.013.
- Bevis, M., et al. (2012), Bedrock displacements in Greenland manifest ice mass variations, climate cycles and climate change, *Proceedings of the National Academy of Sciences*, 109(30), 11944-11948, doi:10.1073/pnas.1204664109.
- Blunier, T., and E. J. Brook (2001), Timing of Millennial-Scale Climate Change in Antarctica and Greenland During the Last Glacial Period, *Science*, 291(5501), 109-112, doi:10.1126/science.291.5501.109.
- Boulton, G., T. Chan, R. Christiansson, L. O. Ericsson, J. Hartikainen, M. R. Jensen, F. W. Stanchell, and T. Wallroth (2004), Thermo-Hydro-Mechanical (T-H-M) Impacts of Glaciation and Implications for Deep Geologic Disposal of Nuclear Waste, in *Elsevier Geo-Engineering Book Series*, edited by S. Ove, pp. 299-304, Elsevier, doi:http://dx.doi.org/10.1016/S1571-9960(04)80057-0.
- Bovis, M. J. (1990), Rock-slope deformation at Affliction Creek, southern Coast Mountains, British Columbia, *Canadian Journal of Earth Sciences*, 27(2), 243-254, doi:10.1139/e90-024.
- Chan, T., R. Christiansson, G. S. Boulton, L. O. Ericsson, J. Hartikainen, M. R. Jensen, D. Mas Ivars, F. W. Stanchell, P. Vistrand, and T. Wallroth (2005), DECOVALEX III BMT3/BENCHPAR WP4: The thermo-hydro-mechanical responses to a glacial cycle and their potential implications for deep geological disposal of nuclear



- fuel waste in a fractured crystalline rock mass, *International Journal of Rock Mechanics and Mining Sciences*, 42(5–6), 805-827, doi:http://dx.doi.org/10.1016/j.ijrmmms.2005.03.017.
- Christl, M., C. Vockenhuber, P. W. Kubik, L. Wacker, J. Lachner, V. Alfimov, and H. A. Synal (2013), The ETH Zurich AMS facilities: Performance parameters and reference materials, *Nuclear Instruments and Methods in Physics Research Section B: Beam Interactions with Materials and Atoms*, 294, 29-38, doi:http://dx.doi.org/10.1016/j.nimb.2012.03.004.
- Clayton, M. A., D. Stead, and D. Kinakin (2013), The Mitchell Creek Landslide, B.C., Canada: Investigation using Remote Sensing and Numerical Modeling, in *47th U.S. Rock Mechanics/Geomechanics Symposium*, edited, American Rock Mechanics Association, San Francisco, California.
- Cohen, D., R. L. Hooke, N. R. Iverson, and J. Kohler (2000), Sliding of ice past an obstacle at Engabreen, Norway, *Journal of Glaciology*, 46(155), 599-610.
- Cohen, D., N. R. Iverson, T. S. Hooyer, U. H. Fischer, M. Jackson, and P. L. Moore (2005), Debris-bed friction of hard-bedded glaciers, *Journal of Geophysical Research: Earth Surface*, 110(F2), F02007, doi:10.1029/2004jf000228.
- Cohen, D., T. S. Hooyer, N. R. Iverson, J. F. Thomason, and M. Jackson (2006), Role of transient water pressure in quarrying: A subglacial experiment using acoustic emissions, *Journal of Geophysical Research: Earth Surface*, 111(F3), F03006, doi:10.1029/2005jf000439.
- Cossart, E., R. Braucher, M. Fort, D. L. Bourlès, and J. Carcaillet (2008), Slope instability in relation to glacial debuttrressing in alpine areas (Upper Durance catchment, southeastern France): Evidence from field data and <sup>10</sup>Be cosmic ray exposure ages, *Geomorphology*, 95(1–2), 3-26, doi:10.1016/j.geomorph.2006.12.022.
- Cossart, E., D. Mercier, A. Decaulne, T. Feuillet, H. P. Jónsson, and Þ. Sæmundsson (2014), Impacts of post-glacial rebound on landslide spatial distribution at a regional scale in northern Iceland (Skagafjörður), *Earth Surface Processes and Landforms*, 39(3), 336-350, doi:10.1002/esp.3450.
- Crisinel, A. (1978), Geologie de la reserve naturelle de la forêt d'Aletsch (Valais-Suisse), *Bull. Murithienne*, 95, 45-58.
- Crosta, G. B., P. Frattini, and F. Agliardi (2013), Deep seated gravitational slope deformations in the European Alps, *Tectonophysics*, 605, 13-33, doi:http://dx.doi.org/10.1016/j.tecto.2013.04.028.
- Cuffey, K. M., and W. S. B. Paterson (2010), *The physics of glaciers*, Butterworth-Heinemann/Elsevier, Burlington.
- Cundall, P. A., and R. D. Hart (1992), Numerical modelling of discontinua, *Engineering Computations*, 9(2), 101-113, doi:doi:10.1108/eb023851.
- Dahl-Jensen, D., et al. (2013), Eemian interglacial reconstructed from a Greenland folded ice core, *Nature*, 493(7433), 489-494, doi:10.1038/nature11789.
- Darnault, R., Y. Rolland, R. Braucher, D. Bourlès, M. Revel, G. Sanchez, and S. Bouissou (2012), Timing of the last deglaciation revealed by receding glaciers at the Alpine-scale: impact on mountain geomorphology, *Quaternary Science Reviews*, 31, 127-142, doi:10.1016/j.quascirev.2011.10.019.
- Deline, P. (2009), Interactions between rock avalanches and glaciers in the Mont Blanc massif during the late Holocene, *Quaternary Science Reviews*, 28(11–12), 1070-1083, doi:10.1016/j.quascirev.2008.09.025.
- Eberhardt, E., D. Stead, and J. S. Coggan (2004), Numerical analysis of initiation and progressive failure in natural rock slopes—the 1991 Randa rockslide, *International Journal of Rock Mechanics and Mining Sciences*, 41(1), 69-87, doi:10.1016/s1365-1609(03)00076-5.
- Eckardt, P., H. Funk, and T. Labhart (1983), Postglaziale Krustenbewegungen an der Rhein-Rhone-Linie, *Mensuration, Photogrammétrie, Génie rural* 2, 43-65.
- Evans, S. G., and J. J. Clague (1994), Recent climatic change and catastrophic geomorphic processes in mountain environments, *Geomorphology*, 10(1–4), 107-128, doi:10.1016/0169-555x(94)90011-6.

- Faillietaz, J., D. Sornette, and M. Funk (2010), Gravity-driven instabilities: Interplay between state- and velocity-dependent frictional sliding and stress corrosion damage cracking, *Journal of Geophysical Research: Solid Earth*, 115(B3), B03409, doi:10.1029/2009jb006512.
- Farinotti, D., M. Huss, A. Bauder, and M. Funk (2009), An estimate of the glacier ice volume in the Swiss Alps, *Global and Planetary Change*, 68(3), 225-231, doi:10.1016/j.gloplacha.2009.05.004.
- Fischer, L., F. Amann, J. R. Moore, and C. Huggel (2010), Assessment of periglacial slope stability for the 1988 Tschierwa rock avalanche (Piz Morteratsch, Switzerland), *Engineering Geology*, 116(1–2), 32-43, doi:10.1016/j.enggeo.2010.07.005.
- Gischig, V., F. Amann, J. R. Moore, S. Loew, H. Eisenbeiss, and W. Stempfhuber (2011a), Composite rock slope kinematics at the current Randa instability, Switzerland, based on remote sensing and numerical modeling, *Engineering Geology*, 118(1–2), 37-53, doi:10.1016/j.enggeo.2010.11.006.
- Gischig, V. S., J. R. Moore, K. F. Evans, F. Amann, and S. Loew (2011b), Thermomechanical forcing of deep rock slope deformation: 1. Conceptual study of a simplified slope, *J. Geophys. Res.*, 116(F4), F04010, doi:10.1029/2011jf002006.
- Gischig, V. S., J. R. Moore, K. F. Evans, F. Amann, and S. Loew (2011c), Thermomechanical forcing of deep rock slope deformation: 2. The Randa rock slope instability, *J. Geophys. Res.*, 116(F4), F04011, doi:10.1029/2011jf002007.
- Gischig, V., G. Preisig, and E. Eberhardt (2015), Numerical Investigation of Seismically Induced Rock Mass Fatigue as a Mechanism Contributing to the Progressive Failure of Deep-Seated Landslides, *Rock Mechanics and Rock Engineering*, 1-22, doi:10.1007/s00603-015-0821-z.
- Glaus, R. (1992), Rutschungsmessungen im Gebiet Blatten-Belalp. Diplomvermessungskurs 1991 Naters Rep., Institute für Geodäsie und Photogrammetrie, ETH Zürich.
- Goehring, B. M., J. M. Schaefer, C. Schluechter, N. A. Lifton, R. C. Finkel, A. J. T. Jull, N. Akçar, and R. B. Alley (2011), The Rhone Glacier was smaller than today for most of the Holocene, *Geology*, doi:10.1130/g32145.1.
- Goodman, D. J., G. C. P. King, D. H. M. Millar, and Q. Robin (1979), Pressure-melting effects in basal ice of temperate glaciers: Laboratory studies and field observations under glacier d'Argentière, *Journal of Glaciology*, 23(89), 259-271.
- Haeuselmann, P., D. E. Granger, P.-Y. Jeannin, and S.-E. Lauritzen (2007), Abrupt glacial valley incision at 0.8 Ma dated from cave deposits in Switzerland, *Geology*, 35(2), 143-146, doi:10.1130/g23094a.
- Hagen, J. O., O. Liestøl, J. L. Sollid, B. Wold, and G. Østrem (1993), Subglacial investigations at Bondhusbreen, Folgefonna, Norway, *Norsk Geografisk Tidsskrift - Norwegian Journal of Geography*, 47(3), 117-162, doi:10.1080/00291959308621974.
- Hales, T. C., and J. J. Roering (2007), Climatic controls on frost cracking and implications for the evolution of bedrock landscapes, *J. of Geophysical Research: Earth Surface*, 112(F2), F02033, doi:10.1029/2006jf000616.
- Hallet, B., L. Hunter, and J. Bogen (1996), Rates of erosion and sediment evacuation by glaciers: A review of field data and their implications, *Global and Planetary Change*, 12(1–4), 213-235, doi:http://dx.doi.org/10.1016/0921-8181(95)00021-6.
- Hansmann, J., S. Loew, and K. Evans (2012), Reversible rock-slope deformations caused by cyclic water-table fluctuations in mountain slopes of the Central Alps, Switzerland, *Hydrogeology Journal*, 20(1), 73-91, doi:10.1007/s10040-011-0801-7.
- Hermanns, R. L., T. Oppikofer, H. Dahle, and T. Eiken (2013), Understanding long-term slope deformation for stability assessment of rock slopes: the case of the Oppstadhornet rockslide, Norway, paper presented at International Conference Vajont 1963-2013. Thoughts and analyses after 50 years since the catastrophic landslide, Padua, Italy - 8-10 October 2013.

- Hock, R., A. Iken, and A. Wangler (1999), Tracer experiments and borehole observations in the overdeepening of Aletschgletscher, Switzerland, *Annals of Glaciology*, 28(1), 253-260, doi:10.3189/172756499781821742.
- Hoek, E., and E. T. Brown (1997), Practical estimates of rock mass strength, *International Journal of Rock Mechanics and Mining Sciences*, 34(8), 1165-1186.
- Hoek, E., C. Carranza-Torres, and B. Corkum (2002), Hoek–Brown failure criterion — 2002 edition, in *NARMS-TAC Conference*, edited, pp. 267–273, Toronto.
- Holm, K., M. Bovis, and M. Jakob (2004), The landslide response of alpine basins to post-Little Ice Age glacial thinning and retreat in southwestern British Columbia, *Geomorphology*, 57(3–4), 201-216, doi:10.1016/s0169-555x(03)00103-x.
- Holzhauser, H. (1995), *Gletscherschwankungen innerhalb der letzten 3200 Jahre am Beispiel des Grossen Aletsch- und des Gornergletschers. Neue Ergebnisse*, vdf Hochschulverlag AG an der ETH Zürich, ETH Zürich.
- Holzhauser, H., M. Magny, and H. J. Zumbühl (2005), Glacier and lake-level variations in west-central Europe over the last 3500 years, *The Holocene*, 15(6), 789-801, doi:10.1191/0959683605hl853ra.
- Hormes, A., B. U. Müller, and C. Schlüchter (2001), The Alps with little ice: evidence for eight Holocene phases of reduced glacier extent in the Central Swiss Alps, *The Holocene*, 11(3), 255-265, doi:10.1191/095968301675275728.
- Hudson, A. J., and P. J. Harrison (1997), *Engineering rock mechanics - An introduction to the principles*.
- Itasca (2014), UDEC - Universal Distinct Element Code, Version 6.0, User's Manual., *Itasca Consulting Group, Inc., Minneapolis*.
- Iverson, N. R., R. W. Baker, R. L. Hooke, H. Brian, and J. Peter (1999), Coupling between a glacier and a soft bed. I. A relation between effective pressure and local shear stress determined from till elasticity, *Journal of Glaciology*, 45(149), 31-40.
- Iverson, N. R., T. S. Hooyer, U. H. Fischer, D. Cohen, P. L. Moore, M. Jackson, G. Lapegard, and J. Kohler (2007), Soft-bed experiments beneath Engabreen, Norway: regelation infiltration, basal slip and bed deformation, *Journal of Glaciology*, 53(182), 323-340, doi:10.3189/002214307783258431.
- Ivy-Ochs, S. (1996), The dating of rock surfaces using in situ produced <sup>10</sup>Be, <sup>26</sup>Al and <sup>36</sup>Cl, with examples from Antarctica and the Swiss Alps Doctoral Thesis thesis, ETH Zurich, Zurich.
- Ivy-Ochs, S. (2015), Glacier variations in the European Alps at the end of the last glaciation, *Cuadernos de Investigacion Geografica*, 41(2), 295-315, doi:http://dx.doi.org/10.18172/cig.2750.
- Ivy-Ochs, S., and F. Kober (2008), Surface exposure dating with cosmogenic nuclides, *Quaternary Science Journal*, 57(1-2), 179-209, doi:10.3285/eg.57.1-2.7.
- Ivy-Ochs, S., H. Kerschner, A. Reuther, F. Preusser, K. Heine, M. Maisch, P. W. Kubik, and C. Schlüchter (2008), Chronology of the last glacial cycle in the European Alps, *Journal of Quaternary Science*, 23(6-7), 559-573, doi:10.1002/jqs.1202.
- Ivy-Ochs, S., A. v. Poschinger, H. A. Synal, and M. Maisch (2009a), Surface exposure dating of the Flims landslide, Graubünden, Switzerland, *Geomorphology*, 103(1), 104-112, doi:10.1016/j.geomorph.2007.10.024.
- Ivy-Ochs, S., H. Kerschner, M. Maisch, M. Christl, P. W. Kubik, and C. Schlüchter (2009b), Latest Pleistocene and Holocene glacier variations in the European Alps, *Quaternary Science Reviews*, 28(21–22), 2137-2149, doi:10.1016/j.quascirev.2009.03.009.
- Jaboyedoff, M., F. Baillifard, E. Bardou, and F. Girod (2004), The effect of weathering on Alpine rock instability, *Quarterly Journal of Engineering Geology and Hydrogeology*, 37(2), 95-103, doi:10.1144/1470-9236/03-046.
- Jaboyedoff, M., M.-H. Derron, J. Jakubowski, T. Oppikofer, and A. Pedrazzini (2012), *The 2006 Eiger rockslide, European Alps*, 1st ed. ed., Cambridge University Press, Cambridge.

- Jennings, J. E. (1970), A mathematical theory for the calculation of the stability of open cast mines, paper presented at Symp. on the Theoretical Background to the Planning of Open Pit Mines, Johannesburg.
- Joerin, U. E., T. F. Stocker, and C. Schlüchter (2006), Multicentury glacier fluctuations in the Swiss Alps during the Holocene, *The Holocene*, 16(5), 697-704, doi:10.1191/0959683606hl964rp.
- Jouvet, G., M. Huss, M. Funk, and H. Blatter (2011), Modelling the retreat of Grosser Aletschgletscher, Switzerland, in a changing climate, *Journal of Glaciology*, 57(206), 1033-1045, doi:10.3189/002214311798843359.
- Kääb, A. (2002), Monitoring high-mountain terrain deformation from repeated air- and spaceborne optical data: examples using digital aerial imagery and ASTER data, *ISPRS Journal of Photogrammetry and Remote Sensing*, 57(1–2), 39-52, doi:10.1016/s0924-2716(02)00114-4.
- Kasser, P., M. Aellen, and H. Siegenthaler (1982), Die Gletscher der Schweizer Alpen 1973/74 und 1974/75 Rep., 159 pp, Zürich.
- Kastrup, U., M. L. Zoback, N. Deichmann, K. F. Evans, D. Giardini, and A. J. Michael (2004), Stress field variations in the Swiss Alps and the northern Alpine foreland derived from inversion of fault plane solutions, *J. Geophys. Res.*, 109(B1), B01402, doi:10.1029/2003jb002550.
- Kelly, M. A., P. W. Kubik, F. Von Blanckenburg, and C. Schlüchter (2004a), Surface exposure dating of the Great Aletsch Glacier Egesen moraine system, western Swiss Alps, using the cosmogenic nuclide <sup>10</sup>Be, *Journal of Quaternary Science*, 19(5), 431-441, doi:10.1002/jqs.854.
- Kelly, M. A., J. F. Buoncristiani, and C. Schluchter (2004b), A reconstruction of the last glacial maximum (LGM) ice-surface geometry in the western Swiss Alps and contiguous Alpine regions in Italy and France, *Eclogae Geol Helv*, 97(1), 57-75, doi:DOI 10.1007/s00015-004-1109-6.
- Khan, S. A., L. Liu, J. Wahr, I. Howat, I. Joughin, T. van Dam, and K. Fleming (2010), GPS measurements of crustal uplift near Jakobshavn Isbræ due to glacial ice mass loss, *Journal of Geophysical Research: Solid Earth*, 115(B9), B09405, doi:10.1029/2010jb007490.
- Kinakin, D., and D. Stead (2005), Analysis of the distributions of stress in natural ridge forms: implications for the deformation mechanisms of rock slopes and the formation of sackung, *Geomorphology*, 65(1–2), 85-100, doi:http://dx.doi.org/10.1016/j.geomorph.2004.08.002.
- Koppes, M. N., and D. R. Montgomery (2009), The relative efficacy of fluvial and glacial erosion over modern to orogenic timescales, *Nature Geosci*, 2(9), 644-647.
- Kos, A., F. Amann, T. Strozzi, R. Delaloye, J. von Ruetten, and S. Springman (2016), Contemporary glacier retreat triggers a rapid landslide response, Great Aletsch Glacier, Switzerland, *Geophysical Research Letters*, 43(24), 12,466-412,474, doi:10.1002/2016GL071708.
- Krautblatter, M., D. Funk, and F. K. Günzel (2013), Why permafrost rocks become unstable: a rock–ice-mechanical model in time and space, *Earth Surface Processes and Landforms*, 38(8), 876-887, doi:10.1002/esp.3374.
- Lal, D. (1991), Cosmic ray labeling of erosion surfaces: in situ nuclide production rates and erosion models, *Earth and Planetary Science Letters*, 104(2–4), 424-439, doi:http://dx.doi.org/10.1016/0012-821X(91)90220-C.
- Landestopographie, and VAW (1962), Aletschgletscher Kartenmaterial - Gletscherausdehnung 1957, Wabern-Bern.
- Leith, K., J. R. Moore, F. Amann, and S. Loew (2014a), Subglacial extensional fracture development and implications for Alpine Valley evolution, *Journal of Geophysical Research: Earth Surface*, 119(1), 62-81, doi:10.1002/2012jf002691.
- Leith, K., J. R. Moore, F. Amann, and S. Loew (2014b), In situ stress control on microcrack generation and macroscopic extensional fracture in exhuming bedrock, *Journal of Geophysical Research: Solid Earth*, 119(1), 594-615, doi:10.1002/2012jb009801.

- Loew, S., V. S. Gischig, F. Glueer, R. Seifert, and J. R. Moore (2017), Multidisciplinary monitoring of progressive failure processes in brittle rock slopes, in *Rock Mechanics and Engineering*, edited by X.-T. Feng and J. A. Hudson, CRC Press / Balkema -Taylor and Francis Group.
- Lorig, L. J., and P. A. Cundall (1989), Modeling of Reinforced Concrete Using the Distinct Element Method, in *Fracture of Concrete and Rock*, edited by S. P. Shah and S. E. Swartz, pp. 276-287, Springer New York, doi:10.1007/978-1-4612-3578-1\_28.
- Luetscher, M., D. L. Hoffmann, S. Frisia, and C. Spötl (2011), Holocene glacier history from alpine speleothems, Milchbach cave, Switzerland, *Earth and Planetary Science Letters*, 302(1–2), 95-106, doi:10.1016/j.epsl.2010.11.042.
- Maisch, M., A. Wipf, B. Denneler, J. Battaglia, and C. Benz (1999), *Die Gletscher der Schweizer Alpen: Gletscherhochstand 1850, Aktuelle Vergletscherung, Gletscherschwund-Szenarien. Schlussbericht NFP 31*, vdf Hochschulverlag.
- Masset, O., and S. Loew (2010), Hydraulic conductivity distribution in crystalline rocks, derived from inflows to tunnels and galleries in the Central Alps, Switzerland, *Hydrogeology Journal*, 18(4), 863-891, doi:10.1007/s10040-009-0569-1.
- McColl, S. T. (2012), Paraglacial rock-slope stability, *Geomorphology*, 153–154, 1-16, doi:10.1016/j.geomorph.2012.02.015.
- McColl, S. T., and T. R. H. Davies (2013), Large ice-contact slope movements: glacial buttressing, deformation and erosion, *Earth Surface Processes and Landforms*, 38(10), 1102-1115, doi:10.1002/esp.3346.
- McColl, S. T., T. R. H. Davies, and M. J. McSaveney (2010), Glacier retreat and rock-slope stability: debunking debuttressing, in *11th Congress of the International Association for Engineering Geology and the Environment*, edited by G. Active, pp. 467-474, Auckland, New Zealand.
- McColl, S. T., T. R. H. Davies, and M. J. McSaveney (2012), The effect of glaciation on the intensity of seismic ground motion, *Earth Surface Processes and Landforms*, 37(12), 1290-1301, doi:10.1002/esp.3251.
- Melini, D., P. Gegout, M. King, M. B., and G. Spada (2015), On the rebound: Modeling Earth's ever-changing shape, *EOS*, 96, doi:10.1029/2015EO033387.
- Memin, A., Y. Rogister, J. Hinderer, M. Llubes, E. Berthier, and J. P. Boy (2009), Ground deformation and gravity variations modelled from present-day ice thinning in the vicinity of glaciers, *Journal of Geodynamics*, 48(3–5), 195-203, doi:10.1016/j.jog.2009.09.006.
- Moran, A. P., S. Ivy-Ochs, M. Schuh, M. Christl, and H. Kerschner (2016), Evidence of central Alpine glacier advances during the Younger Dryas–early Holocene transition period, *Boreas*, 45(3) 398-410, doi:10.1111/bor.12170.
- Muttoni, G., C. Carcano, E. Garzanti, M. Ghielmi, A. Piccin, R. Pini, S. Rogledi, and D. Sciunnach (2003), Onset of major Pleistocene glaciations in the Alps, *Geology*, 31(11), 989-992, doi:10.1130/g19445.1.
- Nicolussi, K., and G. Patzelt (2000), Discovery of early Holocene wood and peat on the forefield of the Pasterze Glacier, Eastern Alps, Austria, *The Holocene*, 10(2), 191-199, doi:10.1191/095968300666855842.
- Nicolussi, K., and C. Schlüchter (2012), The 8.2 ka event—Calendar-dated glacier response in the Alps, *Geology*, doi:10.1130/g32406.1.
- Nicolussi, K., M. Kaufmann, G. Patzelt, J. van der Plicht, and A. Thurner (2005), Holocene tree-line variability in the Kauner Valley, Central Eastern Alps, indicated by dendrochronological analysis of living trees and subfossil logs, *Vegetation History and Archaeobotany*, 14, 221-234.
- Oppikofer, T., M. Jaboyedoff, and H.-R. Keusen (2008), Collapse at the eastern Eiger flank in the Swiss Alps, *Nature Geoscience*, 1(8), 531-535, doi:10.1038/ngeo258.
- Prager, C., C. Zangerl, G. Patzelt, and R. Brandner (2008), Age distribution of fossil landslides in the Tyrol (Austria) and its surrounding areas, *Nat. Haz. Earth Syst. Sci.*, 8(2), 377-407, doi:10.5194/nhess-8-377-2008.

- Preisig, G., E. Eberhardt, M. Smithyman, A. Preh, and L. Bonzanigo (2016), Hydromechanical Rock Mass Fatigue in Deep-Seated Landslides Accompanying Seasonal Variations in Pore Pressures, *Rock Mechanics and Rock Engineering*, 1-19, doi:10.1007/s00603-016-0912-5.
- Röthlisberger, F., and W. Schneebeili (1979), Genesis of lateral moraine complexes, demonstrated by fossil soils and trunks: Indicators of postglacial climatic fluctuations, in *Moraines and Varves; Origin, Genesis, Classification*, edited by C. Schlüchter, pp. 387-419, A.A. Balkema, Rotterdam, Netherlands.
- Sanders, J. W., K. M. Cuffey, J. R. Moore, K. R. MacGregor, and J. L. Kavanaugh (2012), Periglacial weathering and headwall erosion in cirque glacier bergschrunds, *Geology*, doi:10.1130/g33330.1.
- Schimmelpfennig, I., J. M. Schaefer, N. Akçar, S. Ivy-Ochs, R. C. Finkel, and C. Schlüchter (2012), Holocene glacier culminations in the Western Alps and their hemispheric relevance, *Geology*, doi:10.1130/g33169.1.
- Schindelwig, I., N. Akçar, P. W. Kubik, and C. Schlüchter (2012), Lateglacial and early Holocene dynamics of adjacent valley glaciers in the Western Swiss Alps, *Journal of Quaternary Science*, 27(1), 114-124, doi:10.1002/jqs.1523.
- Schulson, E. M. (1990), The brittle compressive fracture of ice, *Acta Metallurgica et Materialia*, 38(10), 1963-1976, doi:http://dx.doi.org/10.1016/0956-7151(90)90308-4.
- Schulson, E. M. (1999), The structure and mechanical behavior of ice, *JOM*, 51(2), 21-27, doi:10.1007/s11837-999-0206-4.
- Selvadurai, A. P. S., A. P. Suvorov, and P. A. Selvadurai (2015), Thermo-hydro-mechanical processes in fractured rock formations during a glacial advance, *Geosci. Model Dev.*, 8(7), 2167-2185, doi:10.5194/gmd-8-2167-2015.
- Slaymaker, O. (2009), Proglacial, periglacial or paraglacial?, *Geological Society, London, Special Publications*, 320(1), 71-84, doi:10.1144/sp320.6.
- Stead, D., and A. Wolter (2015), A critical review of rock slope failure mechanisms: The importance of structural geology, *Journal of Structural Geology*, 74, 1-23, doi:http://dx.doi.org/10.1016/j.jsg.2015.02.002.
- Steck, A. (2011), 1269 Aletschgletscher mit Teil von 1249 Finsteraarhorn, *Geolog. Atlas der Schweiz 1:25000*.
- Steiner, W., U. Graber, and H.-R. Keusen (1996), Construction In Rock At 3550 Meters Elevation (Jungfrauoch, Switzerland), in *EUROCK 96*, edited, pp. p. 543-550, International Society for Rock Mechanics, Torino, Italy.
- Stone, J. O. (2000), Air pressure and cosmogenic isotope production, *Journal of Geophysical Research: Solid Earth*, 105(B10), 23753-23759, doi:10.1029/2000jb900181.
- Strozzi, T., R. Delaloye, A. Käab, C. Ambrosi, E. Perruchoud, and U. Wegmüller (2010), Combined observations of rock mass movements using satellite SAR interferometry, differential GPS, airborne digital photogrammetry, and airborne photography interpretation, *J. Geophys. Res.*, 115(F1), F01014, doi:10.1029/2009jf001311.
- Terzaghi, K. (1962), Stability of Steep Slopes on Hard Unweathered Rock, *Géotechnique*, 12(4), 251-270.
- Tinner, W., and J.-P. Theurillat (2003), Uppermost Limit, Extent, and Fluctuations of the Timberline and Treeline Ecocline in the Swiss Central Alps during the Past 11,500 Years, *Arctic, Antarctic, and Alpine Research*, 35(2), 158-169, doi:10.1657/1523-0430(2003)035[0158:uleafo]2.0.co;2.
- Ustaszewski, M. E., A. Hampel, and O. A. Pfiffner (2008), Composite faults in the Swiss Alps formed by the interplay of tectonics, gravitation and postglacial rebound: an integrated field and modelling study, *Swiss Journal of Geoscience*, 101(1), 223-236.
- Vidstrand, P., T. Wallroth, and L. Ericsson (2008), Coupled HM effects in a crystalline rock mass due to glaciation: indicative results from groundwater flow regimes and stresses from an FEM study, *Bulletin of Engineering Geology and the Environment*, 67(2), 187-197, doi:10.1007/s10064-008-0123-8.
- Vinther, B. M., et al. (2009), Holocene thinning of the Greenland ice sheet, *Nature*, 461(7262), 385-388, doi:10.1038/nature08355.

- Vogler, M. (2015), Hydro-Mechanical Interactions between the Great Aletsch Glacier and the Driest Landslide (Switzerland), M.Sc. thesis, Department of Earth Sciences, ETH, Zurich.
- Wegmann, M. (1998), Frostdynamik in hochalpinen Felswänden - am Beispiel der Region Jungfraujoeh-Aletsch, Ph.D. thesis, ETH, Zurich.
- Wegmann, M., and G. H. Gudmundsson (1999), Thermally induced temporal strain variations in rock walls observed at subzero temperatures, in *Advances in Cold-Region Thermal Engineering and Sciences*, edited by K. Hutter, Y. Wang and H. Beer, pp. 511-518, Springer Berlin Heidelberg, doi:10.1007/BFb0104208.
- Wegmann, M., G. H. Gudmundsson, and W. Haeberli (1998), Permafrost changes in rock walls and the retreat of alpine glaciers: a thermal modelling approach, *Permafrost and Periglacial Processes*, 9(1), 23-33, doi:10.1002/(sici)1099-1530(199801/03)9:1<23::aid-ppp274>3.0.co;2-y.
- Welten, M. (1982), Vegetationsgeschichtliche Untersuchungen in den westlichen Schweizer Alpen: Bern-Wallis, *Denkschrift SNG*, 95, 104.
- Zangerl, C., E. Eberhardt, and S. Loew (2003), Ground settlements above tunnels in fractured crystalline rock: numerical analysis of coupled hydromechanical mechanisms, *Hydrogeology Journal*, 11(1), 162-173, doi:10.1007/s10040-002-0234-4.
- Zangerl, C., K. F. Evans, E. Eberhardt, and S. Loew (2008a), Consolidation settlements above deep tunnels in fractured crystalline rock: Part 1—Investigations above the Gotthard highway tunnel, *International Journal of Rock Mechanics and Mining Sciences*, 45(8), 1195-1210, doi:http://dx.doi.org/10.1016/j.ijrmms.2008.02.002.
- Zangerl, C., E. Eberhardt, K. F. Evans, and S. Loew (2008b), Consolidation settlements above deep tunnels in fractured crystalline rock: Part 2—Numerical analysis of the Gotthard highway tunnel case study, *International J. of Rock Mech. and Mining Sciences*, 45(8), 1211-1225, doi:http://dx.doi.org/10.1016/j.ijrmms.2008.02.005.
- Zangerl, C., K. F. Evans, E. Eberhardt, and S. Loew (2008c), Normal stiffness of fractures in granitic rock: A compilation of laboratory and in-situ experiments, *Inter. J. of Rock Mech. and Mining Sci.*, 45(8), 1500-1507.
- Zerathe, S., T. Lebourg, R. Braucher, and D. Bourlès (2014), Mid-Holocene cluster of large-scale landslides revealed in the Southwestern Alps by <sup>36</sup>Cl dating. Insight on an Alpine-scale landslide activity, *Quaternary Science Reviews*, 90, 106-127, doi:http://dx.doi.org/10.1016/j.quascirev.2014.02.015.





### 3 BEYOND DEBUTTRESSING: THERMO-MECHANICAL ROCK SLOPE DAMAGE DURING REPEAT GLACIAL CYCLES

Lorenz M. Grämiger<sup>1</sup>, Jeffrey R. Moore<sup>1,2</sup>, Valentin S. Gischig<sup>1</sup>, Simon Loew<sup>1</sup>

<sup>1</sup> *Department of Earth Sciences, ETH Zurich, Zurich, Switzerland.*

<sup>2</sup> *Department of Geology and Geophysics, University of Utah, Salt Lake City, Utah, USA.*

**Abstract:** Cycles of glaciation alter the temperature structure in proximal alpine valley flanks, driving rock slope damage through thermo-mechanical stresses. Here we extend simplified assumptions of glacial debuttreassing to quantitatively examine how paraglacial bedrock temperature changes, acting in concert with changing ice loads during Late Pleistocene and Holocene glacial cycles, create damage in adjacent rock slopes and prepare future slope instabilities. When in contact with temperate glacier ice, valley walls maintain near isothermal  $\sim 0$  °C surface temperatures and are shielded from daily and seasonal cycles. With retreat, rock walls are rapidly exposed to strongly varying temperature boundary conditions, a transition we term ‘paraglacial thermal shock’. Using detailed, conceptual numerical models based on the Aletsch Glacier in Switzerland, we show that including thermo-mechanical stresses during simulated glacial cycles creates significantly more rock slope damage than predicted for purely mechanical ice loading and unloading. Glacier advances are especially effective in generating damage as rapid cooling drives contraction of the rock mass reducing joint normal stresses. First time exposure to seasonal temperature cycles during deglaciation induces a shallow damage front that follows the retreating ice margin, generating damage in a complementary process at shorter time scales. Acting on a reduced strength rock mass, modeled thermo-mechanical cycles enhance the development of a slope instability with similar attributes as observed in our study area. Our results demonstrate that thermo-mechanical stresses acting in parallel with changing ice loads are capable of generating considerable rock slope damage with spatial and temporal patterns controlled by glacier extents.

### 3.1 Introduction

Rock slope failures are frequently located in the vicinity of retreating glaciers, shaping alpine landscapes and representing a hazard to mountain communities and infrastructure [Evans and Clague, 1994]. Slope instabilities result from the accumulation of rock mass damage over time (i.e., creation of new fractures, propagation of slip along existing joints, and failure of intact rock bridges), which may occur in conjunction with or independent from an ultimate failure trigger (Figure 3.1a). Slope debuttressing associated with glacier retreat (i.e., removal of an ice buttress) is often suggested to be a principal mechanism driving damage in glacially over-steepened rock walls, preparing post-glacial alpine slope failures [e.g., Bovis, 1990; Cossart et al., 2008; Jaboyedoff et al., 2012]. However, because ice behaves in a ductile manner at long time scales ( $>10^5$  years) and small strain rates ( $<10^{-3} \text{ s}^{-1}$ ; Schulson [1990]), glaciers make a poor buttress for ice-marginal slopes [McColl et al., 2010; McColl and Davis, 2013; Grämiger et al., 2017], loading underlying bedrock by their weight alone and not providing significant rigid lateral support to adjacent valley walls.

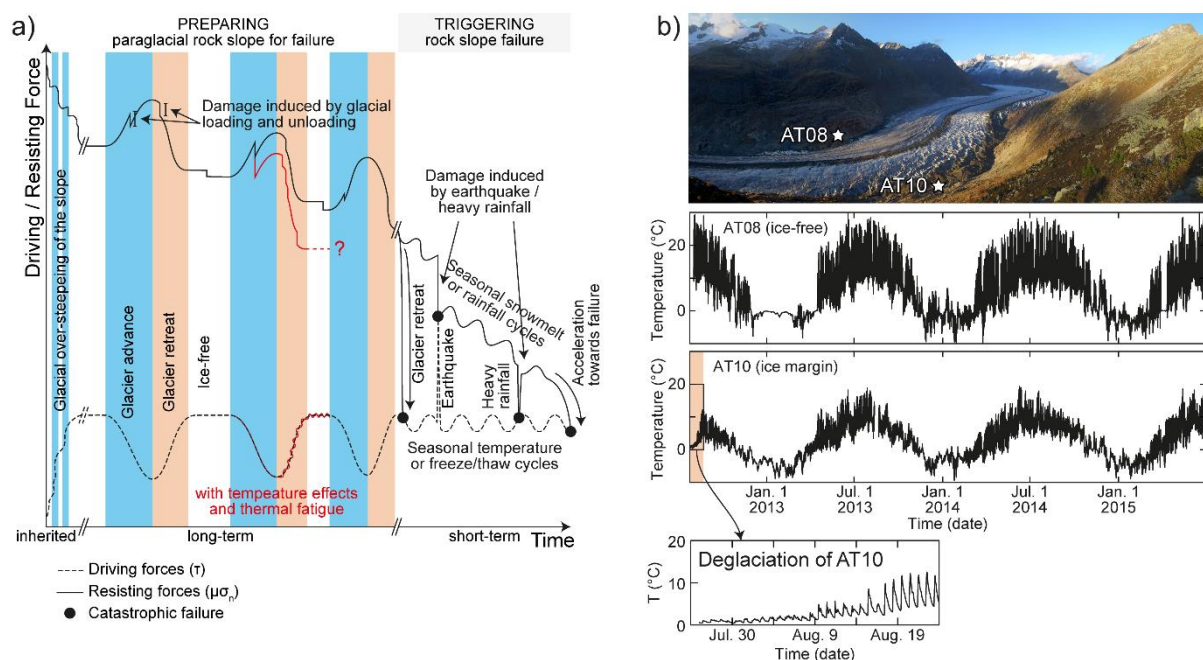


**Figure 3.1.** Concept of paraglacial rock slope preparation until ultimate failure: a) Variation of driving and resisting forces in a rock slope during repeat glacial cycles. Incremental damage induced by glacier advance and retreat as purely mechanical loading and unloading [Grämiger et al., 2017] together with other preparatory factors during ice-free conditions reduces slope stability until a critical state is reached. A single small disturbance can become the ultimate trigger for catastrophic failure (e.g., earthquake, heavy rainfall, seasonal snowmelt or rainfall, or glacier retreat) (adapted from Gunzburger et al. [2005] and Gischig et al. [2015]). Glacier cycles acting in parallel with other fatigue mechanisms, e.g. thermo-mechanical effects, may show greater potential in slope preparation (red line). b) The paraglacial environment of the Great Aletsch Glacier in our study area. Asterisks mark the position of ground temperature measurements. AT08 showing permanent ice-free temperature conditions with daily and seasonal cycles near the glacier. AT10 presents the temperature signal of rock suddenly exposed to new temperature conditions by deglaciation.

However, deglaciation causes more than a simple reduction in the weight of ice at the toe of a proximal rock slope. Glaciers occupying an alpine valley exert strong control on subsurface temperatures and

hydrology [Wegmann *et al.*, 1998; Boulton *et al.*, 2004; McColl *et al.*, 2010], and glacier retreat imposes changes in these primary fields that can drive rock mass damage through coupled mechanical stresses. Notably, glacier advance and retreat creates a transient disturbance in the local temperature field on both short (daily, annual) and long (decadal to millennial) time scales. Bedrock in contact with temperate glacial ice will maintain relatively constant temperatures near the pressure melting point (approximately 0 °C), and is shielded from solar radiation and ambient air temperature changes [Wegmann *et al.*, 1998]. In contrast, bedrock uncovered from beneath retreating ice is rapidly exposed to dramatically different thermal boundary conditions, with daily and annual temperature fluctuations superposed on a new mean temperature, a transition we term *paraglacial thermal shock* and demonstrate with temperature data from our study area in Figure 3.1b. Thermo-mechanical (TM) stresses resulting from these temperature changes are strongest in the near-surface, but also extend below the *thermally active layer* (the area subject to seasonal temperature changes) and can drive progressive failure at depths of 100 m or more [Gischig *et al.*, 2011a, b]. Therefore, as ice retreats and exposes bedrock along marginal valley walls, a rapidly forming shallow TM damage front should follow closely along the ice-rock contact. Meanwhile, the diffusive thermal front at greater depths lags surface temperature changes and can drive delayed rock mass damage as the geothermal gradient adjusts to the new mean annual ground-surface temperature (MAGT). The resulting zone affected by TM stresses may coincide with the area of critically stressed bedrock created by mechanical ice unloading [Grämiger *et al.*, 2017], increasing the degree of rock mass damage associated with glacial cycles.

Thermal effects such as frost cracking [Wegmann and Gudmundsson, 1999; Hales and Roering, 2007; Sanders *et al.*, 2012; Duca *et al.*, 2015] or permafrost degradation [Hasler *et al.*, 2012; Krautblatter *et al.*, 2013; Draebing *et al.*, 2014] have been widely recognized as important physical weathering processes shaping bedrock landscapes, however damage created by thermo-elastic strain in rock masses is likely underestimated and often dismissed [Hall, 1999; Hall and André, 2001; Watson *et al.*, 2004; Gunzburger *et al.*, 2005; Gischig *et al.*, 2011a, b; Bakun-Mazor *et al.*, 2013; Collins and Stock, 2016; Eppes *et al.*, 2016]. Baroni *et al.* [2014] highlighted the importance of considering long-term TM effects during deglaciation of an alpine valley, although the resulting displacement rates from their numerical simulations were too low to explain the development of slope instabilities. Gischig *et al.* [2011a] demonstrated how seasonal temperature changes can drive deep rock slope deformation and damage, and highlighted an initial ~5 year thermal-transient phase of considerable TM damage as the rock mass first adapts to new thermal boundary conditions. Other studies reveal the impact of glacier retreat on permafrost penetration in rock walls at high altitudes, which may enhance frost cracking [Wegmann *et al.*, 1998; Wegmann and Gudmundsson, 1999], but did not analyze damage caused by thermal strain in fractured rock masses. In a paraglacial environment [Slaymaker, 2009], adjusting to the change from glacial to non-glacial conditions, several other processes also act in parallel with glacier advance and retreat, include chemical weathering [Jaboyedoff *et al.*, 2004], stress corrosion at fracture tips [Faillottaz *et al.*, 2010], changes in joint water pressure [Hansmann *et al.*, 2012; Preisig *et al.*, 2016], or seismic fatigue [McColl *et al.*, 2012; Gischig *et al.*, 2015] (Figure 3.1a). Each of these processes is affected by the current and past position of the proximal valley glacier, which controls the location and magnitude of local rock slope damage. Glacier advances generally increase joint normal stresses and decrease shear stresses; i.e. driving forces are reduced and resisting forces enhanced during advance, while the reverse is encountered during retreat. Accumulation of incremental damage with each glacial cycle prepares the slope for failure, reducing slope stability over time until a final trigger leads to catastrophic failure [Eberhardt *et al.*, 2004; Prager *et al.*, 2008; Gischig *et al.*, 2015] (Figure 3.1a).

In this study, we expand on earlier investigations by Grämiger *et al.* [2017] addressing the purely mechanical impact of glacier cycles in driving paraglacial rock slope damage. Here we extend the

general view of glacial debuttressing by accounting for temperature changes and resulting thermal strain induced by glacial advance and retreat. We include TM effects in the distinct-element numerical modeling framework described by *Grämiger et al.* [2017], which is based on field measurements at our Aletsch Valley study site in Switzerland. Our results show how long-term temperature changes and seasonal cycles interact with changing ice loads to drive thermo-mechanical rock mass damage. We compare predictions of TM damage with our previous results of purely mechanical ice loading and unloading, and describe in detail how TM effects acting in parallel with glacier cycles lead to failure of intact rock bridges, propagate fractures, and enhance slip along discontinuities. Our results expand the understanding of processes facilitating the development of paraglacial rock slope instabilities.

## 3.2 Paraglacial setting of the Aletsch region

### 3.2.1 Study site and rock slope instabilities

Our study area comprises rock slopes surrounding the Great Aletsch Glacier in the central Swiss Alps (Figure 3.2). Bedrock consists of gneisses of the metamorphic Altkristallin and Central Aare granites in the Aar Massif [*Steck*, 2011]. Steep to sub-vertical foliation dipping SE (dip / dip direction: 76° / 122°) and faults following the alpine foliation are the dominant geological structures [*Grämiger et al.*, 2017]. An additional steep joint set perpendicular to foliation (83° / 198°) and a joint set dipping gently SW (20° / 240°) are also present in the generally blocky, undisturbed rock mass (GSI 65-80).

Valley flanks in the vicinity of the Great Aletsch Glacier host several rock slope instabilities with different dimensions and kinematics (Figure 3.2), described in detail by *Grämiger et al.* [2017]. We mapped a concentration of landslides around the present-day glacier terminus, some of which have been investigated in detail [e.g. *Kääb*, 2002, *Strozzi et al.*, 2010; *Kos et al.*, 2016; *Loew et al.*, 2017]. Landslides on the eastern valley flank are characterized by toppling kinematics, while the western slope contains compound rock slides. To the south, a large deep-seated gravitational slope deformation (DSGSD) affects the slope around Belalp. The very large DSGSD along the western flank of the Rhone Valley, extending from Riederalp to Fiescheralp, is not directly affected by the Great Aletsch Glacier and is not analyzed in this study.

### 3.2.2 Lateglacial and Holocene glaciation

The Pleistocene epoch was characterized by repeat major glacial / interglacial cycles in the European Alps. Figure 3.2 displays a synopsis of the Lateglacial and Holocene Aletsch glacier extents, while Figure 3.3 illustrates the change in glacier length over time [*Grämiger et al.*, 2017 and references therein]. Likely warmer and ice-free conditions prevailed during the penultimate Eemian interglacial period (~130 to ~115 ky; *Dahl-Jensen et al.*, [2013]). The following glacial period (Würmian) lasted ~100 ky and peaked at the Last Glacial Maximum (LGM) [*Ivy-Ochs et al.*, 2008], dated at ~28 to 18 ky [*Ivy-Ochs*, 2015] (Figure 3.3). Trimlines in our study area provide evidence of the ice elevation at that time (Figure 3.2). Strong retreat of the LGM glacier system occurred by ~19 to 18 ky [*Ivy-Ochs*, 2015; *Wirsig et al.*, 2016], followed by a series of successive Lateglacial readvances (Gschnitz, Clavadel, Daun, and Egesen stadia) (Figure 3.2 and Figure 3.3) [*Maisch et al.*, 1999; *Ivy-Ochs et al.*, 2008; *Darnault et al.*, 2012]. Moraines of the Egesen stadial are well preserved at Aletsch (Figure 3.2) and cosmogenic exposure ages [*Kelly et al.*, 2004; *Schindelwig et al.*, 2012] coincide with the Younger Dryas (YD) cold period (12.8-11.5 ky BP; *Alley et al.* [1993]) (Figure 3.3). Following the YD, the Great Aletsch Glacier retreated significantly. Extrapolating from other glaciers in the Alps, the Great Aletsch Glacier was likely smaller than at present during most of the Holocene, but experienced several readvances culminating in the Little Ice Age (LIA) around 1850 (Figure 3.3) [*Röthlisberger and Schneebeli*, 1979; *Joerin et al.*,

2006; Ivy-Ochs *et al.*, 2009; Nicolussi and Schlüchter, 2012; Schimmelpennig *et al.*, 2012]. Reconstruction of ice extents at the Great Aletsch Glacier during the past ~3500 years reveals more than three advance / retreat cycles, each reaching the Holocene glacial maximum (Figure 3.3) [Holzhauser *et al.*, 2005]. The extent of the LIA is clearly visible (Figure 3.2). Minimum glacier extents, however, are difficult to verify. Holzhauser *et al.* [2005] postulated that during the mid-Holocene, the Great Aletsch Glacier was at least ~1 km shorter than today (Figure 3.2 and 3.3).

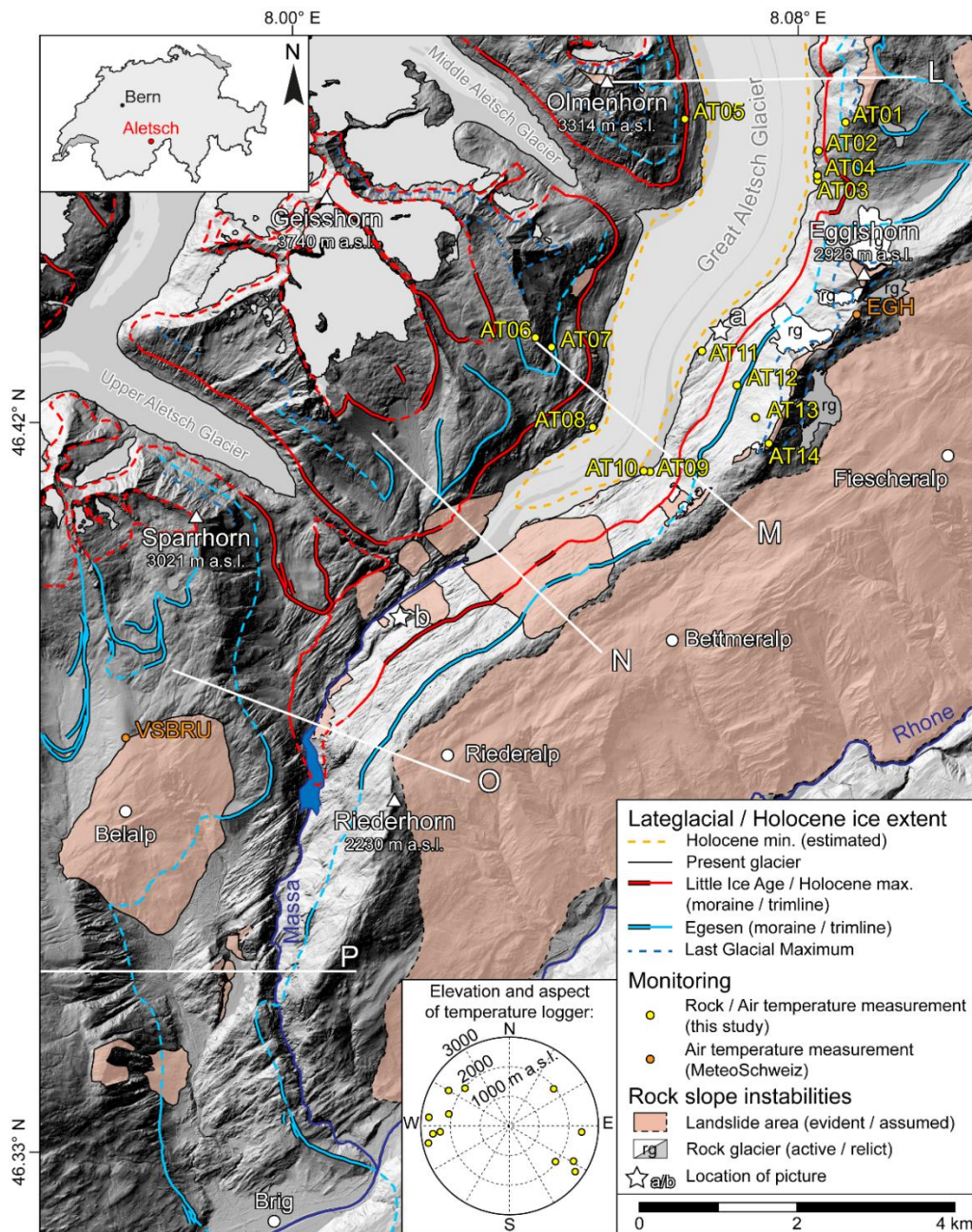


**Figure 3.2.** Synopsis of Lateglacial and Holocene glacier extents combined with spatial landslide extents mapped in the Aletsch region (modified from Grämiger *et al.* [2017]): Hillshade derived from DTM (swissALTI3D by Swisstopo). Position of rock and air temperature measurements (this study) and air temperature measurements at nearby weather stations (MeteoSchweiz). Inset with elevation and aspect of temperature loggers.

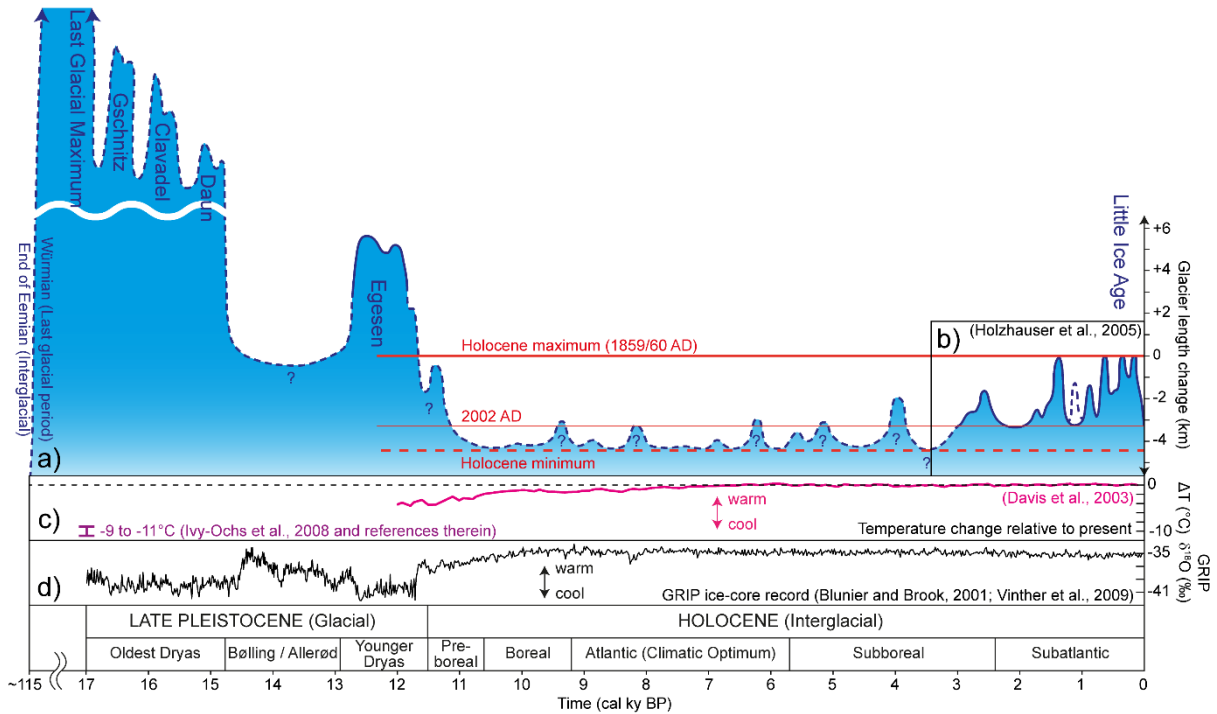


**Figure 3.3.** Synopsis of fluctuations of the Great Aletsch Glacier during the Lateglacial and Holocene (modified from Grämiger et al. [2017]): a) Estimated length of the Great Aletsch Glacier with respect to the LIA extent compiling available information since the onset of last glacial period until today (Grämiger et al. [2017] and references therein). b) Detailed length reconstruction of the Great Aletsch Glacier from fossil tree trunks [Holzhauser et al., 2005]. c) Holocene temperature reconstruction from pollen data [Davis et al., 2003] and estimates of Lateglacial temperature change [Ivy-Ochs et al., 2008 and references therein] relative to present. d) Oxygen isotope record from the Greenland Ice Core Project (GRIP) illustrating climatic fluctuations [Blunier and Brook, 2001; Vinther et al., 2009].

### 3.2.3 Present and Lateglacial temperature regime

Elevations in our study area span more than 3000 m from high-alpine summits exceeding 4000 m to the Rhone Valley at Brig (691 m). We collected continuous *in-situ* rock temperature data over more than three years along valley profiles (Figure 3.2) in order to estimate present spatial and temporal ground temperature variations in the region. We also measured the temperature transition in bedrock experiencing glacier retreat (Figure 3.1b). A detailed description and discussion of our ground temperature measurements is presented in the Appendix. From analysis of these data, we approximate ground-surface temperature ( $T$ ) as a function of time ( $t$ ) and elevation ( $z$ ) as:

$$T(t, z) = 15.3 - 0.005(z) + 10\sin(2\pi ft) \quad (3.1)$$

where  $t$  is in seconds,  $z$  is meters, and  $f$  is the 1-year annual frequency in Hz. This approximation leads to a 0 °C isotherm for the MAGT at 3060 m above sea level.

Air temperatures varied strongly between glacial and interglacial periods. Different geological archives provide insights into paleo-temperatures [Heiri et al., 2014]. Oxygen isotope records from the Greenland Ice Core Project (GRIP) [Blunier and Brook, 2001; Vinther et al., 2009] provide continuous information about the prevailing temperature regime during the last glacial and interglacial periods (Figure 3.3d). Davis et al. [2003] reconstructed Holocene temperature changes from pollen data in central Europe (Figure 3.3c). During the Gschnitz stadial (17-16 ky), summer temperatures were likely 9-11°C colder than today [Ivy-Ochs et al., 2008 and references therein]. Temperatures generally increased towards the onset of the Holocene. Estimated summer temperatures during the YD were 3.5 °C colder than

today [Ivy-Ochs *et al.*, 2008], while in the early Holocene (~8 ky) temperatures had risen to within 1 °C of present conditions [Davis *et al.*, 2003]. Temperatures were slightly warmer than today during the Holocene Climatic Optimum, but in general during the Holocene temperatures likely varied by only about  $\pm 1$  °C [Davis *et al.*, 2003].

Following LGM deglaciation, rock slopes above and outside the LIA extents most likely experienced only a single glacier readvance during the YD, while rock walls within and below the LIA extent were affected by several glacier cycles. Each ice advance and retreat phase altered the thermal boundary conditions in adjacent valley walls. For simplicity, we assume bedrock in contact with temperate glacier ice maintains a constant 0 °C surface temperature, despite small expected variations of the pressure melting point of ice with depth and impurities [Harrison, 1975], while rock outside the ice limits has MAGT controlled by time and elevation with superposed annual cycles. Bedrock in the upper Aletsch Valley may have remained covered by ice and not experienced seasonal thermal cycles since the last interglacial roughly ~110 ky ago. Future climate warming and glacier retreat [Jouvet *et al.*, 2011] will expose this bedrock to drastically different thermal conditions.

### 3.3 Numerical study of TM rock slope damage and displacement

#### 3.3.1 Model approach and inputs

We expand on the purely mechanical numerical modeling framework of Grämiger *et al.* [2017] by including thermo-mechanical (TM) effects associated with glacial cycles. Our approach uses the 2D distinct-element code UDEC [Cundall and Hart, 1992; Itasca, 2014], which is well-suited for analyzing the behavior of a discontinuous rock mass. Thermal calculations in UDEC are based on the finite-difference method and computationally intensive. Therefore, we calculated transient temperature fields using the more efficient finite-element code COMSOL Multiphysics, which were provided as input data for UDEC. Thermal gradients were calculated in COMSOL for each mechanical step, and the UDEC model was run to mechanical equilibrium (quasi-steady-state) including resulting thermal strain. In this semi-coupled approach, temperature gradients induce mechanical strain but the resulting mechanical response does not influence the thermal boundaries, properties, or temperature field.

Figure 3.4 shows our model geometry and TM initialization steps. The model cross-section represents profile M (see Figure 3.2). Model geometry, discontinuities, and rock properties are based on the numerical framework of Grämiger *et al.* [2017], where they are described in further detail. The area of interest is embedded into a large-scale model of the Rhone Valley and contains three rock mass elements: 1. intact rock, 2. discontinuities (joints), and 3. brittle-ductile fault zones (Figure 3.4). Randomly oriented discontinuities (i.e. Voronoi polygons; Lorig and Cundall [1989]) represent intact rock and allow for the formation of new, unassigned failure pathways. The orientation, spacing, persistence and strength parameters for each rock mass constituent are based on field assessment [Grämiger *et al.*, 2017]. Blocks between discontinuities are assigned elastic properties (Table 3.1), while discontinuities (i.e., joints, faults, Voronoi contacts) are assigned a Mohr-Coulomb constitutive law including slip-weakening of friction, cohesion, and tensile strength (Table 3.2). A maximum mesh size of 7 m over the upper 30 m of the model is applied throughout to accommodate the mechanical response of seasonal temperature signals. We otherwise assign a mesh size of 20 m for the upper 300 m of the model, which increases stepwise at greater depths and beyond the area of interest.

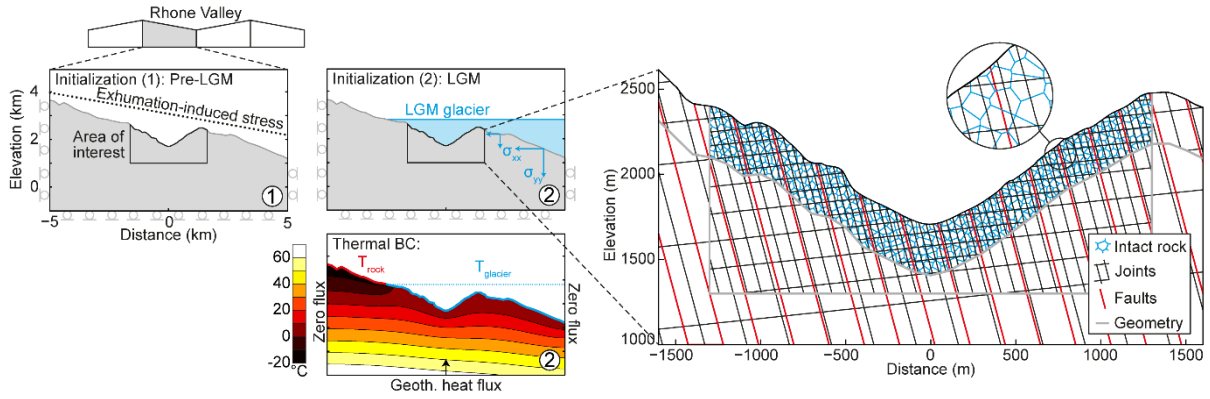


**Figure 3.4.** Initialization procedure, initial temperature field for long-term models with thermal boundary conditions (BC) in COMSOL, and model geometry (cross-section M) in UDEC: Large-scale model with roller boundary conditions representing the western slope of the Rhone Valley undergoing two-stage initialization (Pre-LGM / LGM). Embedded area of interest containing three rock mass elements: intact rock (Voronoi contacts), discontinuities (joints), and fault zones.

We apply roller boundaries at the bottom and sides of our large-scale model (Figure 3.4). We model glacier loading as a hydrostatic stress boundary condition ( $\rho_{\text{ice}} = 917 \text{ kg m}^{-3}$ ) to account for the ductile nature of ice and its limited buttressing effect [McColl *et al.*, 2010; McColl and Davis, 2013; Leith *et al.*, 2014; Grämiger *et al.*, 2017]. Initialization (Figure 3.4) is undertaken in the stepwise procedure described by Grämiger *et al.* [2017]. Initial conditions represent the Aletsch Valley during the ice-free pre-LGM interglacial (Eemian) period. The initial far-field stresses represent combined exhumation-induced and tectonic stresses in a simplified paleo-alpine valley, with a horizontal to vertical stress ratio of  $k = 1$  [Kastrup *et al.*, 2004]. Plastic equilibration with these initial stresses results in an initial (inherited) damage field. We then add LGM ice and allow for subsequent damage. This represents the starting point for our transient TM models.

Heat flow in bedrock is controlled by rock surface temperatures, geothermal heat flux, and the thermal diffusivity of rock [Moore *et al.*, 2011]. Our assigned thermal properties are listed in Table 3.1. Heat transfer in our model occurs through conduction alone, defined by thermal diffusivity  $\alpha = \lambda(\rho C_P)^{-1}$ ; where  $\lambda$  is the thermal conductivity,  $\rho$  is the density, and  $C_P$  is the specific heat capacity at constant pressure. Thermal conductivity is strongly dependent on porosity and pore filling, as well as joints in a rock mass [Moore *et al.*, 2011]. Wegmann [1998] measured the thermal conductivity of dry, saturated, and frozen rock samples from the nearby Jungfrauoch in similar lithology as in our study, finding:  $\lambda_{\text{dry}} = 2.9 \text{ W m}^{-1} \text{ K}^{-1}$ ,  $\lambda_{\text{wet}} = 3.25 \text{ W m}^{-1} \text{ K}^{-1}$ , and  $\lambda_{\text{frozen}} = 3.4 \text{ W m}^{-1} \text{ K}^{-1}$ . We selected the dry thermal conductivity ( $\lambda = 2.9 \text{ W m}^{-1} \text{ K}^{-1}$ ) for our models (Table 3.1), similar to the value identified by Eppelbaum *et al.* [2014]. Rybach and Pfister [1994], on the other hand, measured a mean vertical thermal conductivity of  $3.9 \text{ W m}^{-1} \text{ K}^{-1}$  in the Aar massif and reported a geothermal gradient of  $23 \text{ }^\circ\text{C km}^{-1}$ . Our thermal properties and model boundary conditions yield a geothermal gradient of  $\sim 21 \text{ }^\circ\text{C km}^{-1}$  (see Figure 3.5). Wegmann [1998] also measured the specific heat capacity for gneiss core samples from Jungfrauoch, obtaining on average  $780 \text{ J kg}^{-1} \text{ K}^{-1}$ , a value we adopted in our COMSOL models (Table 3.1) and which is in close agreement with other past studies [Eppelbaum *et al.*, 2014; Rybach and Pfister, 1994; Waples and Waples, 2004]. Together, these parameters result in a thermal diffusivity of  $\alpha = 1.4 \times 10^{-6} \text{ m}^2 \text{ s}^{-1}$  [cf. Gischig *et al.*, 2011b; Moore *et al.*, 2011]. Thermo-mechanical strain results from a thermal expansion coefficient of  $9.5 \times 10^{-6} \text{ K}^{-1}$  [Keusen and Amiguet, 1987] assigned to elastic blocks between discontinuities, a value similar to that used by Gischig *et al.* [2011a].



Temperature fields for each mechanical step of our transient models were calculated in COMSOL. A fine mesh size of maximum 3 m in the upper 20 m and small time step for the solver ( $<0.05$  y) were used to accommodate seasonal temperature signals. Thermal boundary conditions throughout the transient model are tied to the fluctuating glacier elevation (Figure 3.4). Below the glacier, temperatures are held constant at  $0^\circ\text{C}$ , while above the ice rock surface temperatures are influenced by ambient environmental conditions [Gruber *et al.*, 2004]. In our models, rock surface boundary conditions vary with altitude, time, and glacier elevation as:

$$\text{For } z \leq \text{glacier elevation}(t): \quad T(t, z) = 0 \quad (3.2)$$

$$\text{For } z > \text{glacier elevation}(t): \quad T(t, z) = \text{MAGT}(t, z) + A \sin(2\pi ft) \quad (3.3)$$

$$\text{where:} \quad \text{MAGT}(t, z) = 15.3 - 0.005(z) + \Delta T_{\text{paleo}}(t) \quad (3.4)$$

The assigned temperatures represent superposition of mean annual ground-surface temperature (MAGT) and a sinusoidal seasonal signal of amplitude  $A$ . Thermal boundary conditions above the ice are based on our *in-situ* rock temperature measurements at the Aletsch Glacier (Appendix Figure 3.A1). MAGT depends on a lapse rate (here  $0.005^\circ\text{C m}^{-1}$ ), a temperature of  $15.3^\circ\text{C}$  at the reference elevation of  $z = 0$  m, and the paleo-temperature change relative to present ( $\Delta T_{\text{paleo}}$ ). Seasonal amplitude was approximated as independent of altitude or aspect as  $A = 10^\circ\text{C}$ . Zero flux boundary conditions define the sides, while a geothermal heat flux of  $Q_{\text{geotherm}} = 60 \text{ mW m}^{-2}$  is applied at the bottom of the model [Wegmann *et al.*, 1998 and references therein].

Modeling the Aletsch Valley throughout the Lateglacial and Holocene ( $\sim 18$  ky) including annual temperature cycles requires unfeasibly large computation times. Therefore, we divided our modeling strategy into two parts: (1) Long-term TM effects during the Lateglacial and Holocene not including seasonal cycles, and (2) TM effects resulting from seasonal temperature and glacial cycles over a shorter time period. The first suite of models cover the entire Lateglacial / Holocene period on realistic time scales, allowing long-term temperature changes (i.e., Holocene warming, bedrock exposure during deglaciation) to diffuse at depth while neglecting seasonal temperature cycles for efficient computation. To capture the long-term response, it is important to initiate the model with a realistic temperature field. Our initial temperature conditions start under LGM ice occupation at the same point as our transient thermo-mechanical models. We assume thermal steady-state at the LGM, representing a period of sustained ice-cover during the last glacial period. Thermal boundary conditions and the initial temperature field with LGM ice cover are shown in Figure 3.4. Mechanical time steps are two years in our long-term models.

In our second suite of models, we investigate seasonal TM cycles acting in parallel with fluctuating ice loads. Modeling annual cycles throughout  $\sim 18$  ky was not feasible due to long computation times. Therefore, we distribute 500 annual temperature cycles over the same glacier scenario applied in the long-term TM models. We argue this simplification is appropriate to explore the effects of TM cycling, because a rock mass requires  $\sim 5$  years to accommodate new cyclic thermal boundary conditions [Gischig *et al.*, 2011a]. In our modeled Lateglacial / Holocene glacier scenario (see Figure 3.5b) long time periods of several thousand years with constant glacier ice or ice-free conditions prevail, when only TM cycling affects the bedrock. Since after  $\sim 5$  years, TM cycling is insignificant, decreasing the amount of TM cycles throughout our glacier scenario is a reasonable modeling simplification. On the other hand, long-term temperature effects from the presence or absence of ice cover are inadequately simulated over the shortened time span. Therefore, we neglect long-term temperature changes by initiating an overall  $0^\circ\text{C}$  background temperature and assigning zero flux boundary conditions at the model sides and bottom. We apply only seasonal temperature cycles with  $A = 10^\circ\text{C}$  and  $\text{MAGT} = 0^\circ\text{C}$ . Lapse rate

and paleo-temperature effects were omitted. In this second series of simulations we used a mechanical time step of 0.1 years to accommodate the annual temperature signal.

**Table 3.1.** Mechanical and thermal properties of the rock mass implemented in UDEC and COMSOL.

<b>Mechanical properties (UDEC)</b>			
Density $\rho$	(kgm <sup>-3</sup> )	2700	<i>Wegmann [1998]</i>
Poisson's ratio	()	0.2	<i>Grämiger et al. [2016]</i>
Young's modulus	(GPa)	30	<i>Grämiger et al. [2016]</i>
Thermal expansion	(K <sup>-1</sup> )	9.5E-6	<i>Keusen and Amiguet [1987]</i>
<b>Thermal properties (COMSOL)</b>			
Thermal conductivity $\lambda$	(W m <sup>-1</sup> K <sup>-1</sup> )	2.9	<i>Wegmann et al. [1998]</i>
Specific heat capacity at constant pressure $C_p$	(J kg <sup>-1</sup> K <sup>-1</sup> )	780	<i>Wegmann [1998]</i>

**Table 3.2.** Discontinuity properties for the Mohr-Coulomb constitutive law including slip-weakening implemented in UDEC [*Grämiger et al., 2016*].

<b>Discontinuity parameters</b>	<b>Unit</b>	<b>Intact rock (Voronoi)</b>	<b>F1 foliation</b>	<b>F3</b>	<b>F4 faults</b>
Peak friction angle $\varphi$	(°)	50	33.7	37.2	27
Peak cohesion $c$	(MPa)	8	1.8	3.5	0.03
Peak tensile strength $t$	(MPa)	1	0.4	0.8	0
Residual friction angle $\varphi_R$	(°)	27	27	27	27
Residual cohesion $c_R$	(MPa)	0.03	0.03	0.03	0.03
Residual tensile strength $t_R$	(MPa)	0	0	0	0
Dilation angle	(°)	5	5	5	5
Dip angle	(°)	-	75	6	75
Normal stiffness	(GPa m <sup>-1</sup> )	20	10	10	1
Shear stiffness	(GPa m <sup>-1</sup> )	10	5	5	0.5

### 3.3.2 Long-term thermo-mechanical effects

The presence or absence of ice covering bedrock affects the local temperature field during glacial cycles. Here we explore TM rock slope damage induced by long-term temperature changes (Figure 3.5). Initial stresses and temperatures are applied as described previously (Figure 3.4). We model 18 ky of

simplified Lateglacial and Holocene ice fluctuations. Our applied paleo-temperature change relative to the present MAGT ( $\Delta T_{paleo}$ ) matches past air temperature reconstructions [Davis et al., 2003; Ivy-Ochs et al., 2008] (Figure 3.5a). Rock surface temperatures below ice are constant at 0 °C, and above ice the MAGT is a function of time and elevation (Equation 3.4; Figure 3.5e). This model does not include seasonal thermal cycles. The applied hydrostatic glacier loading scenario (Figure 3.5b) is based on mapped ice extents along profile N (Figure 3.2), whereas the timing and number of Lateglacial / Holocene ice fluctuations is simplified (see Figure 3.3). This glacier scenario was selected to simulate the largest changes in ice elevation with ice-free conditions between glacier advances. We included three variations in model temperatures representing the same slope profile at different altitudes corresponding to profiles L, M, and P (Figure 3.2). Profile M represents the actual altitude in the model cross-section. Profile L is located 200 m higher, therefore MAGT is 1 °C cooler, while profile P is 400 m lower resulting in a 2 °C increase in MAGT.

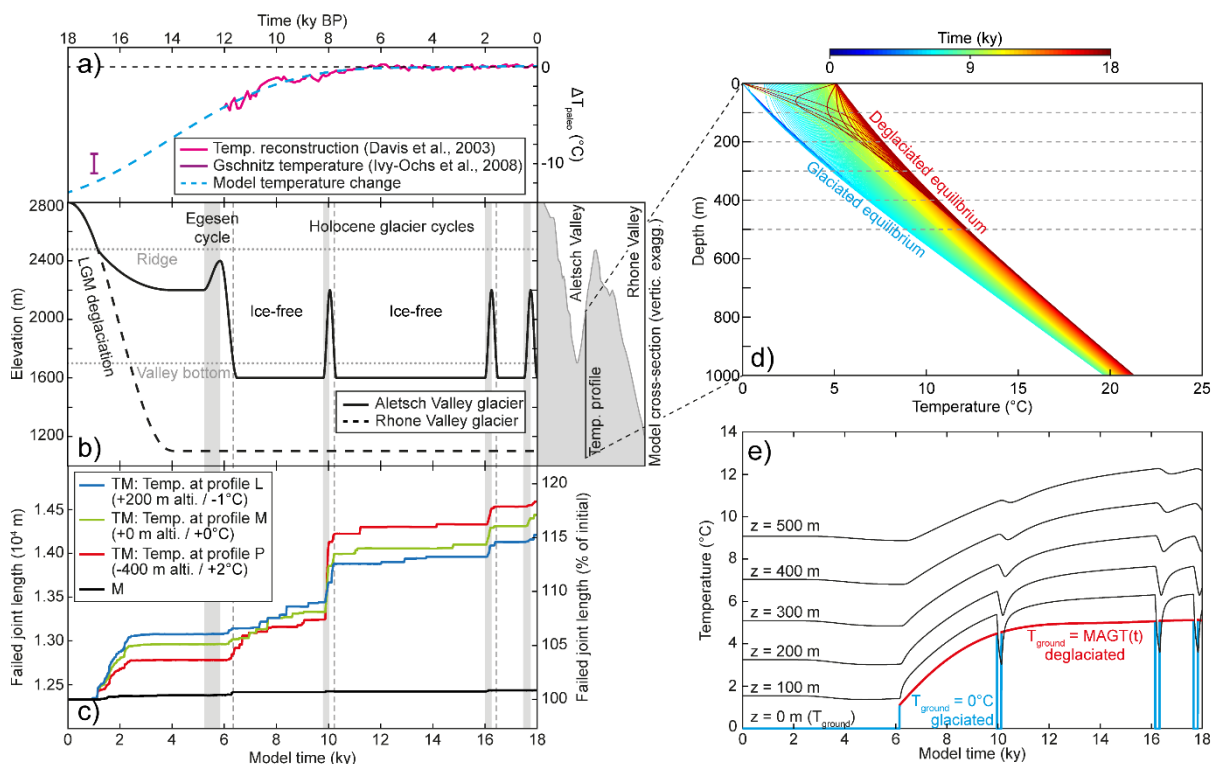


**Figure 3.5.** Transient rock slope damage during repeat glacial cycles in concert with long-term thermo-mechanical (TM) effects induced by Lateglacial / Holocene temperature change: a) Applied model temperature change relative to present fitting paleo-temperature reconstructions [Davis et al., 2003; Ivy-Ochs et al., 2008]. b) Applied glacier scenario with compressed profile M as reference. c) Temporal evolution of damage for applied temperature scenarios illustrated as the sum of failed joint length and percentage of initial damage, in comparison to a purely mechanical (M) model. d) Temperature change with depth at time steps of 50 y for temperature profile in cross-section over 18 ky. e) Corresponding temperature change over time at different depths in the temperature profile and surface temperature signal ( $T_{ground}$ ).

Figure 3.5d,e illustrates how LGM deglaciation and subsequent Holocene glacial cycles affect the temperature regime in the subsurface on ky time scales. The equilibrated LGM geothermal gradient is disturbed by rock surface exposure to MAGT conditions. The temperature signal diffuses downward, shifting the thermal gradient to a new equilibrium under deglaciated conditions (Figure 3.5d).

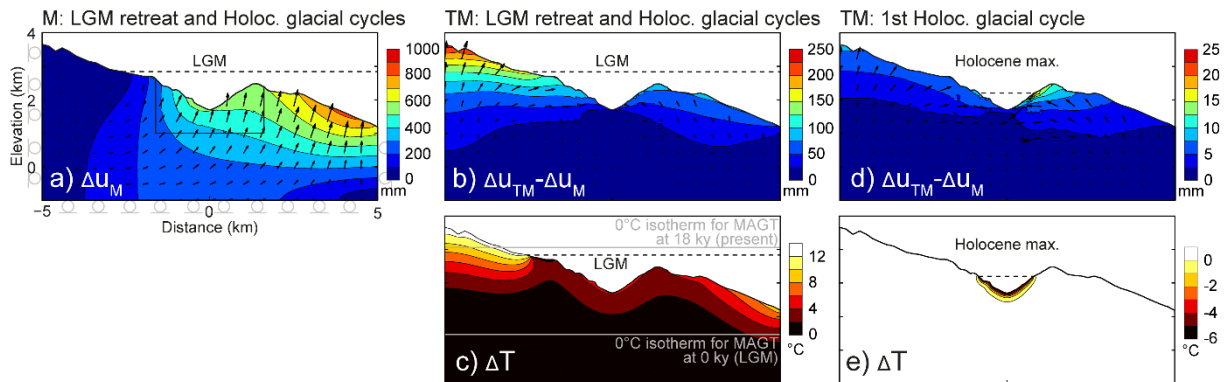
Concurrently, MAGT increases with time. Short interludes of 500 years of ice cover during the Holocene disturb temperatures in the uppermost 200 m of the slope by several degrees, marked by a sudden onset, while the temperature response at larger depths is smaller and delayed (Figure 3.5e).

Figure 3.5c illustrates the temporal evolution of rock slope damage for the applied temperature scenarios, summarized as the sum of failed joint length in comparison to a purely mechanical model. A joint fails when stresses reach the failure criterion, allowing for irreversible displacement, and strength properties drop from peak to residual values. After Egesen deglaciation, damage accumulation persists for ~3 ky between ~6.5 - 9.5 ky model time even though the slope remains ice-free and is unaffected by changing glacier load. MAGT increases by up to 4 °C during this time (Figure 3.5a). The greatest damage increment occurs at the onset of the first Holocene glacier advance around ~10 ky in the model. Later glacial cycles at ~16 and ~17.5 ky model time generate lesser damage. The purely mechanical model results in only ~1% additional damage compared to the initial damage field (i.e., inherited damage from the ice-free pre-LGM period and subsequent LGM ice loading). Including long-term TM effects induced by glacier fluctuations generates between ~15 and 19% additional damage. The differences in total damage between the three model scenarios are small and driven by the temperature contrast between the glacier (0 °C) and MAGT (larger temperature changes result in larger thermal strain). The low-elevation scenario (profile P) experiences the greatest warming from initially 0 °C to ice-free conditions, thereby generating the most damage during the first glacier advance (~10 ky model time) as ice cools the bedrock. Temperatures at profile L are closer to 0 °C and therefore temperature changes with glacier cycles are smaller, generating less damage. Warming of only a few degrees in the upper part of the slope after deglaciation is sufficient to induce incremental damage, even in the absence of changing glacier load. Glacier advances are more effective in generating rock slope damage in parallel with cooling of bedrock beneath the ice.

TM strains for the full model shown in Figure 3.6 help explain observed new damage. LGM deglaciation and Holocene cycles in a purely mechanical model result mostly in elastic post-glacial rebound due to ice unloading (Figure 3.6a). However, long-term temperature changes in parallel with a complete glacial cycle generate significant additional TM displacement (Figure 3.6b). The magnitude of additional displacement scales with temperature change since the LGM (Figure 3.6c). The high-altitude western slope above LGM ice is exposed to MAGT conditions at all times, experiencing the entire modeled temperature increase of up to ~12 °C. The 0 °C annual isotherm rises during the model run from initially 465 m to 3060 m. Bedrock in our area of interest becomes exposed to ambient temperatures for the first time after ~6 ky, when modeled temperature change relative to today is comparably small (see Figure 3.5a). Bedrock warming in this area is mostly related to the temperature contrast between ice and the MAGT. Temperature changes at the surface diffuse with depth, and the long-term temperature increase acting in parallel with deglaciation contributes to greater elastic rebound (Figure 3.6a,b). Subsequent ice readvance cools underlying bedrock and the uppermost ~200 m of the slope by several degrees (Figure 3.6e). Thermal strain results in additional displacement affecting both valley flanks, but the eastern slope with toppling mode rock structure shows enhanced movement of up to ~25 mm (Figure 3.6d). Spatial differences in ground temperature change result on the one hand from MAGT warming through the Lateglacial and Holocene, and on the other hand from a change in the thermal boundary conditions during ice retreat. Cooling within the Aletsch Valley during ice advance leads to thermal contraction of the rock mass, reducing joint normal stresses along steeply dipping discontinuities and promoting toppling [Watson *et al.*, 2004; Gischig *et al.*, 2011a]. On the other hand, thermal expansion is redirected by lateral confinement into elastic rebound and increases stresses.

TM strains can create stress concentrations leading to failure of critically stressed discontinuities. The influence of long-term temperature change on rock slope damage during repeat glacial cycles is

presented in Figure 3.7, which shows the spatial and temporal TM damage distribution. Rock slope damage induced in a purely mechanical model is minor (Figure 3.7b), whereas including long-term changes in thermal boundary conditions leads to significant new damage accumulation with glacial cycles. First deglaciation after the LGM and Egesen generates damage in the upper ~100 m on the valley shoulders (Figure 3.7a). Subsequent Holocene glacial cycles produce damage in deeper areas, propagating pre-existing failed discontinuities. Differences in damage between the three variations in model temperatures are small (Figure 3.7b).



**Figure 3.6.** Thermo-mechanical (TM) reaction of the full model (+0 m altitude / +0°C scenario): a) Maximum displacement ( $\Delta u$ ) as a result of purely mechanical (M) unloading and loading during LGM deglaciation and Holocene glacial cycles. b) Additional TM displacement induced by temperature change during LGM deglaciation and Holocene glacial cycles. c) Temperature change during LGM deglaciation and Holocene cycles (18 ky) with changing 0 °C isotherm for MAGT at 0 ky and 18 ky. d) Additional TM displacement induced by temperature change during the first Holocene glacial cycle. e) Temperature change during first Holocene cycle.

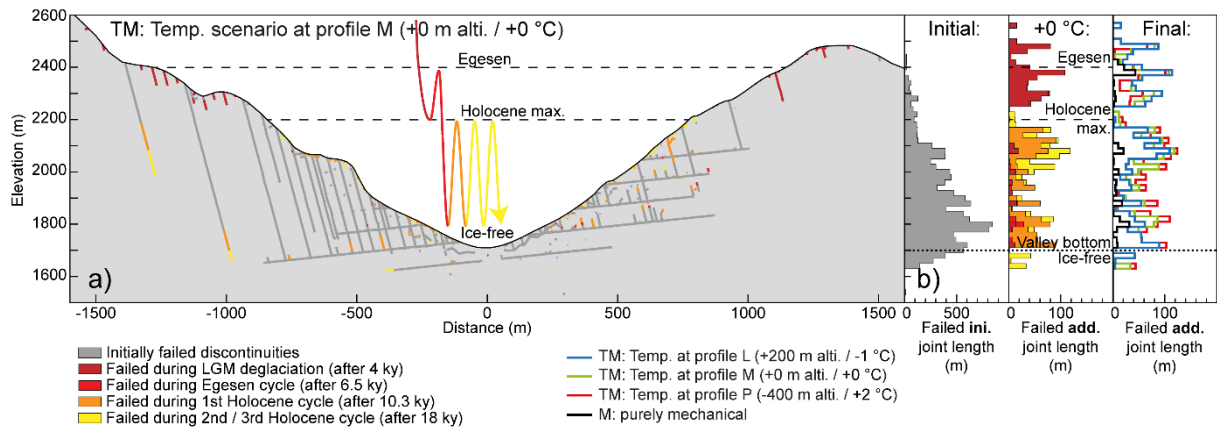
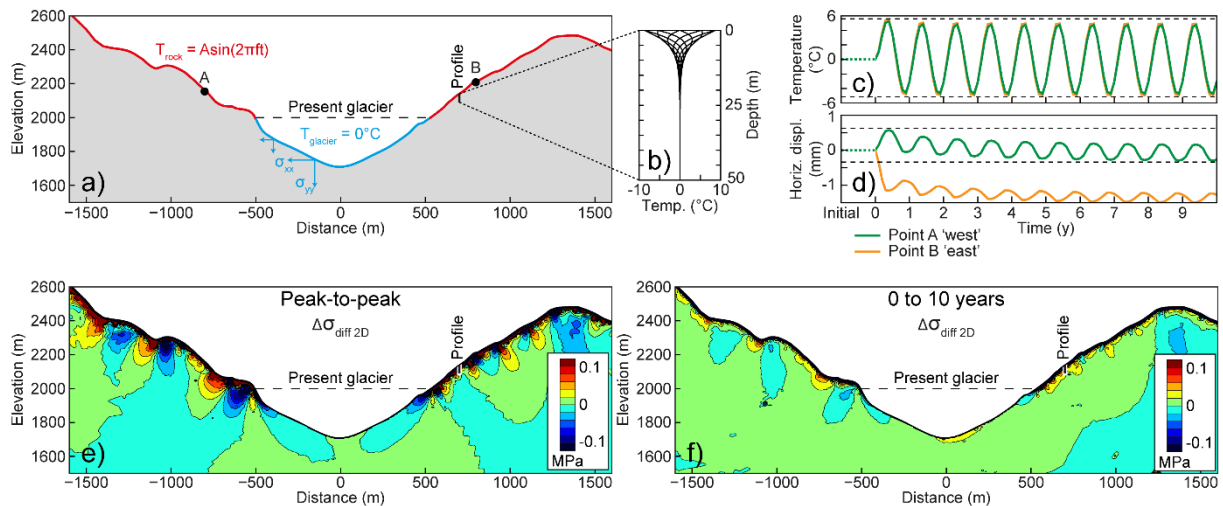


**Figure 3.7.** Influence of long-term temperature change on rock slope damage during repeat glacial cycles: a) Spatial and temporal distribution of thermo-mechanical (TM) damage for the temperature scenario at profile M (+0 m altitude / +0 °C) in the cross-section. b) Damage elevations at initial conditions, additional damage with time for the temperature scenario at profile M, and final additional damage for different temperature scenarios in comparison with purely mechanical (M) model displayed as histogram.

### 3.3.3 Seasonal thermo-mechanical effects

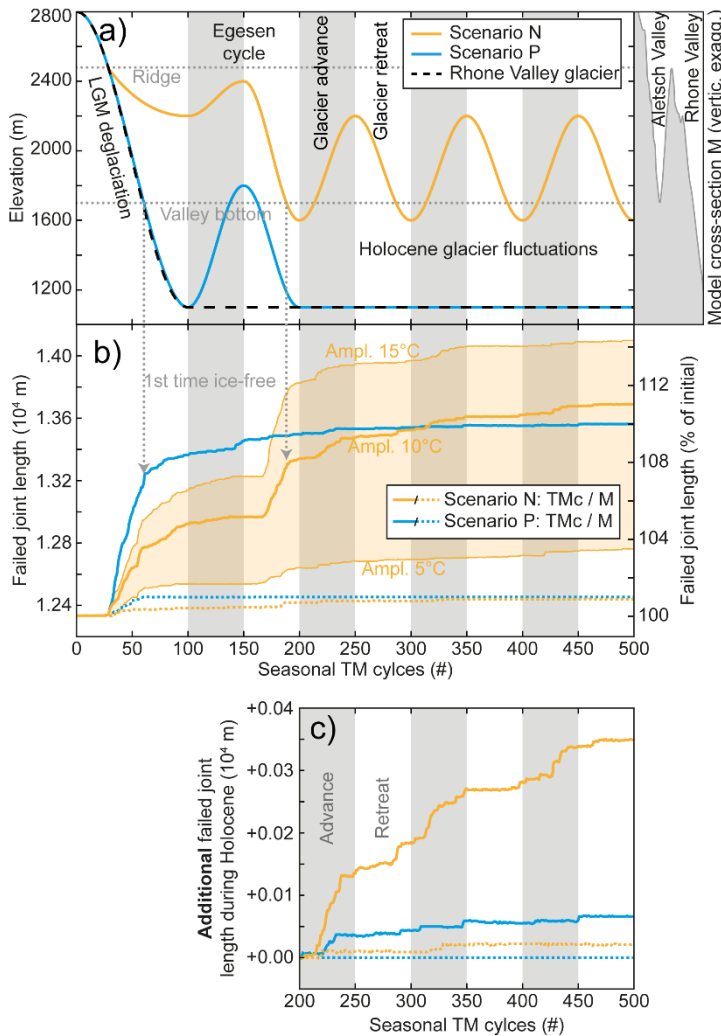
Here we investigate how annual temperature cycles interact with a fluctuating glacier to generate TM damage. We used an identical model geometry and initialization procedure as for our long-term TM models (Figure 3.4). We applied thermal conditions as described previously, initiating a uniform 0 °C background temperature and applying sinusoidal seasonal temperature cycles around this mean value ( $A = 10$  °C;  $MAGT = 0$  °C). Lapse rate and paleo-temperature changes were omitted. Rock surface temperature boundary conditions below ice were 0 °C, while temperatures above ice were a function of time (Equation 3.3).

Figure 3.8 shows stress and displacement results for thermal cycles applied to the surface of an elastic medium with a constant glacier elevation similar to that at present-day profile M (see Figure 3.2). The temperature signal decays in the upper ~20 m, and peak-to-peak displacements at 3 m depth are in the sub-millimeter range (Figure 3.8b-d). The eastern and western slopes move ~0.5 mm inward towards the valley during warming and outward during cooling (Figure 3.8d). This antipodal movement results in annual valley opening and closing of ~1 mm from thermal strain. Warming also leads to upward displacement while cooling results in downward displacement of similar magnitude. The multi-year trend of displacements shown in Figure 3.8d reflects the transient effect of applying a new temperature fluctuation to the model, and requires approximately 5 y to reach quasi-static equilibrium (termed *thermal-transient phase*; *Gischig et al.* [2011a]). Thermal strain in the near-surface induces differential stress changes up to a few hundred kPa, which propagate to depths below the thermally active layer (Figure 3.8e). TM induced stresses are strongly affected by topography [*Harrison and Herbst, 1977*]. Figure 3.8f shows differential stress changes after 10 TM cycles, representing TM induced stresses resulting from accommodation of new cyclic thermal boundary conditions. Maximum stresses are in the range of ~100 kPa in the upper 50 m.



**Figure 3.8.** Elastic effects of seasonal temperature cycles in a glacial environment: a) Thermal and stress boundary conditions of the model with constant glacier at present-day level. Constant 0 °C below ice and seasonal temperature cycles above the ice. Location of observation points at 3 m depth. b) Decreasing peak-to-peak amplitude of temperature signal with depth. c) Temperature change at observation points. d) Horizontal displacement at observation points showing irreversible deformation due to paraglacial thermal shock within 10 annual cycles. Valley opening and closing of ~1 mm with seasonal thermal cycles. e) Peak-to-peak in-plane differential stress in 10<sup>th</sup> cycle. f) In-plane differential stresses after 10 annual cycles showing induced stress by thermal shock.

In the following model scenarios, we combined seasonal TM cycles with fluctuating ice loads, where transient thermal boundary conditions are tied to the changing glacier elevation. Figure 3.9 shows rock slope damage induced by repeat glacial cycles including seasonal TM effects. Five hundred seasonal cycles run in parallel with applied glacier scenarios N and P (adopted from *Grämiger et al.* [2017] and based on mapped glacier extents along profiles in Figure 3.2), comparing an alpine valley undergoing LGM deglaciation with three subsequent Holocene cycles (scenario N) to LGM deglaciation followed by a minor Egesen advance and retreat and subsequent ice-free Holocene conditions (scenario P) (Figure 3.9a).



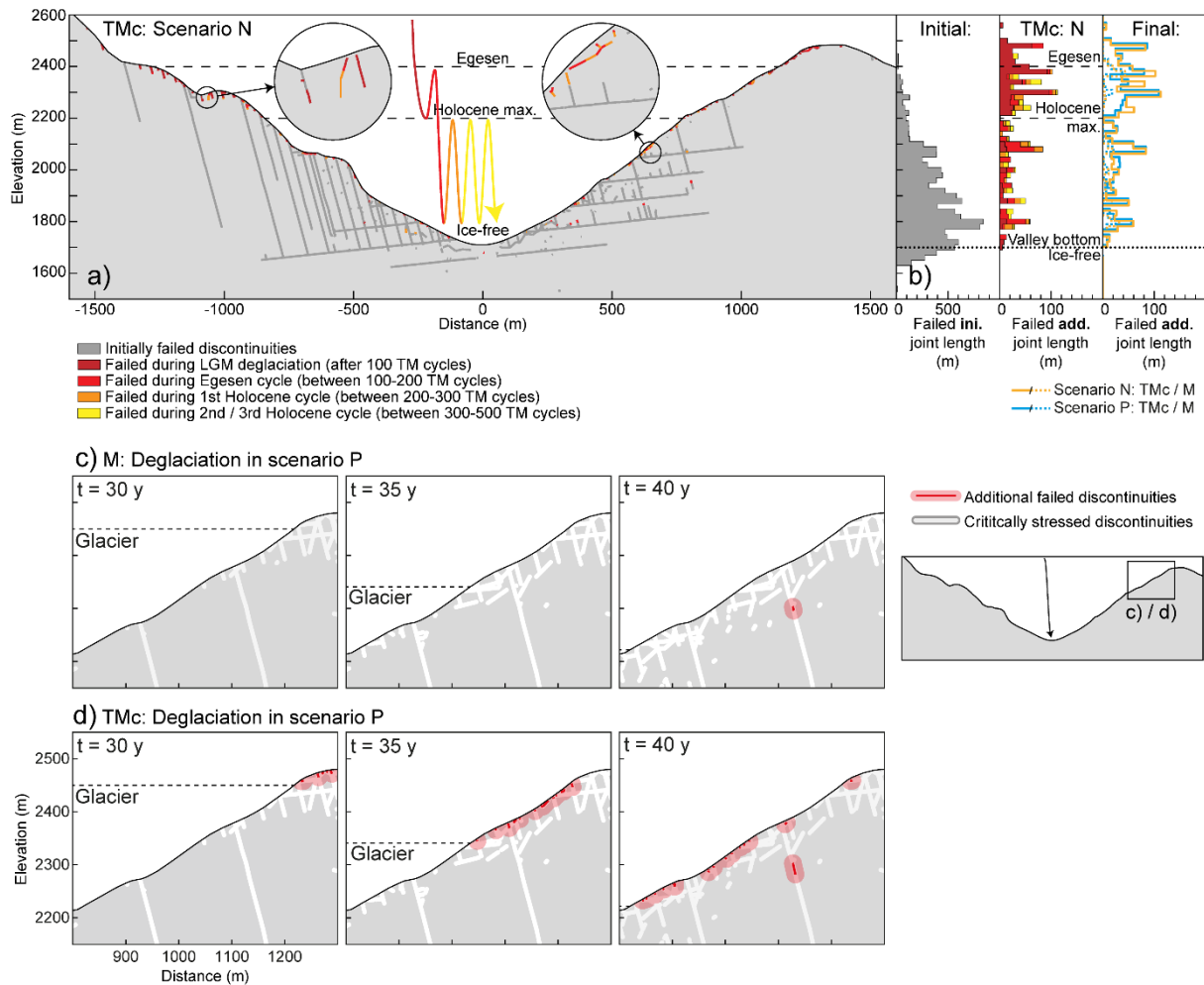
**Figure 3.9.** Transient rock slope damage during repeat glacial loading in concert with thermo-mechanical effects induced by seasonal temperature cycles (TMc): a) Applied glacier scenarios based on mapped glacier extents along profiles N and P (see Figure 3.2) with compressed profile M as reference. b) Temporal evolution of damage for applied glacier scenarios illustrated as the sum of failed joint length and percentage of initial damage, each in comparison to purely mechanical (M) models. c) Additional failed joint length during the Holocene compared in scenarios with (orange) and without (blue) Holocene cycles (each TMc / M).

Figure 3.9b shows the temporal evolution of damage described as the sum of failed joint length across the model. Major damage accumulation occurs during first deglaciation, when bedrock is first exposed to annual temperature cycles. In scenario P this occurs between ~30-50 TM cycles. In scenario N, major damage occurs within ~100 cycles, when the upper rock slope is first exposed, and again between ~150-200 cycles as the lower rock slope is deglaciated for the first time. Both scenarios reach a similar damage level, although subsequent Holocene cycles in scenario N generated slightly more damage. Figure 3.9c highlights new damage occurring during the Holocene. In scenario P, TM stress cycles are capable of inducing rock slope damage even after several hundred cycles and in the absence of changing glacier load. New damage during Holocene cycles in scenario N occurs mainly during glacier advances, similar to our purely mechanical models [*Grämiger et al.*, 2017]. However, including TM

effects leads to increased damage accumulation. Purely mechanical models resulted in only ~1% additional new damage (Figure 3.9b), whereas new TM damage in scenario P reached ~10% and with subsequent Holocene cycles in scenario N ~11%. TM damage during subsequent Holocene cycles is observed, but are minor compared to damage during first retreat. Seasonal TM cycles are thus a significant driver of paraglacial rock slope damage, but the effect of thermal shock appears restricted to first-time deglaciation. Induced damage strongly depends on the applied amplitude of the seasonal temperature cycles (Figure 3.9b).

Figure 3.10 displays the spatial and temporal distribution of rock slope damage induced by seasonal TM cycles in parallel with glacier fluctuations. New joint failures occur mainly in the upper 20-30 m, covering mostly the upper slope (Figure 3.10a,b). Nevertheless, incremental damage also accumulates deeper in the slope, mostly as fracture propagation of initially failed discontinuities. Detailed analysis of the eastern upper slope shows how a damage front propagates with glacier retreat due to paraglacial thermal shock (Figure 3.10c,d). Glacier retreat changes the stress state of discontinuities in the slope. A zone of critically stressed discontinuities (here defined as within 2 MPa of the Mohr-Coulomb failure criterion) follows the decreasing glacier elevation (Figure 3.10c,d). Below the glacier, discontinuities are less critically stressed due to the increased normal stress from the weight of ice. Decreasing normal stresses in the joints accompanying ice loss brings their stress conditions closer to the failure envelope. In a purely mechanical model, this increase in the amount of critically stressed joints leads to only minor additional damage (Figure 3.10c). However, including seasonal TM cycles in parallel with glacier retreat induces new damage. The damage front follows glacier retreat and is mainly shallow, restricted to the upper 20-30 m.





**Figure 3.10.** Influence of seasonal TM cycles on rock slope damage during repeat glacial cycles: a) Spatial and temporal distribution of damage induced by thermo-mechanical stress cycles (TMc) for model scenario N in the cross-section. b) Damage elevations at initial conditions, additional damage with time for scenario N induced by thermo-mechanical stress cycles (TMc), and final additional damage for scenarios N and P (each TM / M) displayed as histogram. c) Rock slope damage evolution during 10 y of deglaciation for scenario P displaying additional failed discontinuities and critically stressed joints (here defined within 2 MPa of the Mohr-Coulomb failure criterion) for a purely mechanical (M) model. d) Rock slope damage evolution during 10 y of deglaciation with thermo-mechanical stress cycles (TMc) showing shallow damage front propagating with glacier retreat by thermal shock.

In Figure 3.11 we compare new damage and displacement along discontinuities during one Holocene glacial cycle for a purely mechanical model and TM model including annual cycles. Mechanical loading during glacier advance leads to downward displacement of the valley, which is expressed as right-handed movement in the west and left-handed movement on the eastern slope along steeply dipping discontinuities below the glacier elevation (Figure 3.11a). On the other hand, steep joints on the eastern valley flank above the glacier undergo right-handed shearing during advance, promoting toppling and new damage. A reversed sense of slip is observed during glacier retreat. This reversible joint displacement amounts to a few millimeters. Irreversible joint slip over the glacial cycle is restricted to the eastern slope at the valley bottom and the mid-slope region, showing toppling mode kinematics. Incorporating seasonal TM cycles in parallel with the glacier loading cycle results in a similar pattern of shear dislocation along discontinuities, while new damage is increased but predominantly shallow (Figure 3.11b). Note that the valley flanks presented in Figure 3.11b have already experienced thermal

shock during LGM deglaciation. Glacier advance generates more damage than glacier retreat. TM models produce displacement along steeply dipping discontinuities on the western slope not observed in our purely mechanical models (Figure 3.11).

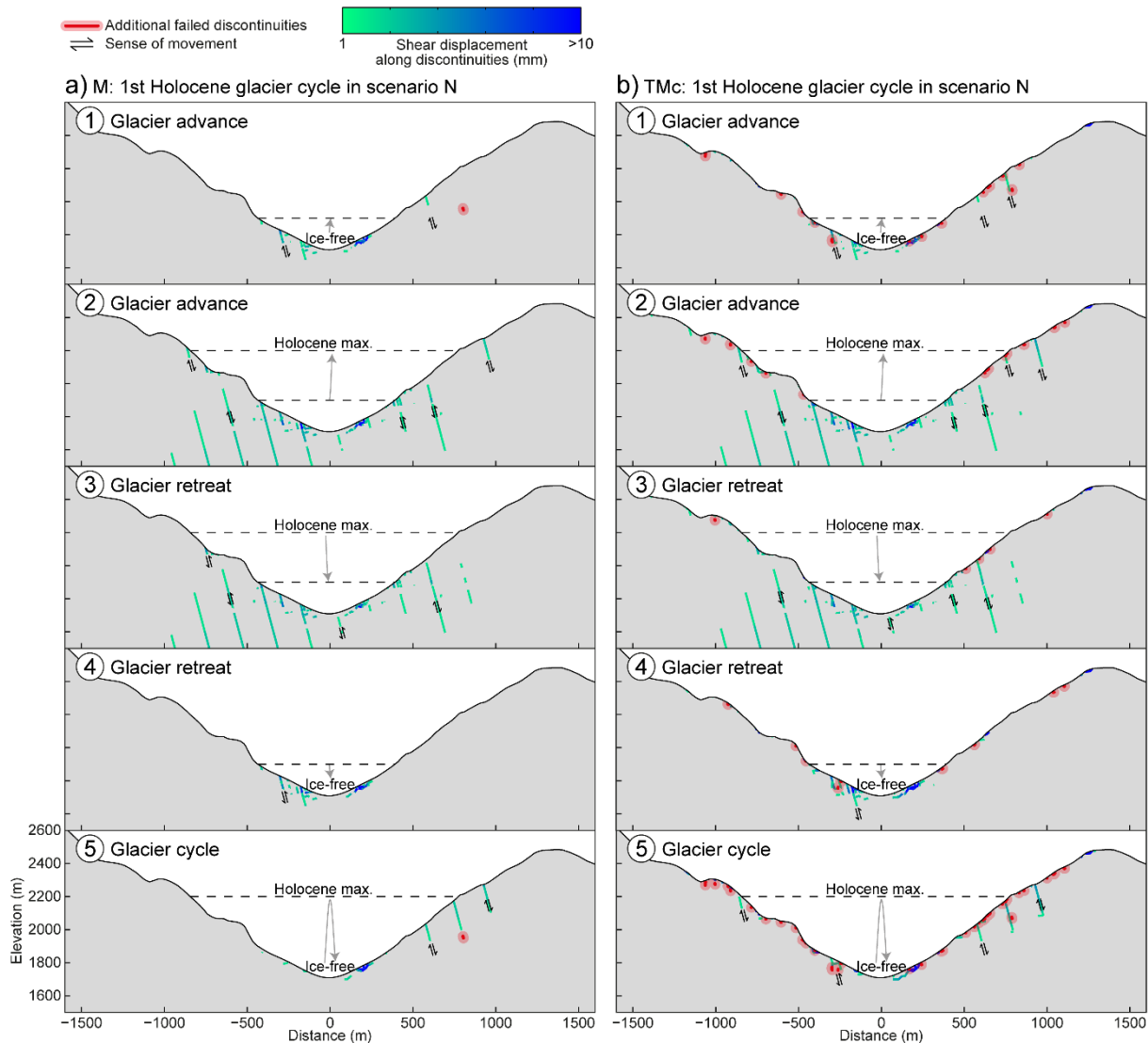


**Figure 3.11.** Shearing and damage during one glacial cycle: a) Shear displacement along discontinuities during first Holocene cycle for model scenario N for purely mechanical (M) model, and b) with thermo-mechanical stress cycles (TMc) included.

### 3.3.4 Influence of initial rock mass strength

TM effects vary with assumed rock mass strength and in turn on the amount of critically stressed discontinuities [Gischig *et al.*, 2011a]. Damage effects from TM and mechanical glacier cycling are both anticipated to be stronger for increased criticality of the slope [Grämiger *et al.*, 2017]. Here we apply our TM model to a weakened slope, i.e., one with reduced rock mass strength. We performed a series of simulations varying initial rock mass strength while keeping initial stress conditions constant. We reduced peak strength properties (friction angle, cohesion, and tensile strength) for all rock mass elements (except fault zones which are already at residual strength). Peak strengths were scaled linearly

between the previously applied peak and residual values (Table 3.2) by a factor  $\alpha$ ; e.g.,  $C_{red} = C_R + \alpha(C - C_R)$  ( $\alpha = 100\%$  represents peak strength properties,  $\alpha = 0\%$  represents residual strength).

Figure 3.12 displays the spatial and temporal distribution of rock slope damage induced by seasonal TM cycles acting in parallel with fluctuating glacial ice loads under reduced initial strength conditions. A weakened rock slope ( $\alpha = 30\%$ ) experiences greater initial and subsequent damage during glacier cycles compared to a slope with the previously implemented moderate strength conditions ( $\alpha = 100\%$ ). New damage occurs mostly on the eastern valley flank as propagation of pre-existing steeply dipping discontinuities (Figure 3.12a). Failure of intact rock bridges (i.e., *Voronoi* contacts) connects existing failed joints generating a shear failure surface. Most damage occurs during first deglaciation and the first Holocene readvance. Figure 3.12b displays histograms of damage elevation for strength reduction factors  $\alpha = 100\%$ , 70%, 50%, and 30% in model scenario N, showing similar damage patterns. Initial damage increases for weaker rock mass strength and new damage is greatest for  $\alpha = 50\%$ . Although damage in a purely mechanical model under reduced strength conditions is significant, in parallel with TM effects this damage increases by 5 to 12% (Figure 3.12b). Peak damage accumulation is located around the Holocene maximum ice elevation and decreases at lower elevations. Glacier fluctuations induce most damage around the elevation of the changing ice surface and a few hundred meters above (see Figure 3.11a). This damage pattern is enhanced under reduced rock strength conditions and strongest when including TM effects (Figure 3.12).

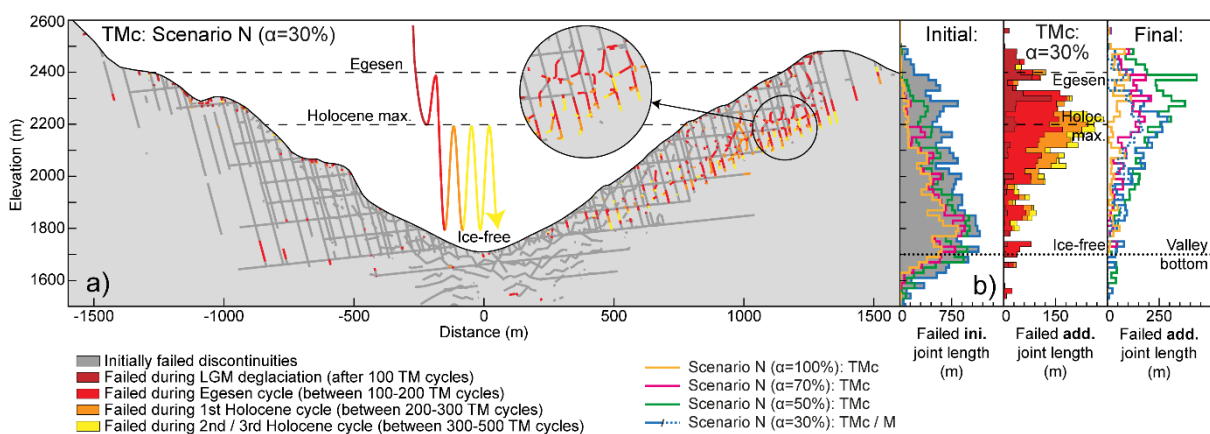


**Figure 3.12.** Influence of seasonal thermal cycles on rock slope damage for a weakened slope during repeat glacial cycles: a) Spatial and temporal distribution of damage induced by thermo-mechanical stress cycles (TMc) for model scenario N with  $\alpha = 30\%$  in the cross-section. b) Damage elevations at initial conditions, additional damage with time for scenario N with  $\alpha = 30\%$  induced by thermo-mechanical stress cycles (TMc), and final additional damage for scenario N with  $\alpha = 100\%$  to  $30\%$  (in comparison to a purely mechanical (M) model with  $\alpha = 30\%$ ) displayed as histogram.

Maximum displacement in a purely mechanical model on the destabilized eastern flank ( $\alpha = 30\%$ ) is up to  $\sim 0.5$  m (Figure 3.13a). Including TM effects, displacements increase to  $\sim 0.7$  m and the extent of the unstable rock mass grows, becoming deeper and extending further toward the valley bottom (Figure 3.13b). In Figure 3.13d we compare horizontal displacement at Point 1 within the unstable rock mass (see Figure 3.13a,b) for applied glacier scenarios N and P (Figure 3.13c). Irreversible displacement is superimposed on the elastic slope response to glacier loading and unloading [Grämiger et al., 2017]. The timing of greatest displacement coincides with first glacier retreat in both scenarios, leading to initiation of a slope instability (Figure 3.13d). Displacement continues steadily during subsequent

Holocene cycles in scenario N. Final displacement at Point 1 is slightly larger including Holocene cycles as compared to LGM deglaciation in scenario P. In Figure 3.13e we compare the additional displacement for models with (N) and without (P) a single Holocene cycle, each also benchmarked against a purely mechanical model. Under permanent ice-free conditions (P), seasonal TM cycles over 100 years result in an additional 1.0 cm displacement ( $\sim 0.1$  mm per cycle) compared to the purely mechanical model. Additional displacement with a single Holocene cycle (N) in a purely mechanical model is  $\sim 3$  cm, while including TM effects this value increases to  $\sim 5.3$  cm; enhanced 2.3 cm through TM cycles ( $\sim 0.2$  mm per cycle).

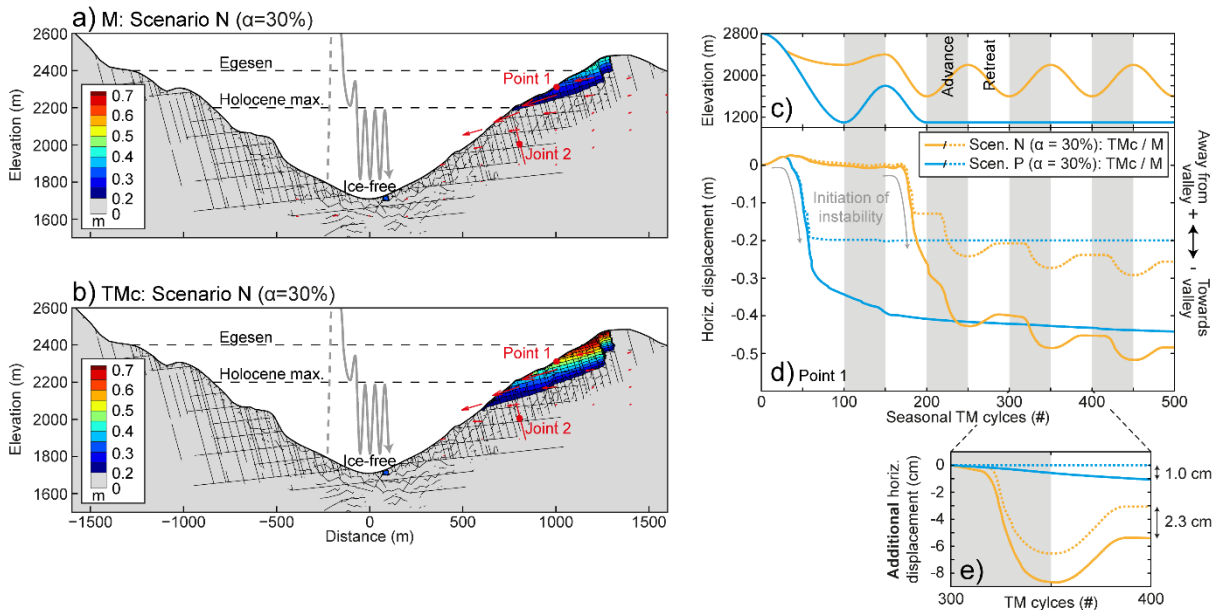


**Figure 3.13.** Displacement in a weakened rock slope illustrating development and temporal evolution of landslide activity during repeat glacial cycles in concert with TM cycles: a) Maximum slope displacement and vectors (red arrows) for scenario N with  $\alpha = 30\%$  for a complete glacial cycle (ice-free initialization until end of 3<sup>rd</sup> Holocene cycle) for a purely mechanical (M) model, and b) with thermo-mechanical stress cycles (TMc) included. Location of observation Point 1 and Joint 2. c) Applied glacier scenarios N and P. d) Absolute horizontal displacement ( $\Delta x$ ) for Point 1 within the instability for glacier scenario N and P under reduced rock mass strength ( $\alpha = 30\%$ ), each comparing M and TMc. e) Additional horizontal displacement ( $+\Delta x$ ) for Point 1 for scenarios without (blue) and with (orange) a single Holocene cycle (each for TMc / M).

In Figure 3.14 we show shear displacement and the corresponding stress path along an example steeply dipping joint located in the mid-slope region at  $\sim 200$  m depth (location shown in Figure 3.13). Right-handed shear displacement along the joint occurs during LGM deglaciation (scenario P) (Figure 3.14a). Shear dislocation during scenario N is similar for mechanical and TM models, although slip magnitudes are enhanced when including TM cycles. Most shearing occurs during first glacier retreat. Subsequent Holocene readvances promote further slip, while shearing during later retreat is smaller. The corresponding stress path for the examined joint during LGM deglaciation and subsequent Holocene cycles is presented in Figure 3.14b. During deglaciation, normal stresses decrease and shear stresses increase, and stress conditions move closer to the failure envelope. The failure criterion restrains any further decrease in normal stress or increase in shear stress. Each subsequent Holocene cycle moves the stress state first away and then toward the failure envelope. Stresses reaching the failure envelope

generate irreversible slip (see Figure 3.14a). Slip and accompanying stress redistribution are greater for TM models.

Figure 3.14c displays the stress path in detail during a single Holocene cycle. Under ice-free conditions, the observed joint is still critically stressed, with stresses at the failure envelope (Figure 3.14c1). TM cycles provoke minor stress redistribution and slip. During glacier advance, the joint becomes increasingly critically stressed as the ice surface reaches the elevation of the joint. TM stress cycles enhance glacially induced slip (Figure 3.14a). Once the glacier elevation rises above the joint, normal stresses increase and shear stresses decrease (Figure 3.14c); the joint becomes less critically stressed and shear dislocation ceases. The opposite occurs with retreat, as stress conditions again wander close to the failure envelope. Stresses reach the failure envelope when the glacier surface is around the elevation of the joint (Figure 3.14c2). Stress redistribution is accompanied by slip, and enhanced by TM stress cycles (Figure 3.14a). After the glacier retreats below the joint elevation, the joint becomes less critically stressed, and stresses cycle away from the failure envelope under ice-free conditions (Figure 3.14c2). Stress conditions in an ice-free slope are critical, but without an additional driving mechanism pushing stresses toward the failure envelope (Figure 3.14c1), TM cycles provoke only minor slip (Figure 3.14a; scenario P). Each glacial cycle, advance in the same way as retreat, shifts joint stress conditions toward the failure envelope when the glacier elevation is around the joint elevation (Figure 3.14b). Glacier ice above the joint increases confining stresses and reduces criticality (Figure 3.14c). Ice lowering below the joint has a smaller influence on the stress conditions, and they remain close to the failure envelope. Compared to a purely mechanical model, resulting TM shear displacements are strongly enhanced (Figure 3.14a).

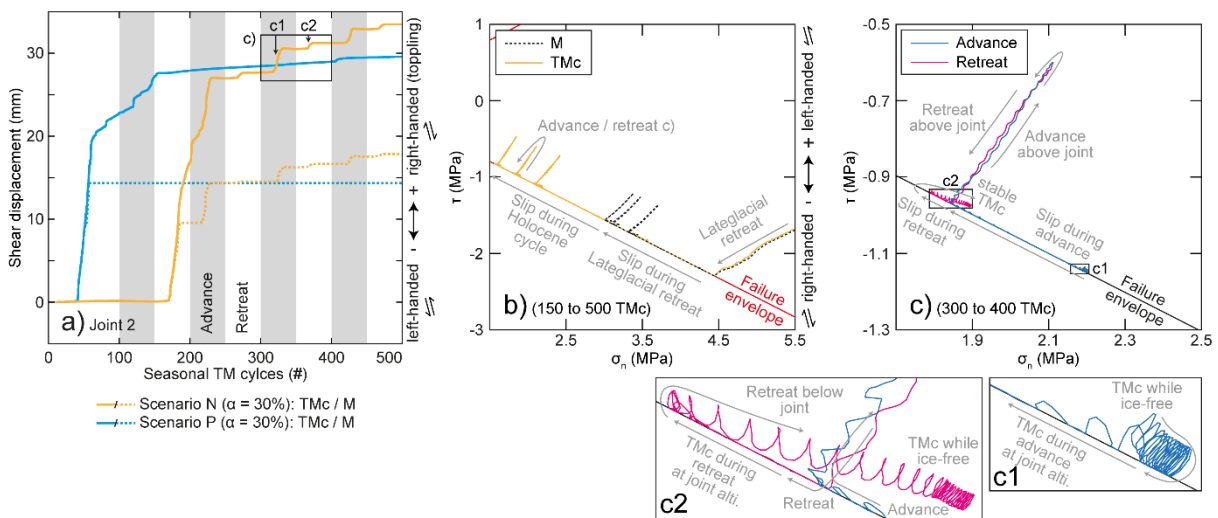


**Figure 3.14.** Shear displacement and corresponding stress path for observation Joint 2 (see location in Figure 3.13) during glacial cycles: a) Shear displacement for scenario N and P with  $\alpha = 30\%$ , each comparing M and TMc. b) Stress path for scenario N comparing M and TMc. c) Stress path for a single Holocene cycle (scenario N) with details of times when joint is most critically stressed during advance (c1) and retreat (c2).

### 3.4 Discussion

Our numerical simulations demonstrate the importance of including TM effects in parallel with glacier loading cycles as a preparatory factor for paraglacial rock slope instabilities. In our models, purely mechanical loading and unloading by a glacier results in downward and upward displacement, respectively, in subglacial bedrock (Figure 3.15a). During advances, the ice mass pushes the valley apart and toppling mode failure is activated on steeply dipping discontinuities above the glacier elevation. In addition to the changing weight of ice, glacier fluctuations also strongly affect bedrock thermal boundary conditions. While bedrock beneath ice is nearly isothermal at 0 °C, rock slopes above the ice are exposed to solar radiation and air temperature changes undergoing long-term, seasonal and daily cycles (Figure 3.15b). Our TM models demonstrate how long-term temperature changes on glacial time scales penetrate to depth, generating thermal strain that affects large areas of the slope and increases rock mass damage during glacial cycles. Furthermore, damage and displacement are strongly enhanced in the presence of annual temperature cycles (Figure 3.15b), representing an additional fatigue mechanism. While glacier loading and unloading affects the criticality of adjacent rock slopes, seasonal TM stress cycles act on these critically stressed joints generating slip and additional damage. Glacier retreat shifts stress conditions along a joint closer to the failure envelope, while TM stress cycles promote enhanced slip and stress redistribution at critical stress conditions during retreat and advance (Figure 3.15c). Once the slope has reached a meta-stable state during ice-free conditions, TM stress cycles become less efficient in driving additional shearing.

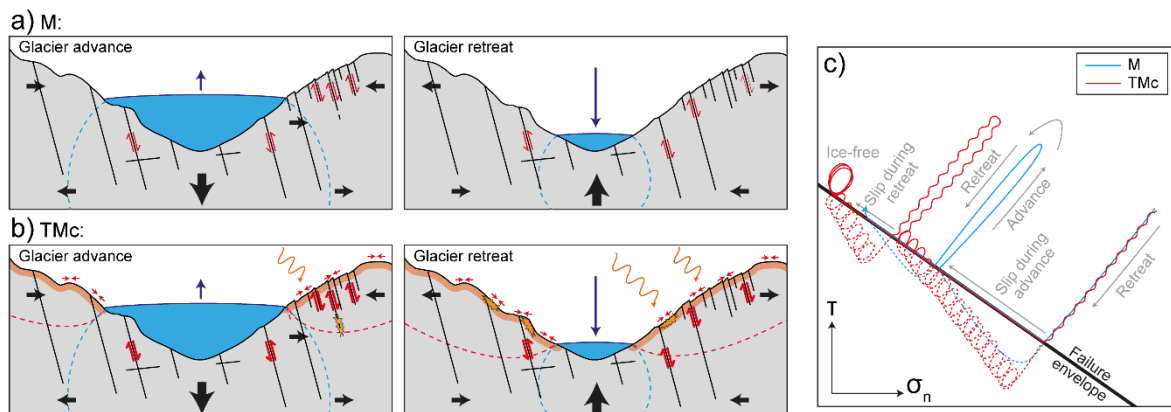


**Figure 3.15.** Conceptual sketch of mechanical and thermo-mechanical processes acting during a glacier cycle: a) Pure mechanics during glacier advance / retreat in a valley. b) Thermo-mechanics including annual temperature changes during glacier advance / retreat. c) Conceptual stress path (shear stress versus normal stress) for a purely mechanical (M) model and including seasonal thermo-mechanical stress cycles (TMc). Dashed stress path showing the potential elastic stresses, while solid line represents the plastic stress path limited by Mohr-Coulomb failure envelope.

Rock slope damage observed in the field at Aletsch supports our modeling results. Shallow new failure through intact rock can be found along the margin of the retreating Great Aletsch Glacier (Figure 3.16a), as similarly predicted by our models including annual TM cycles (Figure 3.10). Although the specific driving force for this particular feature remains speculative, the recent failure indicates that local bedrock is sufficiently critically stressed so that changes in boundary conditions generate fracturing. Under reduced rock mass strength conditions, glacial cycles in our models generated sufficient damage to destabilize the slope and initiate landsliding (Figure 3.13a,b); TM cycles enhanced this displacement. In

the field at Aletsch, we observe rock slope instabilities with dimensions and kinematics closely resembling our model predictions (e.g., Figure 3.16b). TM effects in parallel with fluctuating ice loads may also contribute to preparing slopes for failure around the glacier terminus in the Aletsch region (Figure 3.2), although geological predisposition also plays an important role in local slope stability [Terzaghi, 1962; Augustinus, 1995]. Most damage in our models occurred during first deglaciation and accompanying paraglacial thermal shock. Therefore we propose that rock slopes higher in the Aletsch Valley within the Holocene minimum extent, currently covered by ice and likely never exposed since at least the LGM, may be more susceptible to damage during future deglaciation, especially at shallow depths. New damage may promote enhanced rates of rockfall in these regions. Damage in our long-term TM models occurs not only directly after deglaciation, but increases continuously during subsequent climate warming even as the slope is unaffected by glacier change. Ongoing temperature change can lead to damage delayed by several thousand years (Figure 3.5a-c). Long-term TM effects may thus contribute to time-dependent damage following deglaciation [cf. Prager *et al.*, 2008; McColl, 2012], potentially explaining frequently observed lag-times between deglaciation and the timing of large slope failures [e.g. Ballantyne *et al.*, 2014a, b; McColl, 2012].

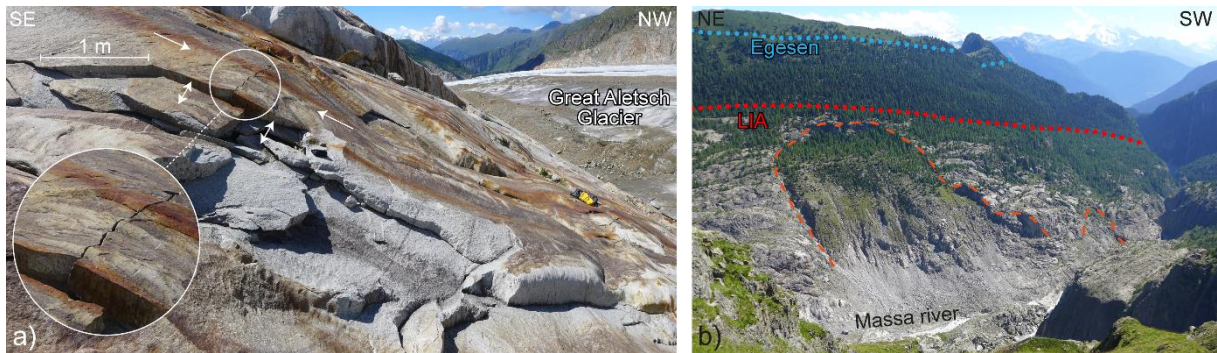


**Figure 3.16.** Example rock slope damage observed in the field at Aletsch (locations marked as asterisks in Figure 3.2): a) A-tent pop-up at the surface on the eastern valley flank at the margin of Great Aletsch Glacier. b) Silbersand landslide and smaller instability further south on the eastern flank of the Aletsch Valley.

Our numerical modeling goes beyond the purely mechanical simulations presented by Grämiger *et al.* [2017] but has its own limitations. Long time scales of interest made it necessary for us to investigate long-term and seasonal thermal effects separately. These processes in reality act in concert and may augment each other, driving increased rates of rock slope damage. Furthermore, we had to reduce to amount of seasonal TM cycles to a feasible value, whereas in reality the number of stress cycles that bedrock has experienced is an order of magnitude larger. Both limitations likely lead to underestimated induced damage. Furthermore, heat transport in our models occurs only by conduction, whereas in reality heat advection by groundwater [Rybach and Pfister, 1994] or air circulation [Moore *et al.*, 2011] likely influences the geothermal gradient. We also neglected secondary snow and ice cover after LGM ice retreat. Seasonal snow cover can reduce the amplitude of annual temperature cycles [Zhang, 2005] because snow insulates underlying bedrock from extreme winter temperatures (see Appendix). Similarly, local permanent ice or snow accumulations in the high mountain areas during the Lateglacial and Holocene warming calculated in our models (Figure 3.6c). We also assume isotropic thermal properties, even though foliation and geological structure may result in anisotropic properties. However,

predicted amplitudes of seasonal surface displacements in our models are in the range of past field measurements [Gischig *et al.*, 2011b; Bakun-Mazor *et al.*, 2013].

We also neglected any secondary thermal effects such as permafrost, which can create rock damage through segregation ice growth [Wegmann and Gudmundsson, 1999; Sanders *et al.*, 2012; Krautblatter *et al.*, 2013; Duca *et al.*, 2015]. While thermal strain depends only on temperature differences, permafrost depends on absolute temperatures. Glacier ice at the pressure melting point of  $\sim 0$  °C insulates subglacial bedrock from prevailing surface temperatures, which may be above or below freezing depending mostly on altitude. Therefore, ground temperature can either increase or decrease after deglaciation. In the latter case, available moisture in the rock can freeze and ice segregation drives damage. Field observation of active rock glaciers in our study area (Figure 3.2) and the current temperature regime (see Appendix) limits the current extent of discontinuous permafrost to altitudes above  $\sim 2600$  m, covering the peaks of Bettmerhorn and Eggishorn. Temperature decrease during the LGM or Egesen stadia may have lowered the permafrost altitude by a few hundred meters, although during that time most of the Aletsch Valley was covered by ice. We believe it is unlikely that permafrost effects were a major driving factor for rock slope damage in the lower Aletsch area, since these rock slopes were either covered by temperate glacial ice during the Lateglacial or mean temperatures were above freezing, e.g., during the Holocene (Figure 3.5d,e). While permafrost may be less relevant for rock slope damage at lower altitudes, frost weathering is an important process to consider for rock slopes experiencing glacier retreat at higher altitudes [Wegmann *et al.*, 1998].

Other TM modeling studies support our results. Baroni *et al.* [2014] noted that TM effects resulting from long-term temperature changes during deglaciation can generate significant strains on adjacent slopes. This agrees with our finding that long-term TM effects have the potential to induce rock slope damage. Wegmann *et al.* [1998] investigated permafrost penetration as a consequence of glacier retreat as a factor leading to frost damage [Hales and Roering, 2007; Krautblatter *et al.*, 2013; Duca *et al.*, 2015]. Both studies showed how glacier change affects thermal boundary conditions in adjacent rock walls on long time scales. On the other hand, Gischig *et al.* [2011a] demonstrated how seasonal TM cycles can drive progressive failure in a critically stressed, unstable rock slope. They showed the most damage occurs during an initial thermal-transient phase as the rock mass first adapts to new cyclic boundary conditions. While this can occur after a slope failure exposes new rock surfaces to ambient air conditions [Gischig *et al.*, 2011a, b], the concept is even more applicable for a rock wall exposed by glacier retreat. We combined seasonal TM cycles with glacier loading and demonstrated that induced displacements are strongly enhanced in the presence of TM stresses. While damage resulting from the initial thermal-transient equilibration was greatest during first deglaciation, repetition of this effect could not be observed in our models, although we suspect in reality glacial erosion may be able to reset the shallow damaged zone. While seasonal TM cycles can act as a driving mechanism for creep of an existing unstable rock slope [Gischig *et al.*, 2011a, b], we demonstrated their potential as preparatory factor for paraglacial rock slope failures. Rock walls in higher alpine areas that have remained ice-covered since the LGM may be especially prone to shallow rock slope damage during first deglaciation, potentially resulting in increased rates of future rockfall in these regions.



### 3.5 Summary and conclusions

Bedrock in alpine valleys experiences dramatic temperature changes as glaciers advance and retreat in conjunction with long-term climatic transitions. Changes in the subsurface temperature field drive strain through thermo-mechanical coupling, and resulting TM stresses can generate rock mass damage conditioning future slope instabilities. We investigated the spatial and temporal evolution of rock slope damage induced by glacier cycles (mechanical loading and unloading by ice) in parallel with long-term and annual thermo-mechanical effects using detailed numerical models based on realistic site conditions at the Great Aletsch Glacier in Switzerland. Key outcomes of our study include:

1. Changing thermal boundary conditions during glacier retreat and advance, as well as ambient temperature trends over glacial / interglacial periods, affects the temperature field of a paraglacial valley to depths exceeding 100 m. Thermal strain induced by long-term temperature changes promotes new rock fracturing in our numerical models. The timing of greatest damage occurs at the onset of the first Holocene ice readvance in parallel with cooling of subglacial bedrock. In addition, a temperature increase of a few degrees over several thousand years after deglaciation is sufficient to induce significant new damage, even in the absence of additional glacier loading and unloading. Warming of bedrock after deglaciation also contributes to post-glacial rebound.
2. Bedrock exposed for the first time to seasonal temperature cycles experiences strong TM stresses within the thermally active layer, generating a shallow damage front that follows the retreating glacier margin. Damage occurs as part of a transition we term *paraglacial thermal shock*; the period of enhanced damage is restricted mostly to the first ice retreat. Although damage is generally shallow, cyclic TM stress propagate below the thermally active layer and enhance slope displacement at greater depths. Future climate warming and glacier retreat will expose bedrock to annual TM cycles that has likely remained beneath ice since at least the LGM, potentially resulting in increased rates of rockfall in these regions.
3. Long-term TM effects in our models generate between 15% and 19% new damage compared to the inherited damage field, while a purely mechanical model driven by glacier loading cycles resulted in only ~1% new damage. Seasonal TM cycles acting in parallel with glacier loading results in between 10% and 11% new damage. Thermal effects (both long- and short-term) in conjunction with glacier loading cycles thus represent a significant driver of paraglacial rock slope damage and preparatory factor for paraglacial rock slope instabilities.
4. Glacier fluctuations acting on a slope with reduced rock mass strength produced considerable damage and displacement, initiating a slope instability on the eastern flank of our models with characteristics comparable to those observed in the field at Aletsch. Seasonal TM cycles alone induced incremental damage and slope displacement, but in parallel with glacier loading cycles strongly enhanced the slope response to fluctuating ice conditions, during both ice retreat and advance.
5. Glacier retreat brings the stress state of joints in the adjacent rock slope closer to the failure envelope, inducing shear dislocation (i.e., slip). Initiation of seasonal TM cycles in parallel with deglaciation results in stress cycles on the Mohr-Coulomb failure envelope, inducing additional slip, as compared to a purely mechanical model, and enhancing slope displacement. Therefore

TM effects must not be neglected when exploring stress changes associated with glacial cycles and rock slope damage. TM damage is an effective preparatory factor for paraglacial rock slope instabilities.

Ice makes a weak buttress for glaciated valley flanks, although it affects the stress field of the slope by adding confinement. Stress redistribution and post-failure strength reduction (i.e., slip-weakening), combined with long-term and seasonal TM effects in parallel with glacier fluctuations are significantly (~10 times) more effective in promoting damage than the purely mechanical effects of glacier loading and unloading. Deglaciation involves a complex, multi-process transition of boundary conditions, including in addition to the mechanical load of ice, changes in temperature and hydrology.

### **3.6 Acknowledgments**

This project was funded by the Swiss National Science Foundation (projects 135184 and 146593). Data used in this study can be found in the citations listed in the references. Data output is included in the tables and figures; raw data are available on request from L.G. (E-mail: graemiger.lorenz@gmail.com). Special thanks to Johnny Sanders for field assistance and Reto Seifert for help with the temperature loggers.

### **3.7 Appendix: Ground temperature measurements at Aletsch**

Rock surface temperatures are required boundary conditions for our thermal model, and depend mainly on air temperature and solar radiation [Gruber *et al.*, 2004]. We measured local ground temperature in bedrock along valley profiles at different altitudes and aspect, compiling this information with other available data to describe the local temperature regime (Figure 3.2). The majority of temperature sensors were used to cover a large span of elevation on the eastern and western valley slopes, while a few loggers were placed close to the ice margin or within ice caves to measure the temperature transition in bedrock experiencing present-day glacier retreat. The altitude of our sensors spanned from ~2000 to 3000 m, measuring on rock surfaces with mainly NW or SE aspect, representative of rock walls in our study area (see Figure 3.2 and Table 3.A1). We used HOBO Pro v2 U23-003 loggers with two external temperature sensors with accuracy of 0.2 °C. Data storage lasted around one year (at the measurement interval of 30 minutes) and data collection was performed manually. The external temperature sensors were grouted into a ~5 cm deep borehole in the rock surface. At two positions (AT08, AT09 in Figure 3.2) the second external temperature sensor was used to measure air temperature ~20 cm above the ground using an aspirated solar shield.

The high alpine environment and remote locations of several loggers presented challenges. Loggers were destroyed by lightning (AT14), snow avalanche (AT07), and glacier movement (AT03, AT04). Snow pressure during winter was difficult to anticipate and therefore cable breach of the external sensor was a problem at many locations (AT01). The redundancy of having two external sensors helped partly overcome this issue. Battery malfunction was also common in the cold weather conditions. Inaccessibility during winter allowed us to identify data gaps only during sporadic checks, resulting in data loss. Despite these difficulties, we were able to collect more than three years of temperature data for most of the sensors. Temperature time series data for sensors with satisfactory data coverage are shown in Figure 3.A1. Applying a sine function fit to the daily average (filtering out times of snow or ice cover around 0 °C) resulted in values for mean annual temperature (MAT) and annual amplitudes (Table

3.A1). The beginning of the time series for sensor AT10 (Figure 3.A1), located at the Aletsch Glacier margin, captured the transition of rock temperature during glacier retreat in summer 2012.

Figure 3.A2 shows detailed analysis of rock surface temperature measurements collected in this study, complemented with MAGT measured at higher altitudes (~2700 – 3600 m) in the Aletsch region by *Wegmann* [1998]. MAGT varies with altitude although with large scatter (Figure 3.A2a). Due to a lack of data, no clear dependency of MAGT or annual amplitude with the position of the sun (azimuth and elevation angle of the sun) with respect to the rock surface was apparent (Figure 3.A2b,c), although it would be expected [*Gruber et al.*, 2004; *Wegmann*, 1998]. However, we observe a clear pattern of the MAGT in relation to altitude and azimuth (Figure 3.A2d). MAGT becomes warmer at lower elevations and southern exposures, as also identified in other studies [e.g., *Gruber et al.*, 2004]. The mean annual amplitude determined in our study is 9.58 °C (Figure 3.A2e). For our thermal models, it was necessary to define a relationship between temperature and altitude. *Wegmann* [1998] used different approximations of MAGT with altitude for northern and southern exposed rock walls at the nearby Jungfrau (Figure 3.A2a). *Moore et al.* [2011] suggested using the same lapse rate for MAGT as for mean annual air temperature (MAAT), where ground temperatures are generally ~1 °C warmer (Figure 3.A2a). We analyzed regional air temperature data available from nearby weather stations (Table 3.A2), and fitted sine functions through one year of daily temperature averages over several years (Table 3.A2 and Figure 3.A2f) to establish a regional MAAT fit with a lapse rate of  $-0.0052 \text{ }^{\circ}\text{Cm}^{-1}$  ( $T(z) = 12.2851 - 0.0052(z)$ ; where  $z$  is meters) (Figure 3.A2g). Using the lapse rate from our regional MAAT analysis, we fit MAGT measured in this study complemented by data from *Wegmann* [1998], resulting in an approximation of  $T(z) = 15.3 - 0.005(z)$  (Figure 3.A2a). MAGT is estimated to be ~3 °C warmer than MAAT. The measured differences in MAT between air and rock at sites AT08 and AT09, respectively, is 2.5 to 3°C (Table 3.A1), matching our approximation. Our final approximation of the transient ground temperature distribution as a function of time ( $t$ ) and elevation ( $z$ ) is:

$$T(t, z) = 15.3 - 0.005(z) + 10\sin(2\pi ft) \quad (3.A1)$$

where  $t$  is in seconds,  $z$  is meters, and  $f$  is the 1-year annual frequency in Hz. Equation 3.A1 results in a 0 °C isotherm for MAGT at 3060 m, while the regional MAAT fit reaches 0 °C isotherm at 2363 m and -1 °C at 2555 m (discontinuous permafrost occurs where the MAAT is between -1 to -6°C).

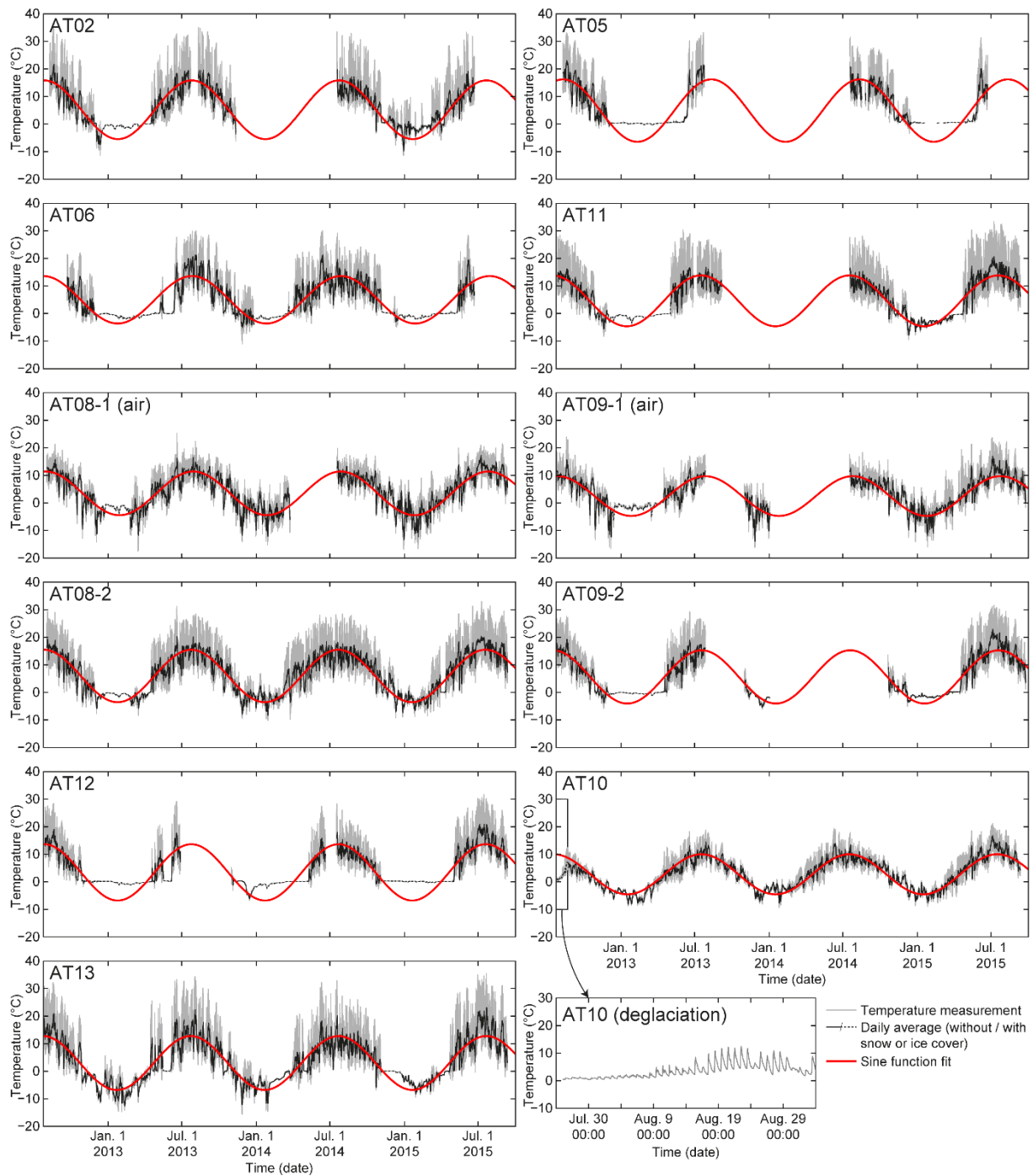


**Figure 3.A1.** Time series of rock (and air) surface temperature measurements in the Aletsch region with daily average and sine function fit (see Table 3.A1). Enlargement of temperature transition in bedrock during present-day glacier retreat from near 0 °C to daily temperature cycles at logger AT10.

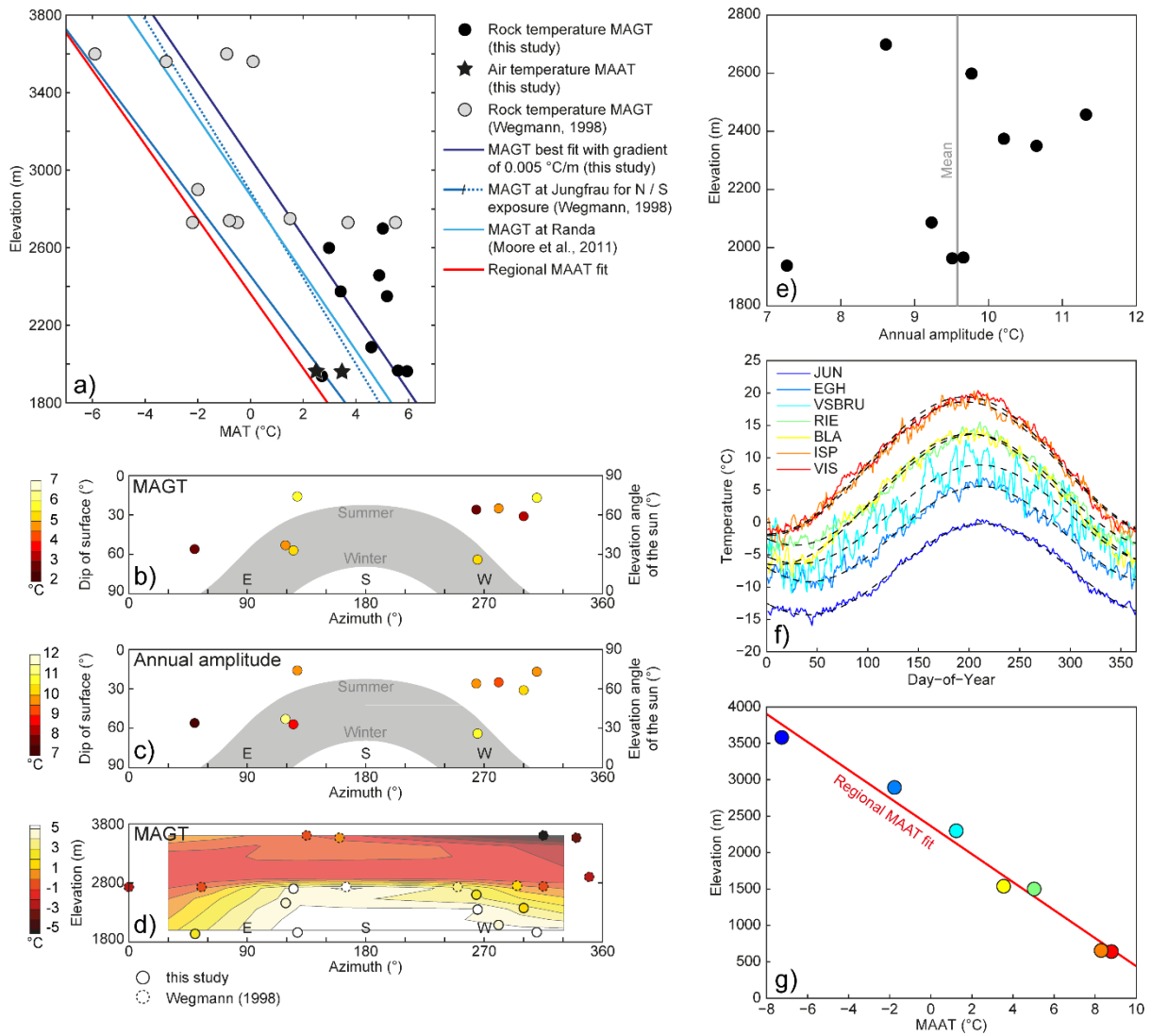


**Figure 3.A2.** Analysis of rock and air temperature data from the Aletsch region: a) MAGT and MAAT measurements (this study) complemented by MAGT from Wegmann [1998] versus altitude. Linear fit for MAGT and MAAT (this study) in comparison with past studies [Wegmann, 1998; Moore et al., 2011]. b) MAGT and c) annual amplitude, respectively, versus position of the sun (azimuth and elevation angle) with respect to the rock surface exposure. d) MAGT (this study complemented with data from Wegmann [1998]) as a function of altitude and azimuth. e) Mean annual amplitude versus altitude. f) Available air temperature data from nearby weather stations, averaging daily temperatures over several years (Table 3.A2) and fitting sine functions through one year. g) Regional MAAT fit from available air temperature data (Table 3.A2).

**Table 3.A1.** Rock (and air) surface temperature measurements from this study in the Aletsch region with values for sine function fit

Name	Type	Elevation (m)	Azimuth (°)	Dip (°)	MA(G)T (°C)	Annual amplitude (°C)	R-Squared ()
AT01	Rock	2736	276	55	-	-	-
AT02	Rock	2350	265	64	5.18	10.65	0.78
AT03	Rock (ice margin)	2242	-	-	-	-	-
AT04	Rock (ice margin)	2251	-	-	-	-	-
AT05	Rock	2458	119	53	4.88	11.32	0.63
AT06	Rock	2699	125	57	5.02	8.61	0.61
AT07	Rock	2440	95	76	-	-	-
AT08-1	Air	1963	-	-	3.47	7.93	0.77
AT08-2	Rock	1963	128	16	5.94	9.51	0.84
AT09-1	Air	1966	-	-	2.49	7.21	0.76
AT09-2	Rock	1966	310	17	5.60	9.66	0.88
AT10	Rock (ice margin)	1938	50	56	2.71	7.27	0.88
AT11	Rock	2087	281	25	4.59	9.23	0.87
AT12	Rock	2374	300	31	3.42	10.21	0.78
AT13	Rock	2599	264	26	2.98	9.77	0.82
AT14	Rock	2800	258	60	-	-	-

**Table 3.A2.** Air temperature data from nearby weather stations (IDAweb by MeteoSchweiz) with values for sine function fit

Name	Longitude / Latitude	Elevation (m)	Time series (Date)	MAAT (°C)	Annual amplitude (°C)	R-Squared ()
JUN; Jungfraujoch	7°59' / 46°33'	3580	Jan. 1933 – Aug. 2015	-7.26	7.04	0.99
EGH; Eggishorn	8°06' / 46°26'	2893	Oct. 1993 – Aug. 2015	-1.77	7.37	0.97
VSBRU; Bruchji	7°58' / 46°23'	2300	Sept. 2012 – Aug. 2015	1.25	7.64	0.85
RIE; Ried	7°48' / 46°25'	1500	Jan. 1974 – Feb. 1999	5.03	8.56	0.98
BLA; Blatten	7°49' / 46°25'	1538	Mar. 2001 – Aug. 2015	3.55	10.12	0.99
ISP; Visp	7°53' / 46°17'	655	Jul. 1959 – Dec. 1970	8.30	10.34	0.98
VIS; Visp	7°51' / 46°18'	639	Dec. 1979 – Aug. 2015	8.80	10.61	0.99

### 3.8 References

- Alley, R. B., et al. (1993), Abrupt increase in Greenland snow accumulation at the end of the Younger Dryas event, *Nature*, 362(6420), 527-529.
- Augustinus, P. C. (1995), Glacial valley cross-profile development: the influence of in situ rock stress and rock mass strength, with examples from the Southern Alps, New Zealand, *Geomorphology*, 14(2), 87-97, doi:10.1016/0169-555x(95)00050-x.
- Bakun-Mazor, D., Y. H. Hatzor, S. D. Glaser, and J. Carlos Santamarina (2013), Thermally vs. seismically induced block displacements in Masada rock slopes, *International Journal of Rock Mechanics and Mining Sciences*, 61, 196-211, doi:http://dx.doi.org/10.1016/j.ijrmms.2013.03.005.
- Ballantyne, C. K., G. F. Sandeman, J. O. Stone, and P. Wilson (2014a), Rock-slope failure following Late Pleistocene deglaciation on tectonically stable mountainous terrain, *Quaternary Science Reviews*, 86, 144-157, doi:http://dx.doi.org/10.1016/j.quascirev.2013.12.021.
- Ballantyne, C. K., P. Wilson, D. Gheorghiu, and À. Rodés (2014b), Enhanced rock-slope failure following ice-sheet deglaciation: timing and causes, *Earth Surface Processes and Landforms*, 39(7), 900-913, doi:10.1002/esp.3495.
- Baroni, C., S. Martino, M. C. Salvatore, G. Scarascia Mugnozza, and L. Schilirò (2014), Thermomechanical stress-strain numerical modelling of deglaciation since the Last Glacial Maximum in the Adamello Group (Rhaetian Alps, Italy), *Geomorphology*, 226, 278-299, doi:http://dx.doi.org/10.1016/j.geomorph.2014.08.013.
- Blunier, T., and E. J. Brook (2001), Timing of Millennial-Scale Climate Change in Antarctica and Greenland During the Last Glacial Period, *Science*, 291(5501), 109-112, doi:10.1126/science.291.5501.109.
- Boulton, G., T. Chan, R. Christiansson, L. O. Ericsson, J. Hartikainen, M. R. Jensen, F. W. Stanchell, and T. Wallroth (2004), Thermo-Hydro-Mechanical (T-H-M) Impacts of Glaciation and Implications for Deep Geologic Disposal of Nuclear Waste, in Elsevier Geo-Engineering Book Series, edited by S. Ove, pp. 299-304, Elsevier, doi:http://dx.doi.org/10.1016/S1571-9960(04)80057-0.
- Bovis, M. J. (1990), Rock-slope deformation at Affliction Creek, southern Coast Mountains, British Columbia, *Canadian Journal of Earth Sciences*, 27(2), 243-254, doi:10.1139/e90-024.
- Collins, B. D., and G. M. Stock (2016), Rockfall triggering by cyclic thermal stressing of exfoliation fractures, *Nature Geoscience*, advance online publication, doi:10.1038/ngeo2686.
- Cossart, E., R. Braucher, M. Fort, D. L. Bourlès, and J. Carcaillet (2008), Slope instability in relation to glacial debuttressing in alpine areas (Upper Durance catchment, southeastern France): Evidence from field data and <sup>10</sup>Be cosmic ray exposure ages, *Geomorphology*, 95(1-2), 3-26, doi:10.1016/j.geomorph.2006.12.022.
- Cundall, P. A., and R. D. Hart (1992), Numerical modelling of discontinua, *Engineering Computations*, 9(2), 101-113, doi:doi:10.1108/eb023851.
- Dahl-Jensen, D., et al. (2013), Eemian interglacial reconstructed from a Greenland folded ice core, *Nature*, 493(7433), 489-494, doi:10.1038/nature11789.
- Darnault, R., Y. Rolland, R. Braucher, D. Bourlès, M. Revel, G. Sanchez, and S. Bouissou (2012), Timing of the last deglaciation revealed by receding glaciers at the Alpine-scale: impact on mountain geomorphology, *Quaternary Science Reviews*, 31, 127-142, doi:10.1016/j.quascirev.2011.10.019.
- Davis, B. A. S., S. Brewer, A. C. Stevenson, and J. Guiot (2003), The temperature of Europe during the Holocene reconstructed from pollen data, *Quaternary Science Reviews*, 22(15-17), 1701-1716, doi:http://dx.doi.org/10.1016/S0277-3791(03)00173-2.
- Draebing, D., M. Krautblatter, and R. Dikau (2014), Interaction of thermal and mechanical processes in steep permafrost rock walls: A conceptual approach, *Geomorphology*, 226, 226-235, doi:http://dx.doi.org/10.1016/j.geomorph.2014.08.009.

- Duca, S., E. E. Alonso, and C. Scavia (2015), A permafrost test on intact gneiss rock, *International Journal of Rock Mechanics and Mining Sciences*, 77, 142-151, doi:<http://dx.doi.org/10.1016/j.ijrmms.2015.02.003>.
- Eberhardt, E., D. Stead, and J. S. Coggan (2004), Numerical analysis of initiation and progressive failure in natural rock slopes—the 1991 Randa rockslide, *International Journal of Rock Mechanics and Mining Sciences*, 41(1), 69-87, doi:10.1016/s1365-1609(03)00076-5.
- Eppelbaum, L., I. Kutasov, and A. Pilchin (2014), Thermal Properties of Rocks and Density of Fluids, in *Applied Geothermics*, edited, pp. 99-149, Springer Berlin Heidelberg, doi:10.1007/978-3-642-34023-9\_2.
- Eppes, M. C., B. Magi, B. Hallet, E. Delmelle, P. Mackenzie-Helnwein, K. Warren, and S. Swami (2016), Deciphering the role of solar-induced thermal stresses in rock weathering, *Geological Society of America Bulletin*, doi:10.1130/b31422.1.
- Evans, S. G., and J. J. Clague (1994), Recent climatic change and catastrophic geomorphic processes in mountain environments, *Geomorphology*, 10(1–4), 107-128, doi:10.1016/0169-555x(94)90011-6.
- Faillettaz, J., D. Sornette, and M. Funk (2010), Gravity-driven instabilities: Interplay between state- and velocity-dependent frictional sliding and stress corrosion damage cracking, *Journal of Geophysical Research: Solid Earth*, 115(B3), B03409, doi:10.1029/2009jb006512.
- Gischig, V. S., J. R. Moore, K. F. Evans, F. Amann, and S. Loew (2011a), Thermomechanical forcing of deep rock slope deformation: 1. Conceptual study of a simplified slope, *J. Geophys. Res.*, 116(F4), F04010, doi:10.1029/2011jf002006.
- Gischig, V. S., J. R. Moore, K. F. Evans, F. Amann, and S. Loew (2011b), Thermomechanical forcing of deep rock slope deformation: 2. The Randa rock slope instability, *J. Geophys. Res.*, 116(F4), F04011, doi:10.1029/2011jf002007.
- Gischig, V., G. Preisig, and E. Eberhardt (2015), Numerical Investigation of Seismically Induced Rock Mass Fatigue as a Mechanism Contributing to the Progressive Failure of Deep-Seated Landslides, *Rock Mechanics and Rock Engineering*, 1-22, doi:10.1007/s00603-015-0821-z.
- Grämiger, L. M., J. R. Moore, V. Gischig, S. Ivy-Ochs, and S. Loew (2017), Beyond debuttressing: Mechanics of paraglacial rock slope damage during repeat glacial cycles, *under review at Journal of Geophysical Research, Earth Surface*, Manuscript # 2016JF003967.
- Gruber, S., M. Hoelzle, and W. Haeberli (2004), Rock-wall temperatures in the Alps: modelling their topographic distribution and regional differences, *Permafrost and Periglacial Processes*, 15(3), 299-307, doi:10.1002/ppp.501.
- Gunzburger, Y., V. Merrien-Soukatchoff, and Y. Guglielmi (2005), Influence of daily surface temperature fluctuations on rock slope stability: case study of the Rochers de Valabres slope (France), *International Journal of Rock Mechanics and Mining Sciences*, 42(3), 331-349, doi:10.1016/j.ijrmms.2004.11.003.
- Hales, T. C., and J. J. Roering (2007), Climatic controls on frost cracking and implications for the evolution of bedrock landscapes, *Journal of Geophysical Research: Earth Surface*, 112(F2), F02033, doi:10.1029/2006jf000616.
- Hall, K. (1999), The role of thermal stress fatigue in the breakdown of rock in cold regions, *Geomorphology*, 31(1–4), 47-63, doi:[http://dx.doi.org/10.1016/S0169-555X\(99\)00072-0](http://dx.doi.org/10.1016/S0169-555X(99)00072-0).
- Hall, K., and M.-F. André (2001), New insights into rock weathering from high-frequency rock temperature data: an Antarctic study of weathering by thermal stress, *Geomorphology*, 41(1), 23-35, doi:[http://dx.doi.org/10.1016/S0169-555X\(01\)00101-5](http://dx.doi.org/10.1016/S0169-555X(01)00101-5).
- Hansmann, J., S. Loew, and K. Evans (2012), Reversible rock-slope deformations caused by cyclic water-table fluctuations in mountain slopes of the Central Alps, Switzerland, *Hydrogeology Journal*, 20(1), 73-91, doi:10.1007/s10040-011-0801-7.



- Harrison, J. C., and K. Herbst (1977), Thermoelastic strains and tilts revisited, *Geophysical Research Letters*, 4(11), 535-537, doi:10.1029/GL004i011p00535.
- Harrison, W. D. (1975), Temperature Measurements in a Temperate Glacier, *Journal of Glaciology*, 14(70), 23-30, doi:10.3198/1975JoG14-70-23-30.
- Hasler, A., S. Gruber, and J. Beutel (2012), Kinematics of steep bedrock permafrost, *J. Geophys. Res.*, 117(F1), F01016, doi:10.1029/2011jf001981.
- Heiri, O., et al. (2014), Palaeoclimate records 60–8 ka in the Austrian and Swiss Alps and their forelands, *Quaternary Science Reviews*, 106, 186-205, doi:http://dx.doi.org/10.1016/j.quascirev.2014.05.021.
- Holzhauser, H., M. Magny, and H. J. Zumbühl (2005), Glacier and lake-level variations in west-central Europe over the last 3500 years, *The Holocene*, 15(6), 789-801, doi:10.1191/0959683605hl853ra.
- Itasca (2014), UDEC - Universal Distinct Element Code, Version 6.0, User's Manual., *Itasca Consulting Group, Inc., Minneapolis*.
- Ivy-Ochs, S. (2015), Glacier variations in the European Alps at the end of the last glaciation, *Cuadernos de Investigacion Geografica*, 41(2), 295-315, doi:http://dx.doi.org/10.18172/cig.2750.
- Ivy-Ochs, S., H. Kerschner, A. Reuther, F. Preusser, K. Heine, M. Maisch, P. W. Kubik, and C. Schlüchter (2008), Chronology of the last glacial cycle in the European Alps, *Journal of Quaternary Science*, 23(6-7), 559-573, doi:10.1002/jqs.1202.
- Ivy-Ochs, S., H. Kerschner, M. Maisch, M. Christl, P. W. Kubik, and C. Schlüchter (2009), Latest Pleistocene and Holocene glacier variations in the European Alps, *Quaternary Science Reviews*, 28(21–22), 2137-2149, doi:10.1016/j.quascirev.2009.03.009.
- Jaboyedoff, M., F. Baillifard, E. Bardou, and F. Girod (2004), The effect of weathering on Alpine rock instability, *Quarterly Journal of Engineering Geology and Hydrogeology*, 37(2), 95-103, doi:10.1144/1470-9236/03-046.
- Jaboyedoff, M., M.-H. Derron, J. Jakubowski, T. Oppikofer, and A. Pedrazzini (2012), *The 2006 Eiger rockslide, European Alps*, 1st ed. ed., Cambridge University Press, Cambridge.
- Joerin, U. E., T. F. Stocker, and C. Schlüchter (2006), Multicentury glacier fluctuations in the Swiss Alps during the Holocene, *The Holocene*, 16(5), 697-704, doi:10.1191/0959683606hl964rp.
- Jouvet, G., M. Huss, M. Funk, and H. Blatter (2011), Modelling the retreat of Grosser Aletschgletscher, Switzerland, in a changing climate, *Journal of Glaciology*, 57(206), 1033-1045, doi:10.3189/002214311798843359.
- Kääb, A. (2002), Monitoring high-mountain terrain deformation from repeated air- and spaceborne optical data: examples using digital aerial imagery and ASTER data, *ISPRS Journal of Photogrammetry and Remote Sensing*, 57(1–2), 39-52, doi:10.1016/s0924-2716(02)00114-4.
- Kastrup, U., M. L. Zoback, N. Deichmann, K. F. Evans, D. Giardini, and A. J. Michael (2004), Stress field variations in the Swiss Alps and the northern Alpine foreland derived from inversion of fault plane solutions, *J. Geophys. Res.*, 109(B1), B01402, doi:10.1029/2003jb002550.
- Kelly, M. A., P. W. Kubik, F. Von Blanckenburg, and C. Schlüchter (2004), Surface exposure dating of the Great Aletsch Glacier Egesen moraine system, western Swiss Alps, using the cosmogenic nuclide <sup>10</sup>Be, *Journal of Quaternary Science*, 19(5), 431-441, doi:10.1002/jqs.854.
- Keusen, H. R., and J. L. Amiguet (1987), Die Neubauten auf dem Jungfrauoch. Geologie, Felseigenschaften, Permafrost, *Schweizer Ingenieur und Architekt*, 30-31, 17-18.
- Kos, A., F. Amann, T. Strozzzi, R. Delaloye, J. von Ruetten, and S. Springman (2016), Contemporary glacier retreat triggers a rapid landslide response, Great Aletsch Glacier, Switzerland, *Geophysical Research Letters*, 43(24), 12,466-412,474, doi:10.1002/2016GL071708.

- Krautblatter, M., D. Funk, and F. K. Günzel (2013), Why permafrost rocks become unstable: a rock–ice-mechanical model in time and space, *Earth Surface Processes and Landforms*, 38(8), 876-887, doi:10.1002/esp.3374.
- Leith, K., J. R. Moore, F. Amann, and S. Loew (2014), In situ stress control on microcrack generation and macroscopic extensional fracture in exhuming bedrock, *Journal of Geophysical Research: Solid Earth*, 119(1), 594-615, doi:10.1002/2012jb009801.
- Loew, S., V. S. Gischig, F. Glueer, R. Seifert, and J. R. Moore (2017), Multidisciplinary monitoring of progressive failure processes in brittle rock slopes, in *Rock Mechanics and Engineering*, edited by X.-T. Feng and J. A. Hudson, CRC Press / Balkema -Taylor and Francis Group.
- Lorig, L. J., and P. A. Cundall (1989), Modeling of Reinforced Concrete Using the Distinct Element Method, in *Fracture of Concrete and Rock*, edited by S. P. Shah and S. E. Swartz, pp. 276-287, Springer New York, doi:10.1007/978-1-4612-3578-1\_28.
- Maisch, M., A. Wipf, B. Denneler, J. Battaglia, and C. Benz (1999), *Die Gletscher der Schweizer Alpen: Gletscherhochstand 1850, Aktuelle Vergletscherung, Gletscherschwund-Szenarien. Schlussbericht NFP 31*, vdf Hochschulverlag.
- McColl, S. T. (2012), Paraglacial rock-slope stability, *Geomorphology*, 153–154, 1-16, doi:10.1016/j.geomorph.2012.02.015.
- McColl, S. T., and T. R. H. Davies (2013), Large ice-contact slope movements: glacial buttressing, deformation and erosion, *Earth Surface Processes and Landforms*, 38(10), 1102-1115, doi:10.1002/esp.3346.
- McColl, S. T., T. R. H. Davies, and M. J. McSaveney (2010), Glacier retreat and rock-slope stability: debunking debuttressing, in *11th Congress of the International Association for Engineering Geology and the Environment*, edited by G. Active, pp. 467-474, Auckland, New Zealand.
- McColl, S. T., T. R. H. Davies, and M. J. McSaveney (2012), The effect of glaciation on the intensity of seismic ground motion, *Earth Surface Processes and Landforms*, 37(12), 1290-1301, doi:10.1002/esp.3251.
- Moore, J. R., V. Gischig, M. Katterbach, and S. Loew (2011), Air circulation in deep fractures and the temperature field of an alpine rock slope, *Earth Surface Processes and Landforms*, 36(15), 1985-1996, doi:10.1002/esp.2217.
- Nicolussi, K., and C. Schlüchter (2012), The 8.2 ka event—Calendar-dated glacier response in the Alps, *Geology*, doi:10.1130/g32406.1.
- Prager, C., C. Zangerl, G. Patzelt, and R. Brandner (2008), Age distribution of fossil landslides in the Tyrol (Austria) and its surrounding areas, *Nat. Hazards Earth Syst. Sci.*, 8(2), 377-407, doi:10.5194/nhess-8-377-2008.
- Preisig, G., E. Eberhardt, M. Smithyman, A. Preh, and L. Bonzanigo (2016), Hydromechanical Rock Mass Fatigue in Deep-Seated Landslides Accompanying Seasonal Variations in Pore Pressures, *Rock Mechanics and Rock Engineering*, 1-19, doi:10.1007/s00603-016-0912-5.
- Röthlisberger, F., and W. Schneebeili (1979), Genesis of lateral moraine complexes, demonstrated by fossil soils and trunks: Indicators of postglacial climatic fluctuations, in *Moraines and Varves; Origin, Genesis, Classification*, edited by C. Schlüchter, pp. 387-419, A.A. Balkema, Rotterdam, Netherlands.
- Rybach, L., and M. Pfister (1994), Temperature predictions and predictive temperatures in deep tunnels, *Rock Mechanics and Rock Engineering*, 27(2), 77-88, doi:10.1007/bf01020206.
- Sanders, J. W., K. M. Cuffey, J. R. Moore, K. R. MacGregor, and J. L. Kavanaugh (2012), Periglacial weathering and headwall erosion in cirque glacier bergschrunds, *Geology*, doi:10.1130/g33330.1.
- Schimmelpfennig, I., J. M. Schaefer, N. Akçar, S. Ivy-Ochs, R. C. Finkel, and C. Schlüchter (2012), Holocene glacier culminations in the Western Alps and their hemispheric relevance, *Geology*, doi:10.1130/g33169.1.

- Schindelwig, I., N. Akçar, P. W. Kubik, and C. Schlüchter (2012), Lateglacial and early Holocene dynamics of adjacent valley glaciers in the Western Swiss Alps, *Journal of Quaternary Science*, 27(1), 114-124, doi:10.1002/jqs.1523.
- Schulson, E. M. (1990), The brittle compressive fracture of ice, *Acta Metallurgica et Materialia*, 38(10), 1963-1976, doi:http://dx.doi.org/10.1016/0956-7151(90)90308-4.
- Slaymaker, O. (2009), Proglacial, periglacial or paraglacial?, *Geological Society, London, Special Publications*, 320(1), 71-84, doi:10.1144/sp320.6.
- Steck, A. (2011), 1269 Aletschgletscher mit Teil von 1249 Finsteraarhorn, *Geologischer Atlas der Schweiz* 1:25000.
- Strozzi, T., R. Delaloye, A. Käab, C. Ambrosi, E. Perruchoud, and U. Wegmüller (2010), Combined observations of rock mass movements using satellite SAR interferometry, differential GPS, airborne digital photogrammetry, and airborne photography interpretation, *J. Geophys. Res.*, 115(F1), F01014, doi:10.1029/2009jf001311.
- Terzaghi, K. (1962), Stability of Steep Slopes on Hard Unweathered Rock, *Géotechnique*, 12(4), 251-270.
- Vinther, B. M., et al. (2009), Holocene thinning of the Greenland ice sheet, *Nature*, 461(7262), 385-388, doi:10.1038/nature08355.
- Waples, D., and J. Waples (2004), A Review and Evaluation of Specific Heat Capacities of Rocks, Minerals, and Subsurface Fluids. Part 1: Minerals and Nonporous Rocks, *Natural Resources Research*, 13(2), 97-122, doi:10.1023/B:NARR.0000032647.41046.e7.
- Watson, A. D., D. P. Moore, and T. W. Stewart (2004), Temperature influence on rock slope movements at Checkerboard Creek, in *Landslides: Evaluation and Stabilization. Proceedings of the Ninth International Symposium on Landslides*, edited by W. Lacerda et al., pp. 1293-1298, Taylor and Francis, London.
- Wegmann, M. (1998), Frostdynamik in hochalpinen Felswänden - am Beispiel der Region Jungfrauoch-Aletsch, Ph.D. thesis, ETH, Zurich.
- Wegmann, M., and G. H. Gudmundsson (1999), Thermally induced temporal strain variations in rock walls observed at subzero temperatures, in *Advances in Cold-Region Thermal Engineering and Sciences*, edited by K. Hutter, Y. Wang and H. Beer, pp. 511-518, Springer Berlin Heidelberg, doi:10.1007/BFb0104208.
- Wegmann, M., G. H. Gudmundsson, and W. Haeberli (1998), Permafrost changes in rock walls and the retreat of alpine glaciers: a thermal modelling approach, *Permafrost and Periglacial Processes*, 9(1), 23-33, doi:10.1002/(sici)1099-1530(199801/03)9:1<23::aid-ppp274>3.0.co;2-y.
- Wirsig, C., J. Zasadni, M. Christl, N. Akçar, and S. Ivy-Ochs (2016), Dating the onset of LGM ice surface lowering in the High Alps, *Quaternary Science Reviews*, 143, 37-50, doi:http://dx.doi.org/10.1016/j.quascirev.2016.05.001.
- Zhang, T. (2005), Influence of the seasonal snow cover on the ground thermal regime: An overview, *Rev. Geophys.*, 43(4), RG4002, doi:10.1029/2004rg000157.



## 4 BEYOND DEBUTTRESSING: HYDRO-MECHANICAL ROCK SLOPE DAMAGE DURING REPEAT GLACIAL CYCLES

Lorenz M. Grämiger<sup>1</sup>, Jeffrey R. Moore<sup>1,2</sup>, Valentin S. Gischig<sup>1</sup>, Simon Loew<sup>1</sup>, Martin Funk<sup>3</sup>, Philippe Limpach<sup>4,5</sup>

<sup>1</sup> *Department of Earth Sciences, ETH Zurich, Zurich, Switzerland.*

<sup>2</sup> *Department of Geology and Geophysics, University of Utah, Salt Lake City, Utah, USA.*

<sup>3</sup> *Laboratory of Hydraulics, Hydrology and Glaciology, ETH Zurich, Zurich, Switzerland.*

<sup>4</sup> *Institute of Geodesy and Photogrammetry, ETH Zurich, Zurich, Switzerland.*

<sup>5</sup> *BSF-Swissphoto, Regensdorf-Watt, Switzerland.*

**Abstract:** Subglacial water pressures influence groundwater conditions in proximal alpine valley rock slopes, and vary with glacier advance and retreat cycles in concert with changing ice thickness. Fluctuating groundwater pressures in turn increase or reduce effective joint normal stresses, affecting the yield strength of discontinuities. Here we extend simplified assumptions of glacial debuttreassing to investigate how glacier loading cycles during the Late Pleistocene and Holocene coupled with changing groundwater pressures generate rock slope damage and prepare future slope instabilities. Using hydro-mechanical coupled numerical models closely based on the Aletsch Glacier valley in Switzerland, we simulate glacier loading cycles with included long-term and annual groundwater fluctuations. Monitoring of transient subglacial water pressures from ice boreholes at the Aletsch Glacier, as well as continuous bedrock deformation monitoring from permanent GNSS stations helps verify our model assumptions. While purely mechanical glacier loading cycles create only limited damage in our models, introducing a fluctuating groundwater table generates substantial fracturing. Superposed annual groundwater cycles increase predicted rock slope damage. The cumulative effects are capable of destabilizing the eastern valley flank of our model in toppling mode failure, similar to field observations of landslide geometry and kinematics. We find that hydro-mechanical fatigue is most effective acting in combination with low-frequency loading of the entire slope, such as during glacial cycles. Including hydro-mechanical effects driven by varying subglacial water pressures, we demonstrate that cycles of glacier advance and retreat are capable of generating substantial rock slope damage, preparing future slope instabilities.

## 4.1 Introduction

Debuitressing during glacier retreat (i.e. removal of an ice buttress) is frequently implicated as the predominant driving mechanism of paraglacial rock slope failures [e.g., *Bovis*, 1990; *Cossart et al.*, 2008; *Jaboyedoff et al.*, 2012]. However, detailed examination of the mechanics behind this process reveals that glaciers make a poor buttress for adjacent valley slopes due to the ductile behavior of ice [*McCull et al.*, 2010; *McCull and Davis*, 2013]. Furthermore, purely mechanical loading and unloading by the weight of glacier ice alone has been shown to have limited effect in creating new rock slope damage [*Grämiger et al.*, 2017a]. In most previous studies investigating the evolution of alpine slope failures, the influence of cleft and pore water pressure during glacier retreat or advance is neglected, despite a potentially strong impact on in-situ stress and strength conditions (i.e., effective stresses being total stress minus pore pressure) [*Terzaghi*, 1923; *Louis*, 1969]. Hazard assessment studies for deep repositories have in the past included hydro-mechanical (HM) feedbacks between bedrock and an advancing ice sheet [*Boulton et al.*, 2004; *Chan et al.*, 2005; *Vidstrand et al.*, 2008; *Selvadurai et al.*, 2015], but with focus on permeability changes and water incursion rather than rock mass damage.

Stress changes during glacier cycles drive fracture propagation in alpine valley rock slopes [*Grämiger et al.*, 2017a, b], therefore it is critical to explore the influence of mountain groundwater on effective stresses in rock joints (Figure 4.1). In a glaciated catchment, portions of the groundwater table may be directly linked to the subglacial hydrology and meltwater cycle, in contrast to unglaciated areas. It is frequently assumed that a thin water film at high overburden pressure is present everywhere between a temperate glacier and the underlying bedrock [*Weertman*, 1957; *Lappegard et al.*, 2006]. Subglacial pressure is the result of limited basal drainage and subject to strong seasonal variability [*Fountain and Walder*, 1998]. Generally stable, high water pressures are seasonally interrupted by changes in the drainage system. Meltwater at the bed of a glacier is drained in summer by a well-developed channel system [*Nye*, 1973; *Röthlisberger*, 1972]. Large and rapid diurnal water pressure fluctuations dropping to atmospheric pressure have been observed in the main channels, which act as low pressure drainage conduits [e.g., *Fountain*, 1994; *Sugiyama and Gudmundsson*, 2004; *Fudge et al.*, 2008]. These fluctuations occur only in summer, ending abruptly in autumn when drainage conduits close after surface melt ceases and basal water pressures return to high, general steady values close to the ice overburden pressure [*Fudge et al.*, 2005; *Lappegard et al.*, 2006]. Occasionally, water pressure can exceed the local ice overburden pressure [e.g., *Murray and Clark*, 1995]. The subglacial drainage system varies substantially over time, but also in space [*Harper et al.*, 2005; *Werder et al.*, 2013]. Diurnal pressure fluctuations are restricted to regions connected to drainage conduits. Unconnected isolated basal regions remain at nearly constant high pressure, although diurnal fluctuations can propagate laterally for tens of meters through permeable subglacial sediments [*Hubbard et al.*, 1995].

Subglacial pressure variations are recognized to drive bedrock fracture propagation at the glacier bed (i.e., quarrying) and enhance glacial erosion [*Iverson*, 1991; *Hallet*, 1996; *Cohen et al.*, 2006; *Herman et al.*, 2011; *Iverson*, 2012]. While large pressure variations can act at the glacier bed on small-scales, overall nearly constant high pressures alter stress fields on the valley-scale. The water pressure partly counteracts the weight of the glacier, and so reduces contact forces between the ice and underlying rock. Although water pressures influence coupling at ice/bed interface and therefore basal slip [e.g., *Iken and Bindshadler*, 1986], normal stresses at the glacier bed remain unaffected being close to the ice overburden pressure (force transmission between ice load and equivalent water pressure). *Boulton et al.* [2004] and *McCull et al.* [2010] have proposed that the change in effective stress due to changing ice overburden within bedrock is small, as the increase in ice load is largely compensated by the increased groundwater pressure. Studies probing subglacial till evidence a reduction in effective stress

resulting from high subglacial water pressure, and show that the yield strength of basal sediments depends strongly on effective stresses [Tulaczyk *et al.*, 2000]. Stress measurements on bedrock under glaciers reveal normal stresses commonly close to the pressure of the ice overburden [Hagen *et al.*, 1993; Cohen *et al.*, 2000; Cohen *et al.*, 2006; Lappégard *et al.*, 2006]. While differences in basal water pressure can increase rates of crack growth during quarrying of a rock step [Cohen *et al.*, 2006], the general influence of *in-situ* effective stresses in bedrock beneath a glacier on the yield strength of intact rock and rock fractures remains vague. We anticipate that changing glacier extents coupled with high subglacial pressures exert strong control on the gradient of the adjacent hillslope groundwater table, influencing effective stresses in fractures [cf. McColl *et al.*, 2010].

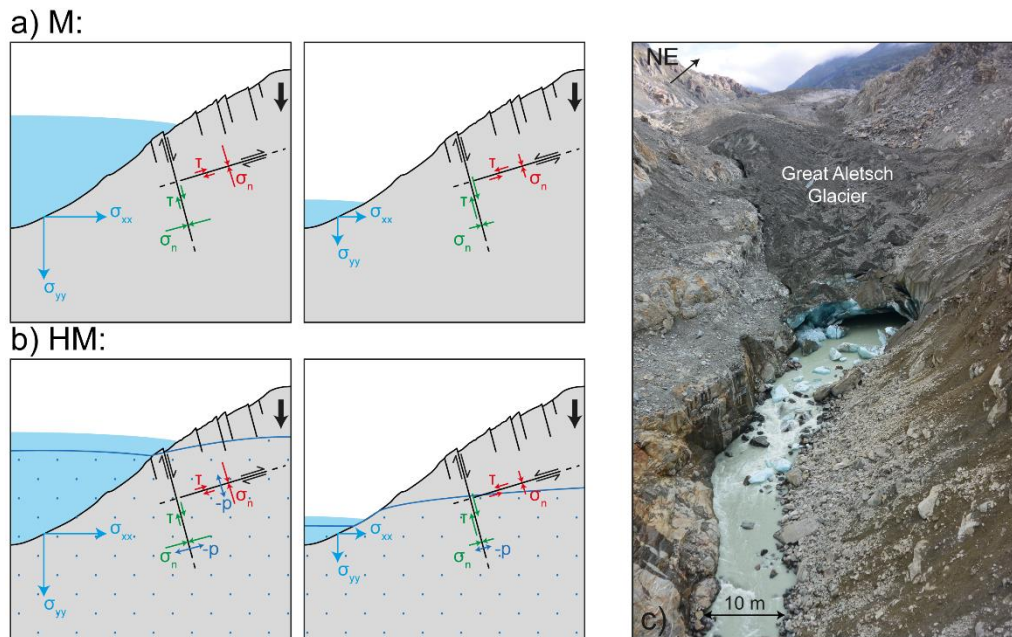


**Figure 4.1.** Concept of a paraglacial rock slope and subglacial hydrology influencing the groundwater table and effective joint stresses in adjacent slopes: a) Rock slope and joint stresses affected by purely mechanical glacial loading / unloading, b) in comparison accounting for effective stresses influenced by high subglacial water pressures. c) Subsurface discharge at the tongue of the Great Aletsch Glacier.

Accounting for the ductile behavior of ice over glacial time scales, and subglacial water pressures close to ice overburden level, glacier fluctuations are more closely comparable to lake level changes at the toe of a rock slope, and poorly conceptualized as a rigid ice buttress. Deep-seated rock slides associated with reservoir level changes have been widely recognized as a precarious hazard [Müller, 1964; Moore, 1999]. HM coupling between unstable rock slopes and changes in reservoir level are the subject of many detailed studies [e.g., Watson *et al.*, 2007; Zangerl *et al.*, 2010; Kalenchuk *et al.*, 2013; Zhang *et al.*, 2013; Loew and Strauhal, 2014; Strauhal *et al.*, 2015]. Hillslope hydrology can be strongly influenced by reservoir level fluctuations, rather than natural groundwater recharge by precipitation and snowmelt, even at substantial distances from the reservoir [Strauhal *et al.*, 2015]. Initial impoundment of the reservoir can cause initiation or reactivation of adjacent rock slope instabilities [e.g., Müller, 1964; Zangerl *et al.*, 2010; Zhang *et al.*, 2013]. In some cases, strong correlation between reservoir levels and landslide velocity have been observed. Whereas landsliding is frequently initiated during first infilling, later accelerations are often encountered at the lowest reservoir levels during rapid draw-down, a process generating a transient pressure imbalance [e.g., Zangerl *et al.*, 2010]. As changing reservoir

levels can be the dominant driving mechanism of large rock slope instabilities, we propose that the subglacial pressure field in parallel with glacier loading cycles can affect slope stability driving damage and displacement.

Groundwater in an alpine valley flank is not only controlled by the presence of glacier ice, but is also subject to seasonal fluctuations. Snowmelt and heavy rainfall contribute to surface recharge, temporarily raising the water table [Hansmann *et al.*, 2012]. Seasonal groundwater changes can be a dominant driving factor for unstable rock slides [Furuya *et al.*, 1999; Guglielmi *et al.*, 2005; Bonzanigo *et al.*, 2007; Preisig *et al.*, 2016; Loew *et al.*, 2017a]. Observations in stable alpine valley flanks have highlighted reversible, natural rock slope deformations with considerable magnitude associated with an annual rising and lowering groundwater table [Loew *et al.*, 2007; Guglielmi *et al.*, 2008; Hansmann *et al.*, 2012; Rouyet *et al.*, 2016]. Such coupled HM processes may play an important role in driving cyclic fracture propagation over longer time scales [cf., Eberhardt *et al.*, 2016; Preisig *et al.*, 2016], especially in concert with low-frequency groundwater table fluctuations, e.g. associated with changing ice elevation, that change the area of influence over time.

In this study, we explore the role of hydro-mechanical coupled stresses associated with glacial cycles in driving rock slope damage and preparing rock slope failures. We expand on the mechanical and thermo-mechanical studies of Grämiger *et al.* [2017a, b], including subglacial water pressures and seasonal groundwater fluctuations and associated effective stress changes, thereby improving the conceptual model of glacial debuitressing. Our HM numerical models are based on field measurements at our Aletsch Valley study site in Switzerland. We present new subglacial pressure measurements in ice boreholes below the Great Aletsch Glacier, as well as mapped spring-lines in the region that help approximate local groundwater conditions. We also measured seasonal rock slope deformation by continuously operating GNSS (Global Navigation Satellite Systems) stations located in the vicinity of the present-day glacier margins, data which are used to calibrate and verify our model results. Here we show how long-term and seasonal groundwater changes, acting in concert with repeat glacier cycles of glacier loading, alter joint effective stresses and induce rock slope damage, preparing paraglacial slope failures.

## 4.2 Paraglacial setting of the Aletsch region

Our study area is located in the Central European Alps in Switzerland and includes the lower valley of the Great Aletsch Glacier (Figure 4.2). Bedrock in the region is part of the Aar Massif and consists of metamorphic gneisses and granites [Steck, 2011]. Discontinuity patterns are dominated by steeply SE dipping foliation with parallel brittle-ductile faults. This rock mass structure provides the geological predisposition for several rock slope instabilities in the Aletsch Valley (Figure 4.2a), described in detail by Grämiger *et al.* [2017a]. Currently active landslides are concentrated on both valley flanks around the retreating, present-day terminus of the Great Aletsch Glacier, and have been investigated in detail [e.g., Kääh, 2002; Strozzi *et al.*, 2010; Kos *et al.*, 2016; Loew *et al.*, 2017b].

Numerous cycles of major glacial / interglacial periods throughout the Pleistocene caused glacier advance and retreat in the Aletsch region (Figure 4.2a). Valley flanks in our study area were likely ice-free during the penultimate Eemian interglacial period (~130 to ~115 ky; Dahl-Jensen *et al.*, [2013]). The subsequent Würmian glaciation lasted ~100 ky and peaked at the Last Glacial Maximum (LGM), in the Alps dated at ~28 to ~18 ky BP [Ivy-Ochs *et al.*, 2008; Ivy-Ochs, 2015], when ice covered the entire Aletsch region aside from a few nunataks. LGM glaciers retreated by 19-18 ky [Ivy-Ochs, 2015], although Lateglacial ice remained at high altitudes for ~2-3 ky [Wirsig *et al.*, 2016]. Alpine glaciers



readvanced during the Egesen stadial at 13.5 to 12.0 ky [Ivy-Ochs et al., 2009a]. In the Aletsch region, moraines of the Egesen stadial are clearly evident (Figure 4.2a) and dated by Kelly et al. [2004] and Schindelwig et al. [2012]. After Egesen retreat, a final glacier readvance around 10.5 ky is observed at a few locations in the Alps, remaining smaller than Egesen extents [Schindelwig et al., 2012; Schimmelpfennig et al., 2014].

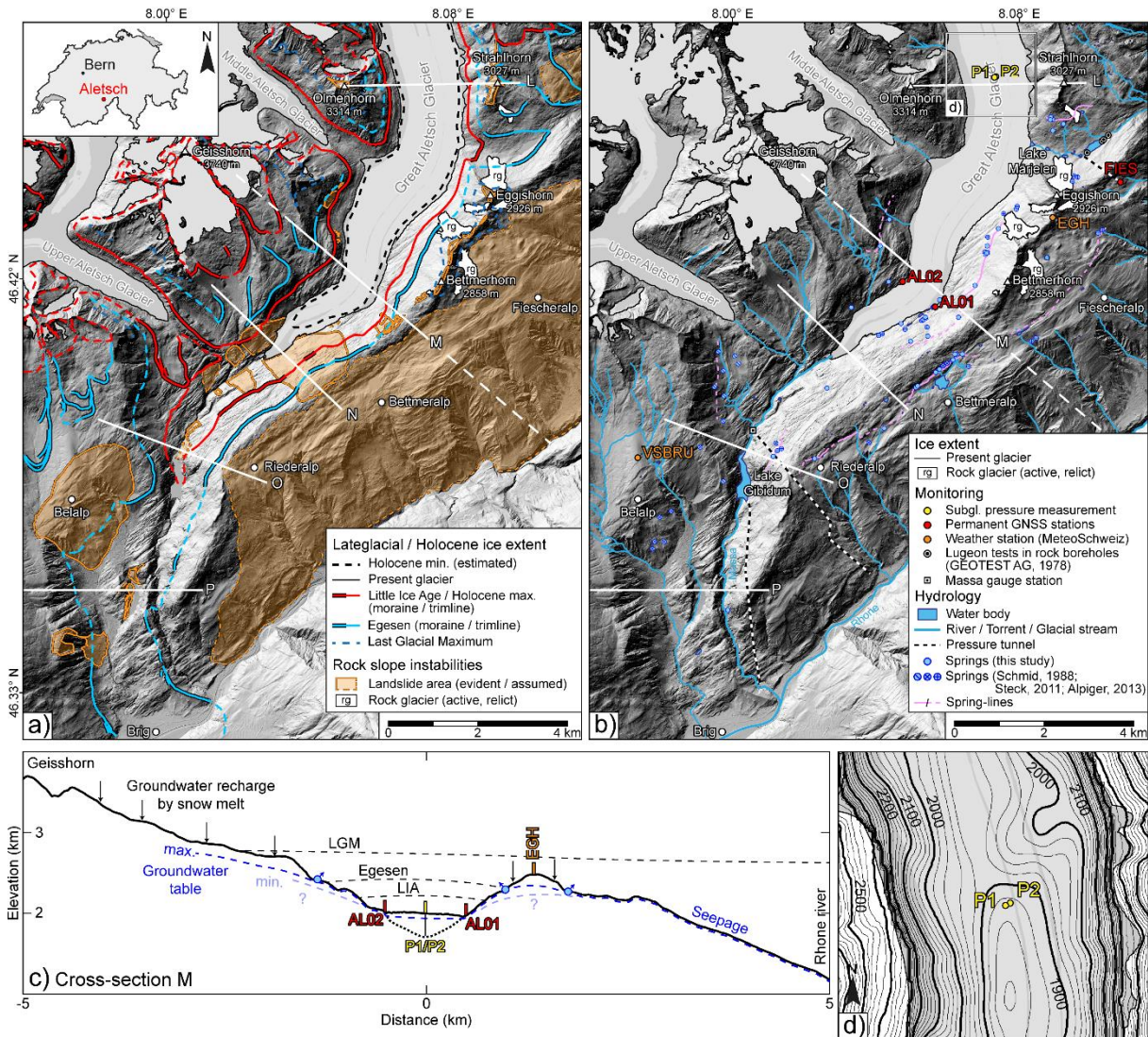


**Figure 4.2.** Data collection in the Aletsch region: a) Synopsis of Lateglacial and Holocene glacier extents combined with spatial landslide extents (modified from Grämiger et al. [2017a]). Hillshade derived from DTM (swissALTI3D by Swisstopo). b) Present glacier situation with position of GNSS stations, nearby weather stations (MeteoSchweiz), ice boreholes for subglacial pressure measurements, Massa river gauge station (BAFU, Switzerland), and location of Lugeon tests in rock boreholes [GEOTEST AG, 1978]. Synopsis of hydrological situation including mapped springs [this study; Schmid, 1988; Steck, 2011; Alpiger, 2013] and approximated maximum spring lines. c) Cross-section M with mapped glacier extents, location of GNSS stations for slope deformation monitoring, nearby weather station, ice boreholes with subglacial pressure measurements, and mapped maximum spring lines, all projected on to the profile. d) Contour lines (20 m interval) of topography (swissALTI3D by Swisstopo) and subglacial bed from ice penetrating radar data [Farinotti et al., 2009] with location of ice boreholes (P1, P2).

During the Holocene, Alpine glaciers receded to extents as small as or smaller than today, and remained as such until the late Holocene [Ivy-Ochs *et al.*, 2009a; Solomina *et al.*, 2015]. Records of readvances during the early and middle-Holocene are scarce [e.g., 8.2 ky event; Nicolussi and Schlüchter, 2012]. Glacier fluctuations during the late Holocene are recorded in detail at the Aletsch Glacier, showing several readvances culminating in the Little Ice Age (LIA) peak extent around 1850 [Holzhauser *et al.*, 2005]. Multiple readvances reaching the Holocene maximum extents during the late Holocene have been observed at other glaciers in the Alps, resulting in the construction of composite moraines [Röthlisberger and Schneebeli, 1979; Schimmelpfennig *et al.*, 2012; Schimmelpfennig *et al.*, 2014]. Moraines and trimlines of the LIA are clearly visible in the Aletsch region (Figure 4.2a). In summary, while the lower Aletsch Valley experienced only a single glacier readvance after LGM deglaciation during the Egesen stadial, rock slopes at higher altitude encountered several minor Holocene cycles after Lateglacial ice retreat.

## 4.3 Hydro-mechanical data

### 4.3.1 Subglacial water pressure and temperature

Local details of the subglacial hydraulic boundary conditions are important for our HM numerical simulations. Investigations of subglacial hydrology at the Great Aletsch Glacier are rare, as compared to the other large glacier systems in the Swiss Alps [e.g., Iken *et al.*, 1996; Iken, 1997; Sugiyama *et al.*, 2008; Walter *et al.*, 2008]. Past monitoring of seasonal water table fluctuations in the firn area [Lang *et al.*, 1976; Schommer, 1976] and tracer experiments investigating subglacial flow [Hock *et al.*, 1999] have been performed at the Great Aletsch Glacier. Ground penetrating radar measurements by Farinotti *et al.* [2009] further resulted in a detailed map of present-day glacier thickness.

We complement these studies with new subglacial water pressure measurements from the Great Aletsch Glacier. Two ice boreholes (P1 and P2) were drilled to the glacier bed in July 2013 using a hot water drilling system (Figure 4.2b). The location was chosen because of accessibility and availability of meltwater on the glacier surface, which is necessary for drilling [cf. Iken *et al.*, 1976]. Our approach was to drill at the deepest point of the glacier cross-section (Figure 4.2d), which was previously estimated from radar measurements [Farinotti *et al.*, 2009], attempting to measure diurnal and annual subglacial pressure fluctuations in the main subglacial drainage channel, as well as the lateral propagation of the pressure signal in less connected areas of the bed. Two out of three planned boreholes were successfully achieved drilling through ~500 m of ice and reaching the glacier bed. The main subglacial drainage channel was not encountered by either borehole. Both holes were equipped with pressure sensors attached to a 500 m long Kevlar encased cable. We used a precise piezo-resistive pressure sensor (Serie 36 X W by KELLER AG, measurement precision of 50 mbar) together with a data logger with remote download capability (GSM-2 by KELLER AG). Water pressure in the boreholes prevented them from closing. P1 and P2 were separated by a distance of 32 m and had ice surface altitudes of 2358 m and 2355 m, respectively. The drilling depth was ~500 m, while ice thickness estimations from radar measurements were 473 m at P1 and 467 m at P2 [Farinotti *et al.*, 2009]. Sensors in P1 and P2 were deployed at a depth below the surface of 465 and 453 m, respectively. Pressure data combined with simultaneous light plummet measurements allowed a correction of the sensor depth from the measured cable length caused by minor borehole inclination. Water pressure measurements were corrected for air pressure, which was continuously measured at the data logger on the ice surface. Pressure sensors installed in these boreholes measured diurnal subglacial water pressure fluctuations

over one year (at a sampling interval of 1 minute) until cable breach caused by glacier flow terminated the monitoring.

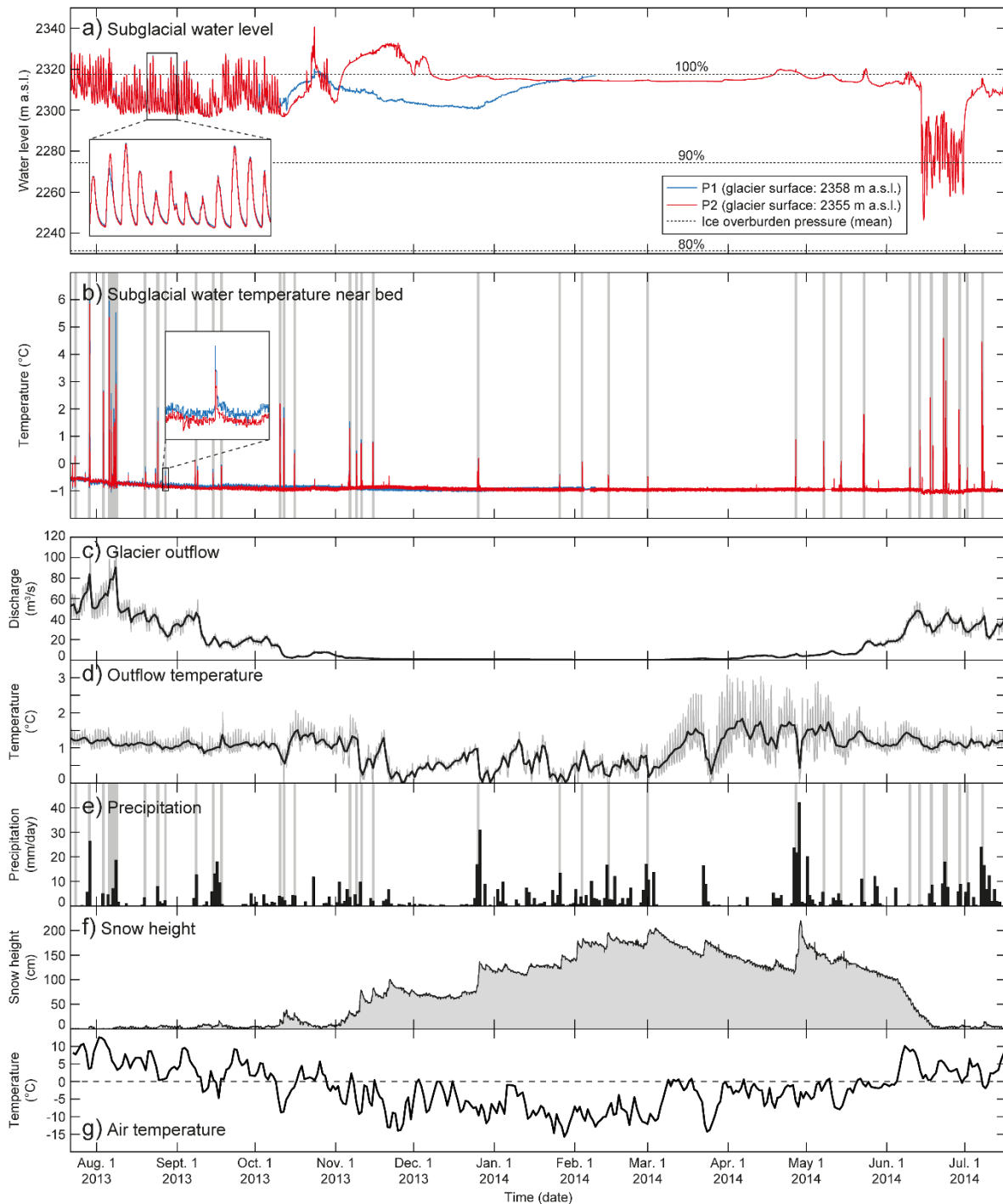


**Figure 4.3.** Seasonal subglacial water pressure measurements at P1 and P2 (see Figure 4.2b): a) Subglacial water pressure fluctuations presented as calculated water level in comparison with mean ice overburden pressure. b) Subglacial water temperature measured at pressure sensor near glacier bed, highlighting short-term temperature peaks in gray. c) Discharge (hourly and daily mean) at Massa gauge station (1446 m) representing combined outflow of Upper and Great Aletsch Glacier (see Figure 4.2b) (BAFU, Switzerland). d) Outflow water temperature (hourly and daily mean) at Massa gauge station (BAFU, Switzerland). e) Daily sum of precipitation at nearby VSBRU (2300 m) weather station (see Figure 4.2b) (MeteoSchweiz) together with highlighted subglacial temperature peaks in gray. f) Current total snow height of nearby EGH (2893 m) weather station (see Figure 4.2b) (MeteoSchweiz). g) Air temperature (daily mean) of EGH weather station (MeteoSchweiz).

Figure 4.3 presents subglacial water pressure data compared with outflow measurements from near the glacier tongue and data from nearby weather stations. Interestingly, although we did not drill directly into the main drainage channel, we measured a diurnal water pressure fluctuations in both boreholes, but with lower amplitude than expected in the main subglacial channel. Other studies have shown daily pressure fluctuations between near atmospheric pressure and ice overburden pressure within the drainage channel [e.g., *Fudge et al.*, 2008]. The calculated water level from surface elevation and corrected sensor depth is nearly identical in both boreholes (Figure 4.3a), therefore they are likely connected to the same hydraulic system. The diurnal fluctuation varies at the beginning of our monitoring between 5-30 m of water column (0.05-0.30 MPa). The subglacial water pressure is generally close to the ice overburden pressure. In mid-October, diurnal pressure fluctuations disappear abruptly and basal water pressures return to a high, generally steady value close to the overburden. This transition indicates closure of the main subglacial conduit system [cf., *Fudge et al.*, 2005]. Water pressure remains near the ice overburden level during winter, until the following June when the subglacial drainage system develops again, and water pressures drop to ~85% of ice overburden. Large, diurnal pressure fluctuations are observed of up to 50 m of water column (0.5 MPa). We compare the pressure record in Figure 4.3a to discharge measurements at the Massa river gauging station (BAFU, Switzerland) in Figure 4.3c, which captures the glacial outflow of the Upper and Great Aletsch Glacier (see Figure 4.2b). Subglacial pressure fluctuations are restricted to summer and autumn (Figure 4.3a) when the subglacial drainage system is well developed and when high river discharge is observed (Figure 4.3c). The subglacial drainage system is driven by surface melt and therefore strongly depends on air temperature (Figure 4.3f); pressure fluctuations cease after air temperatures drop below freezing.

Figure 4.4 presents a more detailed analysis of our subglacial water pressure and temperature data. The pressure signal of P1 lags slightly behind P2 (Figure 4.4b). A phase plot of the water level in P1 versus P2 emphasizes this observation (Figure 4.4c). Analyzing the phase shift and amplitude of the diurnal pressure signals shows in addition to a lag at P1, the measured amplitude also diminishes in P1 as compared to P2. These results indicate that the main subglacial drainage channel with higher pressure fluctuations is located east of P2 (see Figure 4.2d): the pressure signal is diminished and delayed with distance to the main channel [cf., *Hubbard et al.*, 1995].

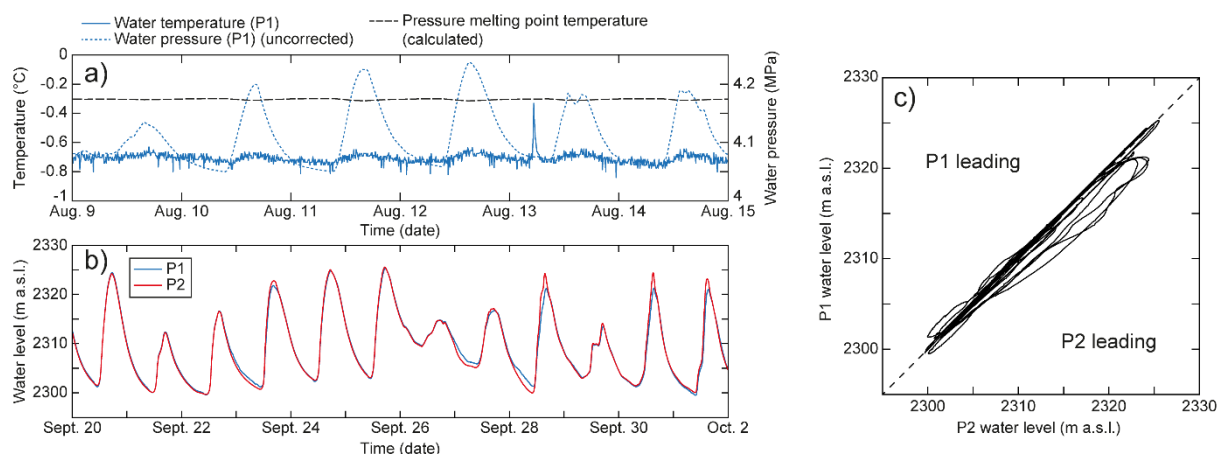


**Figure 4.4.** Detailed analysis of seasonal subglacial water pressure measurements at P1 and P2: a) Pressure and water temperature recorded between Aug. 9 and Aug. 15, 2013 at P1 in comparison with calculated PMP temperature. Water pressure recorded at sensor depth is here uncorrected for air pressure. b) Water level records at P1 and P2 from Sept. 20 to Oct. 2, 2013 against time. c) Phase plot of water level records from Sept. 20 to Oct. 2, 2013 of P1 against P2.

Subglacial water temperature was measured at the pressure sensors for temperature-corrections near the glacier bed. Absolute temperatures may deviate [cf. *Dow et al.*, 2011], but measured temperature differences are reliable. The water temperature remains constant close to the pressure melting point (PMP), interrupted by short temperature excursions of up to 6 °C (Figure 4.3b). Analysis of a single temperature peak in Figure 4.3b shows these consist of a steep rise followed by a near exponential decay. These temperature anomalies are strongly correlated with heavy rainfall events (Figure 4.3d). Relatively warm meteoric water seems to affect the subglacial hydrology, leading to a temperature rise near the bed. Whether this temperature effect is only local in the boreholes or affects larger areas of the bed is uncertain, although fast temperature reactions without significant water level changes suggest good connectivity to the subglacial drainage system. A detailed view of measured water temperature is presented in Figure 4.4a. We calculated the PMP based on the absolute pressure measurement at the logger, where the water temperature is measured, using the Clausius-Clapyron equation ( $T_{PMP} = T_{tp} - \gamma_p(p - p_{tp})$  where  $T_{tp} = 273.16$  K,  $\gamma_p = 7.42 \times 10^{-8}$  K Pa<sup>-1</sup>, and  $p_{tp} = 611.73$  Pa; e.g. *Harrison* [1975]). This results in a PMP temperature fluctuating around -0.3 °C at our drilling site (Figure 4.4a). Assuming the water in the borehole is thermally equilibrated with the surrounding ice and therefore at the PMP [e.g., *Röthlisberger*, 1972; *Iken and Bindshadler*, 1986], our absolute temperature measurement seems to have a systematic error of about -0.4 °C. However, the more reliable measurement of temperature differences show diurnal temperature variations (~0.1 °C) in-phase with pressure measurements (Figure 4.4a). Temperature changes due to a changing PMP would be out of phase with respect to changing water pressure, and observed magnitudes are too large for pressure-dependent temperature changes. Significant diurnal variations above the PMP were also observed by *Dow et al.* [2011], arguing for a basal source. Since our temperature fluctuations are in-phase with pressure variations, they may rather origin from englacial flow.

### 4.3.2 Slope hydrology

Seasonal changes in surface recharge can raise and lower a phreatic groundwater table in mountain slopes over the year. Information about local groundwater conditions is required for our hydraulic models. We collected available data on the locations of springs (i.e., walled-in, free-flowing), still-water bodies, and water channels (e.g., creeks, rivers and glacial streams) in the Aletsch region [*Schmid*, 1988; *Steck*, 2011; *Alpiger*, 2013; *Schnider*, 2013]. We complemented these data with additional spring mapping, especially in remote areas, focusing on springs with the highest altitude (Figure 4.2b). The presence of water is often bound to melting cirque or rock glaciers and our spring data collection in the region is far from complete, however we gathered sufficient information to approximate the location of the mountain water table. We observe still-water bodies and the origin of a few creeks at an altitude of ~2200 m around Fiescheralp, and several springs originate at similar elevations around Bettmeralp. The continuation of this spring line towards the SW drops by around 100 m at Riederalp, which likely is the effect of substantial regional drainage by the Riederhorn pressure tunnel (Figure 4.2b) on the natural groundwater table [*Furrer*, 1948]. Springs on the other side of the ridge (facing towards the Great Aletsch Glacier) are less frequent. Nevertheless, the upper limit of observed springs is between 2200 to 2300 m. Further SW towards Riederalp, the only springs on the NW facing flank are found above the Gibidum reservoir at ~1810 m, named the Aletschwald springs with large discharge rates. The SE facing side of the Aletsch Valley is dominated by glacier streams from the current cirque glaciers. Rare observations of springs that do not directly originate from melting ice were made at ~2400 m. The highest elevation springs are observed in summer after snowmelt (i.e., July, August). Flow from springs on the SE side of the ridge around Bettmeralp ceases completely or decreases strongly in late fall, similar to springs on

the NW side. Past discharge measurements at springs above the lake at Bettmeralp (Figure 4.2b) show the highest discharge in summer with decreasing discharge in winter [Schmid, 1989]. The elevation of the highest springs marks the position of the groundwater table at the intersection with the ground surface (i.e., the seepage face). Excluding water originating from melting ice (i.e., glaciers and rock glaciers), we estimated the elevations of the highest springs in the Aletsch Valley (Figure 4.2b) and projected an approximate groundwater level on to our cross-section M (Figure 4.2c).

### 4.3.3 Bedrock deformations

Natural reversible slope deformation of considerable magnitude has been recognized in alpine valleys and attributed to seasonal groundwater pressure changes [Loew *et al.*, 2007; Hansmann *et al.*, 2012; Rouyet *et al.*, 2016]. Furthermore, significant uplift rates (millimeters to sub-millimeters per year) resulting from elastic rebound of bedrock on the margins of actively retreating ice have been revealed from monitoring data [Khan *et al.*, 2010; Bevis *et al.*, 2012] as well as modeling studies [Barletta *et al.*, 2006; Memin *et al.*, 2009]. In attempting to quantify seasonal bedrock deformations associated with groundwater changes in proximity to a glacier, as well as long-term trends associated with ongoing ice retreat, we installed two single-frequency GNSS stations on bedrock on opposite margins of the retreating Great Aletsch Glacier (stations AL01 at 1966 m and AL02 at 1963 m; Figure 4.2b). The stations have been operating continuously since October 2013. Their positions are computed with respect to a nearby geodetic dual-frequency reference station (FIES at 2361 m; Figure 4.2b). Details of the station equipment and data processing are described by Limpach and Geiger [2016]. We monitored almost three years of coupled HM rock slope deformations associated with annual cycles of hillslope groundwater changes. These data help calibrate and verify our numerical models.

Absolute displacement measured at each GNSS station is shown in Figure 4.5a. Compared with local snow and precipitation data (Figure 4.5b), we recognize that the eastern (AL01) and western (AL02) slopes move inward towards the valley during snowmelt or periods of heavy precipitation. The calculated relative change in horizontal distance (Figure 4.5c) shows a valley closing of ~4 cm during snowmelt and a gradual valley opening of similar magnitude over the subsequent period until the next snowmelt. A long-term trend of ~2 cm distance and ~1 cm height change is observed over our three year monitoring period, where the western slope (AL02) is moving upward and inward towards the valley. The magnitude and timing of seasonal bedrock displacements match reversible slope deformations observed in other alpine valleys, which are thought to be driven by 150-200 m changes in groundwater table elevations within the adjacent slopes [Loew *et al.*, 2007; Hansmann *et al.*, 2012; Rouyet *et al.*, 2016]. The relatively short monitoring period of less than three years is insufficient to conclusively detect long-term trends. Field investigations did not reveal any unstable rock slopes around the GNSS stations, and therefore the observed trends may be related to elastic rebound caused by glacier retreat or long-term groundwater changes. However, it is more likely that due to larger snow accumulations, the current groundwater table is generally higher than during the beginning of monitoring period and had not depleted to its long-term equilibrium before the onset of the following snowmelt, resulting in a temporary trend of valley closing. Our bedrock displacement data reveal strong seasonal HM deformation cycles, which are mainly driven by groundwater recharge during snowmelt. Surface recharge raises the hillslope groundwater table, reducing effective normal stress in discontinuities and increasing their aperture [Loew *et al.*, 2007; Zangerl *et al.*, 2003; 2008a, b; Hansmann *et al.*, 2012]. An increased groundwater table thus leads to rock mass expansion, while groundwater lowering during summer / fall results in settlement and lateral hillslope contraction.

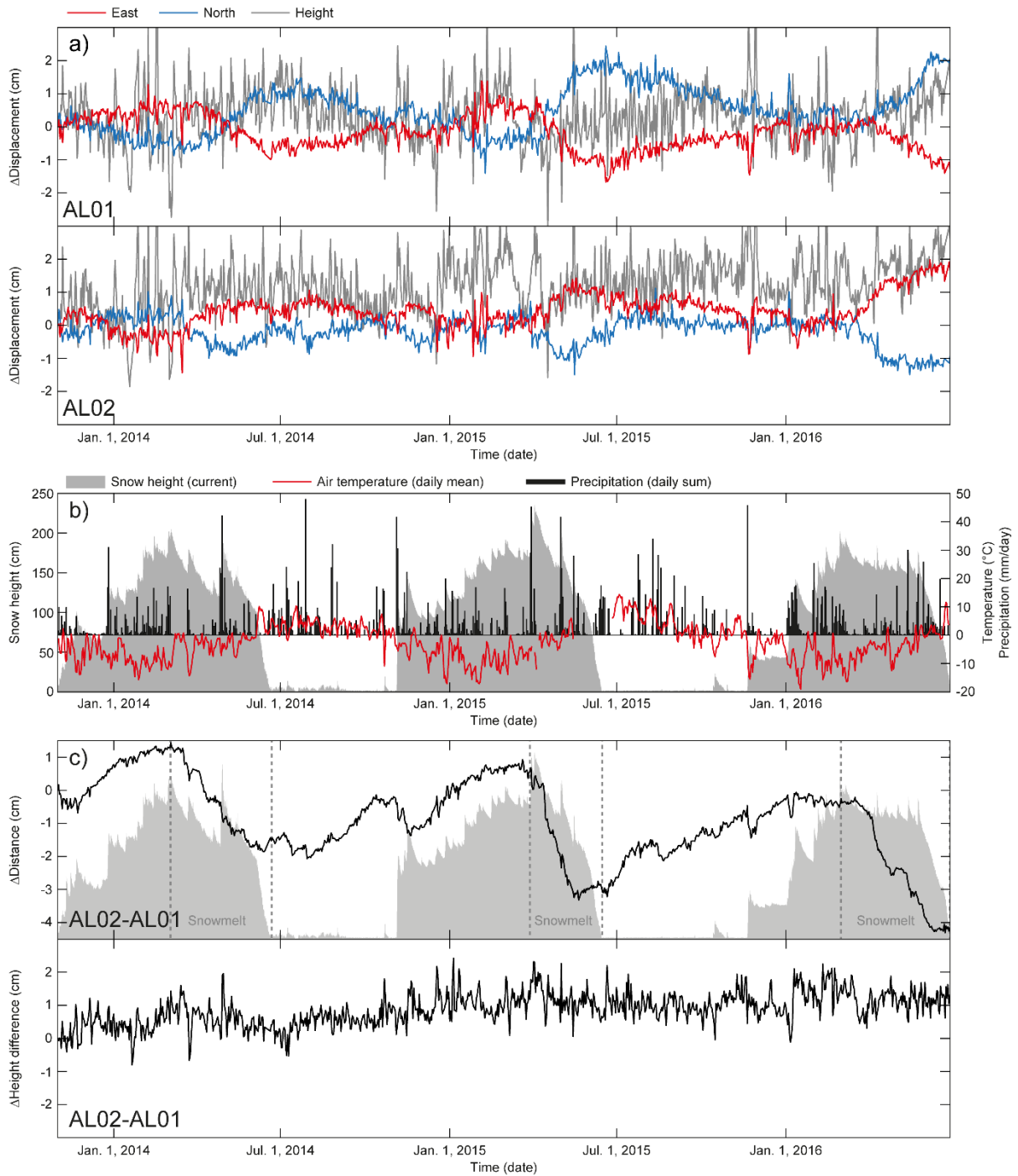


**Figure 4.5.** Seasonal bedrock deformation monitoring with GNSS: a) Absolute displacement (daily solution of east, north, and height component) for GNSS station AL01 at 1966 m and AL02 at 1963 m on either side of the Great Aletsch Glacier (see Figure 4.2b). b) Current total snow height and air temperature (daily mean) at EGH weather station and daily sum of precipitation at VSBRU station (see location in Figure 4.2b) (MeteoSchweiz). c) Relative change (AL02 minus AL01) of distance and height superimposed with snow height and marked snowmelt period.

## 4.4 Numerical study of HM rock slope damage and displacement

### 4.4.1 Model approach and inputs

We expand the numerical investigations of glacier loading cycles from *Grämiger et al.* [2017a] by including HM effects of a phreatic mountain groundwater table. The HM behavior of a discontinuous rock mass is modeled using the 2D distinct-element code UDEC [Cundall and Hart, 1992; Itasca, 2014]. Initialization, model geometry, and boundary conditions are presented in Figure 4.6. The model cross-section represents profile M (see Figure 4.2) based on combined data from a DTM (swissALTI3D by Swisstopo) and ice penetrating radar measurements [Farinotti et al., 2009]. The Aletsch Valley (i.e., area of interest) is embedded into a larger model of the Rhone Valley (Figure 4.6a). The discontinuous rock mass is simulated by three elements: 1. intact rock, 2. discontinuities (joints), and 3. brittle-ductile fault zones (Figure 4.6c). Intact rock is represented by blocks dissected by randomly oriented discontinuities (i.e., Voronoi polygons; Lorig and Cundall [1989]) allowing for the formation of failure pathways not predefined by any joint set. Rock mass strength parameters and properties of rock discontinuities (e.g., orientation, spacing, and persistence) are based on field assessment [Grämiger et al., 2017a]. Blocks intersected by discontinuities and bounded by contacts are assigned elastic properties (Table 4.1). Discontinuities (i.e., joints, faults, Voronoi contacts) mimic fracture compliance and allow for tensile opening or shear slip by the assigned Mohr-Coulomb constitutive law including slip-weakening of friction, cohesion, and tensile strength (Table 4.2). Joint water pressure resulting from a separate hydraulic model (created in COMSOL Multiphysics) can be assigned to the modeled discontinuities, reducing effective joint normal stresses.

Our goal was to start the simulations with similar initial damage conditions as in our preceding companion studies [Grämiger et al., 2017a, b]. Assuming the same effective rock strength properties, but accounting for effective joint stresses would, however, result in a larger initial damage. Therefore, it was necessary to increase the peak strength properties for discontinuities accordingly. Jennings' approach [Jennings, 1970] was used to determine the peak composite Mohr-Coulomb strength properties for discontinuities. We adjusted assumptions in *Grämiger et al.* [2017a]; we assumed F1 contains 15% (instead of 10%) rock bridges, F3 25% (instead of 20%) rock bridges, and intact rock represented by Voronoi contacts contain 100% rock bridges for HM models. The calculated rock strength properties listed in Table 4.2 resulted in an initial damage field similar to the studies by *Grämiger et al.* [2017a, b] including a similar ratio between shear and tensile failure.

Fluid flow in UDEC is limited to the modeled discontinuities, treating blocks as impermeable, and therefore not suited for our full model (Figure 4.6a). We therefore calculated transient pressure fields using the finite-element code COMSOL Multiphysics, implementing infiltration and seepage face boundary conditions as described by *Chui and Freyberg* [2007]. Hydraulic pressures were calculated for each mechanical step ( $\Delta t = 0.02$  y) and interpolated pressure values at modeled discontinuities provided as input data for UDEC. The UDEC model was run to mechanical equilibrium (quasi-steady-state) including effective stresses and resulting hydraulic coupling. In this semi-coupled approach, hydraulic pressures induce joint opening or closure and alter effective joint stresses, but the mechanical response has no feedback on hydraulic properties or joint pressure. Pore pressure changes are not assigned to blocks between discontinuities. Therefore the poroelastic effect of intact rock does not contribute to the modeled HM deformations.



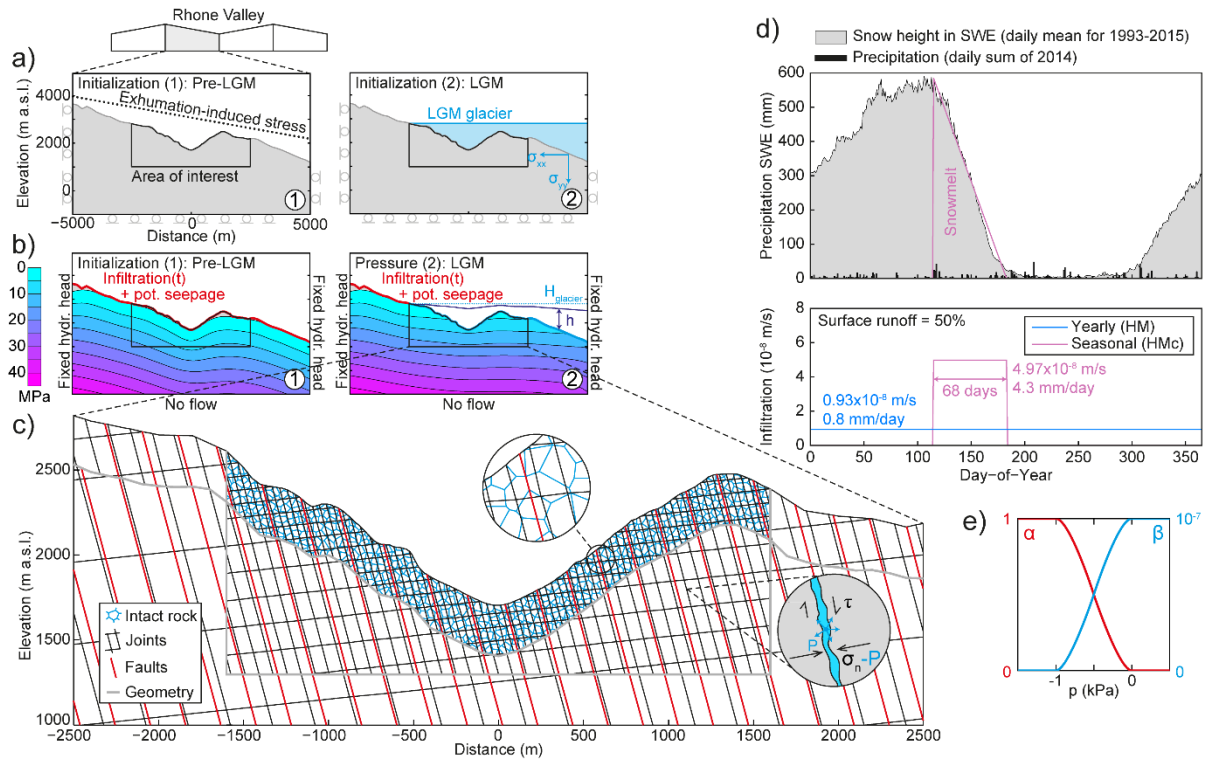


**Figure 4.6.** Model approach and initialization procedure: a) Large-scale model with boundary conditions and two-stage initialization (Pre-LGM/LGM) in UDEC. b) Large-scale model pressure fields with boundary conditions during initialization in COMSOL. c) Model geometry (cross-section M) of area of interest in UDEC, embedded in large-scale model, containing three rock mass elements: intact rock (Voronoi contacts), discontinuities (joints), and fault zones. d) Daily means of snow height record converted into snow water equivalent [Jonas et al., 2009] from 1993 to 2015 of EGH weather station with marked snowmelt period and daily sum of precipitation at station VSBRU for 2014 (see location in Figure 4.2b) (MeteoSchweiz). Derived transient surface infiltration rates from SWE for yearly and seasonal models. e) Pressure-dependent multiplier functions ( $\alpha$  and  $\beta$ ) smoothing boundary condition changes, modified from Chui and Freyberg [2007].

We apply Darcy's Law for hydraulic calculations with assigned hydraulic properties \ listed in Table 4.1. The density of water is  $1000 \text{ kg m}^{-3}$  with a dynamic viscosity of  $0.001 \text{ Pa s}$  (value at  $20 \text{ }^\circ\text{C}$ ). The porosity of the rock matrix is assumed to be  $1\% = 0.01$  [Evans et al., 2003 and references therein]. We implemented a specific storage coefficient of  $1 \times 10^{-6} \text{ m}^{-1}$  at great depth and  $1 \times 10^{-5} \text{ m}^{-1}$  near the surface, as used in past studies in intact low-porosity crystalline rock [Evans et al., 2003]. Masset and Loew [2010] report a range of hydraulic conductivity values for gneisses between  $1 \times 10^{-11}$  to  $1 \times 10^{-4} \text{ m s}^{-1}$ . Conductivity weakly decreases with depth for gneissic rock masses in the Southern Altkristallin of the Aar massif [Masset and Loew, 2010; Welch and Allen, 2014]: At shallow depths (200-400 m) hydraulic conductivity is enhanced due to stress release and slope deformations resulting in a more permeable zone, whereas conductivity decreases at larger depth [Masset and Loew, 2010]. Furthermore, local pressure tests (i.e., Lugeon tests) in shallow boreholes in gneiss near Lake Mürjelen (see Figure 4.2b) resulted in conductivity values of  $0.5 \times 10^{-6}$  to  $5 \times 10^{-6} \text{ m s}^{-1}$  [GEOTEST AG, 1978]. Therefore, our model contains a two-layered hydraulic conductivity. The strong nearly vertical foliation is represented by an anisotropic hydraulic conductivity. The hydraulic properties listed in Table 4.1 ( $K_x = 5 \times 10^{-8} / K_y = 2 \times 10^{-7}$  in the upper 300 m below ground surface, and  $K_x = 1 \times 10^{-10} / K_y = 5 \times 10^{-10}$  below 300 m depth) resulted in groundwater conditions matching the observed springs at Aletsch (Figure 4.2b, c).

**Table 4.1.** Mechanical and hydraulic properties of the rock mass implemented in UDEC and COMSOL.

<b>Mechanical properties (UDEC)</b>			
Density of rock $\rho_{rock}$	(kg m <sup>-3</sup> )	2700	
Poisson's ratio	()	0.2	Grämiger et al. [2017a]
Young's modulus	(Gpa)	30	Grämiger et al. [2017a]
<b>Hydraulic properties (COMSOL)</b>			
Porosity $\epsilon$	()	0.01	Evans et al. [2003]
Specific storage $S_S$ (0 – 300 m depth)	m <sup>-1</sup>	$1 \times 10^{-5}$	Evans et al. [2003]
Specific storage $S_S$ (below 300 m depth)	m <sup>-1</sup>	$1 \times 10^{-6}$	Evans et al. [2003]
Hydraulic conductivity K (0 – 300 m depth)	(m s <sup>-1</sup> )	$K_x = 5 \times 10^{-8} / K_y = 2 \times 10^{-7}$	
Hydraulic conductivity K (below 300 m depth)	(m s <sup>-1</sup> )	$K_x = 1 \times 10^{-10} / K_y = 5 \times 10^{-10}$	

**Table 4.2.** Discontinuity properties for the Mohr-Coulomb constitutive law including slip-weakening implemented in UDEC [Grämiger et al., 2017a].

Discontinuity parameters	Unit	Intact rock (Voronoi)	F1 foliation	F3	F4 faults
Peak friction angle $\phi$	(°)	56	35.5	38.8	27
Peak cohesion c	(MPa)	17	2.6	4.3	0.03
Peak tensile strength t	(MPa)	4	0.6	1.0	0
Residual friction angle $\phi_R$	(°)	27	27	27	27
Residual cohesion $c_R$	(MPa)	0.03	0.03	0.03	0.03
Residual tensile strength $t_R$	(MPa)	0	0	0	0
Dilation angle	(°)	5	5	5	5
Dip angle	(°)	-	75	6	75
Normal stiffness	(GPa m <sup>-1</sup> )	20	1	1	0.1
Shear stiffness	(GPa m <sup>-1</sup> )	10	0.5	0.5	0.05

Hydraulic boundary conditions in COMSOL are shown in Figure 4.6b. No-flow boundaries are assigned at the bottom and fixed hydraulic head at the sides. The water table is held 300 m below surface on the left side and at the surface (1184 m) on the right side defined by the Rhone River. Conditional boundary conditions are implemented at the ground surface, tied to the fluctuating glacier elevation throughout the transient model and depending on resulting pressure. We argue for high subglacial water pressure near the ice overburden pressure throughout the entire cross-section beneath the ice, based on our field observations (Figure 4.3) as well as past studies [e.g., *Weertman, 1957; Hubbard et al., 1995; Lappegard et al., 2006*]. Furthermore, we assume that mountain groundwater recharge is strongly controlled by surface infiltration fed by seasonal snowmelt. Monitored annual bedrock deformation (Figure 4.5) and spring mapping support this assumption, similarly made in other studies [e.g., *Hansmann et al., 2012; Strauhal et al., 2015; Preisig et al., 2016*]. Therefore below the glacier, the hydraulic head ( $H$ ) is held at 90% of glacial overburden pressure, while above the ice transient infiltration ( $\phi_{flux}$ ) with potential seepage face are applied depending on resulting pressure at the model boundary:

$$\text{For } z \leq \text{glacier elevation}(t): \quad H_{glacier} = z + 0.9h_{glacier}(\rho_{ice}/\rho_{water}) \quad (4.1)$$

$$\text{For } z > \text{glacier elevation}(t): \quad \text{if } p < 0; \phi_{flux} \text{ (surface infiltration)} \quad (4.2)$$

$$\text{if } p \geq 0; H = z \text{ or } p = 0 \text{ (seepage face)} \quad (4.3)$$

where  $z$  is the altitude and  $h_{glacier}$  is the ice thickness at this position. We implemented these equations using the generic pervious layer boundary conditions ( $\phi_{flux} = -np_u = \rho R_b(H_b - H)$ ; i.e., describing a mass flux through a semi-pervious layer connected to an external fluid source at hydraulic head), modified following the approach by *Chui and Freyberg [2007]*. Here  $R_b$  is conductance ( $s^{-1}$ ),  $H_b$  the external and  $H$  the prevailing hydraulic head at the boundary condition. The modified surface boundary condition including surface infiltration is:

$$\phi_{flux} = \rho_{water}(\beta(H_b - H) + \alpha(f_{infiltration})) \quad (4.4)$$

where for  $z \leq \text{glacier elevation}$ ;  $H_b = H_{glacier}$  (Equation 4.1) and for  $z > \text{glacier elevation}$ ;  $H_b = z$  (Equation 4.3).  $\alpha$  and  $\beta$  are multiplier smoothening boundary condition switches over a small range of pressure (1 kPa) (Figure 4.6e), modified from *Chui and Freyberg [2007]*. Equation 4.4 will be altered in the following way:

$$\text{For } p < 0 \text{ with } \alpha = 1, \beta = 0: \quad \phi_{flux} = \rho_{water}(f_{infiltration}) \quad (4.5)$$

resulting in surface infiltration boundary conditions.

$$\text{For } p \geq 0 \text{ with } \alpha = 0, \beta = 1 \times 10^{-7}: \quad \phi_{flux} = \rho_{water}(H_b - H) \times 10^{-7} \quad (4.6)$$

the resulting flux is defined by the difference between external and prevailing hydraulic head, and the conductance factor ( $\beta$ ). This head-dependent flux results in a hydraulic head close to the specified external hydraulic head ( $H_b$ ), which is defined as  $H_b = z$  above the ice (Equation 4.3), and  $H_b = H_{glacier}$  below the ice (Equation 4.1). The approximation to an actual fixed hydraulic head boundary condition is improved by setting  $\beta$  as large as possible, but convergence limits this value [cf. *Chui and Freyberg, 2007*].

We derived our transient surface infiltration ( $f_{infiltration}$ ) boundary conditions from daily means of long-term snow height records at a local weather station (Figure 4.6d). Snow height (SH) measurements were converted into snow water equivalent as:  $SWE = (60.1SH^{0.89} + 237)SH$  with  $SWE$  in  $kg\ m^{-2}$ ; *Jonas et al. [2009]*. Since heavy rainfall has less influence on bedrock deformation (Figure 4.5), we neglected groundwater recharge by rainfall. We find that 585 mm SWE (i.e., 174 cm snow) decreases linearly during snowmelt over 68 days, resulting in an assumed surface runoff of 50% and a surface infiltration rate of 4.3 mm per day ( $4.97 \times 10^{-8}\ m\ s^{-1}$ ) (Figure 4.6d), matching assumptions in other studies [e.g.,

Loew and Strauhal, 2014; Strauhal et al., 2015]. Distributing this infiltration spike in early summer over an entire year leads to a rate of 0.8 mm/day ( $0.93 \times 10^{-8} \text{ m s}^{-1}$  or  $292 \text{ mm y}^{-1}$ ) in agreement with assumptions of local groundwater studies [Schmid, 1989; Ofterdinger et al., 2014]. We apply a constant infiltration rate of  $0.93 \times 10^{-8} \text{ m s}^{-1}$  for our models without annual cycles (HM) and a time-dependent infiltration rate with a maximum of  $4.97 \times 10^{-8} \text{ m s}^{-1}$  during snowmelt to induced annual groundwater cycles (HM<sub>c</sub>). Calculated present-day groundwater fluctuations (of ~50 to 100 m) results in a maximum groundwater level (Figure 4.7a) that reasonably matches field observations at Aletsch (see Figure 4.2b,c).

Roller boundaries restrict the bottom and sides of our large-scale model (Figure 4.6a). Glacier loading is implemented as a hydrostatic stress boundary condition ( $\rho_{\text{ice}} = 917 \text{ kg m}^{-3}$ ), which appropriately models the ductile behavior of ice and its limited buttressing effect [McColl et al., 2010; McColl and Davis, 2013; Leith et al., 2014a; Grämiger et al., 2017a]. Initialization occurs in two steps, first representing the Aletsch Valley during the ice-free pre-LGM interglacial (Eemian) period, and second during the LGM (Figure 4.6a). Stresses are initialized during ice-free conditions with far-field stresses representing combined exhumation-induced and tectonic stresses in a simplified paleo-alpine valley with horizontal to vertical stress ratio  $k = 1$  [Kastrup et al., 2004]. We calculate an initial, ice-free groundwater level using the previously described hydraulic boundary conditions with constant surface infiltration ( $0.93 \times 10^{-8} \text{ m s}^{-1}$ ) (Figure 4.6b). Unrealistically high stresses are avoided during this step using an elastoplastic equilibration phase with Mohr-Coulomb failure criterion for blocks ( $\phi = 50^\circ$ ,  $c = 8 \text{ MPa}$ ,  $t = 1 \text{ MPa}$ ). Subsequently, elastoplastic failure criterion for discontinuities is assigned (strength properties listed in Table 4.2) allowing joints to fail. Plastic equilibration with initial stresses in combination with the initial pressure field results in an initial (inherited) damage field during the ice-free pre-LGM interglacial. We then add LGM ice and calculate a new pressure field at this glacier level, again allowing subsequent damage. These stresses, damage and groundwater conditions represent the starting point for our transient HM models.

#### 4.4.2 Slope deformation caused by seasonal groundwater recharge

Monitored seasonal bedrock deformations (Figure 4.5) allow us to verify the modeled HM slope response under present-day glacier conditions and assuming snowmelt driven transient infiltration boundary conditions (Figure 4.7). Our verification model assumes constant, present-day glacier conditions along profile M (Figure 4.2b,c). We apply the previously described model boundary conditions (Figure 4.6) with 5 years of transient surface infiltration, which results in a fluctuating groundwater table with peak-to-peak amplitude between 50 and 100 m in the area of interest (Figure 4.7a,b). Water levels rise with the onset of surface infiltration during snowmelt and fall when infiltration ceases. Storativity and hydraulic conductivity controls drainage of the aquifer. Rising groundwater increases joint water pressures, causing the joints to dilate and resulting in expansion of the rock mass. The cumulative dilation of individual joints results in the displacement field presented in Figure 4.7c. Displacement is smallest below the glacier, where the smallest change in pressure occurs. The spacing and orientation of discontinuities in our model (Figure 4.6) influences the simulated slope response.

Seasonal groundwater changes inducing expansion and contraction of the rock mass result in modeled valley closing during surface infiltration and valley opening when infiltration ceases (Figure 4.7d). The magnitude of this reversible slope deformation is ~1.6 cm horizontal displacement between observation points A and B. Predicted slope deformations are thus comparable to our field observations from GNSS measurements on either side of the Aletsch Glacier (~4 cm; Figure 4.5) at positions comparable to points A and B. This match was achieved by decreasing joint stiffness by a factor of 10 compared to the values

used in our preceding companion studies [Grämiger *et al.*, 2017a, b] and laterally expanding the area of interest containing discontinuities (Figure 4.6). Changes in differential stresses of intact blocks, assuming elastic properties, caused by seasonal slope deformation are shown in Figure 4.7e (note: effective stresses are only accounted for in discontinuities, not intact blocks); the magnitude of these stress changes reaches  $\sim 500$  kPa.

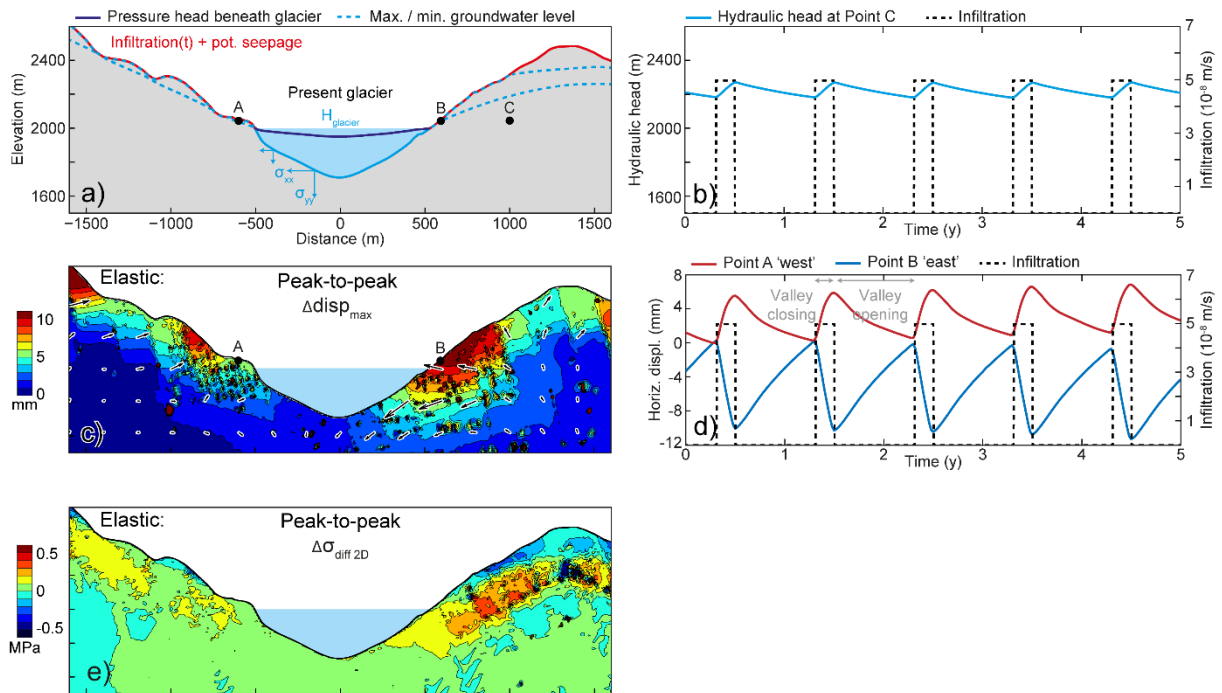


**Figure 4.7.** Slope deformation caused by seasonal groundwater changes: a) Model with hydraulic boundary conditions and resulting maximum and minimum water tables with a constant present-day glacier elevation. b) Transient hydraulic head at Point C together with surface infiltration. c) Maximum slope displacement and vectors (black arrows) assuming elastic properties induced by raising groundwater from minimum to maximum. d) Absolute horizontal displacement ( $\Delta x$ ) for observation points A and B on each side of the glacier showing valley closing and opening. e) Changes in differential stresses of intact blocks (assuming elastic properties) induced by raising groundwater from minimum to maximum (note: effective stresses are only accounted for in discontinuities, not intact blocks).

#### 4.4.3 Pre-LGM and LGM rock slope damage

Joint water pressure reduces effective stress and affects rock slope damage. In Figure 4.8 we show the influence of a groundwater table on the initial damage produced during the ice-free pre-LGM interglacial period and subsequent LGM ice loading. Initial stresses and pressure fields are applied as described previously (Figure 4.6). We compare damage between a purely mechanical model and a HM coupled model including a groundwater table. Neglecting water pressure, new damage during LGM ice loading, is minor and occurs mostly at the valley bottom (Figure 4.8a). Including a groundwater table during ice-free conditions, the predicted initial damage field shows similar characteristics (Figure 4.8b). Adding LGM ice with corresponding high subglacial water pressures results in greater additional damage, notably occurring at the toe of the slope on either side of the valley. Steeply dipping joints are most critical and prone to failure at these stress conditions. This rock slope damage at the LGM including joint water pressures represents the initial damage field for our following HM transient models.

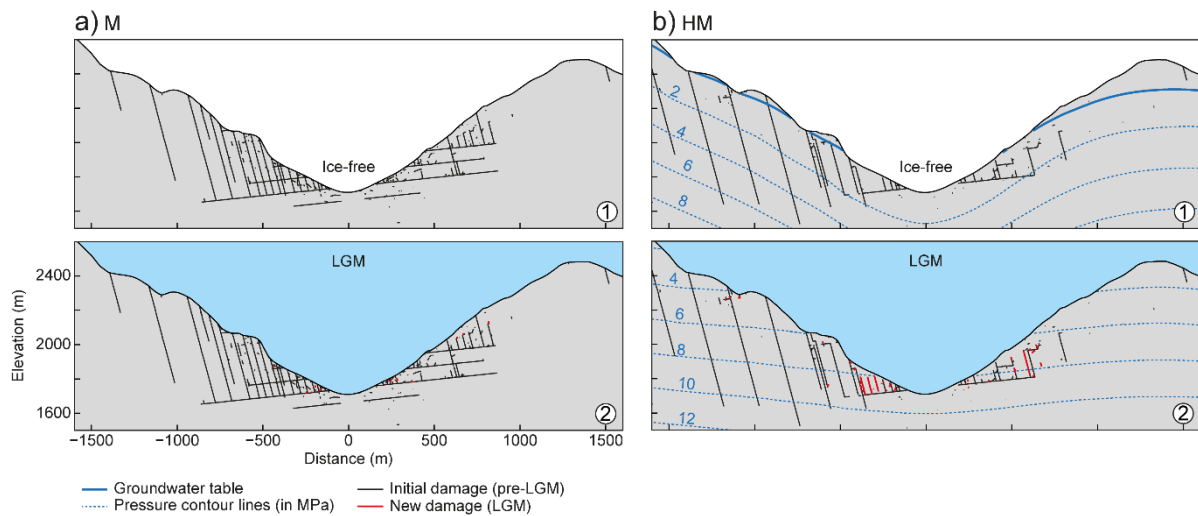


**Figure 4.8.** Pre-LGM and LGM rock slope damage: Initial pre-LGM and new damage with LGM ice loading for a) purely mechanical model [Grämiger et al., 2017a], and b) including groundwater pressure field coupled to high subglacial water pressures.

#### 4.4.4 Transient HM rock slope damage

In the following, we investigate transient HM rock slope damage during LGM deglaciation and subsequent Holocene ice fluctuations (Figure 4.9). The applied glacier scenarios (Figure 4.9a) are adopted from Grämiger et al. [2017a], and based on mapped post-LGM glacier extents along profiles N and P (Figure 4.2a). We compare the Aletsch Valley undergoing LGM deglaciation with three subsequent Holocene cycles (scenario N) to LGM deglaciation followed by a minor Egesen cycle before remaining ice free (scenario P). In these scenarios, we combined fluctuating ice loads with groundwater changes, where hydraulic boundary conditions are tied to the changing glacier elevation (models labeled HM). For comparison, we analyze a similar model but with a static groundwater table after LGM deglaciation (labeled M). Furthermore, we include seasonal groundwater cycles (models labeled HMc) in combination with long-term groundwater changes, distributing 500 annual HM cycles over the applied glacier scenarios. The location of the groundwater table at different stages for HM and HMc models is presented in Figure 4.9c. For computational efficiency, we reduced the number of seasonal groundwater cycles during the Lateglacial and Holocene to 500, although in reality the value would be an order of magnitude larger. Inadequate rapid slope dewatering as glaciers retreat over the shortened time span (500 years) does not occur in our models, since glacier changes are small enough that the long-term hydraulic ‘steady state’ is reached at each stage (aside from short-term transient HMc models).

Transient HM rock slope damage is shown in Figure 4.9b. Including seasonal cycles (HMc) results in greater damage (+7%) compared to only a dynamic groundwater table tied to the glacier elevation (HM) in both scenarios. Most damage occurs during first deglaciation. A single LGM retreat (scenario P) generates slightly more damage than including the Egesen readvance (scenario N). Subsequent Holocene cycles result in minor additional damage when including seasonal cycles (scenario N; HMc). Annual groundwater changes during ice-free conditions in scenario P generate insignificant new damage. Accumulation of new damage ceases during subsequent Holocene ice fluctuations as a steady groundwater table is maintained following LGM deglaciation (scenario N; M).

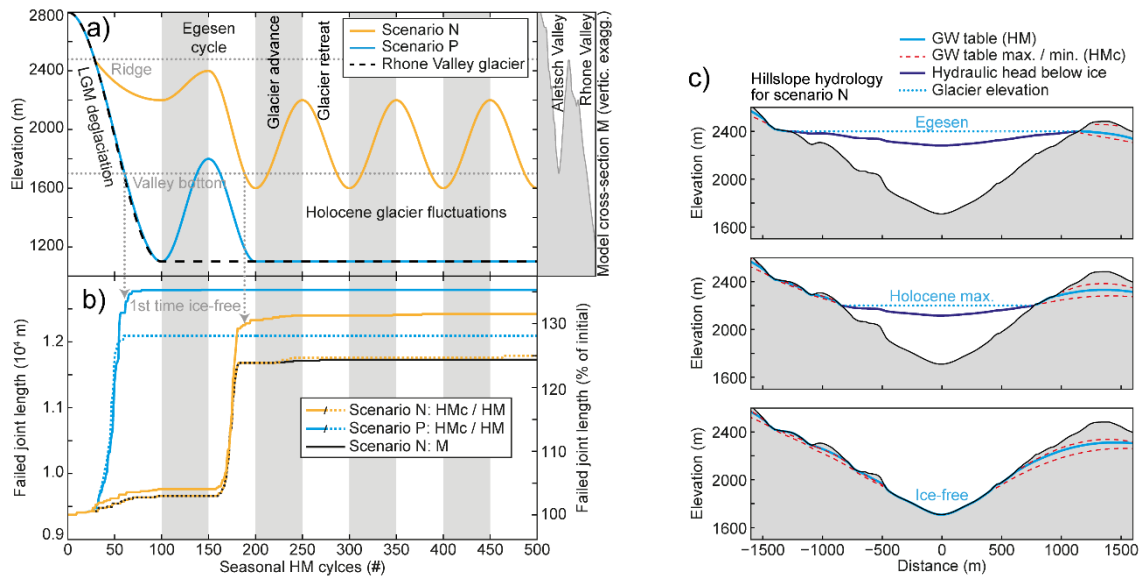


**Figure 4.9.** Transient HM rock slope damage during repeat glacial cycles: a) Applied glacier scenario with compressed profile M as reference. b) Temporal evolution of damage for applied glacier scenarios illustrated as the sum of failed joint length and percentage of initial damage. Changing groundwater table tied to glacier elevation (HM), including seasonal groundwater cycles (HM<sub>c</sub>), and with a static groundwater table after LGM deglaciation (M). c) Applied hillslope hydrology for scenario N at different glacial stages (Egesen, Holocene maximum, and ice-free conditions) with groundwater table (HM) and with seasonal cycles (HM<sub>c</sub>).

Newly failed joints, and fracture propagation along steeply dipping discontinuities, occurs mostly in the upper 400 m on the eastern valley slope (Figure 4.10). Additional damage during subsequent Holocene cycles (green traces in Figure 4.10) is minor and often limited to extension of pre-existing failed joints. Differences between simulations with and without seasonal groundwater cycles (HM and HM<sub>c</sub>) occur mainly on the upper portion of the eastern slope. Observed damage during first glacier retreat includes failing joints, faults, and propagation of pre-existing failed discontinuities.

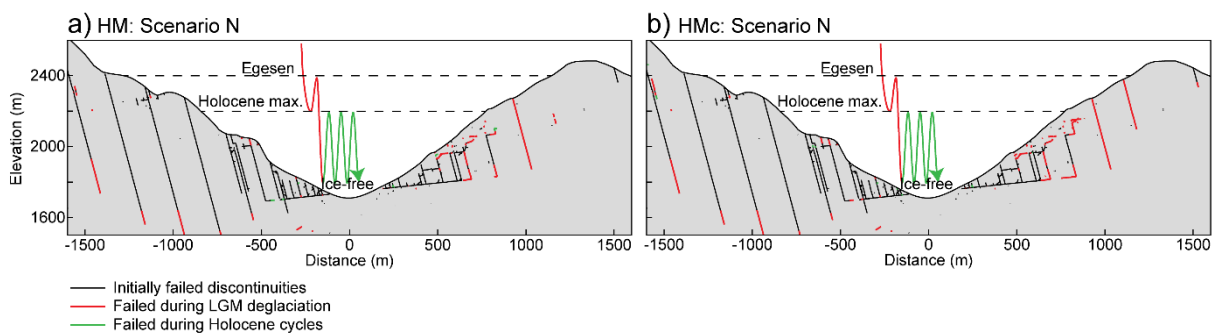


**Figure 4.10.** Spatial and temporal distribution of HM rock slope damage during repeat glacial cycles (scenario N): a) Accounting for a groundwater table tied to changing glacier elevation (HM), and b) including seasonal groundwater table cycles (HM<sub>c</sub>).

#### 4.4.5 Long-term hydro-mechanical effects

We present comparison between a static (i.e. ground water table stays constant despite changing glacier elevation) and a dynamic groundwater table tied to glacier elevation for glacier loading during three Holocene cycles in Figure 4.11. Glacier cycles with a static groundwater table propagate minor fractures

in the eastern mid-slope region (Figure 4.11a). In comparison, a dynamic groundwater table, that changes in parallel with glacier elevation, results in slightly larger damage (Figure 4.11b). Fracture propagation during glacier fluctuations occurs in the eastern mid-slope region, while newly failed discontinuities are also found at the toe of the western valley flank.

Groundwater fluctuations tied to glacier thickness alter effective stresses in rock joints. We compare changes in effective stress ( $\sigma' = \sigma - p$ ) for an example joint during Holocene glacial cycles in Figure 4.12, highlighting the stress path of the steeply dipping discontinuity beneath fluctuating ice (see location in Figure 4.11). Glacier loading with a static groundwater table increases normal stresses during advance, and the joint becomes less critically stressed under the ice load, while the reverse is found during glacier retreat. On the other hand, increasing subglacial water pressure beneath advancing ice counteracts increasing normal stresses. Effective joint stresses remain closer to the failure envelope; i.e., the slope is more critically stressed during glacier cycles when including a dynamic groundwater table. Joint water pressures counteract slope buttressing by glacial ice for steeply dipping joints, increasing the criticality of the slope during glacier occupation. The interplay between ice loading and cleft water pressures are strongly dependent on joint orientation.

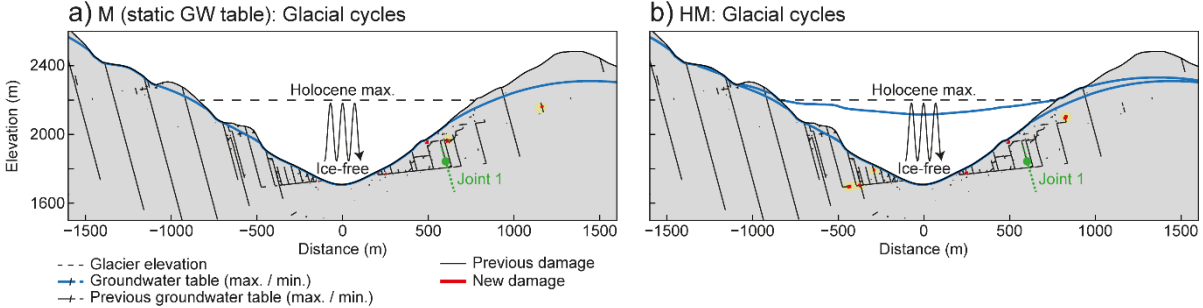


**Figure 4.11.** Influence of long-term glacially induced groundwater changes on rock slope damage: a) Glacier loading during Holocene cycles (Year 200 to 500 in scenario N, Figure 4.9) with a static groundwater table, and b) with a dynamic groundwater table tied to glacier elevation. Major differences in damage are highlighted in yellow. Location of observation joint 1 indicated.

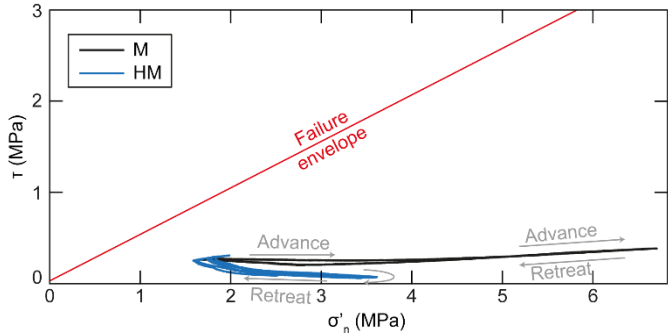


**Figure 4.12.** Effective stresses during a single glacier cycle: Exemple stress path during Holocene glacier cycles with a static groundwater table (M) in comparison with a dynamic groundwater table (HM) tied to the glacier level (see Figure 4.11) for a steeply dipping discontinuity (Joint 1, see location in Figure 4.11).



#### 4.4.6 Seasonal hydro-mechanical effects

Previously we demonstrated the influence of changing cleft water pressures in parallel with changing ice loads during glacier cycles on the stress field in adjacent rock slopes. However, the hillslope groundwater table not only changes in conjunction with adjacent ice thickness but also fluctuates seasonally [Hansmann *et al.*, 2012; Loew and Strauhal, 2014; Strauhal *et al.*, 2015]. Here we investigate damage during glacial cycles for models including seasonal changes of the mountain groundwater table. In Figure 4.13 we show damage propagation during Egesen ice retreat with and without seasonal water table cycles. Although damage is similar, the amount of new joint failure is larger when including seasonal groundwater cycles. Differences are mainly found in the eastern mid- and upper-slope regions, as well as at the toe of the western valley flank. Seasonal groundwater fluctuations create a zone with differential stress cycles of a few hundred kPa (Figure 4.7e). This zone is tied to the glacier elevation and drops during glacier retreat, generating new damage.

Accumulation of incremental shear displacement with repeat glacial cycles results in significant slope displacement (Figure 4.14). Maximum displacement for a complete glacial cycle including seasonal water table fluctuations is about 25 cm. The upper 200 m of the eastern flank becomes destabilized with toppling-mode kinematics. The kinematics and dimensions of this model prediction closely resemble characteristics of rock slope instabilities observed in the field at Aletsch [Strozzi *et al.*, 2010; Kos *et al.*, 2016; Grämiger *et al.*, 2017a]. In Figure 4.14c we compare horizontal displacement at Point 1 within the rock slope instability for glacier scenarios N and P. Both scenarios lead to similar final displacement, while displacement including seasonal groundwater cycles (HM<sub>c</sub>) is slightly larger. The largest irreversible slope displacement occurs during first ice retreat, and Holocene cycles have an insignificant effect. Holocene readvance including a dynamic groundwater table pushes the slope outwards. Interestingly, glacier advance with a static groundwater table (M) results in the opposite [cf., Grämiger *et al.*, 2017a]. Slope movement ceases after LGM deglaciation during ice-free conditions in scenario P, despite ongoing seasonal HM stress cycles. Seasonal slope displacement is of a similar order of magnitude as previously presented (Figure 4.7c) and measured in the field (Figure 4.5).

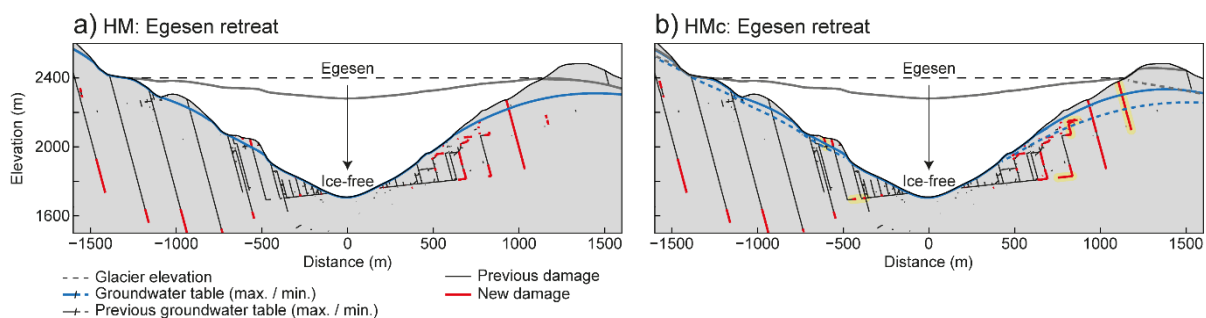


**Figure 4.13.** Influence of glacially induced groundwater change on rock slope damage with and without seasonal groundwater fluctuations during Egesen retreat: a) Glacier unloading from Egesen maximum to ice-free (Year 150 to 200 in scenario N in Figure 4.9) with a changing water table (HM), b) including seasonal groundwater cycles (HM<sub>c</sub>). Major differences in damage are highlighted in yellow.

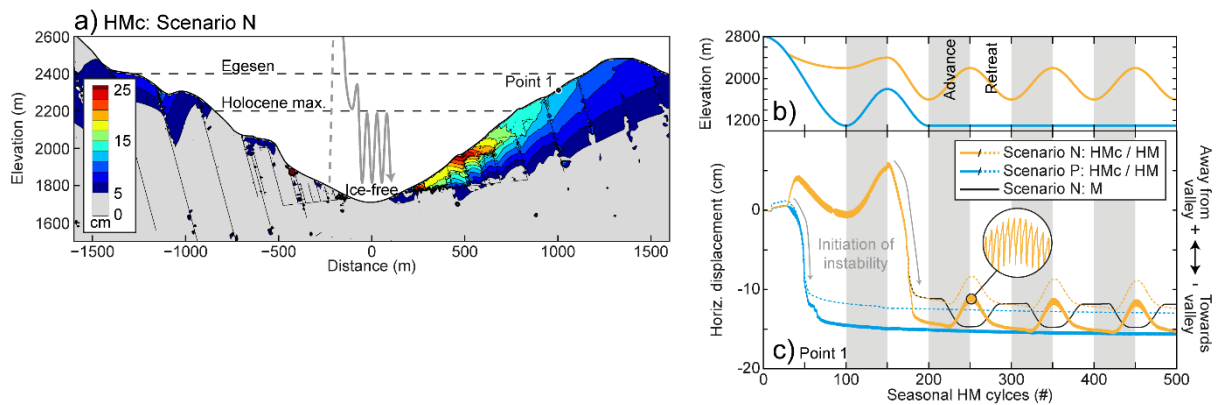


**Figure 4.14.** Displacement during repeat glacial cycles in parallel with groundwater changes illustrating development of landslide activity: a) Maximum slope displacement in scenario N for a complete glacial cycle (ice-free initialization until end of Holocene cycles) including seasonal water table cycles (HMc). b) Applied glacier scenarios N and P. c) Absolute horizontal displacement ( $\Delta x$ ) for Point 1 within the instability for glacier scenarios N and P, each with and without seasonal water table cycles (HMc / HM).

## 4.5 Discussion

We demonstrated through numerical modeling the importance of including groundwater changes on both short (annual) and long (millennial) time scales in parallel with glacier loading cycles for predicting rock slope damage. A changing groundwater table tied to glacier thickness induces substantial damage, and superposed annual cycles increase this damage. However, our numerical simulations have their limitations. Long computation times limited our study to 500 annual groundwater cycles throughout the Lateglacial and Holocene (periods representing  $\sim 18$  ky). Therefore, long-term HM fatigue may be underestimated [cf., *Eberhardt et al., 2016; Preisig et al., 2016*]. Furthermore, although fracture permeability is dependent on effective stress, aperture and shear slip [*Min et al., 2004; Preisig et al., 2012*], the HM slope response in our models is only semi-coupled; i.e., cleft water pressures affect joint aperture and reduce effective stresses, but the mechanical response has no feedback on the hydraulic properties of the rock mass. In reality, we expect an increase in rock mass permeability during glacier unloading (i.e., decreasing joint normal stresses), as well as higher permeability in damage accumulation zones.

Our field observations of groundwater levels is limited to spring-line observations, which indicate the position of the groundwater table at the intersection with the ground surface. The exact position of the water table throughout our cross-section, as well as the influence of geological heterogeneity therefore remains unknown. Furthermore, we calibrated our modeled water table to present-day spring observations in the Aletsch region using snowmelt driven groundwater recharge, while the location of groundwater during past glacier extents remains uncertain. Modeled seasonal HM stress cycles are of similar amplitude as reported in other studies [*Gischig et al., 2015; Preisig et al., 2016*]. Including additional complexity in our hydraulic model may be important for detailed studies of the regional groundwater flow system, though our anisotropic two-layered hydraulic model was sufficient to produce realistic seasonal groundwater cycles appropriate for the scope of this study.

The location of new HM damage created in our models corresponds to the location of rock slope instabilities observed in the field at Aletsch [*Strozzi et al., 2010; Kos et al., 2016*]. Furthermore, the majority of unstable rock slopes at Aletsch have a post-Egesen relative initialization age [*Grämiger et al., 2017a*], correlating with the peak of new damage occurring during first glacier retreat in our models

(Figure 4.9b). First-time HM cycling in a rock slope initiates the greatest damage, while subsequent HM cycles with similar amplitude propagate insignificant new damage (Scenario P, Figure 4.9b). We assume bedrock beneath LGM ice was affected by a nearly constant, high subglacial water pressure field. First seasonal HM cycles affect the hillslope only when slope deglaciation is fairly advanced (Figure 4.9c). The constant pressure conditions in the slope change to a dynamic pressure field with seasonal cycles. So, similar as in our models, we expect that first-time HM cycling in the rock slopes at Aletsch coincided with first glacier retreat, initiating a large amount of new damage. Future glacier retreat in the Aletsch region may affect the local groundwater table substantially and thereby effective joint stresses, resulting in new rock slope damage.

Our modeling conclusions agree with field observations of analog phenomena. We argue that glacier cycles have a similar effect on adjacent slopes as a fluctuating reservoir or lake, due to the ductile behavior of ice and generally high subglacial water pressures. Similar to how a reservoir level influences the groundwater table in adjacent slopes [e.g., *Strauhal et al.*, 2015], glacier cycles induce joint effective stress changes in our study. Slope destabilization in our long-term HM models agrees well with the monitored behavior of landslides influenced by lakes. Initial impoundment of a reservoir frequently causes first-time failure of the adjacent slope [e.g., *Müller*, 1964; *Zangerl et al.*, 2010; *Zhang et al.*, 2013]. In a similar manner, we observe a large amount of new damage during initial LGM ice loading (Figure 4.8b), making the slope more prone to fracture propagation. While low reservoir levels can increase rockslide acceleration [e.g., *Zangerl et al.*, 2010], in our models only the first glacier retreat induced substantial damage (Figure 4.9b; HM scenario N). Reservoir level variations often occur over shorter times. Therefore, rockslide accelerations during low reservoir levels may coincide with rapid dewatering. We do not expect this process to occur over glacial time scales. However, glacially induced groundwater fluctuations seem to be more effective in propagating damage than pure glacier loading cycles (Figure 4.11). We argue that glacier cycling in parallel with subglacial water pressure change is a comparable preparatory factor for rock slope failures as water level changes in a reservoir. Unstable rock slopes in the vicinity of retreating glaciers behave similarly as those adjacent to a reservoir [cf., *Moore*, 1999], but only if glacially induced groundwater changes are included.

*Preisig et al.* [2016] and *Eberhardt et al.* [2016] highlighted the relevance of *hydro-mechanical fatigue* (i.e., time dependent damage associated with seasonal variations in precipitation and groundwater recharge) for progressive rock slope failure. Furthermore they demonstrated that HM cycling becomes more effective in combination with another major, but low-frequency loading process (e.g., *seismic fatigue*; *Gischig et al.*, [2015]) affecting the entire slope and increasing the pre-existing damage level. We propose here that low-frequency glacial loading cycles in combination with annual groundwater fluctuations (Figure 4.13) behave in a similar manner and may drive hydro-mechanical fatigue.

## 4.6 Comparison of preparatory factors for paraglacial rock slope instabilities

Our concept of glacial debuttressing involves not only a reduction of the weight of ice at the toe of a slope, but includes a complex transition of boundary conditions, potentially propagating rock slope damage in a paraglacial environment (Figure 4.15a) [*Grämiger et al.*, 2017a, b]. Mechanical loading by glacier ice affects the stress field of adjacent rock slopes, however deformable ice makes a weak buttress [*Grämiger et al.*, 2017a]. Glacial erosion, i.e., rock debuttressing, on the other hand, creates significant new rock slope damage during subsequent deglaciation [*Leith et al.*, 2014b; *Grämiger et al.*, 2017a]. In addition, bedrock covered by ice is near isothermal at  $\sim 0$  °C and shielded from ambient environmental temperature cycles; glacier retreat rapidly exposes rock slopes to new thermal boundary

conditions. Thermal strain induced by subsurface temperature changes on glacial time scales, as well as annual temperature cycles in combination with fluctuating ice, generates significant rock mass damage and displacement [Baroni *et al.*, 2014; Grämiger *et al.*, 2017b]. Secondary effects such as permafrost, chemical alteration, and earthquakes may lead to further fracture propagation [Wegmann *et al.*, 1998; Sanders *et al.*, 2012; Krautblatter *et al.*, 2013; Duca *et al.*, 2015; Gischig *et al.*, 2015; McColl *et al.*, 2012]. In this study, we investigated in detail hydro-mechanical rock slope damage driven by groundwater changes generated in conjunction with repeat glacial cycles on both short (annual) and long (millennial) time scales.

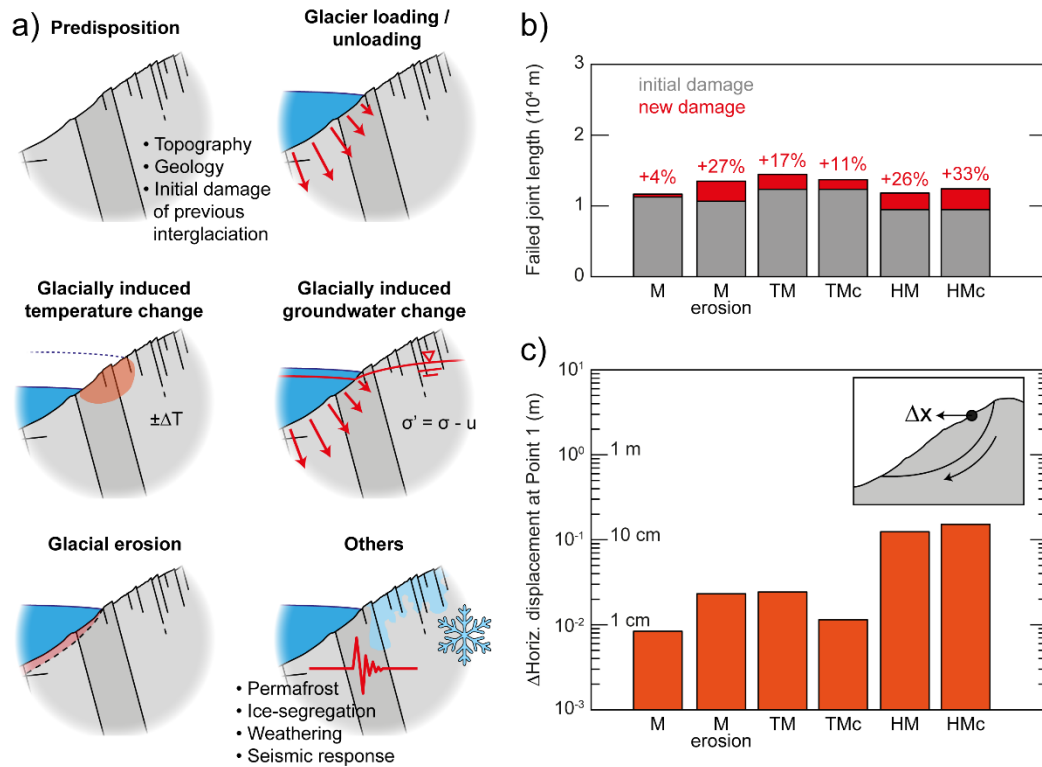


**Figure 4.15.** a) Summary of preparatory factors for paraglacial rock slope instabilities. b) Comparison of rock slope damage, and c) relative horizontal slope displacement at Point 1 (see location in Figure 4.14) during a complete glacier cycle (scenario N) for model predictions with purely mechanical (M) glacier cycles, in combination with LGM valley erosion (M erosion), long-term thermo-mechanical effects (TM), thermo-mechanical effects including seasonal temperature cycles (TMc), long-term glacially induced groundwater change (HM), and glacially induced groundwater change in parallel with seasonal groundwater fluctuations (HMc) [Grämiger *et al.*, 2017a, b; this study]. Horizontal slope displacement at Point 1 is corrected for elastic movement of the entire ridge.

In Figure 4.15b, c we compare new rock slope damage and slope displacement during repeat glacier cycles predicted from numerical models in this study and our preceding companion studies [Grämiger *et al.*, 2017a, b]. Using the same model geometry, glacier scenarios, and appropriately scaled rock mass strength properties allows us to compare purely mechanical, thermo-mechanical, and hydro-mechanical stresses during glacial cycles and their efficacy in generating rock slope damage. Slight modifications of the models were necessary to simulate the different physical processes or pre-erosion topography, which resulted in minor changes in the amount of initial damage. Strength properties in the HM models were slightly increased to account for effective rock strength, allowing initialization of all models with

comparable initial damage. Subsequent damage is strongly dependent on the criticality of initial slope conditions [Gischig *et al.*, 2015]. New damage should therefore be compared relative to initial damage.

Our greatest simulated damage occurs during glacial cycles including long-term groundwater changes in parallel with seasonal fluctuations (HMc) (Figure 4.15b), while long-term HM stress changes alone generated slightly less damage. LGM valley erosion also created significant new rock slope damage during deglaciation. Thermo-mechanical stresses during glacier cycles (TM / TMc) are slightly less effective in generating new damage, although still more significant than purely mechanical glacier loading and unloading. Comparison of slope displacement shows similar patterns (Figure 4.15c). HM effects result in the greatest slope movements, followed by glacial erosion and long-term thermal strain associated with glacier cycles. Purely mechanical glacial loading induces only minor slope displacements, while including HM effects results in an order of magnitude greater slope displacement.

Although simply loading and unloading by ice has limited effect in preparing a rock slope for failure, we demonstrated that associated thermo-hydro-mechanical effects during glacial cycles can generate substantial rock slope damage capable of destabilizing a paraglacial valley flank. We propose that changes in thermal and hydraulic boundary conditions in parallel with *in-situ* stress changes during glacier loading cycles act as long-term driving mechanisms, more significant than a reduction in lateral confinement during ice retreat (i.e., glacial debuttreasing). Geological predisposition defines inherited (i.e., initial) damage and general ability for landsliding, but glacial erosion and changes in cleft water pressure in parallel with glacial cycles are important driving factors of long-term strength degradation. Annual stress cycles in general (induced by water or temperature) in combination with glacier advance and retreat are effective fatigue processes. The greatest damage throughout all our models occurs during LGM deglaciation and first Holocene ice advance. Coupled thermo-hydro-mechanical effects may even augment each other driving rock slope damage, while other preparatory factors such as seismic fatigue [McColl *et al.*, 2012; Gischig *et al.*, 2015] and permafrost change [Wegmann *et al.*, 1998] may interact with thermo-hydro-mechanical stresses and further influence rock slope stability.

Active rock slope instabilities in the Aletsch Glacier region (Figure 4.2a) [e.g., Kääh, 2002; Strozzi *et al.*, 2010; Kos *et al.*, 2016; Loew *et al.*, 2017b; Grämiger *et al.*, 2017a], as well as numerous examples of active rock slope failures located in the vicinity of retreating present-day glaciers [e.g., Bovis, 1990; Evans and Clague, 1994; Holm *et al.*, 2004; Oppikofer *et al.*, 2008; Clayton *et al.*, 2013; Geertsema and Chiarle, 2013; McColl and Davies, 2013] provide evidence linking glacier activity and slope stability. On the other hand, prehistoric slope failures in the main alpine valleys, last occupied by ice during the LGM, often cannot be connected to deglaciation as a direct trigger. These events frequently reveal large lag-times between deglaciation and the timing of failure [e.g. Prager *et al.*, 2008; Ivy-Ochs *et al.*, 2009b; McColl, 2012; Ballantyne *et al.*, 2014a, b]. Ice advance and retreat in the main alpine valleys during the last glaciation, in combination with thermo-hydro-mechanical effects and glacial erosion, may have prepared adjacent slopes with favorable predisposition for failure. Following deglaciation, time-dependent rock mass strength degradation processes further reduced slope stability, until an ultimate triggering led to final failure [cf. Eberhardt *et al.*, 2004; Prager *et al.*, 2008; McColl, 2012]. Ongoing present-day glacier retreat with climate warming may significantly affect *in-situ* stress conditions of currently glaciated rock slopes, changing the temperature and groundwater fields, propagating progressive failure and thereby increasing the hazard posed by these rock walls.

## 4.7 Summary and conclusions

High water pressures beneath glacial ice affect the groundwater table in adjacent valley rock slopes during glacier advance and retreat on long time scales with superposed annual water table fluctuations. We investigated hydro-mechanical rock slope damage generated by repeat glacial cycles. Spatial and temporal damage was predicted using detailed numerical models based on realistic site-specific conditions and monitoring data (e.g., permanent monitoring of bedrock deformation, subglacial pressure measurements in ice boreholes) at the Great Aletsch Glacier in Switzerland. Key outcomes of our study are:

1. One year of transient subglacial water pressure measurements in ice boreholes, combined with three years of bedrock deformation and local snow height data reveal seasonal changes in hydraulic boundary conditions and hydro-mechanical coupled slope deformations caused by seasonal groundwater cycles in a glaciated alpine valley. In our numerical models, annual changes in effective joint stresses due to groundwater fluctuations affect joint apertures, resulting in expansion and contraction of the rock mass. The predicted elastic slope response resembles the timing and magnitude of observed displacements in monitoring data.
2. Purely mechanical loading and unloading by the weight of ice generates limited new damage in our models. However, including a groundwater table tied to the ice surface elevation with high subglacial water pressures changes effective joint stresses in the adjacent slopes during glacial cycles, driving substantial fracture propagation. Increasing cleft water pressures during glacier advances reduce joint normal stresses, partly compensating the ice load. Bedrock beneath ice with a higher water table is more critically stressed.
3. Superposing annual groundwater cycles associated with snowmelt infiltration, in addition to long-term changes in hillslope hydrology, results in a greater amount of predicted new rock mass damage during glacier cycles (~7% more damage). Fracture propagation destabilizes the eastern, toppling-mode valley flank inducing displacement of several cm.
4. Comparing predictions of thermo- and hydro-mechanical paraglacial rock slope damage, we find that geological predisposition defines inherited structural, mechanical and topographic conditions, whereas glacial erosion (i.e., rock debuttreasing) and hydro-mechanical stress changes (especially annual melt infiltration cycles) are the most effective preparatory factors driving progressive rock mass damage during glacier cycles. These mechanisms significantly contribute to development of paraglacial rock slope failures.

## 4.8 Acknowledgments

This project was funded by the Swiss National Science Foundation (projects 135184 and 146593). Data used in this study can be found in the citations listed in the references. Data output is included in the tables and figures; raw data are available on request from L.G. (E-mail: [graemiger.lorenz@gmail.com](mailto:graemiger.lorenz@gmail.com)). Special thanks to Thomas Wyder and Roger Loertscher from VAW, ETH Zurich for their help during the glacier drilling campaign. We thank Johnny Sanders for field assistance and Florian Amann for his input on hydro-mechanical modeling. Thanks also to Andrea Alpiger for her contributions on groundwater during her Master thesis.

## 4.9 References

- Alpiger, A. (2013), Hydrogeology of the Great Aletsch glacier region, 94 pp, *MSc thesis*, ETH Zurich, Zurich.
- Ballantyne, C. K., G. F. Sandeman, J. O. Stone, and P. Wilson (2014a), Rock-slope failure following Late Pleistocene deglaciation on tectonically stable mountainous terrain, *Quaternary Science Reviews*, 86, 144-157, doi:<http://dx.doi.org/10.1016/j.quascirev.2013.12.021>.
- Ballantyne, C. K., P. Wilson, D. Gheorghiu, and À. Rodés (2014b), Enhanced rock-slope failure following ice-sheet deglaciation: timing and causes, *Earth Surface Processes and Landforms*, 39(7), 900-913, doi:10.1002/esp.3495.
- Barletta, V. R., C. Ferrari, G. Diolaiuti, T. Carnielli, R. Sabadini, and C. Smiraglia (2006), Glacier shrinkage and modeled uplift of the Alps, *Geophys. Res. Lett.*, 33(14), L14307, doi:10.1029/2006gl026490.
- Baroni, C., S. Martino, M. C. Salvatore, G. Scarascia Mugnozza, and L. Schilirò (2014), Thermomechanical stress-strain numerical modelling of deglaciation since the Last Glacial Maximum in the Adamello Group (Rhaetian Alps, Italy), *Geomorphology*, 226, 278-299, doi:<http://dx.doi.org/10.1016/j.geomorph.2014.08.013>.
- Bevis, M., et al. (2012), Bedrock displacements in Greenland manifest ice mass variations, climate cycles and climate change, *Proceedings of the National Academy of Sciences*, 109(30), 11944-11948, doi:10.1073/pnas.1204664109.
- Bonzanigo, L., E. Eberhardt, and S. Loew (2007), Long-term investigation of a deep-seated creeping landslide in crystalline rock. Part I. Geological and hydromechanical factors controlling the Campo Vallemaggia landslide, *Canadian Geotechnical Journal*, 44(10), 1157-1180, doi:10.1139/T07-043.
- Boulton, G., T. Chan, R. Christiansson, L. O. Ericsson, J. Hartikainen, M. R. Jensen, F. W. Stanchell, and T. Wallroth (2004), Thermo-Hydro-Mechanical (T-H-M) Impacts of Glaciation and Implications for Deep Geologic Disposal of Nuclear Waste, in *Elsevier Geo-Engineering Book Series*, edited by S. Ove, pp. 299-304, Elsevier, doi:[http://dx.doi.org/10.1016/S1571-9960\(04\)80057-0](http://dx.doi.org/10.1016/S1571-9960(04)80057-0).
- Bovis, M. J. (1990), Rock-slope deformation at Affliction Creek, southern Coast Mountains, British Columbia, *Canadian Journal of Earth Sciences*, 27(2), 243-254, doi:10.1139/e90-024.
- Chan, T., R. Christiansson, G. S. Boulton, L. O. Ericsson, J. Hartikainen, M. R. Jensen, D. Mas Ivars, F. W. Stanchell, P. Vistrand, and T. Wallroth (2005), DECOVALEX III BMT3/BENCHPAR WP4: The thermo-hydro-mechanical responses to a glacial cycle and their potential implications for deep geological disposal of nuclear fuel waste in a fractured crystalline rock mass, *International Journal of Rock Mechanics and Mining Sciences*, 42(5-6), 805-827, doi:<http://dx.doi.org/10.1016/j.ijrmms.2005.03.017>.
- Chui, T. M., and D. L. Freyberg (2007), The Use of COMSOL for Integrated Hydrological Modeling, paper presented at COMSOL Conference 2007, Boston.
- Clayton, M. A., D. Stead, and D. Kinakin (2013), The Mitchell Creek Landslide, B.C., Canada: Investigation using Remote Sensing and Numerical Modeling, in *47th U.S. Rock Mechanics/Geomechanics Symposium*, edited, American Rock Mechanics Association, San Francisco, California.
- Cohen, D., R. L. Hooke, N. R. Iverson, and J. Kohler (2000), Sliding of ice past an obstacle at Engabreen, Norway, *Journal of Glaciology*, 46(155), 599-610.
- Cohen, D., T. S. Hooyer, N. R. Iverson, J. F. Thomason, and M. Jackson (2006), Role of transient water pressure in quarrying: A subglacial experiment using acoustic emissions, *Journal of Geophysical Research: Earth Surface*, 111(F3), F03006, doi:10.1029/2005jf000439.
- Cossart, E., R. Braucher, M. Fort, D. L. Bourlès, and J. Carcaillet (2008), Slope instability in relation to glacial debuitressing in alpine areas (Upper Durance catchment, southeastern France): Evidence from field data and <sup>10</sup>Be cosmic ray exposure ages, *Geomorphology*, 95(1-2), 3-26, doi:10.1016/j.geomorph.2006.12.022.

- Cundall, P. A., and R. D. Hart (1992), Numerical modelling of discontinua, *Engineering Computations*, 9(2), 101-113, doi:doi:10.1108/eb023851.
- Dahl-Jensen, D., et al. (2013), Eemian interglacial reconstructed from a Greenland folded ice core, *Nature*, 493(7433), 489-494, doi:10.1038/nature11789.
- Dow, C. F., J. L. Kavanaugh, J. W. Sanders, K. M. Cuffey, and K. R. MacGregor (2011), Subsurface hydrology of an overdeepened cirque glacier, *Journal of Glaciology*, 57(206), 1067-1078, doi:10.3189/002214311798843412.
- Duca, S., E. E. Alonso, and C. Scavia (2015), A permafrost test on intact gneiss rock, *International Journal of Rock Mechanics and Mining Sciences*, 77, 142-151, doi:http://dx.doi.org/10.1016/j.ijrmms.2015.02.003.
- Eberhardt, E., D. Stead, and J. S. Coggan (2004), Numerical analysis of initiation and progressive failure in natural rock slopes—the 1991 Randa rockslide, *International Journal of Rock Mechanics and Mining Sciences*, 41(1), 69-87, doi:10.1016/s1365-1609(03)00076-5.
- Eberhardt, E., G. Preisig, and V. Gischig (2016), Progressive failure in deep-seated rockslides due to seasonal fluctuations in pore pressures and rock mass fatigue, in *Landslides and Engineered Slopes. Experience, Theory and Practice*, edited, pp. 121-136, CRC Press, doi:doi:10.1201/b21520-13.
- Evans, K., T. Dahlø, and J. A. Roti (2003), Mechanisms of Pore Pressure-stress Coupling which Can Adversely Affect Stress Measurements Conducted in Deep Tunnels, *Pure and Applied Geophysics*, 160(5), 1087-1102, doi:10.1007/pl00012562.
- Evans, S. G., and J. J. Clague (1994), Recent climatic change and catastrophic geomorphic processes in mountain environments, *Geomorphology*, 10(1-4), 107-128, doi:10.1016/0169-555x(94)90011-6.
- Farinotti, D., M. Huss, A. Bauder, and M. Funk (2009), An estimate of the glacier ice volume in the Swiss Alps, *Global and Planetary Change*, 68(3), 225-231, doi:10.1016/j.gloplacha.2009.05.004.
- Fountain, A. G. (1994), Borehole water-level variations and implications for the subglacial hydraulics of South Cascade Glacier, Washington State, U.S.A., *Journal of Glaciology*, 40(135), 293-304.
- Fountain, A. G., and J. S. Walder (1998), Water flow through temperate glaciers, *Rev. Geophys.*, 36(3), 299-328, doi:10.1029/97rg03579.
- Fudge, T. J., J. T. Harper, N. F. Humphrey, and W. T. Pfeffer (2005), Diurnal water-pressure fluctuations: timing and pattern of termination below Bench Glacier, Alaska, USA, *Annals of Glaciology*, 40(1), 102-106, doi:10.3189/172756405781813799.
- Fudge, T. J., N. F. Humphrey, J. T. Harper, and W. T. Pfeffer (2008), Diurnal fluctuations in borehole water levels: configuration of the drainage system beneath Bench Glacier, Alaska, USA, *Journal of Glaciology*, 54(185), 297-306, doi:10.3189/002214308784886072.
- Furrer, H. (1948), Das Sackungsgebiet von Greich-Goppisberg, nördlich Mörel, und der Riederhornstollen (Oberwallis), *Eclogae Geol Helv*, 41(2), 291-296.
- Furuya, G., K. Sassa, H. Hiura, and H. Fukuoka (1999), Mechanism of creep movement caused by landslide activity and underground erosion in crystalline schist, Shikoku Island, southwestern Japan, *Engineering Geology*, 53(3-4), 311-325, doi:http://dx.doi.org/10.1016/S0013-7952(98)00084-2.
- Geertsema, M., and M. Chiarle (2013), Mass-Movement Causes: Glacier Thinning, in *Treatise on Geomorphology*, edited by J. F. Shroder, pp. 217-222, Academic Press, San Diego.
- GEOTEST AG (1978), Geotechnische Voruntersuchung für das Speicherbecken Vordersee, in Zusammenhang mit der Wasserversorgung Aletschgebiet, rund 1.5 km NE Eggishorn, Fieschertal, *Geotechnical Report*, 39 pp.
- Gischig, V., G. Preisig, and E. Eberhardt (2015), Numerical Investigation of Seismically Induced Rock Mass Fatigue as a Mechanism Contributing to the Progressive Failure of Deep-Seated Landslides, *Rock Mechanics and Rock Engineering*, 1-22, doi:10.1007/s00603-015-0821-z.



- Grämiger, L. M., J. R. Moore, V. Gischig, S. Ivy-Ochs, and S. Loew (2017a), Beyond debuttressing: Mechanics of paraglacial rock slope damage during repeat glacial cycles, *under review at JGR, Earth Surface*, Manuscript # 2016JF003967.
- Grämiger, L. M., J. R. Moore, V. Gischig, and S. Loew (2017b), Beyond debuttressing: Thermo-mechanical rock slope damage during repeat glacial cycles, *under review at JGR, Earth Surface*, Manuscript # 2016JF004029.
- Guglielmi, Y., F. Cappa, and S. Binet (2005), Coupling between hydrogeology and deformation of mountainous rock slopes: Insights from La Clapière area (southern Alps, France), *Comptes Rendus Geoscience*, 337(13), 1154-1163, doi:10.1016/j.crte.2005.04.016.
- Guglielmi, Y., F. Cappa, J. Rutqvist, C. F. Tsang, and A. Thoraval (2008), Mesoscale characterization of coupled hydromechanical behavior of a fractured-porous slope in response to free water-surface movement, *International Journal of Rock Mechanics and Mining Sciences*, 45(6), 862-878, doi:http://dx.doi.org/10.1016/j.ijrmms.2007.09.010.
- Hagen, J. O., O. Liestøl, J. L. Sollid, B. Wold, and G. Østrem (1993), Subglacial investigations at Bondhusbreen, Folgefonna, Norway, *Norsk Geografisk Tidsskrift - Norwegian Journal of Geography*, 47(3), 117-162, doi:10.1080/00291959308621974.
- Hallet, B. (1996), Glacial quarrying: a simple theoretical model, *Annals of Glaciology*, 22, 1-8.
- Hansmann, J., S. Loew, and K. Evans (2012), Reversible rock-slope deformations caused by cyclic water-table fluctuations in mountain slopes of the Central Alps, Switzerland, *Hydrogeology Journal*, 20(1), 73-91, doi:10.1007/s10040-011-0801-7.
- Harper, J. T., N. F. Humphrey, W. T. Pfeffer, T. Fudge, and S. O'Neel (2005), Evolution of subglacial water pressure along a glacier's length, *Annals of Glaciology*, 40(1), 31-36, doi:10.3189/172756405781813573.
- Harrison, W. D. (1975), Temperature Measurements in a Temperate Glacier, *Journal of Glaciology*, 14(70), 23-30, doi:10.3198/1975JoG14-70-23-30.
- Herman, F., F. Beaud, J.-D. Champagnac, J.-M. Lemieux, and P. Sternai (2011), Glacial hydrology and erosion patterns: A mechanism for carving glacial valleys, *Earth and Planetary Science Letters*, 310(3-4), 498-508, doi:10.1016/j.epsl.2011.08.022.
- Hock, R., A. Iken, and A. Wangler (1999), Tracer experiments and borehole observations in the overdeepening of Aletschgletscher, Switzerland, *Annals of Glaciology*, 28(1), 253-260, doi:10.3189/172756499781821742.
- Holm, K., M. Bovis, and M. Jakob (2004), The landslide response of alpine basins to post-Little Ice Age glacial thinning and retreat in southwestern British Columbia, *Geomorphology*, 57(3-4), 201-216, doi:10.1016/s0169-555x(03)00103-x.
- Holzhauser, H., M. Magny, and H. J. Zumbühl (2005), Glacier and lake-level variations in west-central Europe over the last 3500 years, *The Holocene*, 15(6), 789-801, doi:10.1191/0959683605hl853ra.
- Hubbard, B. P., M. J. Sharp, I. C. Willis, M. K. Nielsen, and C. C. Smart (1995), Borehole water-level variations and the structure of the subglacial hydrological system of Haut Glacier d' Arolla, Valais, Switzerland, *Journal of Glaciology*, 41(139), 572-583.
- Iken, A. (1997), The relationship between subglacial water pressure and velocity of Findelengletscher, Switzerland, during its advance and retreat, *Journal of Glaciology*, 43(144), 328-338.
- Iken, A., and R. A. Bindschadler (1986), Combined measurements of subglacial water pressure and surface velocity at Findelengletscher, Switzerland: conclusions about drainage system and sliding mechanism, *Journal of Glaciology*, 32(110), 101-119.
- Iken, A., H. Röthlisberger, and K. Hutter (1976), Deep Drilling With A Hot Water Jet, *Zeitschrift für Gletscherkunde und Glazialgeologie*, 12(2), 143-156.
- Iken, A., K. Fabri, and M. Funk (1996), Water storage and subglacial drainage conditions inferred from borehole measurements on Gornergletscher, Valais, Switzerland, *Journal of Glaciology*, 42(141), 233-248.

- Itasca (2014), UDEC - Universal Distinct Element Code, Version 6.0, User's Manual., *Itasca Consulting Group, Inc., Minneapolis.*
- Iverson, N. R. (1991), Potential effects of subglacial water-pressure fluctuations on quarrying, *Journal of Glaciology*, 37(125), 27-36.
- Iverson, N. R. (2012), A theory of glacial quarrying for landscape evolution models, *Geology*, doi:10.1130/g33079.1.
- Ivy-Ochs, S. (2015), Glacier variations in the European Alps at the end of the last glaciation, *Cuadernos de Investigacion Geografica*, 41(2), 295-315, doi:http://dx.doi.org/10.18172/cig.2750.
- Ivy-Ochs, S., H. Kerschner, A. Reuther, F. Preusser, K. Heine, M. Maisch, P. W. Kubik, and C. Schlüchter (2008), Chronology of the last glacial cycle in the European Alps, *Journal of Quaternary Science*, 23(6-7), 559-573, doi:10.1002/jqs.1202.
- Ivy-Ochs, S., H. Kerschner, M. Maisch, M. Christl, P. W. Kubik, and C. Schlüchter (2009a), Latest Pleistocene and Holocene glacier variations in the European Alps, *Quaternary Science Reviews*, 28(21-22), 2137-2149, doi:10.1016/j.quascirev.2009.03.009.
- Ivy-Ochs, S., A. v. Poschinger, H. A. Synal, and M. Maisch (2009b), Surface exposure dating of the Flims landslide, Graubünden, Switzerland, *Geomorphology*, 103(1), 104-112, doi:10.1016/j.geomorph.2007.10.024.
- Jaboyedoff, M., M.-H. Derron, J. Jakubowski, T. Oppikofer, and A. Pedrazzini (2012), *The 2006 Eiger rockslide, European Alps*, 1st ed. ed., Cambridge University Press, Cambridge.
- Jennings, J. E. (1970), A mathematical theory for the calculation of the stability of open cast mines, paper presented at Symp. on the Theoretical Background to the Planning of Open Pit Mines, Johannesburg.
- Jonas, T., C. Marty, and J. Magnusson (2009), Estimating the snow water equivalent from snow depth measurements in the Swiss Alps, *Journal of Hydrology*, 378(1-2), 161-167, doi:10.1016/j.jhydrol.2009.09.021.
- Kääb, A. (2002), Monitoring high-mountain terrain deformation from repeated air- and spaceborne optical data: examples using digital aerial imagery and ASTER data, *ISPRS Journal of Photogrammetry and Remote Sensing*, 57(1-2), 39-52, doi:10.1016/s0924-2716(02)00114-4.
- Kalenchuk, K. S., D. J. Hutchinson, and M. S. Diederichs (2013), Downie Slide: numerical simulation of groundwater fluctuations influencing the behaviour of a massive landslide, *Bulletin of Engineering Geology and the Environment*, 72(3), 397-412, doi:10.1007/s10064-013-0484-5.
- Kastrup, U., M. L. Zoback, N. Deichmann, K. F. Evans, D. Giardini, and A. J. Michael (2004), Stress field variations in the Swiss Alps and the northern Alpine foreland derived from inversion of fault plane solutions, *J. Geophys. Res.*, 109(B1), B01402, doi:10.1029/2003jb002550.
- Kelly, M. A., P. W. Kubik, F. Von Blanckenburg, and C. Schlüchter (2004), Surface exposure dating of the Great Aletsch Glacier Egesen moraine system, western Swiss Alps, using the cosmogenic nuclide <sup>10</sup>Be, *Journal of Quaternary Science*, 19(5), 431-441, doi:10.1002/jqs.854.
- Khan, S. A., L. Liu, J. Wahr, I. Howat, I. Joughin, T. van Dam, and K. Fleming (2010), GPS measurements of crustal uplift near Jakobshavn Isbræ due to glacial ice mass loss, *Journal of Geophysical Research: Solid Earth*, 115(B9), B09405, doi:10.1029/2010jb007490.
- Kos, A., F. Amann, T. Strozzi, R. Delaloye, J. von Ruetten, and S. Springman (2016), Contemporary glacier retreat triggers a rapid landslide response, Great Aletsch Glacier, Switzerland, *Geophysical Research Letters*, 43(24), 12,466-412,474, doi:10.1002/2016GL071708.
- Krautblatter, M., D. Funk, and F. K. Günzel (2013), Why permafrost rocks become unstable: a rock-ice-mechanical model in time and space, *Earth Surface Processes and Landforms*, 38(8), 876-887, doi:10.1002/esp.3374.
- Lang, H., B. Schädler, and G. Davidson (1976), Hydroglaciological Investigations on the Ewigschneefeld - Gr. Aletschgletscher, *Zeitschrift für Gletscherkunde und Glazialgeologie*, 12(2), 109-124.

- Lappegard, G., J. Kohler, M. Jackson, and J. O. Hagen (2006), Characteristics of subglacial drainage systems deduced from load-cell measurements, *Journal of Glaciology*, 52(176), 137-148, doi:10.3189/172756506781828908.
- Leith, K., J. R. Moore, F. Amann, and S. Loew (2014a), In situ stress control on microcrack generation and macroscopic extensional fracture in exhuming bedrock, *Journal of Geophysical Research: Solid Earth*, 119(1), 594-615, doi:10.1002/2012jb009801.
- Leith, K., J. R. Moore, F. Amann, and S. Loew (2014b), Subglacial extensional fracture development and implications for Alpine Valley evolution, *Journal of Geophysical Research: Earth Surface*, 119(1), 62-81, doi:10.1002/2012jf002691.
- Limpach, P., and A. Geiger (2016), Low-cost GNSS for Deformation and Geohazard Monitoring in the Swiss Alps, in *JISDM 2016*, edited, Vienna.
- Loew, S., F. Ebnetter, R. Bremen, M. Herfort, V. Lützenkirchen, and F. Matousek (2007), Annual opening and closure of alpine valleys, *Felsbau: rock and soil engineering*, 25(5), 60-65.
- Loew, S., and T. Strauhal (2014), Pore Pressure Transients in Brittle Translational Rockslides, in *Landslide Science for a Safer Geoenvironment*, edited by K. Sassa, P. Canuti and Y. Yin, pp. 115-122, Springer International Publishing, doi:10.1007/978-3-319-04996-0\_19.
- Loew, S., S. Gschwind, V. Gischig, A. Keller-Signer, and G. Valenti (2017a), Monitoring and early warning of the 2012 Preonzo catastrophic rockslope failure, *Landslides*, 14(1), 141-154, doi:10.1007/s10346-016-0701-y.
- Loew, S., V. S. Gischig, F. Glueer, R. Seifert, and J. R. Moore (2017b), Multidisciplinary monitoring of progressive failure processes in brittle rock slopes, in *Rock Mechanics and Engineering*, edited by X.-T. Feng and J. A. Hudson, CRC Press / Balkema -Taylor and Francis Group.
- Lorig, L. J., and P. A. Cundall (1989), Modeling of Reinforced Concrete Using the Distinct Element Method, in *Fracture of Concrete and Rock*, edited by S. P. Shah and S. E. Swartz, pp. 276-287, Springer New York, doi:10.1007/978-1-4612-3578-1\_28.
- Louis, C. (1969), A study of groundwater flow in jointed rock and its influence on the stability of rock masses, *Technical Report 9, Rock Mechanics*, Imperial College, London, United Kingdom.
- Masset, O., and S. Loew (2010), Hydraulic conductivity distribution in crystalline rocks, derived from inflows to tunnels and galleries in the Central Alps, Switzerland, *Hydrogeology Journal*, 18(4), 863-891, doi:10.1007/s10040-009-0569-1.
- McColl, S. T. (2012), Paraglacial rock-slope stability, *Geomorphology*, 153-154, 1-16, doi:10.1016/j.geomorph.2012.02.015.
- McColl, S. T., and T. R. H. Davies (2013), Large ice-contact slope movements: glacial buttressing, deformation and erosion, *Earth Surface Processes and Landforms*, 38(10), 1102-1115, doi:10.1002/esp.3346.
- McColl, S. T., T. R. H. Davies, and M. J. McSaveney (2010), Glacier retreat and rock-slope stability: debunking debuttressing, in *11th Congress of the International Association for Engineering Geology and the Environment*, edited by G. Active, pp. 467-474, Auckland, New Zealand.
- McColl, S. T., T. R. H. Davies, and M. J. McSaveney (2012), The effect of glaciation on the intensity of seismic ground motion, *Earth Surface Processes and Landforms*, 37(12), 1290-1301, doi:10.1002/esp.3251.
- Memin, A., Y. Rogister, J. Hinderer, M. Llubes, E. Berthier, and J. P. Boy (2009), Ground deformation and gravity variations modelled from present-day ice thinning in the vicinity of glaciers, *Journal of Geodynamics*, 48(3-5), 195-203, doi:10.1016/j.jog.2009.09.006.
- Min, K.-B., J. Rutqvist, C.-F. Tsang, and L. Jing (2004), Stress-dependent permeability of fractured rock masses: a numerical study, *International Journal of Rock Mechanics and Mining Sciences*, 41(7), 1191-1210, doi:http://dx.doi.org/10.1016/j.ijrmms.2004.05.005.

- Moore, D. P. (1999), Rock slopes and reservoirs - lessons learned, paper presented at 13th Annual Vancouver Geotechnical Society Symposium, BiTech Publishers Ltd., Vancouver, BC (Canada).
- Müller, L. (1964), The rock slide in the Vajont valley, *Rock Mechanics and Rock Engineering*, 2, 148-212.
- Murray, T., and G. K. C. Clarke (1995), Black-box modeling of the subglacial water system, *J. Geophys. Res.*, 100(B6), 10231-10245, doi:10.1029/95jb00671.
- Nicolussi, K., and C. Schlüchter (2012), The 8.2 ka event—Calendar-dated glacier response in the Alps, *Geology*, doi:10.1130/g32406.1.
- Nye, J. F. (1973), Water at the bed of a glacier, *International Association of Scientific Hydrology Publication*, 95, 189-194.
- Offerding, U. S., P. Renard, and S. Loew (2014), Hydraulic subsurface measurements and hydrodynamic modelling as indicators for groundwater flow systems in the Rotondo granite, Central Alps (Switzerland), *Hydrological Processes*, 28(2), 255-278, doi:10.1002/hyp.9568.
- Oppikofer, T., M. Jaboyedoff, and H.-R. Keusen (2008), Collapse at the eastern Eiger flank in the Swiss Alps, *Nature Geosci*, 1(8), 531-535, doi: 10.1038/ngeo258.
- Prager, C., C. Zangerl, G. Patzelt, and R. Brandner (2008), Age distribution of fossil landslides in the Tyrol (Austria) and its surrounding areas, *Nat. Hazards Earth Syst. Sci.*, 8(2), 377-407, doi:10.5194/nhess-8-377-2008.
- Preisig, G., F. Joel Cornaton, and P. Perrochet (2012), Regional Flow Simulation in Fractured Aquifers Using Stress-Dependent Parameters, *Ground Water*, 50(3), 376-385, doi:10.1111/j.1745-6584.2011.00853.x.
- Preisig, G., E. Eberhardt, M. Smithyman, A. Preh, and L. Bonzanigo (2016), Hydromechanical Rock Mass Fatigue in Deep-Seated Landslides Accompanying Seasonal Variations in Pore Pressures, *Rock Mechanics and Rock Engineering*, 1-19, doi:10.1007/s00603-016-0912-5.
- Röthlisberger, F., and W. Schneebeli (1979), Genesis of lateral moraine complexes, demonstrated by fossil soils and trunks: Indicators of postglacial climatic fluctuations, in *Moraines and Varves; Origin, Genesis, Classification*, edited by C. Schlüchter, pp. 387-419, A.A. Balkema, Rotterdam, Netherlands.
- Röthlisberger, H. (1972), Water Pressure in Intra- and Subglacial Channels, *Journal of Glaciology*, 11(62), 177-203.
- Rouyet, L., L. Kristensen, M.-H. Derron, C. Michoud, L. H. Blikra, M. Jaboyedoff, and T. R. Lauknes Evidence of rock slope breathing using ground-based InSAR, *Geomorphology*, doi:http://dx.doi.org/10.1016/j.geomorph.2016.07.005.
- Sanders, J. W., K. M. Cuffey, J. R. Moore, K. R. MacGregor, and J. L. Kavanaugh (2012), Periglacial weathering and headwall erosion in cirque glacier bergschrunds, *Geology*, doi:10.1130/g33330.1.
- Schimmelpfennig, I., J. M. Schaefer, N. Akçar, S. Ivy-Ochs, R. C. Finkel, and C. Schlüchter (2012), Holocene glacier culminations in the Western Alps and their hemispheric relevance, *Geology*, doi:10.1130/g33169.1.
- Schimmelpfennig, I., J. M. Schaefer, N. Akçar, T. Koffman, S. Ivy-Ochs, R. Schwartz, R. C. Finkel, S. Zimmerman, and C. Schlüchter (2014), A chronology of Holocene and Little Ice Age glacier culminations of the Steingletscher, Central Alps, Switzerland, based on high-sensitivity beryllium-10 moraine dating, *Earth and Planetary Science Letters*, 393, 220-230, doi:http://dx.doi.org/10.1016/j.epsl.2014.02.046.
- Schindelwig, I., N. Akçar, P. W. Kubik, and C. Schlüchter (2012), Lateglacial and early Holocene dynamics of adjacent valley glaciers in the Western Swiss Alps, *Journal of Quaternary Science*, 27(1), 114-124, doi:10.1002/jqs.1523.
- Schmid, O. (1988), Hydrogeologische Untersuchung im Gebiet Oberaletsch-Gibidum, *Geotechnical Report*, 9 pp.
- Schmid, O. (1989), Hydrogeologischer Bericht: Sesselbahn Biel-Mossflue, Steli-Quellen, Riederalp, *Geotechnical Report*, 8 pp.

- Schnider, F. (2013), Hydrochemie im periglazialen Aletschgebiet, 42 pp, *BSc thesis*, ETH Zurich, Zurich.
- Schommer, P. (1976), Wasserspiegelmessungen im Firn des Ewigschneefeldes (Schweizer Alpen) 1976, *Zeitschrift für Gletscherkunde und Glazialgeologie*, 12(2), 125-141.
- Selvadurai, A. P. S., A. P. Suvorov, and P. A. Selvadurai (2015), Thermo-hydro-mechanical processes in fractured rock formations during a glacial advance, *Geosci. Model Dev.*, 8(7), 2167-2185, doi:10.5194/gmd-8-2167-2015.
- Solomina, O. N., et al. (2015), Holocene glacier fluctuations, *Quaternary Science Reviews*, 111, 9-34, doi:http://dx.doi.org/10.1016/j.quascirev.2014.11.018.
- Steck, A. (2011), 1269 Aletschgletscher mit Teil von 1249 Finsteraarhorn, *Geologischer Atlas der Schweiz 1:25000*.
- Strauhal, T., S. Loew, M. Holzmann, and C. Zangerl (2015), Detailed hydrogeological analysis of a deep-seated rockslide at the Gepatsch reservoir (Klasgarten, Austria), *Hydrogeology Journal*, 1-23, doi:10.1007/s10040-015-1341-3.
- Strozzi, T., R. Delaloye, A. Käab, C. Ambrosi, E. Perruchoud, and U. Wegmüller (2010), Combined observations of rock mass movements using satellite SAR interferometry, differential GPS, airborne digital photogrammetry, and airborne photography interpretation, *J. Geophys. Res.*, 115(F1), F01014, doi:10.1029/2009jf001311.
- Sugiyama, S., and G. H. Gudmundsson (2004), Short-term variations in glacier flow controlled by subglacial water pressure at Lauteraargletscher, Bernese Alps, Switzerland, *Journal of Glaciology*, 50(170), 353-362.
- Sugiyama, S., S. Tsutaki, D. Nishimura, H. Blatter, A. Bauder, and M. Funk (2008), Hot water drilling and glaciological observations at the terminal part of Rhonegletscher, Switzerland in 2007, *Bulletin of Glaciological Research*, 26, 41-47.
- Terzaghi, K. (1923), Die Berechnung der Durchlässigkeitsziffer der Tone aus dem Verlauf der hydrodynamischen Spannungserscheinungen, *Akad. Wissensch. Wien Sitzungsberichte*, Math.naturwissensch. Klasse, Ila 142, No. 3-4, 125-138.
- Tulaczyk, S., W. B. Kamb, and H. F. Engelhardt (2000), Basal mechanics of Ice Stream B, West Antarctica 1. Till mechanics, *J. Geophys. Res.*, 105(B1), 463-481, doi:10.1029/1999jb900329.
- Vidstrand, P., T. Wallroth, and L. Ericsson (2008), Coupled HM effects in a crystalline rock mass due to glaciation: indicative results from groundwater flow regimes and stresses from an FEM study, *Bulletin of Engineering Geology and the Environment*, 67(2), 187-197, doi:10.1007/s10064-008-0123-8.
- Walter, F., N. Deichmann, and M. Funk (2008), Basal icequakes during changing subglacial water pressures beneath Gornergletscher, Switzerland, *Journal of Glaciology*, 54(186), 511-521.
- Watson, A. D., J. F. Psutka, T. W. Stewart, and D. P. Moore (2007), Investigations And Monitoring of Rock Slopes At Checkerboard Creek And Little Chief Slide, in *ARMA 2007*, edited, p. 9, American Rock Mechanics Association.
- Weertman, J. (1957), On the sliding of glaciers, *Journal of Glaciology*, 3(21), 33-38.
- Wegmann, M., G. H. Gudmundsson, and W. Haeberli (1998), Permafrost changes in rock walls and the retreat of alpine glaciers: a thermal modelling approach, *Permafrost and Periglacial Processes*, 9(1), 23-33, doi:10.1002/(sici)1099-1530(199801/03)9:1<23::aid-ppp274>3.0.co;2-y.
- Welch, L. A., and D. M. Allen (2014), Hydraulic conductivity characteristics in mountains and implications for conceptualizing bedrock groundwater flow, *Hydrogeology Journal*, 22(5), 1003-1026, doi:10.1007/s10040-014-1121-5.
- Werder, M. A., I. J. Hewitt, C. G. Schoof, and G. E. Flowers (2013), Modeling channelized and distributed subglacial drainage in two dimensions, *Journal of Geophysical Research: Earth Surface*, 118(4), 2140-2158, doi:10.1002/jgrf.20146.

- Wirsig, C., J. Zasadni, M. Christl, N. Akçar, and S. Ivy-Ochs (2016), Dating the onset of LGM ice surface lowering in the High Alps, *Quaternary Science Reviews*, 143, 37-50, doi:<http://dx.doi.org/10.1016/j.quascirev.2016.05.001>.
- Zangerl, C., E. Eberhardt, and S. Loew (2003), Ground settlements above tunnels in fractured crystalline rock: numerical analysis of coupled hydromechanical mechanisms, *Hydrogeology Journal*, 11(1), 162-173, doi:10.1007/s10040-002-0234-4.
- Zangerl, C., E. Eberhardt, K. F. Evans, and S. Loew (2008a), Consolidation settlements above deep tunnels in fractured crystalline rock: Part 2—Numerical analysis of the Gotthard highway tunnel case study, *International Journal of Rock Mechanics and Mining Sciences*, 45(8), 1211-1225, doi:<http://dx.doi.org/10.1016/j.ijrmms.2008.02.005>.
- Zangerl, C., K. F. Evans, E. Eberhardt, and S. Loew (2008b), Consolidation settlements above deep tunnels in fractured crystalline rock: Part 1—Investigations above the Gotthard highway tunnel, *International Journal of Rock Mechanics and Mining Sciences*, 45(8), 1195-1210, doi:<http://dx.doi.org/10.1016/j.ijrmms.2008.02.002>.
- Zangerl, C., E. Eberhardt, and S. Perzlmaier (2010), Kinematic behaviour and velocity characteristics of a complex deep-seated crystalline rockslide system in relation to its interaction with a dam reservoir, *Engineering Geology*, 112(1–4), 53-67, doi:<http://dx.doi.org/10.1016/j.enggeo.2010.01.001>.
- Zhang, D., G. Wang, T. Yang, M. Zhang, S. Chen, and F. Zhang (2013), Satellite remote sensing-based detection of the deformation of a reservoir bank slope in Laxiwa Hydropower Station, China, *Landslides*, 10(2), 231-238, doi:10.1007/s10346-012-0378-9.

## 5 CONCLUSIONS

### 5.1 Summary

Using numerical models based on the Aletsch Glacier in Switzerland, our results extend simplified assumptions of glacial debuitressing. We demonstrate how glacial loading cycles in concert with thermo-hydro-mechanical effects drive paraglacial rock slope damage and act as preparatory factors for paraglacial rock slope instabilities. Major outcomes of our study include:

1. Steeply dipping foliation with parallel brittle-ductile faults provides the geological predisposition for several rock slope instabilities in the Aletsch valley. Active landslides are concentrated on both valley flanks around the retreating, present-day terminus of the Great Aletsch Glacier. After LGM deglaciation, the surrounding rock walls of the Aletsch valley experienced several minor glacier cycles during the Holocene. Using relative age constraints and surface exposure dating at one site, the majority of instabilities are believed to have a post-Egesen and pre-LIA initiation age.
2. We simulated rock slope stability during repeat glacier cycles representing Lateglacial and Holocene ice fluctuations with numerical models. We argued for the use of stress boundary conditions to appropriately simulate the ductile behavior of ice and its limited buttressing effect. Furthermore, we emphasized proper initialization under ice-free conditions, representing the penultimate Eemian interglacial period. Our models demonstrate that purely mechanical loading and unloading by glacier ice generates relatively limited new damage. However, glacial erosion (i.e., rock debuitressing) generates significant new damage during first deglaciation. A rock slope with reduced rock mass strength is more susceptible to damage from glacier loading cycles, which may destabilize the slope with kinematics and dimensions of rock slope instabilities resembling observations in the field at Aletsch. Ice advance and retreat both generate damage, but with different damage kinematics: ice advance favors toppling while retreat promotes sliding.
3. Bedrock in contact with temperate ice is near isothermal at  $\sim 0$  °C, and shielded from daily and seasonal temperature cycles. Glacier retreat exposes rock walls to new thermal boundary conditions, a transition termed *paraglacial thermal shock*. We demonstrated in our models that subsurface temperature changes on glacial time scales can generate rock mass damage through thermo-mechanical coupled stresses. Glacier advances are most effective in producing rock slope damage as cooling drives contraction of subglacial bedrock reducing joint normal stresses and promoting toppling. Furthermore, thermal shock during deglaciation creates a shallow damage front as bedrock is first exposed to annual temperature cycles. Thermal stress cycles in concert with glacier load fluctuations result in enhanced slope displacement.
4. Subglacial water pressures near the ice overburden level alter groundwater conditions in adjacent rock slopes. Groundwater changes in concert with glacier cycles, with superimposed annual water table variations. Reducing or increasing effective joint stresses in combination with changing in-situ stresses from ice fluctuations drives substantial rock slope damage. Increased joint water pressure during glacier advances reduces joint normal stresses, partly compensating the buttressing effect of ice. Furthermore, we demonstrate the effectiveness of hydro-mechanical fatigue in parallel with glacier loading cycles in propagating rock slope damage.

Glaciers make a poor buttress for proximal alpine valley rock slopes, and variations in loading by the weight of ice have limited damage effect. However, we demonstrated that glacial cycles in concert with thermo-hydro-mechanical effects can significantly contribute to new damage and aiding the development of paraglacial rock slope failures.

## 5.2 Outlook

We have thoroughly evaluated glacier cycles as preparatory factor for paraglacial rock slope instabilities using extensive modeling studies based on field observations. However, open questions and additional verification of our model predictions invites further research on this topic:

Today's observations in the landscape represent only a snapshot of the investigated processes acting over glacial time scales. Long-term *in-situ* monitoring data from an alpine rock slope in the vicinity of a currently retreating glacier can provide valuable insight into the mechanics of these thermo-hydro-mechanical processes during deglaciation. Because of relatively high present-day glacier retreat rates, a feasible monitoring period may reveal long-term trends, although current glacier changes are small compared to Lateglacial and Holocene ice fluctuations. Boreholes in the bedrock near the glacier margin may allow for direct detection of incremental slope displacement, ground temperature change and groundwater variations during glacier retreat. We expect long-term trends in the slope response superimposed by seasonal fluctuations with changing thermal and hydraulic boundary conditions during ice retreat. In addition, acoustic emission detection may be used to identify potential fracture propagation in bedrock [e.g., Girard *et al.*, 2013]. Monitoring data can be used to further calibrate and verify expected slope behavior from this and future modeling studies.

In addition to fluctuating glacial ice loads in concert with thermo-hydro-mechanical stress cycles, other potential preparatory factors for paraglacial rock instabilities may also be important. Repeat seismic activity can act as a rock slope fatigue process [Gischig *et al.*, 2015], and glacier ice has been suggested to affect seismic ground motion in adjacent rock slopes [McColl *et al.*, 2012]. Lake sediment records show evidence for enhanced earthquake activity during post-glacial periods, suggested to be caused by isostatic rebound [Monecke *et al.*, 2006; Strasser *et al.*, 2013]. Increased seismicity in combination with amplified seismic ground motion of a deglaciated valley slope [McColl *et al.*, 2012] may be an additional important preparatory factor and should be considered in future studies.



## 6 BIBLIOGRAPHY

- Alley, R. B., D. E. Lawson, G. J. Larson, E. B. Evenson, and G. S. Baker (2003), Stabilizing feedbacks in glacier-bed erosion, *Nature*, 424(6950), 758-760.
- Augustinus, P. C. (1995), Glacial valley cross-profile development: the influence of in situ rock stress and rock mass strength, with examples from the Southern Alps, New Zealand, *Geomorphology*, 14(2), 87-97, doi:10.1016/0169-555x(95)00050-x.
- Ballantyne, C. K. (2002), Paraglacial geomorphology, *Quaternary Science Reviews*, 21(18–19), 1935-2017, doi:10.1016/s0277-3791(02)00005-7.
- Ballantyne, C. K., G. F. Sandeman, J. O. Stone, and P. Wilson (2014a), Rock-slope failure following Late Pleistocene deglaciation on tectonically stable mountainous terrain, *Quaternary Science Reviews*, 86, 144-157, doi:http://dx.doi.org/10.1016/j.quascirev.2013.12.021.
- Ballantyne, C. K., P. Wilson, D. Gheorghiu, and À. Rodés (2014b), Enhanced rock-slope failure following ice-sheet deglaciation: timing and causes, *Earth Surface Processes and Landforms*, 39(7), 900-913, doi:10.1002/esp.3495.
- Baroni, C., S. Martino, M. C. Salvatore, G. Scarascia Mugnozza, and L. Schilirò (2014), Thermomechanical stress–strain numerical modelling of deglaciation since the Last Glacial Maximum in the Adamello Group (Rhaetian Alps, Italy), *Geomorphology*, 226, 278-299, doi:http://dx.doi.org/10.1016/j.geomorph.2014.08.013.
- Boulton, G., and J. Hartikainen (2004), Thermo-Hydro-Mechanical Impacts of Coupling Between Glaciers and Permafrost, in *Elsevier Geo-Engineering Book Series*, edited by S. Ove, pp. 293-298, Elsevier, doi:http://dx.doi.org/10.1016/S1571-9960(04)80056-9.
- Boulton, G., T. Chan, R. Christiansson, L. O. Ericsson, J. Hartikainen, M. R. Jensen, F. W. Stanchell, and T. Wallroth (2004), Thermo-Hydro-Mechanical (T-H-M) Impacts of Glaciation and Implications for Deep Geologic Disposal of Nuclear Waste, in *Elsevier Geo-Engineering Book Series*, edited by S. Ove, pp. 299-304, Elsevier, doi:http://dx.doi.org/10.1016/S1571-9960(04)80057-0.
- Bovis, M. J. (1990), Rock-slope deformation at Affliction Creek, southern Coast Mountains, British Columbia, *Canadian Journal of Earth Sciences*, 27(2), 243-254, doi:10.1139/e90-024.
- Chan, T., R. Christiansson, G. S. Boulton, L. O. Ericsson, J. Hartikainen, M. R. Jensen, D. Mas Ivars, F. W. Stanchell, P. Vistrand, and T. Wallroth (2005), DECOVALEX III BMT3/BENCHPAR WP4: The thermo-hydro-mechanical responses to a glacial cycle and their potential implications for deep geological disposal of nuclear fuel waste in a fractured crystalline rock mass, *International Journal of Rock Mechanics and Mining Sciences*, 42(5–6), 805-827, doi:http://dx.doi.org/10.1016/j.ijrmmms.2005.03.017.
- Clayton, M. A., D. Stead, and D. Kinakin (2013), The Mitchell Creek Landslide, B.C., Canada: Investigation using Remote Sensing and Numerical Modeling, in *47th U.S. Rock Mechanics/Geomechanics Symposium*, edited, American Rock Mechanics Association, San Francisco, California.
- Cohen, D., T. S. Hooyer, N. R. Iverson, J. F. Thomason, and M. Jackson (2006), Role of transient water pressure in quarrying: A subglacial experiment using acoustic emissions, *J. Geophys. Res.*, 111(F3), F03006, doi:10.1029/2005jf000439.
- Collins, B. D., and G. M. Stock (2016), Rockfall triggering by cyclic thermal stressing of exfoliation fractures, *Nature Geoscience*, advance online publication, doi:10.1038/ngeo2686.
- Cossart, E., R. Braucher, M. Fort, D. L. Bourlès, and J. Carcaillet (2008), Slope instability in relation to glacial debuttressing in alpine areas (Upper Durance catchment, southeastern France): Evidence from field data and <sup>10</sup>Be cosmic ray exposure ages, *Geomorphology*, 95(1–2), 3-26, doi:10.1016/j.geomorph.2006.12.022.
- Eberhardt, E., G. Preisig, and V. Gischig (2016), Progressive failure in deep-seated rockslides due to seasonal fluctuations in pore pressures and rock mass fatigue, in *Landslides and Engineered Slopes. Experience, Theory and Practice*, edited, pp. 121-136, CRC Press, doi:doi:10.1201/b21520-13.

- Eppes, M. C., B. Magi, B. Hallet, E. Delmelle, P. Mackenzie-Helnwein, K. Warren, and S. Swami (2016), Deciphering the role of solar-induced thermal stresses in rock weathering, *Geological Society of America Bulletin*, doi:10.1130/b31422.1.
- Evans, S. G., and J. J. Clague (1994), Recent climatic change and catastrophic geomorphic processes in mountain environments, *Geomorphology*, 10(1–4), 107-128, doi:10.1016/0169-555x(94)90011-6.
- Fountain, A. G., and J. S. Walder (1998), Water flow through temperate glaciers, *Rev. Geophys.*, 36(3), 299-328, doi:10.1029/97rg03579.
- Fudge, T. J., J. T. Harper, N. F. Humphrey, and W. T. Pfeffer (2005), Diurnal water-pressure fluctuations: timing and pattern of termination below Bench Glacier, Alaska, USA, *Annals of Glaciology*, 40(1), 102-106, doi:10.3189/172756405781813799.
- Girard, L., S. Gruber, S. Weber, and J. Beutel (2013), Environmental controls of frost cracking revealed through in situ acoustic emission measurements in steep bedrock, *Geophysical Research Letters*, 40(9), 1748-1753, doi:10.1002/grl.50384.
- Gischig, V. S., J. R. Moore, K. F. Evans, F. Amann, and S. Loew (2011a), Thermomechanical forcing of deep rock slope deformation: 1. Conceptual study of a simplified slope, *J. Geophys. Res.*, 116(F4), F04010, doi:10.1029/2011jf002006.
- Gischig, V. S., J. R. Moore, K. F. Evans, F. Amann, and S. Loew (2011b), Thermomechanical forcing of deep rock slope deformation: 2. The Randa rock slope instability, *J. Geophys. Res.*, 116(F4), F04011, doi:10.1029/2011jf002007.
- Gischig, V., G. Preisig, and E. Eberhardt (2015), Numerical Investigation of Seismically Induced Rock Mass Fatigue as a Mechanism Contributing to the Progressive Failure of Deep-Seated Landslides, *Rock Mechanics and Rock Engineering*, 1-22, doi:10.1007/s00603-015-0821-z.
- Gruber, S., and W. Haeberli (2007), Permafrost in steep bedrock slopes and its temperature-related destabilization following climate change, *J. Geophys. Res.*, 112(F2), F02S18, doi:10.1029/2006jf000547.
- Guglielmi, Y., F. Cappa, and S. Binet (2005), Coupling between hydrogeology and deformation of mountainous rock slopes: Insights from La Clapière area (southern Alps, France), *Comptes Rendus Geoscience*, 337(13), 1154-1163, doi:10.1016/j.crte.2005.04.016.
- Gunzburger, Y., V. Merrien-Soukatchoff, and Y. Guglielmi (2005), Influence of daily surface temperature fluctuations on rock slope stability: case study of the Rochers de Valabres slope (France), *International Journal of Rock Mechanics and Mining Sciences*, 42(3), 331-349, doi:10.1016/j.ijrmms.2004.11.003.
- Hallet, B. (1996), Glacial quarrying: a simple theoretical model, *Annals of Glaciology*, 22, 1-8.
- Harper, J. T., N. F. Humphrey, W. T. Pfeffer, T. Fudge, and S. O'Neel (2005), Evolution of subglacial water pressure along a glacier's length, *Annals of Glaciology*, 40(1), 31-36, doi:10.3189/172756405781813573.
- Harrison, J. C., and K. Herbst (1977), Thermoelastic strains and tilts revisited, *Geophysical Research Letters*, 4(11), 535-537, doi:10.1029/GL004i011p00535.
- Herman, F., O. Beyssac, M. Brughelli, S. N. Lane, S. Leprince, T. Adatte, J. Y. Y. Lin, J.-P. Avouac, and S. C. Cox (2015), Erosion by an Alpine glacier, *Science*, 350(6257), 193-195, doi:10.1126/science.aab2386.
- Holm, K., M. Bovis, and M. Jakob (2004), The landslide response of alpine basins to post-Little Ice Age glacial thinning and retreat in southwestern British Columbia, *Geomorphology*, 57(3–4), 201-216, doi:10.1016/s0169-555x(03)00103-x.
- Iverson, N. R. (1991), Potential effects of subglacial water-pressure fluctuations on quarrying, *Journal of Glaciology*, 37(125), 27-36.
- Iverson, N. R. (2012), A theory of glacial quarrying for landscape evolution models, *Geology*, doi:10.1130/g33079.1.

- Ivy-Ochs, S., A. v. Poschinger, H. A. Synal, and M. Maisch (2009), Surface exposure dating of the Flims landslide, Graubünden, Switzerland, *Geomorphology*, 103(1), 104-112, doi:10.1016/j.geomorph.2007.10.024.
- Jaboyedoff, M., M.-H. Derron, J. Jakubowski, T. Oppikofer, and A. Pedrazzini (2012), *The 2006 Eiger rockslide, European Alps*, 1st ed. ed., Cambridge University Press, Cambridge.
- Leith, K., J. R. Moore, F. Amann, and S. Loew (2014), Subglacial extensional fracture development and implications for Alpine Valley evolution, *Journal of Geophysical Research: Earth Surface*, 119(1), 62-81, doi:10.1002/2012jf002691.
- McColl, S. T. (2012), Paraglacial rock-slope stability, *Geomorphology*, 153–154, 1-16, doi:10.1016/j.geomorph.2012.02.015.
- McColl, S. T., and T. R. H. Davies (2013), Large ice-contact slope movements: glacial buttressing, deformation and erosion, *Earth Surface Processes and Landforms*, 38(10), 1102-1115, doi:10.1002/esp.3346.
- McColl, S. T., T. R. H. Davies, and M. J. McSaveney (2010), Glacier retreat and rock-slope stability: debunking debuttressing, in *11th Congress of the International Association for Engineering Geology and the Environment*, edited by G. Active, pp. 467-474, Auckland, New Zealand.
- McColl, S. T., T. R. H. Davies, and M. J. McSaveney (2012), The effect of glaciation on the intensity of seismic ground motion, *Earth Surface Processes and Landforms*, 37(12), 1290-1301, doi:10.1002/esp.3251.
- Monecke, K., F. Anselmetti, A. Becker, M. Schnellmann, M. Sturm, and D. Giardini (2006), Earthquake-induced deformation structures in lake deposits: A Late Pleistocene to Holocene paleoseismic record for Central Switzerland, *Eclogae Geol Helv*, 99(3), 343-362, doi:10.1007/s00015-006-1193-x.
- Murton, J. B., R. Peterson, and J.-C. Ozouf (2006), Bedrock Fracture by Ice Segregation in Cold Regions, *Science*, 314(5802), 1127-1129, doi:10.1126/science.1132127.
- Nicholson, D. T. (2008), Rock control on microweathering of bedrock surfaces in a periglacial environment, *Geomorphology*, 101(4), 655-665, doi:10.1016/j.geomorph.2008.03.009.
- Oppikofer, T., M. Jaboyedoff, and H.-R. Keusen (2008), Collapse at the eastern Eiger flank in the Swiss Alps, *Nature Geosci*, 1(8), 531-535, doi: 10.1038/ngeo258.
- Prager, C., C. Zangerl, G. Patzelt, and R. Brandner (2008), Age distribution of fossil landslides in the Tyrol (Austria) and its surrounding areas, *Nat. Hazards Earth Syst. Sci.*, 8(2), 377-407, doi:10.5194/nhess-8-377-2008.
- Preisig, G., E. Eberhardt, M. Smithyman, A. Preh, and L. Bonzanigo (2016), Hydromechanical Rock Mass Fatigue in Deep-Seated Landslides Accompanying Seasonal Variations in Pore Pressures, *Rock Mechanics and Rock Engineering*, 1-19, doi:10.1007/s00603-016-0912-5.
- Selvadurai, A. P. S., A. P. Suvorov, and P. A. Selvadurai (2015), Thermo-hydro-mechanical processes in fractured rock formations during a glacial advance, *Geosci. Model Dev.*, 8(7), 2167-2185, doi:10.5194/gmd-8-2167-2015.
- Strasser, M., K. Monecke, M. Schnellmann, and F. S. Anselmetti (2013), Lake sediments as natural seismographs: A compiled record of Late Quaternary earthquakes in Central Switzerland and its implication for Alpine deformation, *Sedimentology*, 60(1), 319-341, doi:10.1111/sed.12003.
- Strozzi, T., R. Delaloye, A. Käab, C. Ambrosi, E. Perruchoud, and U. Wegmüller (2010), Combined observations of rock mass movements using satellite SAR interferometry, differential GPS, airborne digital photogrammetry, and airborne photography interpretation, *J. Geophys. Res.*, 115(F1), F01014, doi:10.1029/2009jf001311.
- Vidstrand, P., T. Wallroth, and L. Ericsson (2008), Coupled HM effects in a crystalline rock mass due to glaciation: indicative results from groundwater flow regimes and stresses from an FEM study, *Bulletin of Engineering Geology and the Environment*, 67(2), 187-197, doi:10.1007/s10064-008-0123-8.
- Weertman, J. (1957), On the sliding of glaciers, *Journal of Glaciology*, 3(21), 33-38.

Wegmann, M., G. H. Gudmundsson, and W. Haeberli (1998), Permafrost changes in rock walls and the retreat of alpine glaciers: a thermal modelling approach, *Permafrost and Periglacial Processes*, 9(1), 23-33, doi:10.1002/(sici)1099-1530(199801/03)9:1<23::aid-ppp274>3.0.co;2-y.

## Acknowledgements

First I would like to thank Prof. Simon Löw for granting me the possibility to do research at the most beautiful field site in the Swiss Alps and supporting me during this time. Special gratitude goes to Jeff Moore, who introduced me to the world of science and guided me on my scientific path. He supported and motivated me throughout my Ph.D., even when an ocean lay between our offices. I am very grateful for the time and energy he invested in this project. His ideas, enthusiasm and inspiration were the driving engine of this project. Special thanks also to Valentin Gischig for inviting me to UBC in Vancouver and handing me the necessary tools to address our research questions. His inputs, modeling expertise and constant support contributed strongly to the success of this study. Thank you to Susan Ivy-Ochs for your insights on the Quaternary and all our friendly chats. I also would like to thank Florian Amann for sharing his great expertise in rock mechanics and modeling. Many thanks to Kerry Leith for sharing ideas and for fruitful discussions. Thank you Matt Perras for experimenting with me in the rock laboratory. Gratitude further goes to Prof. Oliver Korup for acting as the external co-referee on my thesis committee.

The value of this study was increased greatly through collaborations with other researchers for which we are very thankful. Philippe Limpach from IGP tested his newly developed GNSS stations at Aletsch and thereby enabled the collection of novel field data. Besides sharing his knowledge about glaciers, Prof. Martin Funk from VAW was willing to drill with us through the Great Aletsch Glacier. With the help of his team (Thomas Wyder and Roger Loertscher) this intense glacier drilling campaign was a success and a great experience. Many thanks to Marcus Christl from the LIP who provided us with  $^{10}\text{Be}$  accelerator mass spectrometry measurements and Christian Wirsig for his help in the lab. Thanks to Reto Seifert and Stewart Bishop for help with monitoring installations. Very special thanks to Johnny Sanders for accompanying me on so many field visits. I will never forget our adventurous trip to the Driest hut, collecting rock samples dangling from the rope on the cliff. Furthermore, I would like to thank to Franziska Glüer for many demanding but wonderful shared field experiences, working also in the Aletsch region, as well as the Master students contributing to the overall project (Andrea Alpiger, Maité Eisner, Matthias Vogler). Thanks to Marc Hoffmann, Jörg Donau and Stephan Bolay for their assistance in the field.

I would like to thank to the engineering geology group for many amusing lunch hours and enjoyable discussions during coffee breaks. I am grateful to my fellow students and office mates, who shared with me the ups and downs during everyone's Ph.D. (Kerry Leith, Reto Thöny, Martin Ziegler, Santos Jiménez Parras, Franziska Dammeier, Katrin Wild, Peter Achtziger, Linwei Hu, Jaime Rivera Cardona, Sophie Gschwind, Franziska Glüer, Mark Somogyvari, Daniel Vogler, Benedetta Dini and Mohammad Afshari Moein, Hannes Krietsch, Bernard Brixel and Larissa de Palézieux dit Falconnet).

Special thanks to my parents, Urs and Ruth, who made it possible for me to study in the first place and supported me on my path. The help of Mira and Patric in the field was also greatly appreciated. Finally, my warmest thanks to Szandra, who I met during my last year at ETH, accompanying me and making this a lovely experience.



# Curriculum Vitae

Lorenz M. Grämiger

Born on 29. October 1986 in Sarnen, Switzerland

10/2016 – present	Geologist at the geological consulting company Dr. von Moos AG, Zurich
03/2012 – 09/2016	Ph.D. Engineering Geology, Department of Earth Sciences, ETH Zurich
08/2010 – 03/2012	M.Sc. Earth Sciences, Major in Engineering Geology, ETH Zurich
06/2007 – 08/2010	B.Sc. Earth Sciences, ETH Zurich

## Publications

### *Peer Reviewed Journals:*

Grämiger, L. M., J. R. Moore, V. Gischig, S. Loew, M. Funk, and P. Limpach (2017), Beyond debuttreassing: Hydro-mechanical rock slope damage during repeat glacial cycles, *in preparation*.

Grämiger, L. M., J. R. Moore, V. Gischig, and S. Loew (2017), Beyond debuttreassing: Thermo-mechanical rock slope damage during repeat glacial cycles, *under review at Journal for Geophysical Research, Earth Surface*, Manuscript # 2016JF004029.

Grämiger, L. M., J. R. Moore, V. Gischig, S. Ivy-Ochs, and S. Loew (2017), Beyond debuttreassing: Mechanics of paraglacial rock slope damage during repeat glacial cycles, *under review at Journal for Geophysical Research, Earth Surface*, Manuscript # 2016JF003967.

Grämiger, L. M., J.R. Moore, C. Vockenhuber, J. Aaron, I. Hajdas, and S. Ivy-Ochs (2016). Two early Holocene rock avalanches in the Bernese Alps (Rinderhorn, Switzerland). *Geomorphology* 268, 207-221.

### *Conference Abstracts:*

Grämiger, L. M., J.R. Moore, V.S. Gischig, and S. Loew (2016). Paraglacial rock mass damage during repeat glacial cycles in preparing slope instabilities (Aletsch region, Switzerland). *Geophysical Research Abstracts*, Vol. 18, EGU2016-15114.

Vogler, M., S. Loew, F. Glueer, and L. M. Grämiger (2016). Glacial Debuttreassing and Displacement History of the Driest Rockslide (Central Alps, Switzerland). *Geophysical Research Abstracts*, Vol. 18, EGU2016-8040-1.

Selçuk, A., S. Ivy-Ochs, K. Hippe, L. M. Grämiger, and C. Vockenhuber (2016). The Geomorphological Evolution of a Landscape in a Tectonically Active Region: the Sennwald Landslide. *Geophysical Research Abstracts*, Vol. 18, EGU2016-13112.

Grämiger, L. M., J.R. Moore, V.S. Gischig, and S. Loew (2015). Thermo-hydro-mechanical stresses during repeat glacial cycles as preparatory factors for paraglacial rock slope instabilities. Geophysical Research Abstracts, Vol. 17, EGU2015-8831-1.

Grämiger, L. M., M.A. Perras, J.R. Moore, and S. Loew (2015). Cyclic Fatigue Testing for Application for paraglacial rock slope stability modelling. Geophysical Research Abstracts, Vol. 17, EGU2015-15551.

Grämiger, L. M., J.R. Moore, V.S. Gischig, and S. Loew (2014). Thermo-hydro-mechanical stresses and induced rock mass damage during repeat glacial cycles. Proceedings 3<sup>rd</sup> Slope Tectonics Conference, 8-12 September 2014, Trondheim, Norway.

Grämiger, L. M., J.R. Moore, and S. Ivy-Ochs (2012). Prehistoric rock avalanches at Rinderhorn, Switzerland. Geophysical Research Abstracts, Vol. 14, EGU2012-10769.

*Monographs:*

Grämiger, L.M. (2010). Prädisposition für Felsrutschungen bei Brandstock (Obwalden, Schweiz) – Cholrüti Felsrutsch im August 2005. B.Sc thesis, ETH, Zurich.

Grämiger, L.M. (2012). Prehistoric Rock Avalanches at Rinderhorn, Switzerland. M.Sc thesis, ETH, Zurich.